

THESE DE DOCTORAT DE

L'UNIVERSITE DE NANTES
COMUE UNIVERSITE BRETAGNE LOIRE

ECOLE DOCTORALE N° 596

Matière, Molécules, Matériaux

Discipline : Ondes et Matériaux

Par

Daniel FUNES-HERNANDO

Advanced gold-based nanowires: from hybrid structures to original plasmonic and optical properties

Thèse présentée et soutenue à Nantes, le 30 novembre 2018

Unité Mixte de Recherche : Institut des Matériaux Jean Rouxel de Nantes (IMN)

Rapporteurs avant soutenance :

Stéphane PAROLA	-	Professeur, Ecole Normale Supérieure de Lyon
Olivier PLUCHERY	-	Professeur, Sorbonne Université

Composition du Jury :

Président :	Marc LAMY DE LA CHAPELLE	Professeur, Le Mans Université	
Examineurs :	Elizabeth BOER-DUCHEMIN	-	Maître de Conférences, Université Paris-Sud
	Dario PISIGNANO	-	Professore, Università di Pisa (Italy)
	Sophie QUILLARD	-	Maître de Conférences, Université de Nantes
	Bernard HUMBERT	-	Professeur, Université de Nantes
Dir. de thèse :	Jean-Luc DUVAIL	-	Professeur, Université de Nantes

Invité(s)

Alan DALTON	-	Professor, University of Sussex (United Kingdom)
-------------	---	--

Acknowledgements

And finally the day has come. In the two hundred following pages I try to describe the whole project which I have developed during the last three years. Everything has changed during this time, not only my scientific knowledge but at a personal level. A PhD project makes you to give the most and the best of yourself and pose yourself some questions that you have not even imagined before. Thus, I consider this manuscript not only a mere definition and discussion of a scientific project, it also contains a piece of myself that has matured since October 2015. I hope you enjoy reading it as much as I enjoyed developing this project and writing this manuscript.

All this project in particular and my successful career in general would not have been possible without the inestimable support of my parents who have always encouraged my curiosity, and my brother Samuel who in part is following my steps.

This PhD project has been carried out in the “Enabling Excellence” project framework. The “Enabling Excellence” project has received funding from the European Union’s Horizon 2020 research and innovation programme under the Marie Skłodowska-Curie grant agreement No 642742. I would like to thank the head of this project, Chris Ewels, for giving me this marvellous opportunity and all the fruitful discussion that we had during these three years.

This project would not have been possible without my director Jean-Luc Duvail who has guided me and helped me in everything he could. It has been a pleasure to learn from him. I would like to specially thank his patience and constant hard-work.

I am particularly grateful to both reporters and all the jury members of my thesis defence for their constructive feedback and fruitful discussion.

When I began this project my knowledge about Raman spectroscopy was basic. All the advanced spectroscopic techniques that we discuss in this manuscript would not have been possible without the expertise of Jean-Yves Mevellec. They would have neither been possible without the constant advice of Bernard Humbert. I would like to give a special thanks to Maxime Bayle who helped me analysing and discussing the finest results. Finally, a very particular gratitude to Dominik Winterauer and Tim Batten, from Renishaw plc. shared with us their ideas for the advanced nano-spectroscopic techniques described in the last Chapter of this manuscript.

My work in the lab would not have been as smooth as it was without the help of Françoise Lary. I would also like to thank Nicolas Stephant from who I learnt all that I know about SEM manipulation and handling. I would like to express my very great appreciation to Nicolas Gautier and Eric Gautron who made the first TEM analysis of my samples and answered to all my questions and problems. I would like to express my deep gratitude to Raúl Arenal and Mario Peláez-Fernández from the Institute of Nanoscience of Aragón who carried out the finest TEM measurements and always gave us a fruitful feedback. I greatly

appreciated the assistance provided by Florian Massuyeau in the UV-vis-nIR and bulk spectroscopy analysis.

My grateful thanks are also extended to Frank Petitgas who managed all the physical vapour deposition system and always found dates for treating my alumina templates. I wish to thank Julien Tranchant who made these depositions in his absence.

I wish to acknowledge Sebastian Nufer for the laser ablation of the silicon substrates in order to make correlated studies.

A special thanks for Soumaya Khelifi, John Bigeon and Stephane Cordier, our collaborators from Rennes.

I am particularly grateful and I still owe a couple of pints to Virgile Leroux who unlocked me from the IMN a Saturday evening during the hardest time of my thesis.

I would like to dedicate some lines to my group, the Physique des Matériaux et Nanostructures (PMN) group, for their constant "invisible" support and friendliness. My special thanks are also extended to the administrative, the workshop and the IT staff.

It is totally necessary to mention that in order to make a brilliant scientific research you need a great scientific team as I described but you also need some people that make your days better and encourage you to follow. All these students from the IMN, Maria, Sofia, Guillaume, Sandra, Angélica, Angélica, Jordan, Thibaud, Shunsuke, Danilo, Coline, Jérémy, Romain, Patricia, Angélique, Thomas, Théo, Emilie, Anthony, Alia, Vincent, Justine, Xenia, Jianhan, Julio...

The EnExers, Emin, Lorenzo, Ana, Dominik, Mario, Antonia, Rubén, Manuela, Giussepe, Seb and Elodie.

My spanish crew, which I found one day and became my family here, Laia, Arantxa, Irene, Dani, (H)Elena, Lucía, Clara, Manuel, Inma, Mario, Judith, Fabián, Adrián, Bea, Elisa

Among all these people that I met here in Nantes there are three of them that have accompanied me in my journey from the beginning and have made my stay here easier or even possible, Pablo, Yuman and Raquel. And moreover Yuman, for sharing the office and his patience with me.

I am particularly grateful to those ones who stand me during the whole Chemistry Degree (and even part of the Master) and even though they came to my defence and cheered me up, Martín, Edu, Clara, Pablo, Miguel Ángel, Isolda and Néstor.

A special thanks to my whole family and to my uncle Jesús that when I was a children started showing me the vast world of the chemistry.

To Chema for coming to Nantes almost every weekend during this last year (and sometimes I went there), and accompanying me for eating the "filetit".

I cannot forget Pablo and Cristian, my old friends, although not being here physically we managed to meet every night. Our long conversations that could last more than we expected.

*"La fantasía abandonada de la razón produce monstruos, pero unida a
ella es la madre de las artes"*

- Francisco de Goya

"Inin di biningui"

"Audentis fortuna iuvat"

- Vergilius

Résumé

Le très fort intérêt porté à l'étude des nanostructures plasmoniques provient à la fois de leurs comportements optiques remarquables à une échelle inférieure à la longueur d'onde (plasmon de surface localisée: LSP; polariton de plasmon de surface: SPP) et de leurs fonctionnalités améliorées ou nouvelles associées à d'autres espèces photoactives. En raison de leurs propriétés plasmoniques exceptionnelles, ces nanostructures sont des briques élémentaires (multifonctionnelles) exploitées de nos jours pour des applications dans les domaines de la nano-photonique, du photovoltaïque, ainsi que de la biologie et de la médecine, par exemple en tant que nano-capteurs ou agents d'imagerie ou de traitement in vivo et in vitro.

Dans ce travail de thèse, j'ai abordé ce sujet du point de vue des nanostructures unidimensionnelles (1D) avec un très grand rapport de longueur permettant l'étude des effets à base de SPP. Cette géométrie a été moins étudiée que celle des nanoparticules 0D. La plupart des études menées depuis plus d'une décennie concernent les nanofils d'argent et d'or avec l'étude de la propagation du SPP. Récemment, des comportements optiques originaux excitants ont été mis en évidence lors de l'association de nanofils plasmoniques à une espèce photoactive, favorisant des effets fortement renforcés et des effets nouveaux basés notamment sur le couplage plasmon-exciton.

Le développement et l'étude des propriétés électriques et optiques des nanofils et des nanotubes est un sujet fort des 20 dernières années au sein de l'équipe Physique des matériaux et nanostructures (PMN) du Jean Rouxel Materials Institute (IMN). Après avoir étudié les effets de petites dimensions sur les propriétés électriques et électrochromiques de nanofils de PEDOT, un polymère conjugué conducteur (thèse de P. Rétho ; postdoctorats de Y. Long et Y. Zhao), les travaux de l'équipe ont davantage porté sur l'étude et le contrôle du comportement de photoluminescence et des propriétés photoconductrices de nanofils/nanotubes composés d'un ou plusieurs polymères π -conjugués semiconducteurs tels que PPV, P3HT, PFO et de nanocomposites (travaux de thèse de F. Massuyeau, JM Lorcy, M. Mbarek, A. Garreau et D. Khlaifia). Des nanofils coaxiaux à cœur magnétique et gaine fluorescente ont également été développés pour permettre la manipulation magnétique de tels nano-objets 1D (thèse de JM Lorcy). Plus récemment, c'est le comportement photonique de nanofils et nanotubes à base de polymères conjugués ainsi que de nano-guides d'onde de résine SUV et UV-210 (thèse de J. Bignon) qui a été étudié en collaboration avec B. Bêche et N. Huby de l'Institut de Physique de Rennes. L'ensemble de ces travaux ont

permis de développer l'expertise locale dans la synthèse de nanostructures 1D complexes par des stratégies de type template.

Ma thèse se situe dans ce contexte et dans le cadre du réseau international de formation (International Training Network) Marie Skłodowska-Curie «Enabling Excellence» coordonné par C. Ewels à l'IMN. Ainsi, j'ai bénéficié de différentes formations sur des techniques avancées (en plus de celles proposées par l'ED 3M) ainsi que des compétences disponibles dans ce consortium regroupant 7 partenaires. En particulier, j'ai collaboré avec T. Batton et D. Winterauer de Renishaw, Inc (GB) pour la mise en place sur notre spectromètre Raman InVia de divers équipements de pointe : un dispositif porte-échantillon nano-piezoelectrique pour le positionnement et la cartographie de nano-objets individuels, un protocole de réglage optique permettant de positionner l'excitation laser et la collection du signal à quelques micromètres l'un de l'autre (géométrie « remote »), un dispositif permettant de mesurer en géométrie réflexion le signal de diffusion Rayleigh de nano-objets individuels. J'ai également collaboré avec R. Arenal et M. Pelaez pour la caractérisation avancée de mes nanofils par microscopie électronique en transmission à haute résolution et par spectroscopie de perte d'énergie électronique dans la gamme des basses énergies (LL-EELS-TEM).

Au cours de ma thèse, je me suis concentré sur la conception de nouveaux types de nanofils supportant les polaritons de plasmons de surface afin de réaliser une excitation à distance médiée par ces plasmons polaritons de surface. Un premier objectif visait à améliorer à la fois l'excitation SPP et l'efficacité des émissions lumineuses. Il a été réalisé en transformant les pointes en nanofils d'or avec des traitements au laser optimisés. Il en résulte des nanofils comportant à leurs extrémités des protubérances d'or qui doivent améliorer le couplage avec la lumière d'excitation et augmenter la lumière diffusée à l'extrémité opposée.

Un deuxième objectif visait à atteindre la détection à distance Raman médiée par le plasmon promue par des nanofils coaxiaux. La spectroscopie Raman à distance est basée sur la séparation par plusieurs micromètres du point laser d'excitation sur une extrémité du nanofil et de la détection Raman sur l'autre extrémité. La très faible efficacité de l'émission Raman le rend difficile. Des nanofils coaxiaux ont été synthétisés pour la preuve de concept. Ces études constituent des approches alternatives pour la télédétection de très petites quantités d'espèces et pour l'exploration de nanosources 1D et de nano-antennes pour des systèmes photoniques et plasmoniques intégrés.

L'essentiel des travaux menés durant ma thèse sont reportés dans ce manuscrit organisé en quatre chapitres.

Le premier chapitre est consacré à l'introduction des principales notions nécessaires à la compréhension des propriétés physiques, en particulier plasmoniques étudiées dans mon travail de thèse. Il est complété par une revue bibliographique des

comportements plasmoniques de nanofils hybrides d'or ou d'argent associés à une espèce, en particulier fluorescente. Cela permet de préciser et justifier la stratégie utilisée pour concevoir divers types de nanofils, ainsi que l'originalité des résultats obtenus au cours de ma thèse.

Dans le deuxième chapitre, la synthèse et la caractérisation des différents nanofils fabriqués au cours de ma thèse sont présentés. Le procédé de fabrication utilisé est la méthode template, qui consiste à exploiter les nanopores cylindriques de membranes poreuses d'alumine (dans mon cas) comme nano-réacteurs. A l'aide de procédés électrochimiques, il est ainsi possible de synthétiser des nanofils ou nanotubes cylindriques. En particulier, j'ai exploité un procédé permettant d'élargir de quelques nanomètres le diamètre de pores par une attaque chimique douce et ce afin d'élaborer des nanofils coaxiaux à cœur d'or et gaine de poly(3,4-éthylènedioxythiophène). J'ai été amené à contrôler la localisation du PEDOT à une des extrémités du nanofil uniquement afin de mettre en évidence sans ambiguïté un effet Raman propagé par l'intermédiaire des plasmons de surface de l'or (chapitre 4). Enfin, j'ai développé un protocole original de traitement thermique post-synthèse des nanofils par échauffement sous faisceau laser afin de créer des protubérances d'or à l'une ou aux deux extrémités des nanofils d'or. Les différents types de nanofils originaux que j'ai synthétisés sont représentés schématiquement sur la Figure 1.

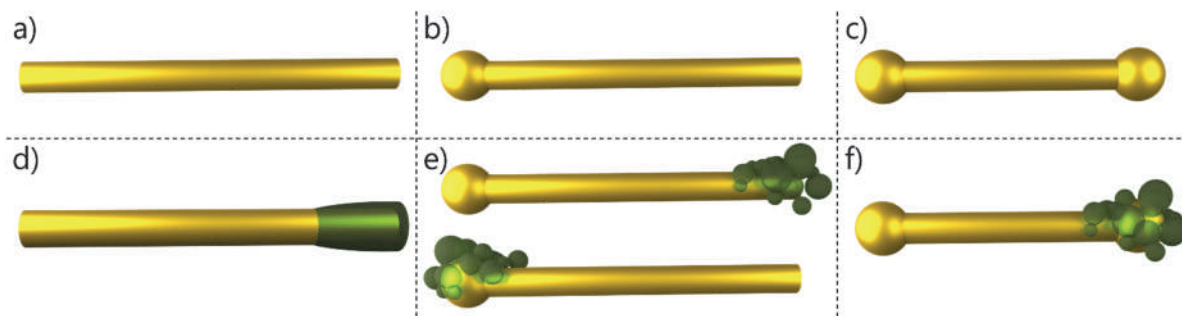


Figure 1 : a) nanofil d'or ; b) « half-dog-bone » : nanofil d'or avec une protubérance d'or à l'une de ses extrémités ; c) « dog-bone » : nanofil d'or avec une protubérance d'or à chacune des extrémités ; d) nanofil coaxial Au@PEDOT avec une gaine de PEDOT (en vert) d'épaisseur quelques nanomètres localisée à l'une de ses pointes uniquement ; e) nanofil « half-dog-bone » décrit en (b) entouré de particules de PEDOT sur la pointe du nanofil (en haut) et sur la protubérance d'or (en bas) ; f) nanofil « dog-bone » décrit en (c) entouré de particules de PEDOT sur une des protubérances d'or.

Le troisième chapitre est consacré à la caractérisation structurale moléculaire et supramoléculaire du PEDOT dans les nanofils coaxiaux Au@PEDOT. Cela a été effectué par une étude corrélant caractérisation chimique et morphologique par microscopie électronique à balayage et à transmission et caractérisation par micro-spectroscopie

Raman sur de même nanofils individuels. L'étude par spectroscopie Raman a été approfondie en utilisant différentes longueurs d'onde d'excitation (488, 514, 633 et 785 nm) et en faisant varier la polarisation lors de l'excitation et de la collecte. Cela a permis de mettre en évidence l'effet sur la conjugaison des chaînes de polymère de l'électropolymérisation extrêmement confinée du polymère conjugué autour du nanofil d'or. En particulier, l'orientation préférentielle des segments π -conjugués transversalement à l'axe des nanofils a été mise en évidence et un mécanisme de croissance a été proposé. Les effets du diamètre du nanofil et de l'emplacement du PEDOT sur l'ordre supramoléculaire ont été déterminés.

Dans le dernier chapitre, deux études du comportement optique et plasmonique des nanofils présentés précédemment sont reportées. Les méthodes permettant de corrélérer spatialement ces études en utilisant un spectromètre couplé à un microscope optique, avec une caractérisation morphologique précise par microscopie électronique, sont présentées au préalable. Dans la première étude effectuée en configuration habituelle d'excitation et collection, la diffusion Rayleigh de nanofils individuels par excitation laser et détection en géométrie réflectance a été mesurée systématiquement avec des pas de 30 nm de manière à obtenir des cartographies détaillées. Les comportements des trois types de nanofils d'or présentés sur la figure en (a), (b) et (c) ont ainsi pu être comparés, mettant en évidence l'effet des protubérances d'or et de la polarisation. Dans la deuxième série de résultats, une configuration « remote » à excitation déportée par rapport à la collecte du signal a été utilisée. Ainsi, la mise en évidence sans ambiguïté du signal Raman provenant du PEDOT lorsque l'excitation est effectuée à l'extrémité opposée du nanofil distante de plusieurs micromètres, jusqu'à 9 μm , constitue un résultat majeur de ma thèse (Figure 2). Egalement, une étude exploratoire a été menée afin d'apprécier l'apport des protubérances d'or dans les nanofils « dog-bone » et « half dog-bone » sur l'intensité du signal détecté mesuré à distance.

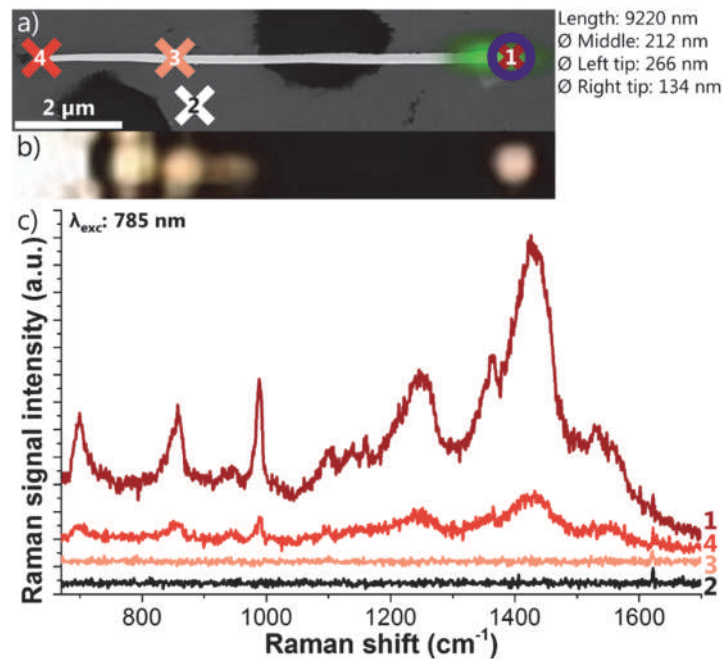


Figure 2: a) Superposition d'un cliché MEB et du signal Raman (en vert : intensité à 1447 cm^{-1}) d'un nanofil d'or couvert de PEDOT uniquement à l'extrémité droite. Les croix repèrent les positions d'excitation (X : indexées 1 à 4), la zone de collection du signal Raman est repérée par O. b) Image au microscope optique (objectif x100, LF) pour une excitation laser (785 nm) en position 4. c) Spectres Raman mesurés à la zone 1 pour une excitation aux quatre positions X.

En conclusion, ce travail de thèse a permis de synthétiser de nouveaux types de nano-objets unidimensionnels fonctionnels comportant un cœur plasmonique. Des comportements plasmoniques originaux ont été mis en évidence. Dans la suite de mes travaux, la détermination du comportement plasmonique par EELS-HRTEM apportera des informations utiles pour une analyse complète des différents effets étudiés. Il sera intéressant de préciser l'effet de l'excitation soit locale d'un nanofil plasmonique par un faisceau d'électrons ou par une sonde laser sub-micrométrique, soit une excitation du nanofil entier par un faisceau optique. Des études spectroscopiques dépendant du temps sur de tels systèmes seraient également pertinentes pour identifier le (s) mécanisme(s) impliqué(s) dans le couplage entre le nanofil métallique « dog-bone » et l'espèce Raman. Le couplage de tels nanofils « dog-bone » avec des espèces photoluminescentes est un projet très intéressant pour étudier le couplage faible et fort entre plasmon et excitons. Il s'agit d'un domaine de recherche en pleine croissance offrant de nouveaux effets fondamentaux qui pourraient avoir un impact significatif sur les dispositifs nanophotoniques.

List of acronyms

1D	1-Dimension
AAO	Anodic aluminium oxide
AFM	Atomic force microscopy
ATR	Attenuated total reflection
BIIPP	Bleach-imaged plasmon propagation
BSE	Backscattered electrons
CCD	Charge-coupled device
CL	Cathodoluminescence
CVD	Chemical vapour deposition
DBSA	Dodecylbenzenesulfonic acid
e-beam	Electron beam
EDS, EDX	Energy-dispersive X-ray spectroscopy
EELS	Electron energy loss spectroscopy
EF	Enhancement factor
FDTD	Finite difference time-domain
FEM	Finite element method
FIB	Focused ion-beam
FWHM	Full-width-at-half-maximum
HOMO	Highest Occupied Molecular Orbital
HRTEM	High resolution transmission electron microscopy
ITN	International Training Network
LECB	Light-emitting colour barcode
LF	Long focal (Objective)
LSP	Localized surface plasmon
LSPR	Localized surface plasmon resonance
LUMO	Lowest Unoccupied Molecular Orbital
MGITC	Malachite green isothiocyanate
NA	Numerical aperture
NIR	Near-infrared

NP	Nanoparticle
NW	Nanowire
OLED	Organic light-emitting diode
P3BT	Poly(3-butylthiophene-2,5-diyl)
P3HT	Poly(3-hexylthiophene-2,5-diyl)
PANI	Polyaniline
PATP	4-aminothiophenol
PC	Polycarbonate
PEDOT	Poly(3,4-ethylenedioxythiophene)
PET	Polyethylene terephthalate
PIRAS	Polarized infrared absorption spectroscopy
PL	Photoluminescence
PPE	Personal protective equipment
PSS	Polystyrene sulfonate
PTFE	Polytetrafluoroethylene
PU	Polyurethane
PVD	Physical vapour deposition
RESERS	Remotely excited surface-enhanced Raman spectroscopy
SCCM	Standard cubic centimetres per minute (fluid flow)
SCE	Saturated calomel electrode
SE	Secondary electrons
SEIRA	Surface enhanced infrared absorption spectroscopy
SEM	Scanning electron microscopy
SERS	Surface-enhanced Raman spectroscopy
SNOM	Scanning near-field optical microscope
SP	Surface plasmon
SPASER	Surface Plasmon Amplification by Stimulated Emission of Radiation
SPP	Surface plasmon polariton
SPR	Surface plasmon resonance
STEM	Scanning transmission electron microscopy
STM	Scanning tunnelling microscopy

List of acronyms

TAM	Transient absorption microscopy
TEM	Transmission electron microscopy
T-LSPR	Transversal localized surface plasmon resonance
UV	Ultraviolet
Vis	Visible (radiation)
XPS	X-ray photoelectron spectroscopy
XRD	X-ray diffraction
ZC	Z-contrast

General introduction

The very strong interest in the study of plasmonic nanostructures stems from both their remarkable optical behaviours at a sub-wavelength scale (localized surface plasmon: LSP; surface plasmon polariton: SPP) and their enhanced or new functionalities when coupled with other photoactive species. Due to these outstanding plasmonic properties, such nanostructures are elementary (multi)functional bricks exploited nowadays for applications in the fields of nano-photonics, photovoltaics, as well as in biology and medicine, for example as nano-sensors or in-vitro and in-vivo imaging or treatment agent.

In this thesis work, I approached this topic from the point of view of one-dimensional (1D) nanostructures with a very high aspect ratio that permits the study of SPP based effects. This geometry has been less investigated than the 0D nanoparticles case. Most of the studies carried out for more than a decade concerns silver and gold nanowires with the study of the SPP propagation. Recently, exciting original optical behaviours were highlighted when associating plasmonic nanowires with a photoactive species, promoting strongly enhanced effects and novel effects based notably on plasmon-exciton coupling.

The development and study of the electrical and optical properties of nanowires and nanotubes is a strong subject for 20 years within the Materials Physics and Nanostructures (PMN) team at the Jean Rouxel Materials Institute (IMN). After studying the electrical and electrochromic properties of conductive conjugated polymer nanowires (thesis of P. Rétho, Y. Long postdoctoral researchers), the work focused on the study and tuning of the photoluminescence and photoconductive properties of nanowires / nanotubes composed of one or more photoluminescent polymers and nanocomposites (thesis work of F. Massuyeau, JM Lorcy, M. Mbarek, A. Garreau, D. Khlaifia) eventually coupled to a magnetic counterpart for magnetic manipulation (thesis of J.M. Lorcy). More recently, the nanophotonic behaviour of such polymer-based nanowires and nanotubes was investigated (thesis of J. Bigeon) in collaboration with B. Bêche and N. Huby at the Institute of Physics in Rennes. These studies exploited and developed the local expertise in the synthesis of complex 1D nanostructures by hard-template based strategies.

My thesis takes place in this context and in the framework of the International Training Network (ITN) Marie Skłodowska-Curie "Enabling Excellence". I benefited of different trainings, advanced techniques and skills available in this consortium of 7 partners, in particular high-resolution transmission electron microscopy and low energy electron energy loss spectroscopy (EELS-TEM).

During my thesis, I focused on the design of new kinds of nanowires that support surface plasmon polaritons for achieving SPP-mediated remote excitation.

A first objective aimed to enhance both the SPP excitation and the light emission efficiency. It has been realized by transforming the gold nanowire tips with optimized laser treatments. It results in dog bones like nanowires, whose gold nanoparticles are expected to improve the coupling with the excitation light and to increase the scattered light at the opposite tip.

A second objective aimed to achieve the plasmon-mediated remote Raman sensing promoted by coaxial nanowires. Remote Raman spectroscopy is based on the separation by many micrometres of the excitation laser spot on one tip of the nanowire, and the Raman detection at the other tip. The very weak efficiency of Raman emission makes it challenging. Coaxial nanowires were synthesized for the proof-of-concept.

These studies constitute alternative approaches for the remote sensing of very small quantities of species and for exploring 1D nanosources and nanoantennae for integrated photonic and plasmonic systems.

This thesis report is composed of four Chapters.

The first Chapter is dedicated to the introduction of the main notions required to understand the physical properties investigated in my thesis work. It is completed by an up-to-date bibliographic review of the recent advances to evaluate the strategy exploited to design our original nanowires, as well as to assess the novelty of the results obtained during my thesis.

In the second Chapter, the synthesis and characterization of the different nanowires fabricated during my thesis are reported. Principally two kinds of original nanowires were synthesized:

- Coaxial nanowires with a gold core and a shell of poly(3,4-ethylenedioxythiophene) (PEDOT), a conjugated polymer, with the control of the position of PEDOT along the cylindrical core (all along, just at the tips or just at the top tip), a must requirement for the remote studies
- Dog-bone and half dog-bone gold nanowires, i.e. gold nanowires modified by a post-synthesis processes using laser heating, which produces gold nanoparticles at the tip(s) of the nanowire.

In the third Chapter, the investigation of the molecular and supramolecular structure of PEDOT in the coaxial Au@PEDOT nanowires is reported. A complete Raman spectroscopy study of individual nanowires was made using different excitation wavelengths and polarization at the excitation and the collection. It aimed to determine the effect of the extremely confined electropolymerization of the conjugated polymer around the gold nanocylinder, a unique geometry. The effects of the nanowire

diameter and the location of the PEDOT on the supramolecular ordering were determined.

In the last Chapter, the optical and plasmonic properties of single dog-bone and coaxial nanowires were investigated by laser nano-reflectance and by remote Raman spectroscopy. We present first the methods that permit to spatially correlate these studies made by using an optical microscope coupled spectrometer, with a precise morphological characterization by electron microscopy. It required some developments of the experimental set-up to achieve - the measurements in the remote configuration, which consists in a different location for the excitation laser and for the collection area, and - the laser nano-reflectance mapping of individual nano-objects. Then, the mapping in a direct mode of the laser nano-reflectance (i.e. at a given wavelength) of gold nanowires with different morphologies is reported before presenting their remote nano-reflectance. Finally, the remote Raman spectroscopy study of the coaxial Au@PEDOT nanowires and of (half) dog-bones nanowires coupled with PEDOT nanoparticles is proposed.

Table of contents

Acknowledgements	i
Résumé	v
List of acronyms	xi
General introduction	1
Table of contents	5
I. State of the art and strategies	11
I.1. Plasmonics and related spectroscopy	11
I.1.1. Introduction to plasmonics	11
I.1.2. Localized surface plasmon resonance (LSPR)	14
I.1.2.1. Nanoparticles: spheres and rods	14
I.1.2.2. Plasmonic nanowires.....	17
I.1.2.3. Surface-enhanced Raman spectroscopy (SERS).....	18
I.1.2.4. Enhanced photoluminescence (PL).....	21
I.1.2.5. Other effects and applications	25
I.1.3. Surface plasmon polaritons (SPP)	25
I.1.3.1. Generalities on SPP	25
I.1.3.2. SPP in metal thin films	30
I.1.3.3. SPP in Nanowires.....	32
I.1.3.3.1. Isolated nanowires.....	34
I.1.3.3.2. Nanowires on a dielectric surface	38
I.1.3.3.3. Characterization of plasmons in nanowires	42
I.1.4. Exploitation of plasmonic nanowires with surrounding species	45
I.1.4.1. Plasmon-exciton coupling: weak and strong coupling regime.....	45
I.1.4.1.1. Strong coupling regime.....	46
I.1.4.1.2. Weak coupling regime.....	46
I.1.4.2. Nanowires for remote sensing	48
I.1.4.2.1. Remote Raman spectroscopy	48
I.1.4.2.2. Remote photoluminescence.....	52
I.1.4.3. Other nanowire-SPP related applications and effects	54
I.1.5. Improving the SPP propagation	55
I.1.5.1. Gain materials for SPP	56
I.1.5.2. Antenna-coupled SPP.....	57
I.2. Synthesis of advanced 1D nanostructures for plasmonics	59
I.2.1. Synthesis of 1D Nanostructures	59
I.2.1.1. Main strategies	59
I.2.1.2. Hard-template method and filling strategies.....	61
I.2.1.2.1. Electrochemical method.....	62
I.2.1.2.1.1. Noble metals	63
I.2.1.2.1.2. Conjugated polymers	65

I.2.1.3. Core@shell nanowires	67
I.2.1.3.1. Main strategies for core@shell nanostructures	68
I.2.1.3.2. Hard template method	68
I.2.1.4. Direct optical nanolithography of polymers	70
I.2.1.5. Coupling antennae with nanowires	72
I.2.1.5.1. Main strategies	72
I.2.1.5.2. Metal etching by thermal or laser treatment	73
I.3. Strategy and methods selected for my thesis project	76
II. Synthesis & Characterization	81
II.1. Introduction	81
II.2. Template-based synthesis	82
II.2.1. AAO membranes	82
II.2.2. Gold electrode on AAO	84
II.2.3. Supporting materials for studying individual nanowires	85
II.2.4. Other key aspects to perform reproducible synthesis and dispersion processes	88
II.3. Synthesis and characterization of Au nanowires	90
II.3.1. Synthesis and dispersion of Au nanowires	90
II.3.2. Characterization	93
II.3.2.1. SEM and TEM study of Au nanowires	93
II.3.2.2. NIR-UV-vis spectroscopy	94
II.4. Synthesis and characterization of PEDOT nanowires	97
II.4.1. Synthesis of PEDOT nanowires	98
II.4.2. Characterization of PEDOT nanowires	100
II.4.2.1. Characterization by SEM and TEM	101
II.4.2.2. NIR-UV-vis spectroscopy study	102
II.4.2.3. Raman spectroscopy study	104
II.4.2.3.1. Attribution of the main Raman bands of PEDOT	104
II.4.2.3.2. Effect of the treatment with phosphoric acid	105
II.4.2.3.3. Effect of the confined electropolymerization	106
II.4.2.3.4. Effect of the laser excitation wavelength on the Raman spectrum	106
II.4.2.3.5. Raman intensity study along single nanowires	108
II.5. Synthesis and characterization of Au@PEDOT nanowires	109
II.5.1. Synthesis and morphological characterization	110
II.5.2. Characterization of the Au@PEDOT NW	115
II.6. Post-treatment: Laser dry treatments and PEDOT particles	116
II.6.1. Laser dry etching of PEDOT	117
II.6.2. Laser-induced formation of Au nanoparticles	118
II.6.3. PEDOT nanoparticles synthesis and dispersion	119
II.7. Conclusions	121
III. Supramolecular ordering in PEDOT and Au@PEDOT nanowires	125
III.1. Short review of supramolecular ordering in polymer nanowires	125
III.2. Methods and measurement: polarized nano-Raman spectroscopy	129

III.3. PEDOT and Au@PEDOT nanowires Raman comparison: Wavelength effect.....	132
III.3.1. Optimal Raman conditions for the study of PEDOT-containing nanostructures.....	132
III.3.2. Spectral comparison for Au@PEDOT and PEDOT nanowires.....	134
III.4. Supramolecular polymer ordering in nanowires analysed by polarized Raman spectroscopy	137
III.4.1. PEDOT nanowires: Effect of the diameter on the supramolecular structure	137
III.4.2. Au@PEDOT nanowires	140
III.4.2.1. Effect of the diameter on the supramolecular structure	140
III.4.2.2. Effect of the diameter and the morphology on the supramolecular structure	141
III.4.2.3. Correlated studies: micro-Raman and SEM.....	143
III.5. Proposed mechanism	146
III.6. Conclusions.....	148
IV. Advanced optical and remote plasmonic study of individual nanowires	151
IV.1. Introduction	151
IV.2. Selection of plasmonic systems	152
IV.2.1. Methods for correlated optical, spectroscopic and morphological study.....	153
IV.3. Laser nano-reflectance of advanced gold nanowires	158
IV.3.1. Methodology.....	158
IV.3.2. Results.....	160
IV.3.2.1. Effect of the morphology	161
IV.3.2.2. Effect of the polarization and the wavelength.....	162
IV.4. Remote configuration for laser reflectance and Raman spectroscopy	164
IV.4.1. Laser excitation shifted from the collection area	166
IV.4.2. Remote laser nano-reflectance	168
IV.4.2.1. Analysis for the Direct configuration.....	171
IV.4.2.2. Analysis for the Remote configuration	171
IV.4.3. Remote nano-Raman spectroscopy	173
IV.4.3.1. Proof of concept	173
IV.4.3.2. Simple gold nanowires of different lengths.....	177
IV.4.3.3. Half dog-bone nanowire with PEDOT particles on one tip.....	179
IV.4.3.4. Dog-bone nanowire with PEDOT particles on one tip.....	181
IV.5. Conclusions.....	183
Conclusions and Perspectives	185
Appendix I. Polarized nano-Raman spectroscopy.....	189
Appendix II. Laser nano-reflectance 3D plots.....	195
List of references	201

CHAPTER I

State of the art and strategies

I. State of the art and strategies

This Chapter is dedicated to the introduction of the main notions required to understand the studies reported therein. It is completed by an up-to-date bibliographic review of the recent advances to evaluate the strategy exploited to design our original nanowires, as well as to assess the novelty of the results obtained during my thesis.

In the Part 1, the two main plasmonic effects (localized surface plasmons (LSP) and surface plasmon polaritons (SPP)) of metallic nanostructures are briefly introduced, altogether with their broad exploitation for both fundamental progress and applied goals when combined with other species located in a close environment. After general considerations for nanoparticles, the review of previous studies on 1D-like geometry is privileged, motivated by my work exploiting nanowires. The Part 2 is dedicated to a review of the synthesis of advanced metal and polymer-based nanowires, mainly by template strategies in direct relation with the original developments I achieved.

I.1. Plasmonics and related spectroscopy

I.1.1. Introduction to plasmonics

Plasmon is a quantum of collective oscillations of the free electron gas density in a metal. Surface plasmons (SP) are confined at the metal-dielectric interface. The requisite for a material to support surface plasmons is to have a dielectric constant with a large negative real component and a small positive imaginary component, normally metals. The atomic structure of metals can be roughly described as a lattice of positively charged ions embedded in a cloud of delocalized free conduction electrons. When these free electrons are excited by an electromagnetic field, they can collectively move with respect to the cations lattice resulting in a plasmon oscillation analogously to a mechanical oscillator. The incident electromagnetic field would act as sinusoidal driving force and the Coulombic attraction from the cations lattice would act as restoring force. In the case of subwavelength-sized structures, this effect is extremely confined, resulting in new optoelectronic properties at the nanometre scale. The resonance energy corresponds to the maximum of scattering and absorption by the plasmon, called surface plasmon resonance (SPR). It is defined by the nanostructure nature, its morphology and the medium surrounding it.¹⁻⁶

First reports of plasmonic behaviours were made by Faraday in 1857 when he observed the colours of different dispersions of gold nanoparticles that he prepared⁷, and by Wood when he observed an uneven distribution of light in a diffraction grating⁸. In the beginning of the XX Century, Siedentopf and Zsigmondy followed their work when

they were capable to see “ultramicroscopic” (nanometric) gold particles embedded in a gold ruby glass.⁹ J.C. Maxwell Garnett and later Mie explained the behaviour of these “less than 0.1 μm spherical” gold particles according to Maxwell equations.¹⁰⁻¹² Ritchie, in 1957, following the work of Pines¹³⁻¹⁵ explained the “energy loss of electrons to plasma oscillations” in thin metal foils (propagating surface plasmons).^{5,16} Since then, the study of plasmonics has grown enormously and nowadays is one of the hot topics in nanophotonics.^{2,17-19}

The possibility of manipulating the light under the diffraction limit and the new properties given by the plasmonic nanomaterials opens a new range of applications in such diverse fields as medicine^{3,20,21}, photovoltaics^{22,23}, nanophotonics²⁴⁻²⁹ or trace sensing^{3,20}.

These plasmons can be promoted by incident electrons³⁰⁻³⁴ or photons^{4,5,35,36}.

The case of activating plasmons by electron bombardment, first reported in 1930 by Rudberg³⁰ and furtherly studied in 1959 by Powell and Swan³⁷ and in 1967 by Teng and Stern³⁸, can be evidenced by techniques as the Scanning Tunnelling Microscopy (STM)^{34,39,40}, Scanning Electron Microscopy (SEM)³², Cathodoluminescence (CL)^{33,38}, Electron Energy Loss Spectroscopy (EELS)^{30,33,37} or indirectly by X-ray photoelectron spectroscopy (XPS)⁴¹

But the most common technique is irradiating these nanostructures with an electromagnetic field, i.e. light. Due to its interaction with the confined free electrons in the nanostructures, a plasmonic extinction (absorption + scattering) band appears (Figure I.1),⁴² different to the bulk material, that is transduced in a colour change.^{1,5,9,10,43-50} The magnification of the electromagnetic field at the metal-dielectric interface can be utilized to enhance by orders of magnitude the signal of closely packed active materials. This enhancement can be tuned by designing rational plasmonic nanostructures up to detect single molecules.^{3,51-53} Different spectroscopic techniques have been used to investigate or to exploit this phenomenon: refractive index measurement^{54,55}, surface-enhanced Raman spectroscopy (SERS)^{3,51,53,56-59}, surface enhanced infrared absorption spectroscopy (SEIRA)¹⁷ and enhanced photoluminescence^{3,60-63}.

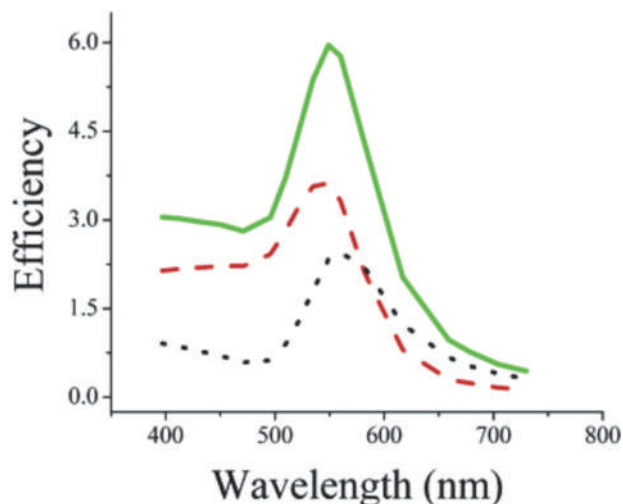


Figure I.1. Calculated spectra of the efficiency of absorption Q_{abs} (red dashed), scattering Q_{sca} (black dotted), and extinction Q_{ext} (green solid) for $D = 80$ nm gold nanospheres.⁴²

Two types of surface plasmons have been described (Figure I.2). First, the localized surface plasmon is confined in single nanostructures, whose size are smaller than the wavelength of the excitation light. Second, the surface plasmon, are found normally in thin metallic surfaces and in 1-dimensional (1D) nanostructures. Additionally, when a photon interacts with a SP, it can create a SPP which propagates at the metal-dielectric interface.^{3,5,64,65}

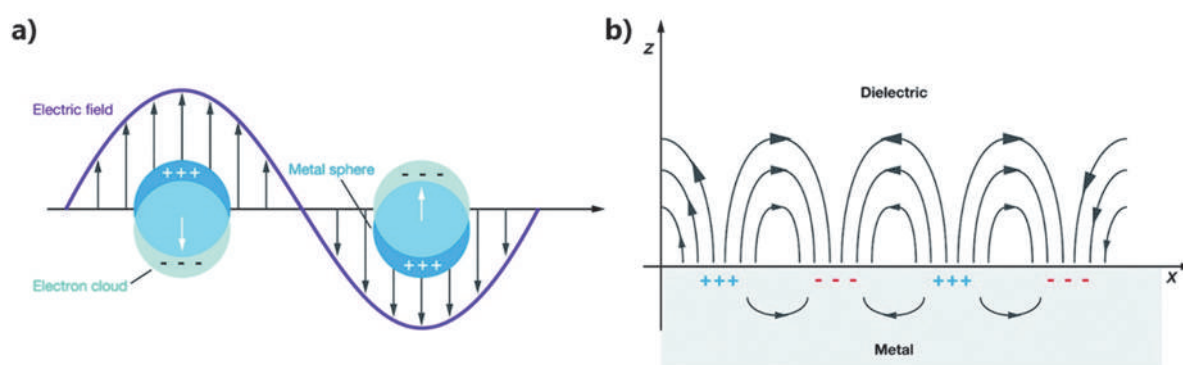


Figure I.2. Schema illustrating a) a localized surface plasmon resonance and b) surface plasmon. Adapted from Willets and Van Duyne.³⁵

I.1.2. Localized surface plasmon resonance (LSPR)

When light interacts with a metal particle smaller than its wavelength ($\emptyset \leq \lambda$), the surface plasmon is confined in the nanoparticle, this is called a localized surface plasmon (Figure I.2a). When the light frequency matches the eigenfrequency (frequency of a system at which it would freely oscillate) of the NP plasmon, a resonance (LSPR) phenomenon occurs. The LSPR enhanced strongly the surrounding electromagnetic field up to 10000 times but it is confined very close to the metal particle surface.^{20,45,66} The resonance frequency of a nanoparticle is influenced by different parameters: its material^{1,43,67,68}, size^{11,12,43,48}, shape^{33,36,43,48,69} and the dielectric environment^{63,70-73}. Most frequently used materials are gold and silver due to their strong LSPR in the visible and near-infrared (NIR) regions of the spectrum.^{1,43,44,68,74}

I.1.2.1. Nanoparticles: spheres and rods

Normally, small spherical particles only have a single and sharp absorption band corresponding to their plasmon resonance. A dipole is excited in the nanoparticle by the incident electromagnetic field and the whole cloud of free electrons oscillates at that frequency.^{1,20,66,75} Different authors have refer to Mie theory to calculate the extinction coefficient (γ) for each wavelength (λ) (Equation (I.1)), although it is necessary to note that it is only valid for well dispersed spherical nanoparticles with a small radius.^{11,20,66,76,77}

$$\gamma = \frac{24\pi^2 R^3 N \varepsilon_d^{3/2}}{\lambda} \frac{\varepsilon_{mi}}{(\varepsilon_{mr} + 2\varepsilon_d)^2 + \varepsilon_{mi}^2} \quad (\text{I.1})$$

where R is the radius of the nanoparticle, N is the number of particles per unit volume, and ε_d , ε_{mr} , and ε_{mi} are the dielectric constant of the medium surrounding the nanoparticle, and the real part and imaginary part of the metal nanoparticle dielectric constant, respectively. Other theories, such as the electrostatic approach, have also been used in order to elucidate the plasmonic behaviour of these dispersed nanoparticles.⁶⁶

In the case of larger spherical particles, quadrupoles and multipoles are generated due to the fact that different domains of free electrons inside the nanoparticle oscillate at different resonance frequencies (Figure I.3).^{1,3,65,76,78}

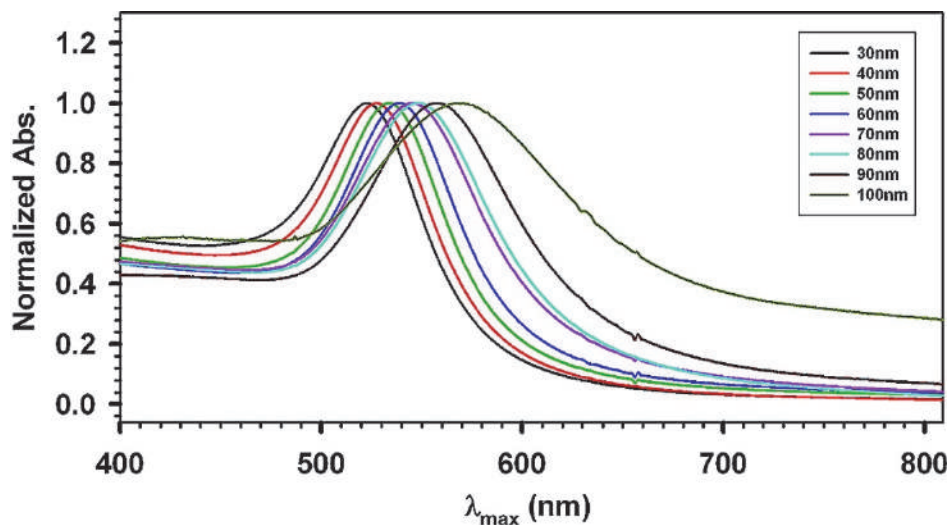


Figure I.3. UV-vis spectra (normalized) of Au nanoparticles of different particle sizes in aqueous solution.⁷⁶

Non-spherical and anisotropic particles have other LSPR modes due to their unequal dimensions between their main axes. Nanorods (aspect ratio <10-20) have certainly been the most studied non-spherical nanoparticles (Figure I.4). They normally present a dipole plasmon resonance longitudinal to their main axis and another transversal one that can be tuned by their aspect ratio and absolute dimensions.^{6,43,69,77,79}

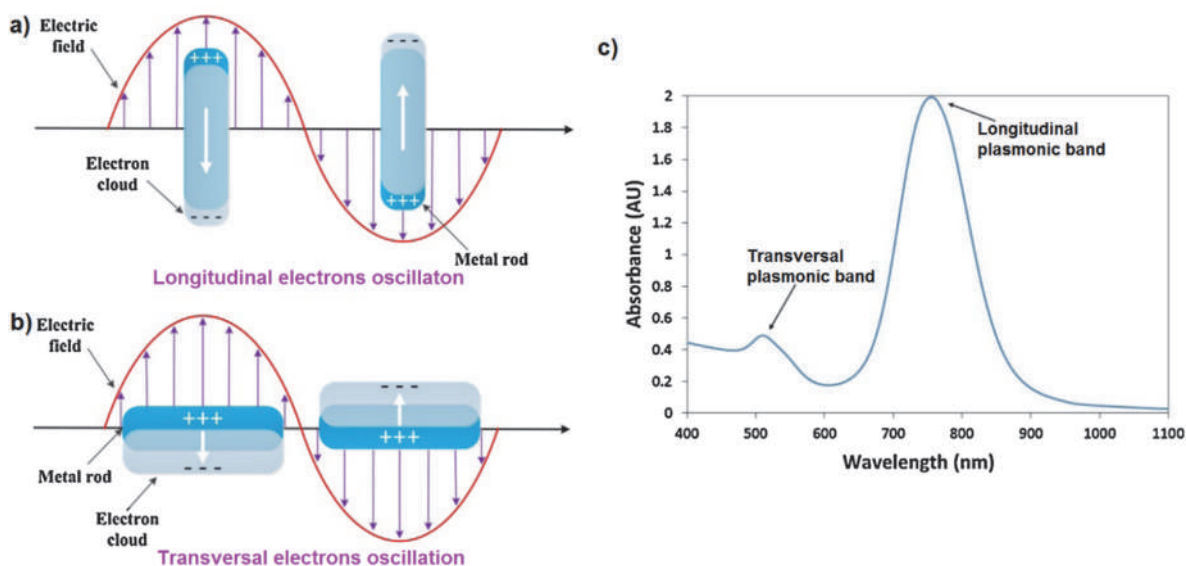


Figure I.4. Schema illustrating the a) longitudinal and b) transversal LSPR excitation for gold nanorods and c) LSPR longitudinal and transversal absorption bands. Adapted from Cao et al.⁷⁷

Gans proposed a theory to calculate the extinction coefficient for metallic nanorods describing them as ellipsoidal nanoparticles.^{69,80} The plasmonic behaviour of both kinds of nanoparticles should barely differ, appearing the two characteristics bands described before.

In the case of larger and differently shaped nanoparticles, higher ordered resonances appear, that are in general less intense than dipole ones.⁵ But some anisotropic particles can have multipolar resonances with a large absorption.^{20,78} Different particles sizes and shapes, and their interactions with an incoming electromagnetic field, have been theoretically and experimentally studied, giving similar results (Figure I.5).^{20,48,78,81,82} It should be noted that the two peaks found for the sphere correspond to the dipole (the band closer to 400 nm) and to the quadrupole (the band closer to 350 nm) modes.⁷⁵

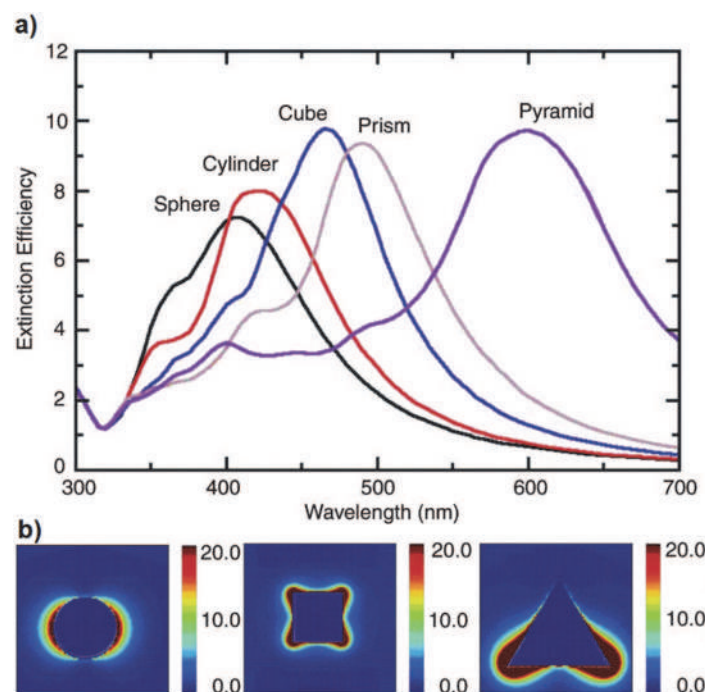


Figure I.5. a) Extinction efficiency (ratio of cross section to effective area) of silver nanoparticles in vacuum having the indicated shapes. Each particle has the same volume, taken to be that of a sphere with a radius of 50 nm. b) $|E|^2$ contours (E is electric field) for a sphere, cube, and pyramid, plotted for wavelengths corresponding to the plasmon peak in (a), with peak $|E|^2$ values of 54, 745, and 9770, respectively. The corresponding polarizations were chosen for a maximum value of $|E|^2$. Adapted from Haes et al.²⁰

Sharp irregularities act as antennas due to the crowding effect of the electric field lines, this "lightning rod" effect increase the electromagnetic field in their surroundings.^{65,83-85} LSPR modes are also found in metal film nano-roughness, their optical properties are similar to those of the corresponding solid particles of same size and shape.^{65,86,87}

Surface plasmons of nanoparticles in close proximity can also interact and yield new resonances. In this case, the generated electric field can be extremely high and confined to this "hot spot".^{43,45,65,88}

I.1.2.2. Plasmonic nanowires

1-dimensional high aspect ratio nanoparticles (>10), i.e. nanowires, are a special kind of plasmonic entities. Their transversal size is smaller than the visible light wavelengths, supporting LSPR as a nanorod. But its longitudinal dimension is normally much larger and it can support multipolar LSPR and SPP. Furthermore, the sharpness of their tips can induce a lightning rod effect, making these special kind of nanoparticles an interesting subject of study with a broad field of potential applications.^{57,77,79,89–91}

Several research have been made in both single and arrays of nanowires. Different lengths have been studied, reporting the existence of multi-order plasmonic modes for longitudinal LSPR.^{57,89,90,92,93} Polarized studies revealed that the transversal mode is perpendicularly polarized and the longitudinal mode is parallel polarized.^{89,90}

Hot spots occurring between nanowires or between a nanowire and a substrate are also investigated, notably for SERS or photoluminescence enhancement effect.^{79,88,89,94}

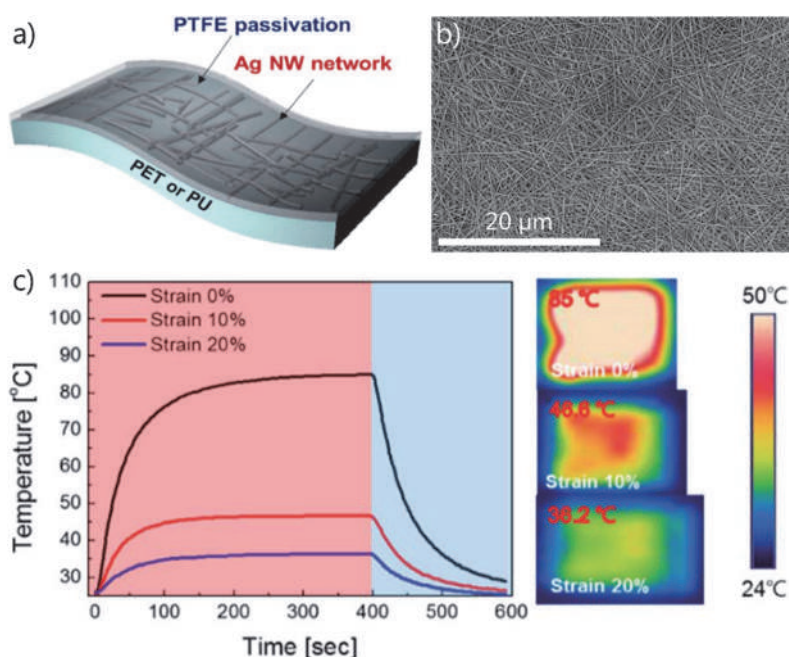


Figure I.6. a) Schematic of a polytetrafluoroethylene (PTFE)/Ag NW hybrid electrode on flexible polyethylene terephthalate (PET) or stretchable polyurethane (PU) substrates.⁹⁵ b) Typical SEM image of a Ag nanowires network (nanowire diameter of 130 nm).⁹⁶ c) Temperature profiles and IR images of a stretchable transparent thin film heaters with PTFE/Ag NW electrodes as a function of strain while operating at 8 V of input voltage. Adapted from Lee et al.⁹⁵ and Bi et al.⁹⁶

One of the most studied architectures involving nanowires and their LSPRs is the 2D nanowires network (Figure I.6a&b). This geometry allows the combination of the plasmonic, electric and mechanical properties of billions of nanowires on a macrosurface. Novel transparent and flexible devices sensitive to stretching, heat, light, pressure or chemical species that exploit such metal nanowire arrays are under investigation (Figure I.6c).^{95–104} Alternatively, the plasmonic hot spots between silver nanowires have also been exploited to generate a local welding in order to improve the electrical percolation between nanowires. It results in an improved conductivity of these 2D nanowires networks.^{95–104}

But among of all the plasmonic properties of nanowires are their capacity to transmit SPP along its main axis. We discuss this phenomena later in this Chapter, as it is a main research axis of my thesis work.

I.1.2.3. Surface-enhanced Raman spectroscopy (SERS)

The enhanced and confined electromagnetic field that appears in close proximity of a plasmonic nanoparticle due to a LSPR can couple with a Raman active species placed in that region and increase its Raman spectroscopy signal (Figure I.7). It was first reported in 1974 by Fleischmann and collaborators when they observed the enhancement of some Raman peaks of the pyridine when adsorbed on a silver electrode.⁵¹ Although they did not explain the phenomena by a plasmonic behaviour, Philpott in 1975¹⁰⁵ and Albrecht and Creighton in 1977¹⁰⁶ claimed that the enhancement was due to the SPP on the silver electrode. But Moskovits in 1978¹⁰⁷ and Creighton, Blatchford and Albrecht changing their first theory in 1979⁵², defended that the SERS effect was caused by the LSPR due to the roughness of the metal surface.

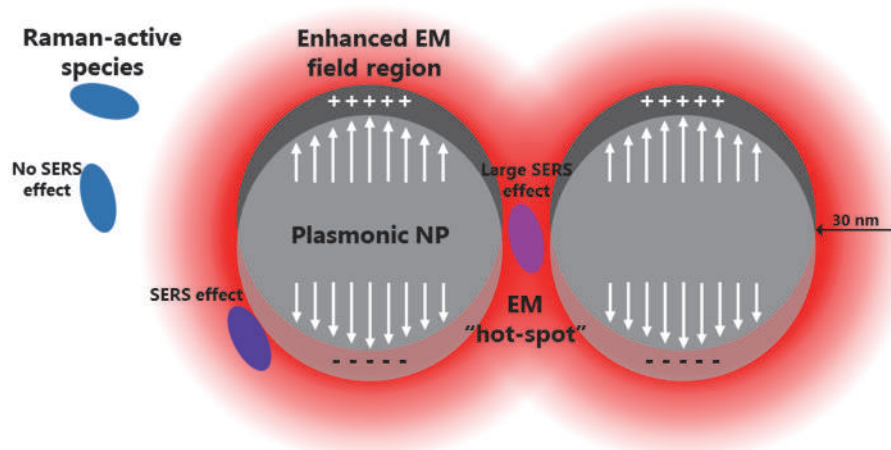


Figure I.7. Schema of the typical configuration for SERS effect within spherical nanoparticles.

Different studies have been made since then and nowadays the enhancement of Raman signal by SERS effect is widely studied and exploited (Figure I.8). In order to get an optimal enhancement, the maximum of the extinction spectra of the Raman active species and the plasmonic nanoparticle should superpose.^{58,108–110}

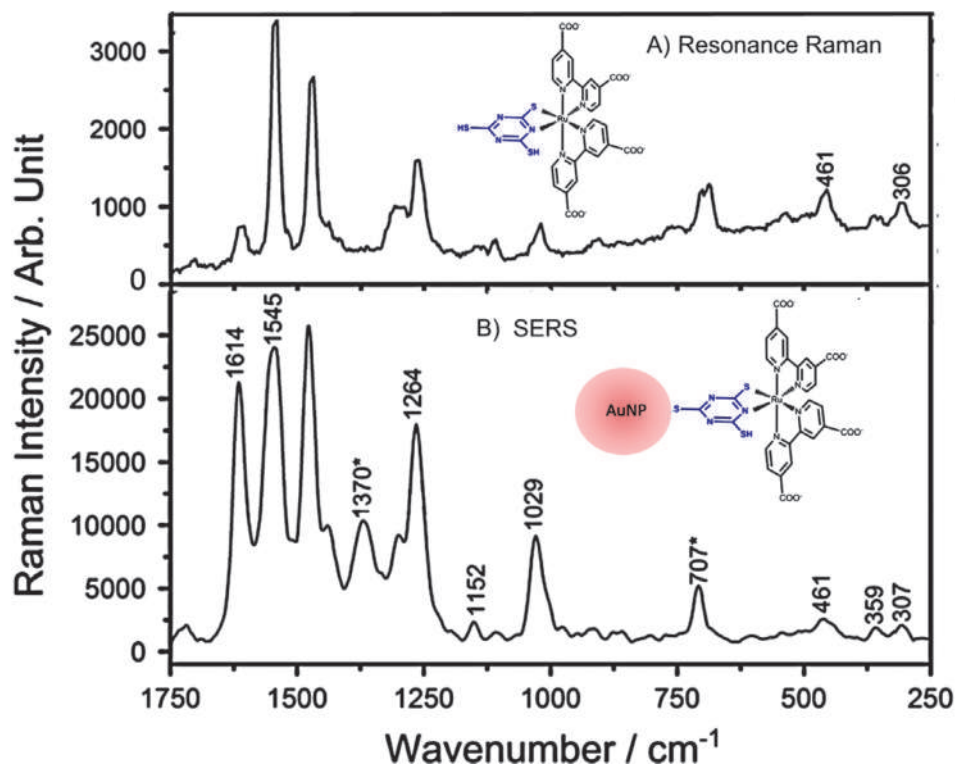


Figure I.8. Comparison of the resonance Raman spectrum of $[Ru(dcbpy)_2(tmt)]_3$ in aqueous solution (A), and SERS spectrum in presence of functionalized gold nanoparticles (B) ($\lambda_{exc} = 532 \text{ nm}$).^{109,110}

Two main mechanisms have been proposed to explain the SERS effect: the electromagnetic enhancement and the chemical enhancement. Although most of the authors support that both mechanisms coexists, the discussion comes from the relative contribution of each mechanism to the enhancement.^{58,108,111}

The electromagnetic theory is directly related to the plasmonic nanostructure, as it describes the enhancement of the electromagnetic field (light) in its surroundings. When a Raman active species is placed in this region, its Raman signal is enhanced purely due to the increased light radiation that it receives.^{108,111}

The chemical theory, in opposition, describes the behaviour of the Raman active species. When this species can chemisorb to the plasmon active metal surface (normally by a free pair of electrons), a charge transfer can be produced between them. This charge transfer can provide the electrons for a resonant Raman transition, that in a normal case would be avoided because of the HOMO and LUMO level positions of the Raman active species.^{108,111,112}

The combination of both phenomena produces a huge enhancement of the Raman signal that directly depends on the nature and geometry of the substrate and the analyte, and the excitation wavelength. This increase of the signal can be measured through the enhancement factor (EF).^{20,108,111} The enhancement factor of the Raman signal is directly related to the LSPR-generated confined electromagnetic field and decreases quickly with the distance. The influence distance have been reported to be from few nm up to 30 nm (Figure I.9).^{3,20,56,59,80,89} In order to achieve large enhancements, the morphology and the distribution of the nanostructures is finely tuned. Arrays of coupled nanoparticles or sharp edges are used to generate "hot-spots" where the Raman-active molecules should be placed. When the enhancement is very strong, single molecule detection can be achieved.^{58,80,113}

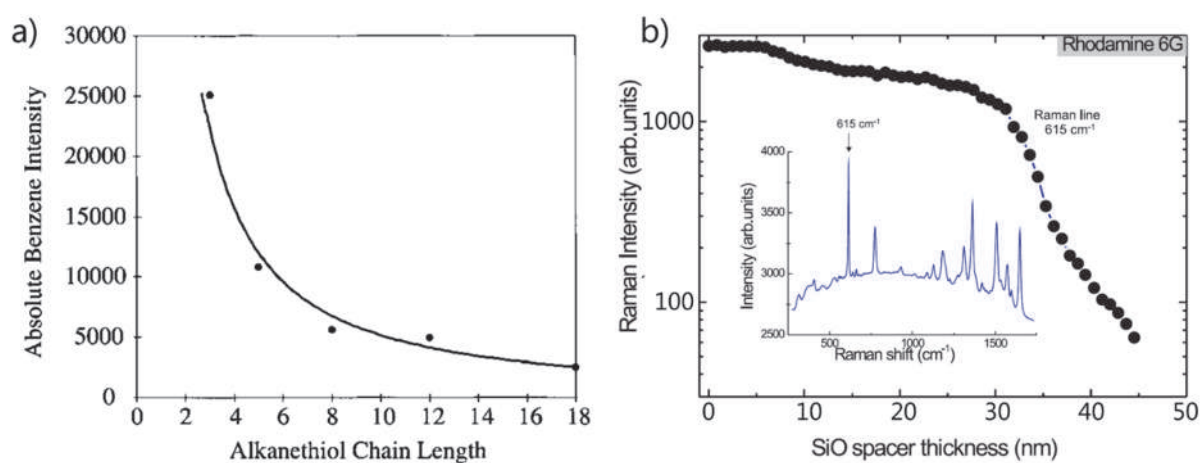


Figure I.9. a) Plot of SERS intensity (I) for 8.6×10^{-3} M benzene in water on a silver roughened substrate coated with an alkanethiol as a function of increasing alkanethiol chain length, illustrating the SERS interfacial distance dependence. (exposure times: 240 s ; 647 nm excitation ; 30 mW).⁵⁶ b) SERS signal distance dependencies for Rhodamine-6G molecules obtained for Ag roughened substrates with gradually increasing SiO spacer thicknesses across the surface. SERS spectrum is shown in the inset. Excitation power is 10 μ W at 532 nm and exposure time is 1 s.⁵⁹ Adapted from Kennedy et al.⁵⁶ and Kukushkin et al.⁵⁹

Le Ru and co-workers published in 2007 a careful and detailed study about the EF for colloidal dispersions and single molecule SERS samples. They defended that in order to make a reproducible study and to give a clear EF, a non-SERS sample should be prepared and measured under the same conditions of the SERS sample. This would allow to get the same cross-section of the sample excited (the same quantity of analyte that gives Raman scattering). The other option is to know exactly the cross-section for each measured analyte. They compared and analysed their results and those from other authors giving a clear image of up to $\sim 10^6$ enhancements for normal SERS and up to $\sim 10^{10}$ for single molecule SERS.⁵⁸

The big difference in the EF for colloidal samples and single molecules samples resides in two causes. The main one originates from the uniformity distribution of the plasmonic enhancement. A single molecule is placed in a hot-spot, taking the full LSPR enhancement. While in a colloidal dispersion, the molecules are placed at different positions and the final Raman signal is an average of different levels of LSPR enhancements. Additionally, the non-strictly uniform shape of colloidal samples: while in the single molecule test, the optimal conditions of coupling and polarization are selected. In the colloidal sample the plasmonic particles have different orientations and sizes, so with different optimal conditions for SERS effect.⁵⁸ In that study they also reported that an EF of 105 may be sufficient to detect single molecule by SERS.⁵⁸

The main application of SERS effect is for the detection of analytes in very low concentration (trace sensing and single-molecule sensing).^{58,80} Biological analysis and chemical warfare agents are among the others most studied systems. It has also been applied in spectroelectrochemistry, motivated by the presence of a plasmon-active metal electrode.¹¹⁴ SERS effect has also been involved in the study of art works¹¹⁵ and, recently, in the design of labels for anticounterfeiting^{116,117} and food safety¹¹⁸ among others.

I.1.2.4. Enhanced photoluminescence (PL)

When a photoluminescent species is in the vicinity of a nanoparticle, its emission can couple with the LSPR to get enhancement up to 400 times (Figure I.10).^{71,80,119–122}

First theoretical studies about the behaviour of photoluminescent molecules in close proximity to metal surfaces, including emission quenching or enhancement were made during the 1970s by Kuhn¹²³ and Philpott^{124,105}. In 1980, Glass¹²⁵ and Chen¹²⁶ reported the enhanced luminescence of molecules adsorbed on noble metal particles. Several groups focused their studies in this topic and 5 years later, Moskovits reviewed their research.¹²⁷

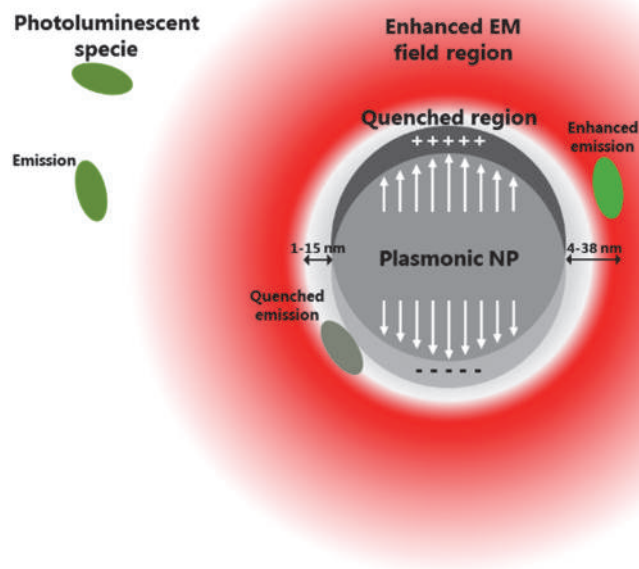


Figure I.10. Schema of the typical configuration for enhanced photoluminescence effect within a spherical nanoparticle with the quenching distance and the maximum enhanced distance plotted.

The combination of a plasmonic nanostructure with a photoluminescent species forms a very useful hybrid. While a metal nanoparticle normally shows almost no photoluminescence, its optical extinction cross section is high, transforming a big amount of that light into LSPR and enhancing the electromagnetic field in their surroundings. In opposition, photoluminescent species offer a strong photoluminescent but a relative low extinction cross section compared to the metal nanoparticles. Positioning a photoluminescent species in the electromagnetic field enhanced volume produced by a plasmonic nanoparticle forms a hybrid that have both high extinction and enhanced emission cross-section. In the other hand, if the emission frequency of the PL species is in resonance with the LSPR of the plasmonic nanoparticle, the enhanced emission observed will be caused by the radiation of light from the metal at the same frequency due to elastic scattering through the LSPR. Because of this extremely high PL signal in both cases, it is very sensitive to any changes in the environment of the hybrid nanoparticle, offering a powerful tool for detection of different species (Figure I.11 & Figure I.12).¹²²

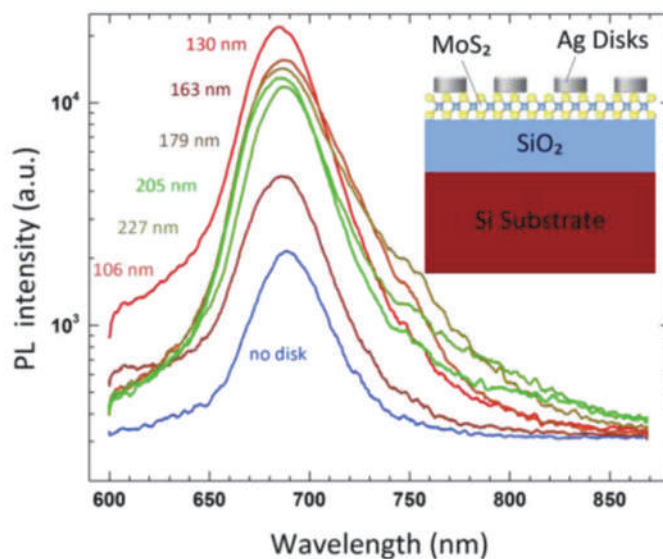


Figure I.11. Enhanced PL at plasmonic array/MoS₂ heterostructures. PL intensity comparison of each array. Inset shows the cross-section of the plasmonic/MoS₂ heterostructure. Adapted from Butun et al.¹²¹

It can be inferred that the maximum PL enhancement occurs when the overlap between the plasmonic LSPR band of the nanoparticle and the extinction of photoluminescent spectra of the PL species yields a maximum, similar to what we exposed for the SERS effect (Figure I.12).^{122,128}

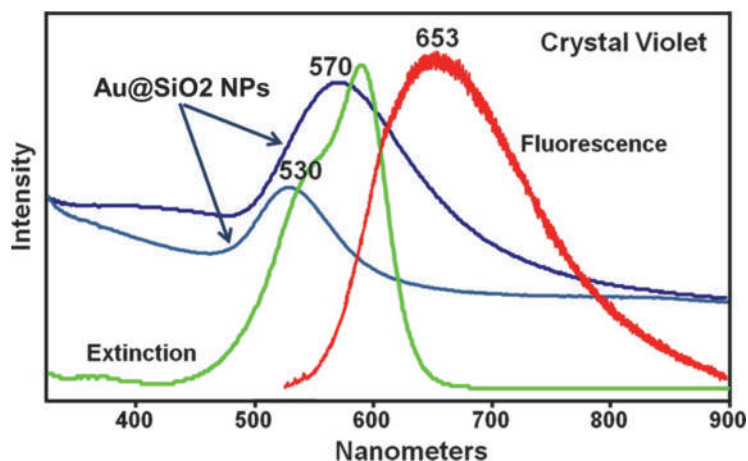


Figure I.12. Qualitative extinction spectra of small Au@SiO₂ 40 nm nanoparticles (light blue), large 100 nm Au@SiO₂ nanoparticles (dark blue) extinction (green) and emission (red) spectra of crystal violet. The more overlapping between the LSPR band of the nanoparticles and the extinction band of the crystal violet, the stronger PL enhancement will be achieved. In this study they were reported EF of 29 to 53 for the small nanoparticles and 47 to 155 for the large ones. The higher EF were got when the nanoparticles were forming aggregates. Adapted from Camacho et al.¹²⁸

A main difference with SERS effect is that a quenching effect of the PL is observed when the emitter is in contact, or very close to the plasmonic nanoparticle. This is due to a charge or an energy transfer between the metal and the PL species, resulting in a non-radiative decay. When the metal-emitter distance is gradually increased to few nanometres, a fast transition toward a maximum enhanced photoluminescence is observed. Then, the enhanced photoluminescence starts to decrease, phenomenon attributed to the decay in the enhanced field (Figure I.10). The optimal separation to maximize the photoluminescence enhancement has been both theoretically¹²⁹ and experimentally¹²⁹ investigated (Figure I.13), with some discrepancies between the different studies, possibly due to the type of the plasmonic nanostructure and the PL species.^{61–63,71,72,120,122,129,130} The quenching distances reported vary from 1 nm^{61,131} to 15 nm¹³² and the maximum PL enhancement distances ranges between 4 nm¹³¹ and 38 nm¹³². Some authors have reported the plasmon enhanced photoluminescence neglecting the quenching effect. In the case of a thick layer of PL species, the quenching effect affects only a limited thickness.^{119,133}

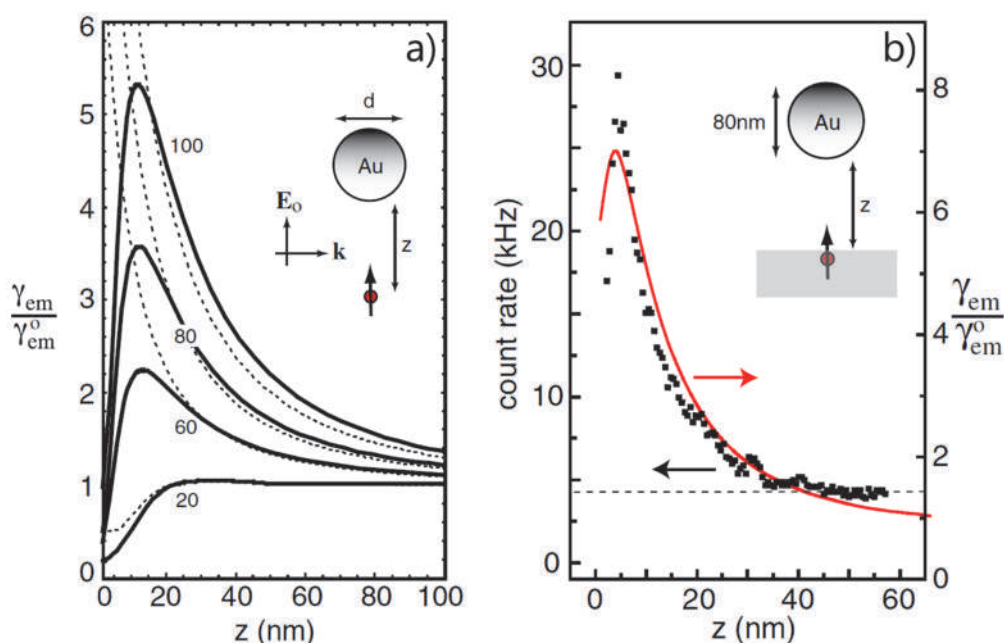


Figure I.13. a) Calculated fluorescence rate γ_{em} as a function of molecule-particle separation for different particle diameters. γ_{em} are normalized with their corresponding free-space values γ_{em}^0 (no nanoparticle $z \rightarrow \infty$). The solid curves are the result of multiple multipole calculations, whereas the dashed curves correspond to the dipole approximation which fails for short distances z . ($\lambda_{exc} = 650$ nm; $\epsilon = -12.99 + i1.09$ for gold). b) Fluorescence rate as a function of particle-surface distance z for a vertically oriented molecule (solid curve: theory, dots: experiment). The horizontal dashed line indicates the background level. ($\lambda_{exc} = 637$ nm). Adapted from Anger et al.¹²⁹

The applications of plasmon enhanced photoluminescence have grown during the last years, mainly thanks to the inclusion of weak emitters and its development in a broader region of the electromagnetic spectrum.¹²² Greater enhancements and novel properties can be achieved by tuning the morphology at the nanoscale of both the plasmonic nanostructure and the photoluminescent material.¹³⁴

Up to now, the main areas of application are trace sensing¹³⁵, bioimaging¹³⁶ and super-resolution imaging¹³⁷. This enhanced PL effect also permits to study the dynamic behaviour of single molecules by live tracking, such as in catalytic reactions¹³⁸, DNA hybridization¹³⁹ or electrochemical reactions¹⁴⁰.

I.1.2.5. Other effects and applications

Other exploitations or other effects arise due to the enhancement of the electromagnetic field in the surroundings of the metal particle and its coupling with a target species. We should cite the sensing by refraction index variation,^{54,77,141,142} enhanced photochemistry,^{122,143,144} selective and monitored catalysis,¹⁴⁵ or hyperthermia,^{3,21} improved efficiency of light emission or of light absorption and photoconversion in organic light-emitting diode (OLED)¹⁴⁶ or photovoltaics¹⁴⁶, respectively.

Their straightforward application is for sensors based on the enhancement of the electromagnetic field in the metal-target species interface. This allows the detection of traces of species that bind to the metal surface using spectroscopic techniques as described before. Both metallic thin films and particles arrays have been used as plasmonic substrates, through excitation of SPP and LSPR respectively, monitoring the signal change in real time.^{53,58,59,113,147,148}

Another SPR-based sensing technique is the colorimetry. These sensors allow the detection of target species that induce an aggregation of plasmonic particles in solution. The colour of the solution changes between non-aggregate and aggregate state due to the coupling between the LSPR of the particles.^{5,50}

I.1.3. Surface plasmon polaritons (SPP)

I.1.3.1. Generalities on SPP

The first observation of SPP on metal films was made by Wood in 1902⁸. In 1907 Zennek¹⁴⁹, and 1909 Sommerfeld¹⁵⁰, predicted the propagation of electromagnetic waves on flat metallic surfaces but did not give a plasmonic explanation. In 1930 Rudberg³⁰ and during the 50s Pines and Bohm^{13,14} and Ferrell¹⁵¹ observed energy losses of electrons in metal films. Pines in 1956¹⁵ introduced the term "plasmon". Ritchie in 1957¹⁶ and Powell and Swan in 1959³⁷ gave the first theoretical descriptions

of surface plasmons. During the 60s³⁸ and the 70s^{41,152} there was a deeper research of this effect, and in 1974, Cunningham used the term "surface plasmon polariton" for the first time to explain this effect¹⁵².

It is defined as the coupling between collective oscillations of electrons in the metal (surface plasmons) and the resulting confined electromagnetic field (polariton). This polariton is evanescently confined in the direction perpendicular to the interface. The term polariton is used to define a field that is strongly coupled to a dipolar excitation, i.e. electrons oscillations in the metal. The SPP are confined at the metal surface in the perpendicular direction and they can propagate non-radiatively along the surface (Figure I.2b).¹⁵³ When they are excited and coupled with an incoming electromagnetic field, they greatly enhance the optical near-field. These evanescent waves follow the geometry of the interface and they can be manipulated under the light diffraction limit. Their propagation length will depend on the dielectric constants of the metal and the dielectric material (a material with a lower imaginary part of dielectric constant help to reduce SPP losses)¹⁸ and their geometry (flat interfaces give smaller SPP losses than rough ones).^{5,18,64,154}

A central point deals with the excitation of SPP. According to the conservation rule of momentum, it is necessary that the momentum of the vector of the excitation light (incident wave) be equal to the plasmon polariton mode one (\tilde{k}_{SPP} , propagative wave) (Equation (I.2)),^{91,155} a critical point as a mismatch is generally obtained (Figure I.14a).^{1,2,18,64,154,156-158}

$$\tilde{k}_{SPP} = \beta + i\alpha \quad (I.2)$$

where β and α are the propagation and attenuation constants, respectively.^{91,148,155}

In order to solve it and to excite the SPP in the interface, the Kretschmann configuration (Figure I.14b) uses a prism with a different dielectric constant than air, normally glass, making the in-plane component of the light wavevector to match with the SPP wavevector (Figure I.14a).^{1,2,18,64,154,156-158} In a two-layer conformation (Figure I.14c), a dielectric layer is added between the prism and the metal and the light tunnels through it, making possible to have different excitation angles.^{1,18} In the Otto configuration (Figure I.14d), this dielectric layer is an air gap between the metal and the prism.^{1,18,159} The light can also be introduced with the matched wavevector via a fibre coupler^{18,160} or, by a scanning near-field optical microscope (SNOM) probe¹⁶¹ (Figure I.14e) in order to excite directly the SPP. Alternatively, irregularities or gratings in the metal-dielectric interface (Figure I.14f&g) transform the momentum of the incident wavevector into a distribution of new wavevectors, and some of them can match the conservation rule.^{1,8,18,65,83,87,162-166}

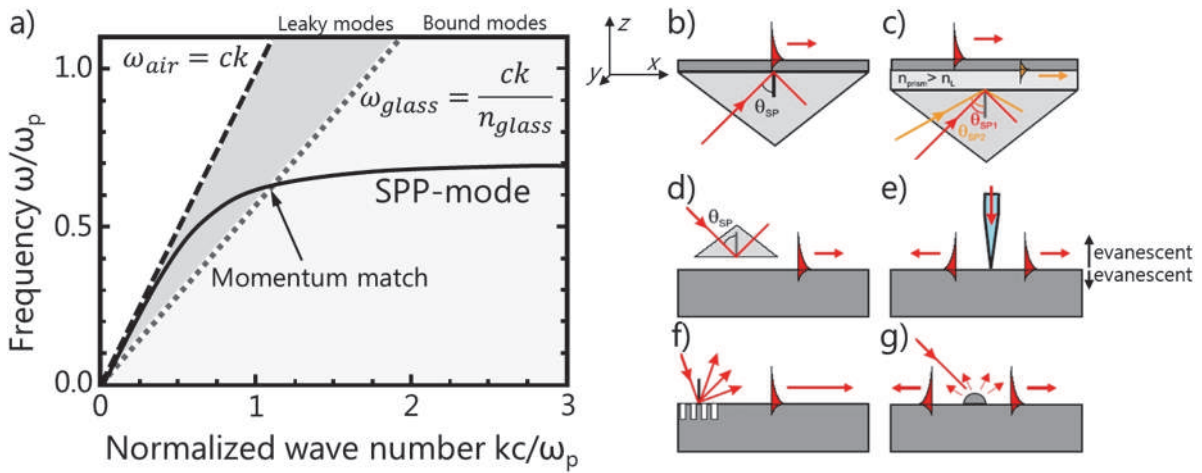


Figure I.14. a) Dispersion relation for the momentum conservation Kretschmann configuration in the attenuated total reflection (ATR) system which demonstrates that SPP excited by ATR are leaky modes, which can reradiate in the glass and couple to SPP at the air-metal interface. It is possible only for frequencies corresponding to the SSP-curve confined between the air and the glass curves (dark grey area).^{2,155} b) Kretschmann geometry, c) two-layer Kretschmann geometry, d) Otto geometry, e) excitation with a SNOM probe, f) diffraction on a grating and g) diffraction on surface features.¹⁸ Adapted from Zia et al.,¹⁵⁵ Gaponenko² and Zhang et al.¹⁸

Once the SPP is coupled on the metal-dielectric interface, it propagates up to a length L_{SPP} that depends on the dielectric constants of both the media and the excited light wavelength λ (Equation(I.3)):^{18,167,168}

$$L_{SPP} = \frac{\lambda}{2\pi} \left(\frac{\varepsilon_{mr} + \varepsilon_d}{\varepsilon_{mr} \varepsilon_d} \right)^{3/2} \frac{\varepsilon_{mr}^2}{\varepsilon_{mi}} \quad (\text{I.3})$$

As analogy with Equation(I.1), ε_d is defined as the dielectric constant of the media above the metal and ε_{mr} and ε_{mi} are the real and imaginary parts of the dielectric constant of the metal, respectively. The L_{SPP} is the distance after which the SPP intensity is $1/e$ of its initial value.^{18,167,168}

For that reason, it is important to consider the real and imaginary parts of the dielectric constants of metals in order to predict their SPP behaviour (Figure I.15). It can be observed that there are notable differences in the dielectric constants of Au and Ag in the visible/ultraviolet range.^{44,169}

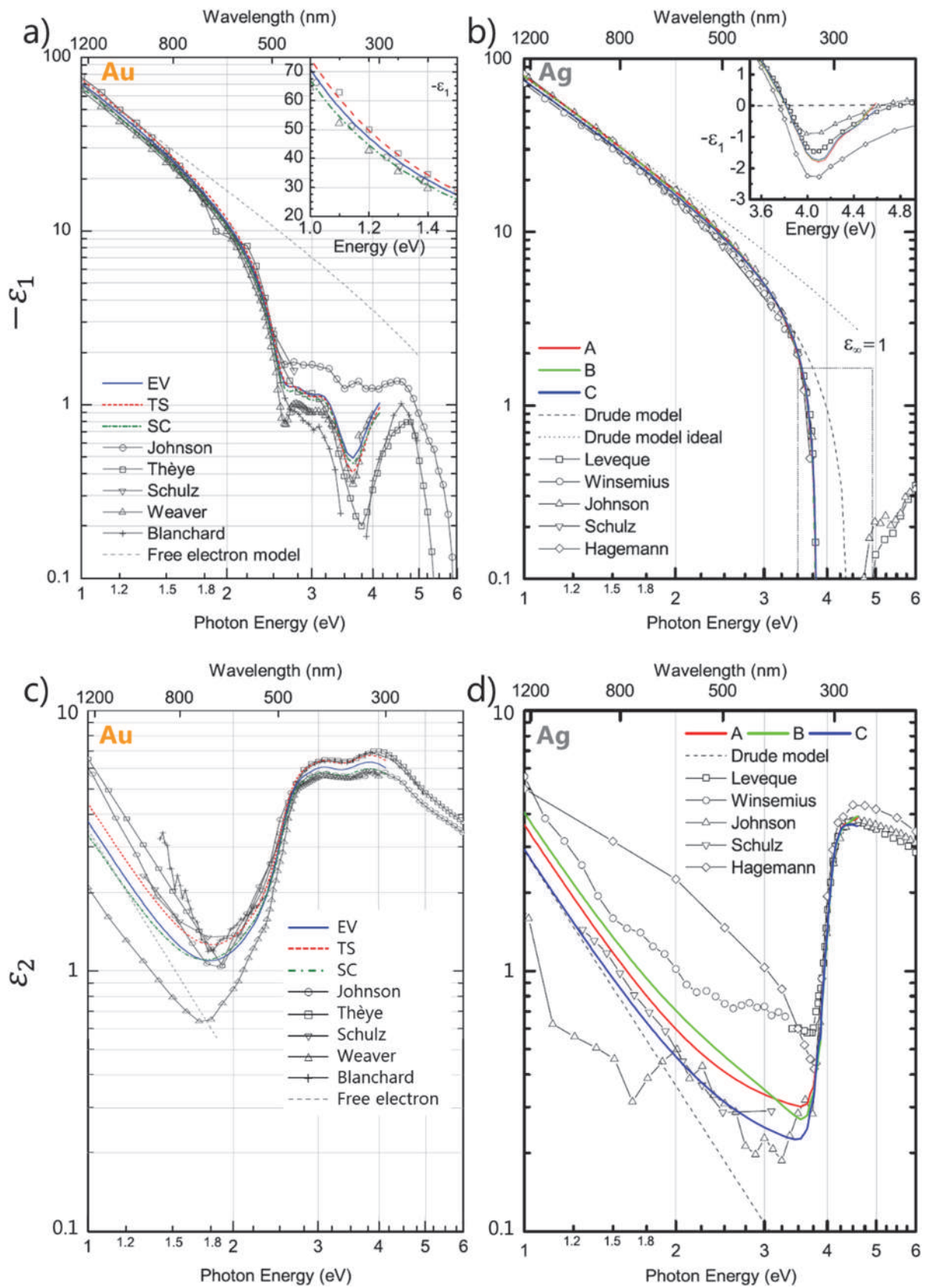


Figure I.15. Negative real part of the dielectric function $-\varepsilon_1$ ($-\varepsilon_{mr}$ in the text) of a gold and b) silver in the nIR/visible/UV spectral range. In a) Evaporated (EV), template-stripped (TS), and single-crystal (SC) gold samples. For comparison, data from Johnson and Christy¹⁷⁰, Thèye¹⁷¹, Schulz^{172,173}, Weaver et al.¹⁷⁴, and Blanchard et al.¹⁷⁵ are shown, as well as the dielectric function calculated for a Drude free-electron metal with $\hbar\omega_p = 8.5$ eV and $\tau_D = 14$ fs. Solid lines are guides for the eye. Inset: Linear scale plot of $-\varepsilon_1$ for 1.0 – 1.6 eV photon energy. In (b) three samples A (red), B (green), and C (blue) prepared by the same method. Data from Leveque et al.¹⁷⁶ (squares), Winsemius et al.¹⁷⁷ (circles), Johnson and Christy¹⁷⁰ (triangle), Schulz^{172,173} (inverted triangle), and Hagemann et al.¹⁷⁸ (diamond) are shown for comparison. Drude fit for sample C with $\hbar\omega_p = 8.9$ eV, $\tau = 18$ fs, and $\varepsilon_\infty = 5$ (dashed) or $\varepsilon_\infty = 1$ (dotted line). Inset: Data near 3.8 eV shown in linear scale, where $-\varepsilon_1(\omega)$ transitions from positive to negative values due to the interband transition. ε_2 (ε_{mi} in the text): imaginary part of dielectric function of c) gold and d) silver in the nIR/visible/UV spectral range. The references from the spectra in c) and d) are analogous to the references from a) and b), respectively. Adapted from Olmon et al.^{44,169}

Typical L_{SPP} values for metals such as gold and silver and aluminium at different excitation wavelengths can be calculated and have been confirmed experimentally. For Ag, it has been found to be 20 μm at a wavelength of 500 nm and 1 mm for an infrared excitation wavelength of 1550 nm.¹⁶⁷ For aluminium, typical values have been found to be 2 μm for an excitation wavelength of 500 nm.¹⁶⁷ In the case of Au, in the visible range the propagation length is lower (around 0.3 μm for wavelength values around 500 nm)¹⁷⁹, but it increases above (Figure I.16a). Values of 10 μm for $\lambda_{exc} = 600$ nm and up to 80 μm for $\lambda_{exc} = 750$ nm (Figure I.16b) have been calculated and measured.¹⁸⁰ Other authors have reported experimental values of L_{SPP} above 10 mm for $\lambda_{exc} = 1060$ nm, that agrees with the theoretical value $L_{SPP} = 12.3$ mm¹⁸¹.

New optoelectronic devices rely on trapping the electromagnetic field at subwavelength dimensions. The SPP-coupled light is concentrated and localized in the metal-dielectric interface even when changing dimensions or directions. This allows the creation of subwavelength waveguides.^{64,87,182}

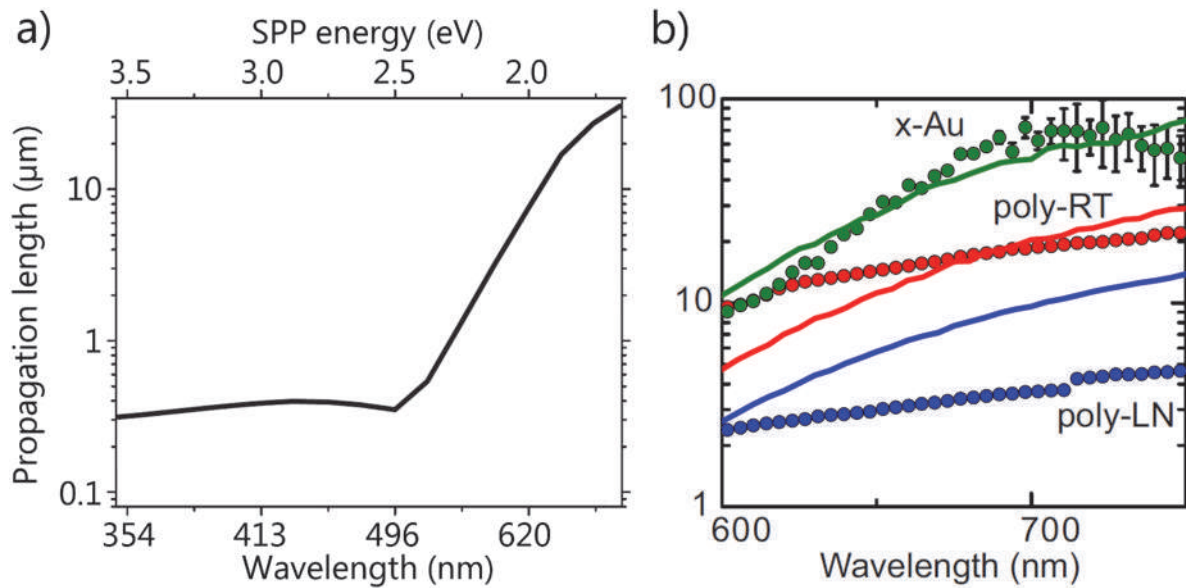


Figure I.16. a) Characteristic theoretical SPP lengths on gold in vacuum as a function of excitation wavelength and SPP energy.¹⁷⁹ b) SPP propagation length in air as a function of wavelengths for three different samples. The green dots are for single-crystalline gold (x-Au) and the red and blue dots are for polycrystalline gold films deposited at room temperature (poly-RT) and liquid-nitrogen temperature (poly-LN), respectively. The solid lines are propagation lengths calculated from the dielectric constants measured for the respective samples. Adapted from Kuttge et al.¹⁸⁰

I.1.3.2. SPP in metal thin films

When an incident electromagnetic field interacts with a thin metal film-dielectric interface, it can become trapped at this interface. It couples with the free conduction electrons of the metal, normally by using a coupler, as it was reported above.^{2,5,148,168}

The coupled plasmonic wave propagates at the metal-dielectric interface in all directions (Figure I.17a). It can propagate along several micrometre distances in the interface plane (x and y coordinates) depending on scattering by defects (grain boundaries, roughness of the interface), until it reaches these distances or if the metal-dielectric interface is interrupted.

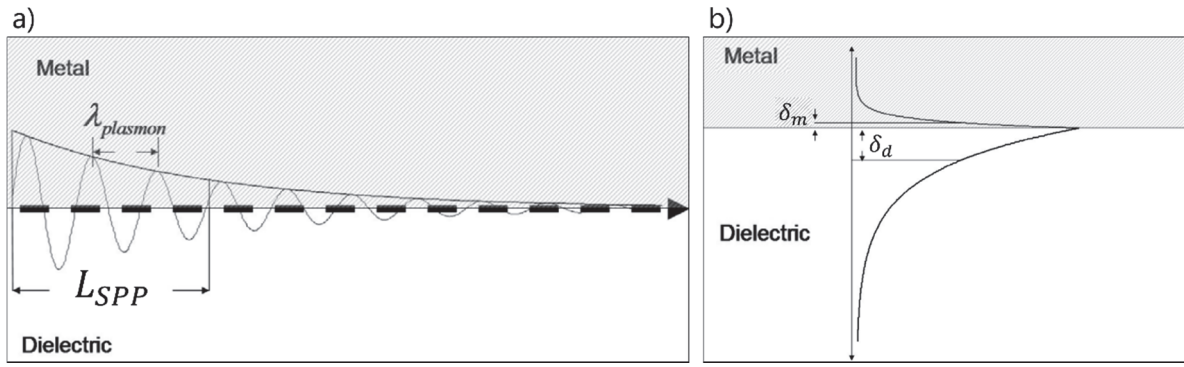


Figure I.17. a) Schema of surface plasmon polariton and its propagation length. Taking the electric field at the interface $z=0$, we see that the plasmon oscillates with a wavelength $\lambda_{plasmon}$ which is close to the wavelength of light in the dielectric. The surface wave continues to propagate and drops to $1/e$ of its original magnitude in a characteristic distance L_{SPP} , which is typically tens to hundreds of μm in the visible part of the electromagnetic spectrum. b) Decay lengths of the evanescent field perpendicular to the propagation direction. For a given value, the electric field exponentially decays into the bulk of both media. The electric field decays with a characteristic length approximately of the penetration depth in the metal (δ_m). In the dielectric, the decay is slower being closer to the wavelength of light (δ_d). Adapted from Sanders.¹

The corresponding evanescent field inside the metal and the dielectric media decays exponentially in the normal z direction with typical values of one hundred nanometres (δ_{metal} and $\delta_{dielectric}$, respectively) (Figure I.17b, Equation (I.4) & Equation (I.5)).^{1,5,147,183,184}

$$\delta_{metal} = \delta_m = \frac{c}{\omega} \sqrt{\frac{\epsilon_d + \epsilon_m}{\epsilon_m^2}} \quad (\text{I.4})$$

$$\delta_{dielectric} = \delta_d = \frac{c}{\omega} \sqrt{\frac{\epsilon_d + \epsilon_m}{\epsilon_d^2}} \quad (\text{I.5})$$

where ϵ_m and ϵ_d are the dielectric constants of the metal and the dielectric media, respectively. c is the speed of light, and ω is the angular frequency of the wave.¹

The physical features of the metal film, random roughness or ordered patterns, can drastically change the SPP. They are used to tune the propagation and enhancement of the electromagnetic field on the metallic surface in lithographic plasmonic devices (Figure I.18).^{5,86,87,181,185-187}

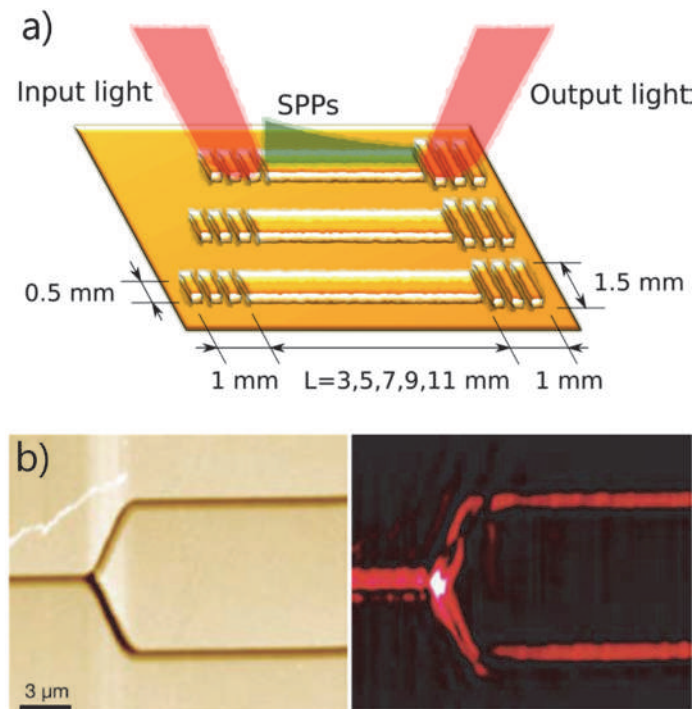


Figure I.18. a) Schematic of a SPP waveguide device, both coupling and out-coupling of the SPP are designed by an ordered pattern.¹⁸¹ b) Plasmonic Y-splitter. Topographical and SNOM images when a SPP is launched from the left by a laser at $\lambda_{exc} = 1600 \text{ nm}$. Adapted from Bozhevolnyi et al.¹⁸⁵

I.1.3.3. SPP in Nanowires

Nanowires are a special kind of SPP waveguides, as the plasmon is laterally confined in two dimensions (Figure I.19). The Maxwell equations were solved for these nanostructures, discovering that this extreme confinement promotes a good plasmon propagation.^{1,188–191} Importantly, their tips act as light-SPP couplers. When an incident electromagnetic field interacts with a tip, a large number of new electric field vectors are created. Some of them match with the metal nanowire SPP, promoting the propagation. Once the SPP arrives to the opposite end of the nanowire, another momentum matching is obtained, which results in photons emission, although the reflection or backscattering of the SPP can also be produced. For that reason, kinks, sharp points or other features can be used to couple the incoming electromagnetic radiation with the SPP. Reciprocally, they act as radiative points and alter the propagation of the SPP.^{1,29,91,188,191–195}

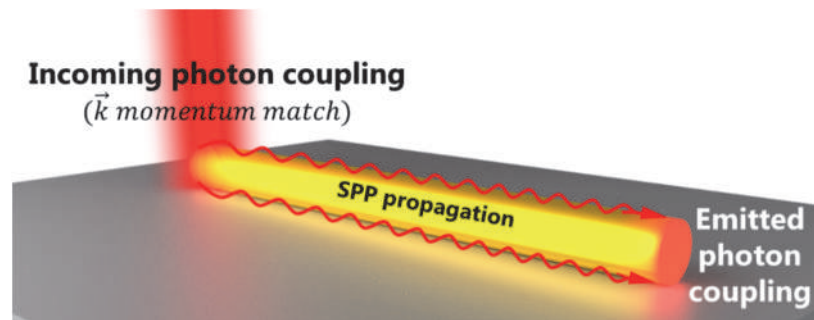


Figure I.19. Schema of a nanowire supporting a SPP waveguide mode. The plasmon-photon coupling occurs at both tips (promotion of SPP mode and emission of photons).

First studies of wires supporting electromagnetic waves were made by Sommerfeld in 1899¹⁹⁶ and Hondros in 1909¹⁹⁷, reporting the propagation of radio and micro-waves in metallic wires. Although they did not relate this behaviour to a plasmonic effect, they started the research in the interaction of electromagnetic waves with metallic surfaces.^{15,16,37,152} It was not until 1972 when Miziumski made an experimental study about propagation on plasma waves in aluminium and silver microcylinders.¹⁹² Ashley and Emerson¹⁸⁸ followed his work making the first theoretical study of surface plasmons dispersion on 80 and 500 Å radius Al cylinders according to the Maxwell equation solutions¹⁹⁸. A few months later, Pfeiffer, Economou and Ngai made a more extended theoretical study on this topic, relating it to the previous experimental results.¹⁸⁹

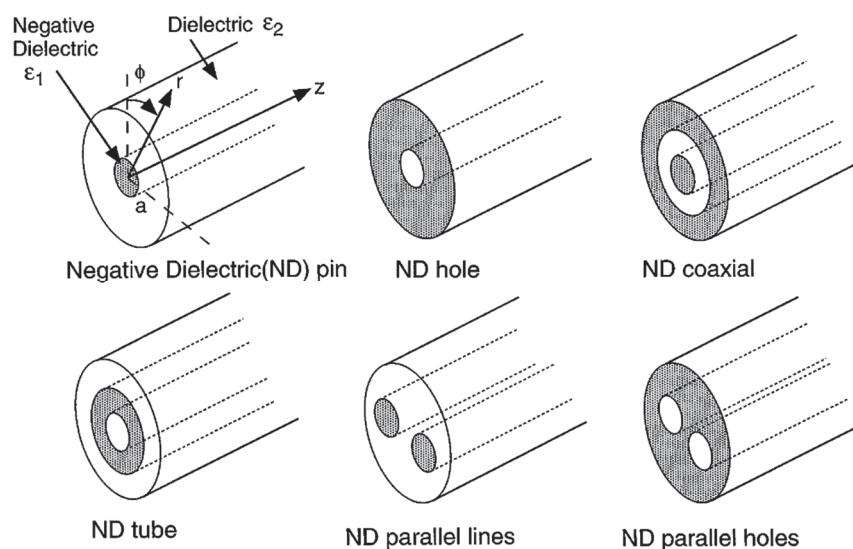


Figure I.20. Coaxial nanowires designs proposed by Takahara in 1997. It should be noted that it is mentioned “negative dielectric (ND) ϵ_1 ” instead of metal. Adapted from Takahara et al.¹⁹⁹

In 1994, Novotny and Hafner studied the SNOM probes by a plasmonic approach, considering them as aluminium nanotubes with a dielectric core.²⁰⁰ In 1997, Takahara designed different one dimensional dielectric-metal nanostructures and studied theoretically the SPP propagation along their metallic cores (Figure I.20).¹⁹⁹ Weeber made a theoretical design of the system to excite the SPP in nanowires using the Kretschmann configuration.^{156,201} In 2000, Dickson and Lyon made one of the first experimental reports of SPP propagation in Au and Ag nanowires.¹⁵⁷ Since then, many theoretical and experimental studies have been made to explore and exploit this particular confined SPP propagation.^{26,29,91,153,154,158,194,195,202-209}

I.1.3.3.1. Isolated nanowires

The Maxwell equations can be solved for an isolated nanowire embedded in a homogeneous dielectric media, which is excited by an electromagnetic field in one of its tips. SPP-related electric and magnetic fields are obtained. Some authors have solve the equations using orthogonal coordinates^{29,190,195,199} and others by cylindrical coordinates^{1,189,200,202,210-212}, obtaining similar results. The SPP-promoted electric and magnetic field are in function of m , that is the order of the mode and acquires integers values. They depend on the dielectric function of the metal and the surrounding dielectric media, the excitation frequency and the interface geometry.^{26,29,188,202}

For understanding the experimental studies reported in this manuscript, it is interesting to consider the first main modes of SPP in a nanowire. A horizontal nanowire in orthogonal coordinates, whose tip is positioned in $(0, 0, 0)$ is considered. Its longitudinal axis is along z , it is perpendicular to both x and y axis and the plane yz is considered as the horizontal plane.

The lower order, or fundamental mode ($m = 0$) corresponds to the transverse magnetic mode TM_0 . The charges oscillate along the nanowire (z axis) and the field intensity is axisymmetrically distributed on the surface of the wire (Figure I.21 and first row of Figure I.22).^{26,29,189,202,212}

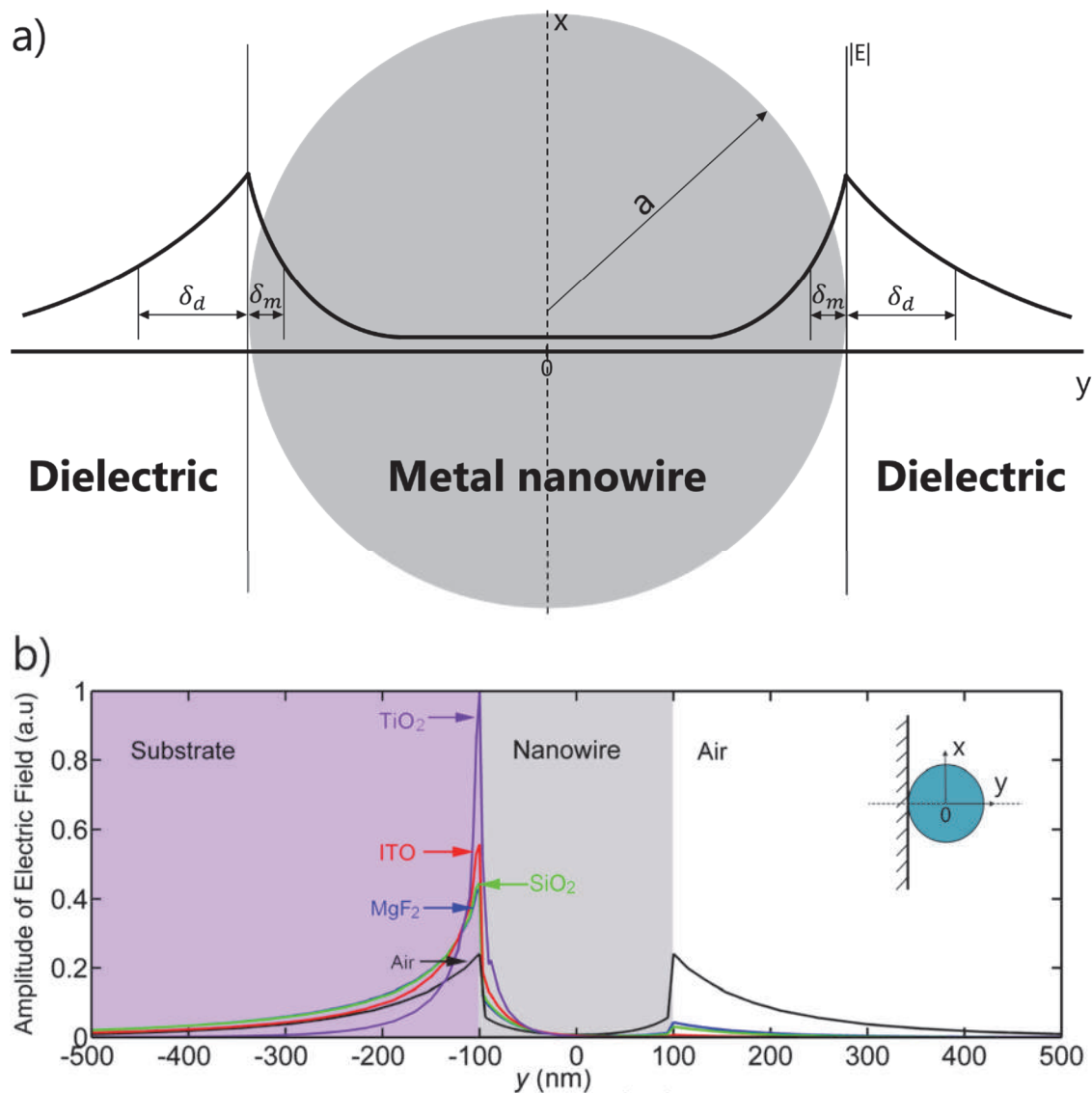


Figure I.21. a) Schematic cross section of penetrating depths of SPP-generated electric field $|E|$ in a metal nanowire of radius a along the y axis in the xy plane for the fundamental mode TM_0 and propagation in the z axis direction (perpendicular to viewer). δ_d & δ_m represent the penetration lengths of the SPP electric field in the dielectric environment and the metal, respectively (penetration in the media for a given value $|E|$ at the interface).^{1,202} b) Normalized amplitude of the electric field along y direction of a 200-nm-diameter Au nanowire lying on different substrates ($\lambda_{exc} = 660$ nm). Inset: coordinates on the cross section of the nanowire.²⁰³ Adapted from Schröter and Dereux,²⁰² Sanders¹ and Wang et al.²⁰³

Two higher order degenerated modes ($m = 1$) are denoted as HE_1^x and HE_1^y and correspond to charges oscillation in the transverse x and y axis, respectively. The electric field intensity is distributed symmetrically from the z axis on the two sides of the nanowire (second and third rows of Figure I.22).^{29,189,202,212} Some authors prefer to

consider HE_1^x as HE_{-1} ($m = -1$) as the excitation of HE_1^x and HE_1^y modes by a vertical incident beam is made by parallel and perpendicular polarization, respectively.^{200,212,213}

Another higher mode has been described as HE_2 ($m = 2$) (not shown in Figure I.22). It is produced by antisymmetry with respect to z axis charges oscillation and distribution in both x and y axis. The electric field intensity forms four symmetric lobes along the z axis.²¹²

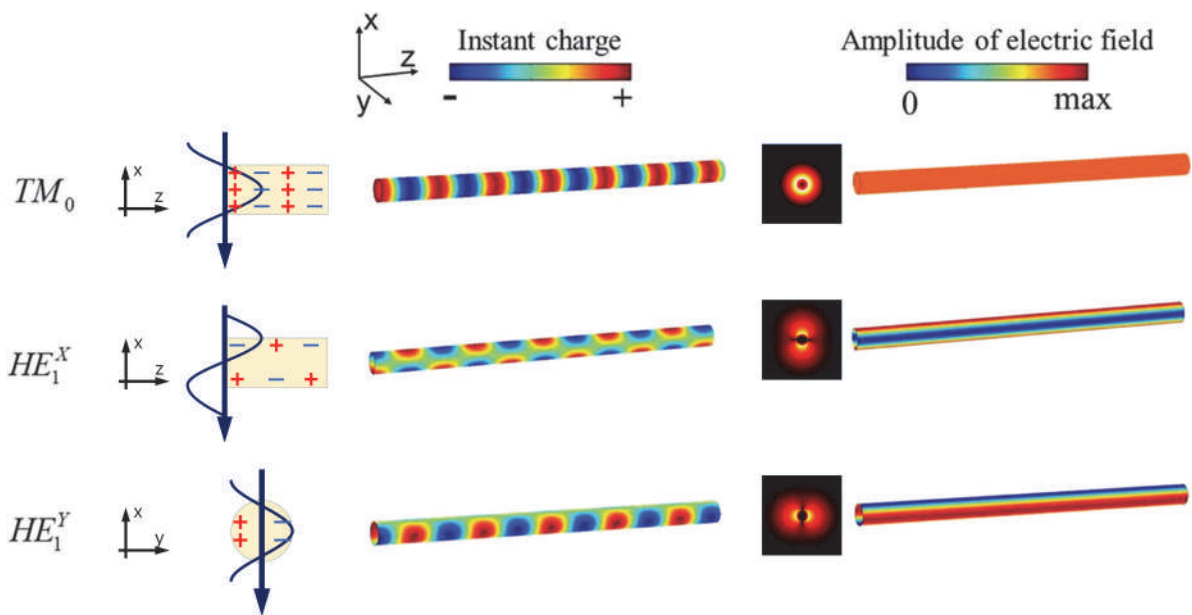


Figure I.22. Simulation via finite element method (FEM) of distributions of instant charges and amplitude of electric field on the Ag NW surface for different plasmonic modes. (diameter = 120 nm, section shown: 2 μ m long). In the simulation, the solved principal eigenmodes ($m = 0$ and 1) for the cylindrical NW were directly used as the excitation source of 633 nm at the left end via a perpendicular Gaussian beam with its electric field parallel (first and second row) or perpendicular (third row) to the NW main axis. The propagating SPP were perfectly absorbed with no reflection at the right end. The zero phases were taken for TM_0 and HE_1^x when the electric field reached the maximum along the positive direction of the x axis and for HE_1^y when the electric field reached the maximum along the positive direction of the y axis. Due to the perfect absorption of the boundary, the distributions of the field amplitude were uniform along the propagation. Adapted from Zhang et al.²¹² and Wei et al.²⁹

New electric field distributions are expected along the nanowire when two or more modes are combined. When the fundamental mode TM_0 is combined with one of the HE_1 modes, they interact constructively and destructively accumulating different phases. The resulting electric field direction is the same as the HE_1 mode but its intensity follows a zig-zag distribution (first and second rows of Figure I.23). Combining two HE_1 without phase difference will result in a mode with the same distribution of HE_1 but with a rotation.^{29,212}

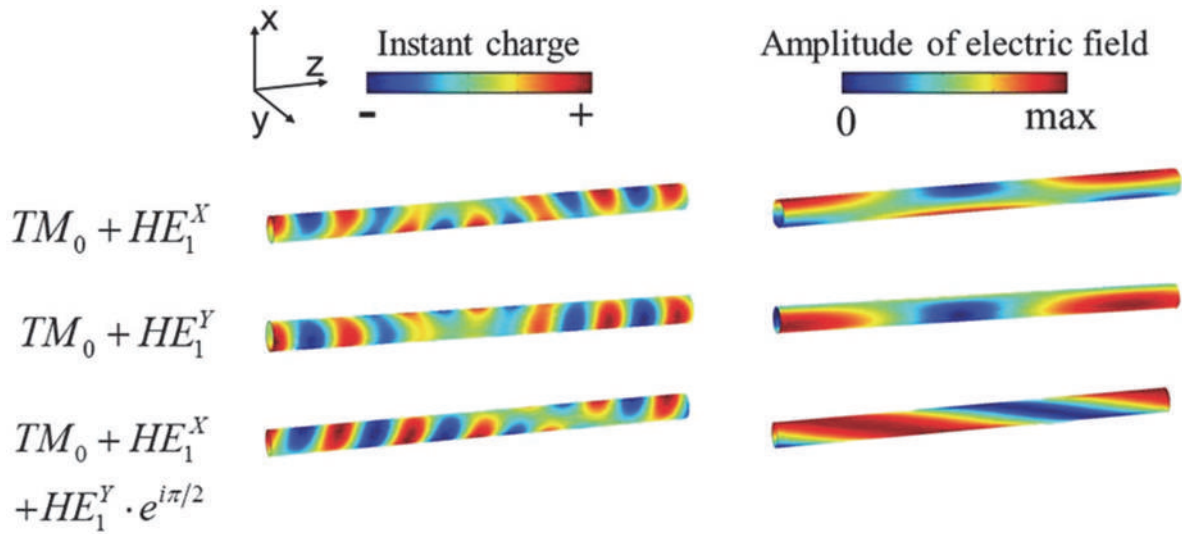


Figure I.23. Simulation via FEM of distributions of instant charges and amplitude of electric field on the Ag NW surface for different superposed plasmonic modes from the individual modes shown before (Figure I.22). (diameter = 120 nm, section shown: 2 μ m long). In the simulation, the solved superposed eigenmodes for the cylindrical NW were directly used as the excitation source of 633 nm at the left end, and the propagating SPP were perfectly absorbed with no reflection at the right end. The expressions in the left column denote the superposition of modes with relative phase difference at the input port. The phase difference further accumulated during the propagation. The distributions of the field amplitude showed zigzag (first and second rows) and chiral (lowest row) shapes in contrast with the individual modes shown before (Figure I.22). Adapted from Wei et al.²⁹

When a phase difference between both HE_1 modes is introduced and the fundamental TM_0 is also present, a chiral helicoidal electric field is obtained (third row of Figure I.23). The period and chirality of the helix is determined by the phase difference between the first order modes. When the HE_1^x is phase-advanced respect to HE_1^y , the resulting electric field motion is anticlockwise (left-handed SPP). The opposite phase distribution will result in a clockwise motion (right-handed SPP). This effect allows the transformation of linearly polarized electromagnetic fields in tuned circularly polarized ones by the introduction of a nanowire in an optoelectronic device.^{29,212}

In order to excite the modes exposed before, the dielectric surrounding of the metal nanowire must be homogeneous. Wei, Pan and Xu achieved this by immersing the nanowire in an oil with the same refractive index as the substrate where it is deposited.²⁹

A vertical incident beam was focused in one of the tips of the nanowire in order to excite the different SPP modes. When the input light is polarized parallel to the longitudinal axis of the nanowire, both TM_0 and HE_1^x were excited resulting in the SPP

distribution explained before (first row of Figure I.23 and Figure I.24a). When the polarization is perpendicular to the nanowire, the excited modes are the HE_1^y (third row of Figure I.22) and HE_2 (Figure I.24b). When the polarization is in between both cases, all the modes are excited with a phase difference given by the angle of polarization. As explained before, the SPP follows a characteristically chiral helicoid distribution.^{29,212,214}

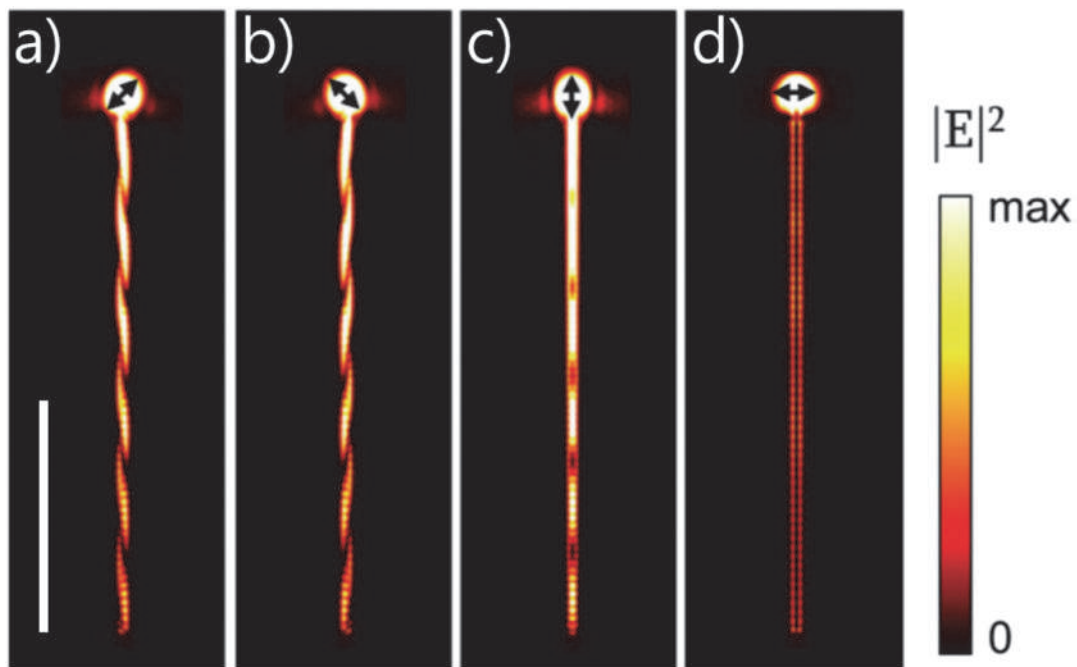


Figure I.24. a–d) Simulation results by FEM for an Ag NW under excitation of different polarizations indicated by the arrows. A Gaussian beam with a wavelength of 633 nm and a waist of 400 nm is incident onto the top end of the Ag NW (radius = 65 nm, length = 11.7 μm). The NW is covered by a 10 nm-thick Al_2O_3 shell ($n = 1.62$) and then placed in a uniform environment ($n = 1.5$). The field is shown for the section across the centre of the NW. But for the section inside the Al_2O_3 and the NW, the outer surface of the Al_2O_3 layer is used instead. So the field is shown for the combined 3D surface viewed along the incident direction of the Gaussian beam. The length of the scale bar is 5 μm . Adapted from Wei et al.²⁹

I.1.3.3.2. Nanowires on a dielectric surface

The previous results corresponded to the simple case of a nanowire embedded in a homogeneous dielectric environment. But, in most experimental cases, the nanowire is deposited on a dielectric surface and the rest is surrounded by another dielectric media, breaking the cylindrical symmetry. New modes that take into account the substrate have to be introduced and superposed with the already discussed modes.^{29,213}

These new defined modes are englobed in bound and leaky modes. In bound modes, the electric field is concentrated in the metal-substrate interface (third and fourth rows of Figure I.25) and in the case of leaky modes, it is in the air-metal interface (first and second rows of Figure I.25). This is because the effective refractive index for bound modes is higher than that for the substrate and, inversely, is lower for leaky modes. ^{29,155,161,204,213}

The new hybridized modes simulated by different authors are denoted as H_0 , H_1 , H_2 , etc. H_0 and H_2 are the main bound and leaky modes respectively that propagate when the excitation polarization is parallel to the nanowire. H_1 and H_3 are the analogous for a perpendicular polarization but the energy of H_3 mode leakage is so high that normally it is not considered (Figure I.25). ^{29,91,161,213,215}

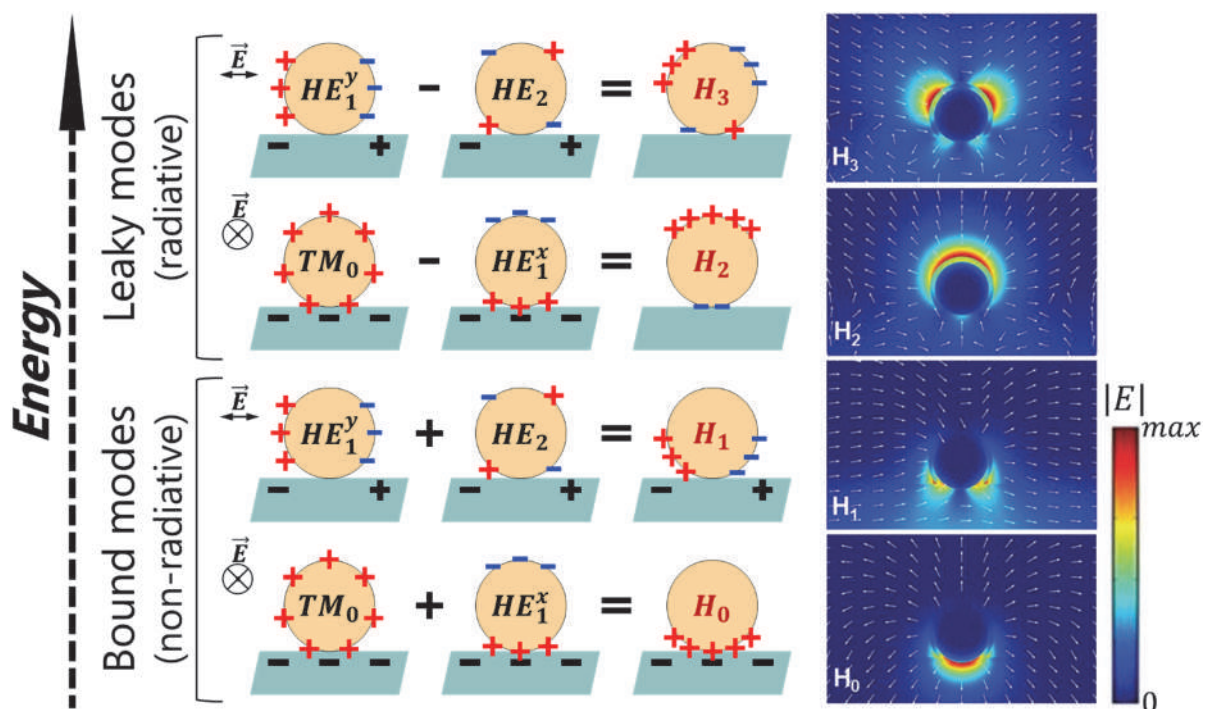


Figure I.25. Substrate-mediated surface plasmon hybridization. Schematic drawing of how the different primary wire plasmon modes (Figure I.22) interact through the dielectric substrate to give the four lowest order hybrid modes and their field amplitude distributions. ($\lambda_{exc} = 633 \text{ nm}$, NW diameter = 320 nm covered with an Al_2O_3 shell of 30 nm (not present in the schematic part of the figure). Adapted from Wei et al.²⁹ and Zhang and Xu²¹³

We consider important to note that all these simulations have been done considering the nanowires as perfect cylinders and their tips as totally flat and perpendicular cross section. In reality, the ends of the nanowires can acquire different shapes. Huang et al. made a research in this field, revealing that the SPP coupling and transmission can change with the shape of the nanowires tips.²¹⁶

The SPP propagation of leaky modes is normally smaller than for bound modes, its propagation constant β is small enough to couple with the photons in the substrate (Figure I.14a) and it results in radiation losses. The bound modes cannot couple to free space photons and their losses are smaller, coming principally from resistive heating.^{91,155,195}

For both leaky and bound modes, the propagation length increases with the nanowire diameter (Figure I.26a).^{91,204,213} In the case of bound modes, the first explanation for this phenomenon is that the evanescent length of the decay of the field into the dielectric environment increases with the diameter. Furthermore, as the field decay length into the metal does not depend on the diameter, the SPP bound modes are less confined at higher diameters. This is transduced in a lower amount of relative electromagnetic field inside the nanowire thus, lower losses due to resistive heating.⁹¹

Leaky modes are less confined at smaller diameters but their losses comes principally from radiation to their environment and not from resistive heating. At small diameters, the leaky modes couple strongly with the photonic modes of the substrate, having huge losses by radiation and disappearing completely.^{91,148,205}

For the general case, that SPP propagation length is longer when the real part of the dielectric constant of the metal is larger. For this reason, Ag nanowires propagate better SPP than Au nanowires (Figure I.15 & Figure I.26b). This is also the reason because SPP modes propagate further at higher wavelengths. Nevertheless, above a critical wavelength, the SPP mode momentum is lower than that for the light in the substrate and H_0 becomes leaky (Figure I.14a & Figure I.26).^{155,204,213,217} As proof of concept, it can be clearly observed that silver nanowires propagate a relative higher quantity of radiation for longer wavelengths (Figure I.26c).^{169,217}

Another important remark is the crystallinity of the noble metal conforming the nanowire. A monocrystalline nanowire offers less SPP losses than a polycrystalline one, where some plasmon propagation damping can happen at the grain boundaries.^{25,154,207,218}

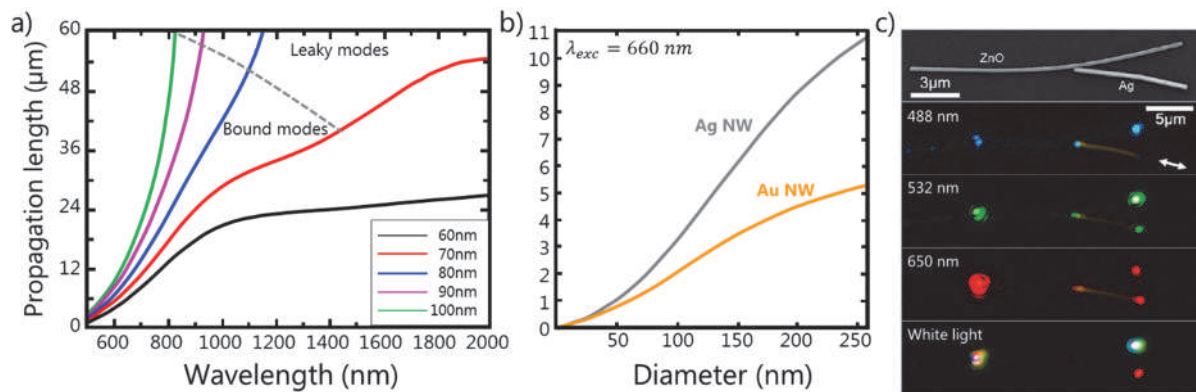


Figure I.26. a) Propagation length (μm) in silver nanowires on SiO_2 in air for different diameter. The propagation length is considered as the distance when the mode power decays to $1/e$.²⁰⁴ b) Propagation length (μm) comparison of silver and gold nanowires for an excitation wavelength of 660 nm. The propagation length (L_m) is defined as $L_m = [2\text{Im}(\beta)]^{-1}$ where β is the propagation constant.²⁰³ c) From top to bottom: SEM image and optical micrographs of a ZnO-Ag nanowire coupler with excitation polarized parallel to the Ag nanowire at 488, 532 and 650 nm laser and white light from an halogen lamp.²¹⁷ Adapted from Li and Qiu,²⁰⁴ Wang et al.²⁰³ and Guo et al.²¹⁷

The dielectric constant of the substrate is also crucial in the propagation length and losses of SPP in metallic nanowires. It was calculated, for single-mode plasmonic gold nanowires, that the smaller the dielectric constant of the substrate, less electric field is confined inside the nanowire, giving smaller propagation losses and higher propagation lengths (Figure I.21b & Figure I.27).²⁰³

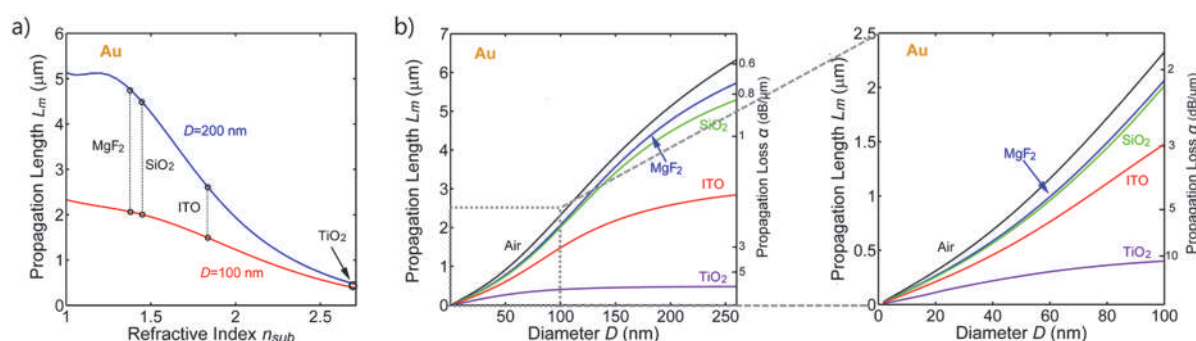


Figure I.27. (a) Substrate index (n_{sub})-dependent propagation length (L_m) of the plasmon mode and (b) propagation lengths (L_m) and losses (α) of Au nanowires on different substrates, with a focus on $D = 0$ to 100 nm (right). ($\lambda_{exc} = 660$ nm). Adapted from Wang et al.²⁰³

I.1.3.3.3. Characterization of plasmons in nanowires

In order to investigate the SPP propagation in a nanowire, an excitation source to promote the SPP and a detector to quantify its propagation are required. Different methods and configurations are briefly reviewed here (Figure I.28).

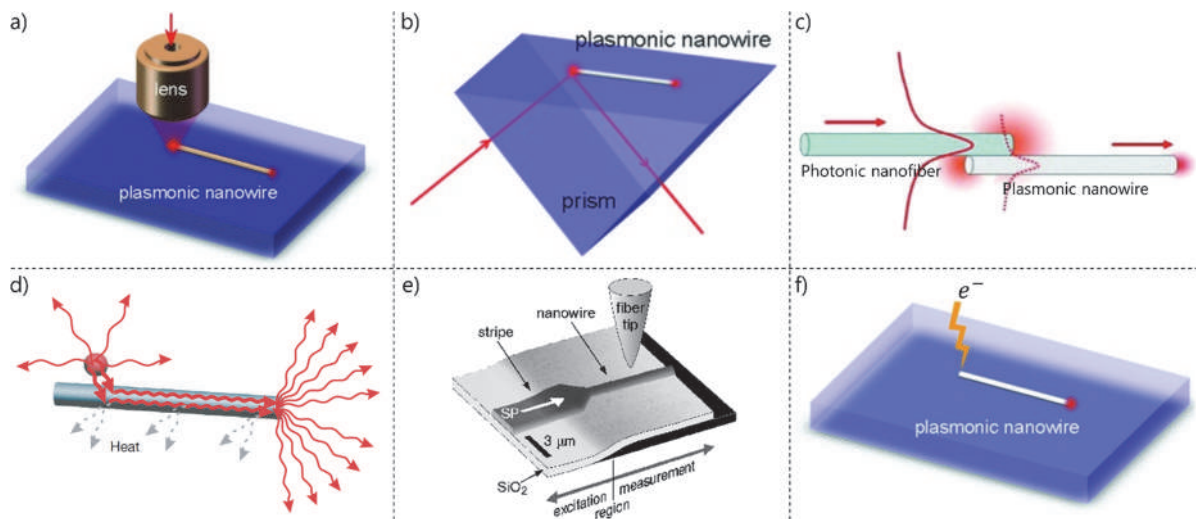


Figure I.28. Schema of methods used to excite SPP in a nanowire excited using a) the lens-focus coupling technique, b) the Kretschmann method, c) a photonic nanowire, d) a surrounding exciton from a photoluminescent species,²¹⁹ e) a width decreasing metal stripe²²⁰ and f) the excitation by electrons from a STM or an e-beam. Adapted from Guo et al.,²⁶ Akimov et al.²¹⁹ and Krenn et al.²²⁰

The simplest and most straightforward method of exciting a SPP in a nanowire is by the lens-focus coupling, i.e. focusing light using an optical microscope objective on one end of the nanowire (Figure I.28a).^{29,195,208} But the first studies were made by using the Kretschmann method using a glass prism as coupler, by analogy with the more reported SPP in metal thin films (Figure I.28b).^{157,158,220,221} Several couplers and coupling methods have been developed in the past years: a photonic nanowire^{217,222,223} or a SNOM probe¹⁶¹ can be used as a local coupler to the metal nanowire SPP (Figure I.28c). Excitons from a photoluminescent species can generate SPP in a nearby nanowire (Figure I.28d).^{219,224–229} A width-decreasing metal stripe can transform the SPP along it to match the nanowire mode (Figure I.28e).^{220,230} Alternatively to photons, high and low-energy electrons coming from a direct electron beam^{231,232} in an electron microscope or a tunnel current^{40,233–236} from a STM tip, respectively, can couple with the nanowire SPP as they do in metal films (Figure I.28f).

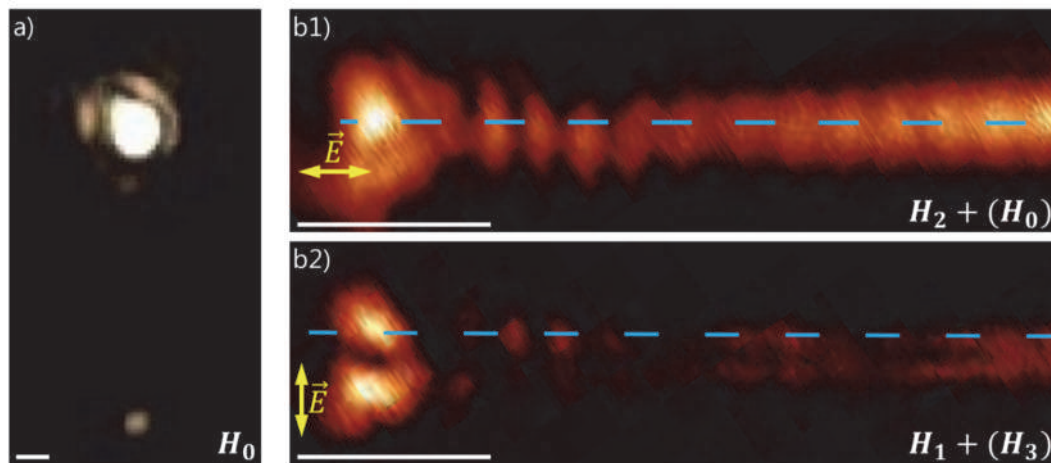


Figure I.29. a) Optical microscopy image without back light when focusing with a 785 nm laser on one end of a gold nanowire. b) SNOM images intensity of the surface waves detected on a silver nanowire by b1) static excitation: the excitation probe is on one end of the nanowire and the collection probe scans along the nanowire. b2) dynamic excitation: the excitation probe scans along the nanowire and the excitation probe rests in one end of the nanowire. Light is only polarized at the excitation probe. Ag nanowire average diameter = 250 nm. $\lambda_{exc} = 671$ nm. Scale bars are 1 μ m long. Adapted from Liu et al.¹⁶¹

In order to investigate the SPP propagation, several methods have been reported. The simplest way is observing directly the light propagated from the excited tip under an optical microscope (Figure I.29a). The SPP bound modes propagation can be estimated by directly measuring the light intensity on the other end of the nanowire or the signal emitted by an active species located along the nanowire or at the tip.^{25,91,193,208,237} Some authors measured this SPP propagation by quantifying the degree of degradation by bleach-imaged plasmon propagation (BIIPP) of a species located along the nanowire.^{25,215,238,239} A more advanced technique, the transient absorption microscopy (TAM) uses an additional laser probe to monitor the transient absorption signal in the nanowire created by the hot electrons from the SPP.^{91,205,240–242} Other methods are described in the literature, as analysing both the real and Fourier spaces images to extract the leaky modes of the nanowires.^{91,206,207} Alternatively, the intensity of the hybrid SPP modes have been analysed separately by a fine tuning of the polarization and detection with a SNOM probe (Figure I.29b) or an optical fibre. These techniques allowed to measure quantitatively the SPP decay along the nanowires (Figure I.30).^{91,161,243}

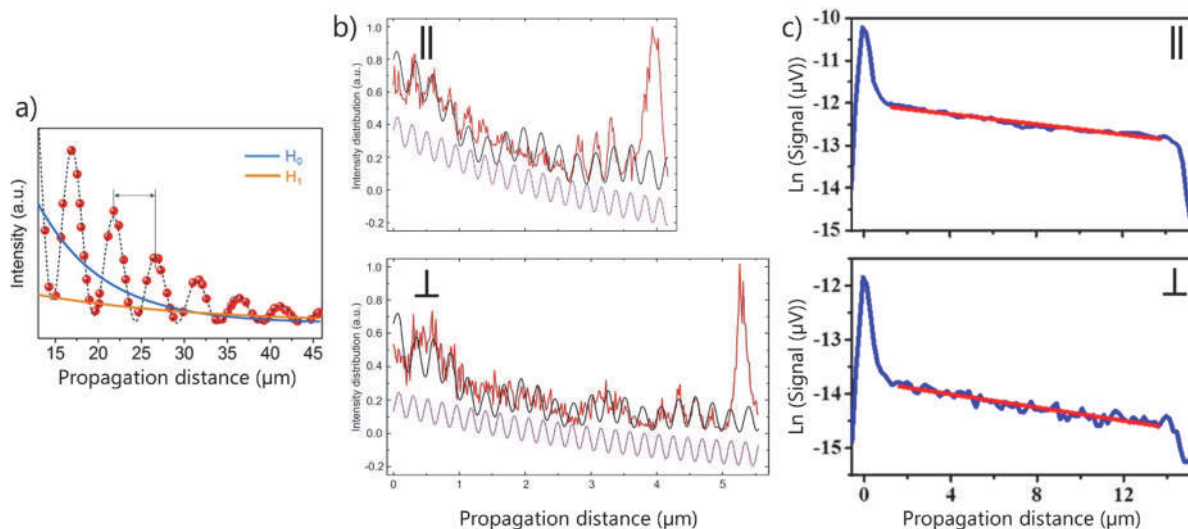


Figure I.30. a) Measured pentagonal Ag NW tip emission intensity (red dots) plotted as a function of the propagation distance. Blue and orange curves are the attenuation curves of the H_0 and H_1 modes, respectively, deconvoluted from the experimental data. The Ag NW was 160 nm in diameter. The incident light had a wavelength λ of 532 nm.²⁴³ b) Intensity profile of surface waves on Ag NW. The red solid line is intensity profile of surface waves along the blue dashed cut line in (Figure I.29b1&b2) The black (purple) solid lines are the calculated result fitted with the SPP modes active for each polarization (normalized with an intensity offset of -0.2). Ag nanowire average diameter of 250 nm. $\lambda_{exc} = 671$ nm.¹⁶¹ c) SPP propagation in a Au nanobar by TAM. The pump beam is spatially fixed on the end of the nanobar. Transient absorption line profiles with pump excitation parallel (top) and perpendicular (bottom) to the long axis of the Au nanobar. Note that the intensities are on a logarithmic scale. Bar dimensions were 450 nm x 250 nm x 15 μ m. $\lambda_{exc} = 800$ nm.²⁰⁵ Adapted from Kim et al,²⁴³ Liu et al,¹⁶¹ and Yu et al.²⁰⁵

The term hot electrons refers to electrons that have highly increased their kinetic energy to a level high enough to be ejected from their lattice ($E \geq h\nu$). Being h the Planck's constant and ν their frequency.^{244,245} They can be injected and trapped in zones of the material normally forbidden due to that high kinetic energy, for instance injected from a plasmonic nanostructure into a molecular electronic device or in a catalytic chemical reaction.^{246–248} Hot electrons can be created when dephasing of SPP by non-radiative relaxation.²⁴² They cause a transient absorption signal that can be measured via a visible laser. The intensity of that absorption grows with the number of hot electrons, that will be higher for more intense SPPs.^{91,249} This phenomena can also be achieved using a STM probe.²³⁴

I.1.4. Exploitation of plasmonic nanowires with surrounding species

Plasmonic nanowires and nanotubes are attracting huge fundamental and applicative interests as they combine two main advantages of plasmonics over photonics: the concentration of optical fields far beyond the diffraction limit of light and the propagation of optical waves along nanometre-scale waveguides. Most of the previous studies concentrated on the simplest type of 1D plasmonic nanostructures, i.e. metallic nanowires (gold or silver, mainly). However, while the coupling of plasmonic 0D-like nanoparticles and nanorods (aspect ratio smaller than 10, typically) with other species has been tremendously studied and exploited for surface-enhanced Raman scattering and plasmon-enhanced photoluminescence, the coupling between plasmonic nanowires and surrounding species is getting a lot of attention nowadays. It is precisely one goal of the present thesis to explore the optical and spectroscopic properties of such hybrid nanowires. We should remark that we do not have found any literature where in a single hybrid nanowire were combined the initial coupling, the propagation and the final remote coupling with a perfectly placed Raman or photoluminescent active species.²⁰⁸ We found an interesting study from Prymaczek et al. where, after dispersion of the nanowires, they could exactly deposit a photoactive species on one of their tips.²⁵⁰

In the recent literature, the plasmon-exciton coupling in hybrid nanostructures has particularly been reported for studying the weak and strong coupling regimes. These notions are introduced below.

I.1.4.1. Plasmon-exciton coupling: weak and strong coupling regime

Weak and strong coupling are two regimes of interaction between quantum systems, which are related to slow and fast energy transfer rate from a donor to an acceptor. In the weak coupling regime, the slow transfer rate from donor to acceptor is smaller than the relaxation rate of the acceptor. Thus, after the energy is transferred to the acceptor, a back transfer to the donor is improbable before the acceptor decays. Within this so-called weak regime, the interaction between the two systems can be treated within perturbation theory.²⁵¹ On the contrary, in the strong coupling regime, the interaction energy is large enough to make possible a fast back transfer to the donor before the acceptor decays. Thus, the excitation becomes delocalized over the donor and acceptor resulting in Rabi oscillations.²⁵² The system is considered as hybridized, with an energy level splitting (Rabi splitting) which increases with the coupling strength. These strong and weak coupling regimes between plasmon and exciton are much investigated

nowadays and are exploited for example in metal nanoparticle arrays for emerging applications such as nanoscale lasing, solid-state lighting, and optical devices.²⁵³

I.1.4.1.1. Strong coupling regime.

For an ensemble of N dipoles, the mechanism of cooperative emission relies on the photon exchange between the N emitters that gives rise to superradiant states with enhanced radiative decay rate $N\Gamma_0$, where Γ_0 is the decay rate of an isolated dipole. In 2009, a cooperative emission similar to superradiance of an ensemble of dipoles in the vicinity of a metallic nanosphere has been described theoretically.²⁵⁴ Experimentally, the coherence of spatially remote emitters induced by hybridization with the propagating SPP of a silver film has been shown.²⁵⁵ The strong-coupling regime has been reported in various hybridized systems of SPP with semiconductor quantum dots^{256–258} and with disordered organic materials^{255,259–261}. It is important to note that for these studies, the SPP results from a planar metallic surface, not from nanowires.

I.1.4.1.2. Weak coupling regime

Only few studies have investigated weak plasmon-exciton coupling in hybrid nanowires or nanotubes. CdSe nanocrystals grafted on Ag nanowires exhibit enhanced and spectrally modified spontaneous emission compared to isolated CdSe nanocrystals (Figure I.31).²²⁴ These effects were attributed to the weak coupling of the nanocrystal excitons to the SPP cavity modes of the metallic nanowires.

Silver nanotubes containing a CdS nanowire have also been studied.²⁶² The resonant excitation of the non-propagating whispering-gallery modes of the silver nanotubes produces a strong field enhancement in the hollow cavity. It results in an enlarged spontaneous emission rate of the semiconducting CdS. Other photoluminescent species such as MoS₂²²⁸ or quantum dots²²⁵ have also been reported to couple with the SPP of silver nanowires.

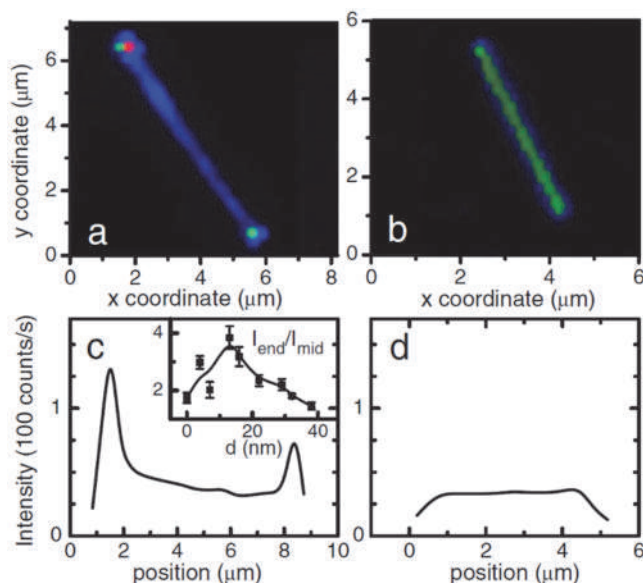


Figure I.31. a) Microphotoluminescence image of the 635 nm CdSe nanocrystals emission for a 7.5 μm long multishell Ag nanowire with a SiO_2 shell of 22 nm. b) The same for a hollow CdSe nanocrystals- SiO_2 shell system of $\sim 4 \mu\text{m}$ length after dissolving the inner Ag core. c) & d) The spatially resolved emission intensity measured along the nanowire axis with c) and without d) Ag core. The inset of c) shows the ratio of the emission intensity measured for the nanowire end and middle part $I_{\text{end}}/I_{\text{mid}}$ as a function of SiO_2 shell thickness d . $\lambda_{\text{pump}} = 532 \text{ nm}$, pump power 60 mW, spot size 30 μm , $T = 300 \text{ K}$. Adapted from Fedutik et al.²²⁴

An original study related to the plasmon-exciton coupling in nanowires was made by Park et al. in 2010.²⁶³ They synthesized barcode nanowires including different photoluminescent and non-photoluminescent polymers and a Cu coating that enhanced their PL and protected them against oxidation (Figure I.32).

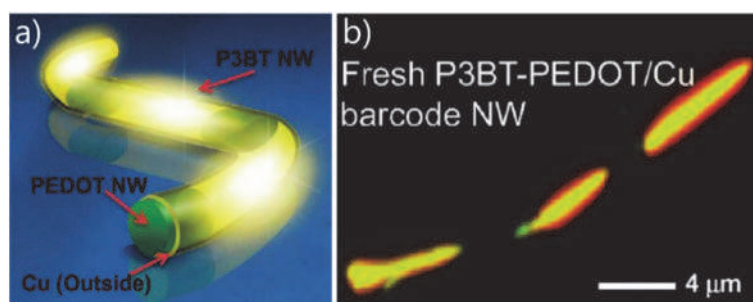


Figure I.32. a) Schematic illustration of a poly(3-butylthiophene-2,5-diyl) - poly(3,4-ethylenedioxythiophene) / Cu light-emitting colour barcode nanowire (P3BT-PEDOT/Cu LECB-NW). b) Luminescence colour of charge-coupled device (CCD) camera image of an isolated single strand of a fresh P3BT-PEDOT/Cu LECB-NW. Adapted from Park et al.²⁶³

I.1.4.2. Nanowires for remote sensing

A very promising application for these SPP waveguides deals with remote nanosensing. Delicate analytes can undergo photodegradation when making spectroscopic analysis directly on them. In solid heterogeneous samples, most of the radiation that is focused on the analyte is not transduced in signal but in heat which can degrade such analyte. By introducing a plasmonic waveguide, the analyte can be excited remotely and it minimizes that useless but harmful radiation. Furthermore, it is a way to transmit information at the nanoscale.^{193,208,219,224,228,229,237,264,265}

The remote sensing mediated by nanowires consists basically in exciting one tip of a nanowire with a light source (normally a laser), and collecting the signal given by the analyte that is located on the opposite tip.^{208,228,264} It is important to note that most of the research groups deposit a thin layer of the analyte on the sample, so it covers the whole length of the nanowire. This method can result in an ambiguous interpretation of the results, as the signal can partly come from other region of the sample but the tip of the nanowire.^{25,193,216,224,227,237,266}

The most common spectroscopic techniques that have been developed for these plasmonic-mediated remote nanosensors are the Raman spectroscopy and photoluminescence.

I.1.4.2.1. Remote Raman spectroscopy

Firstly reported in 2009^{237,266}, different systems have been proposed to excite remotely Raman species by nanowires. Only a few authors studied the single nanowire based system, mostly due to its lower signal intensity because of the lack of signal amplification.^{208,216,267} This drawback was addressed mainly by using the antenna effect of nanoparticles that we present in the next section. So, the nanowire-nanoparticle configuration have been the most studied case (Figure I.33).^{237,266,268–271} Other reported systems are nanowire-nanowire because of the electromagnetic field concentration at their intersection,^{269,272} or bundles of nanowires as collective signal collectors²⁶⁴. Several reviews have been made about this topic until the date.^{25,82,193,209,273,274}

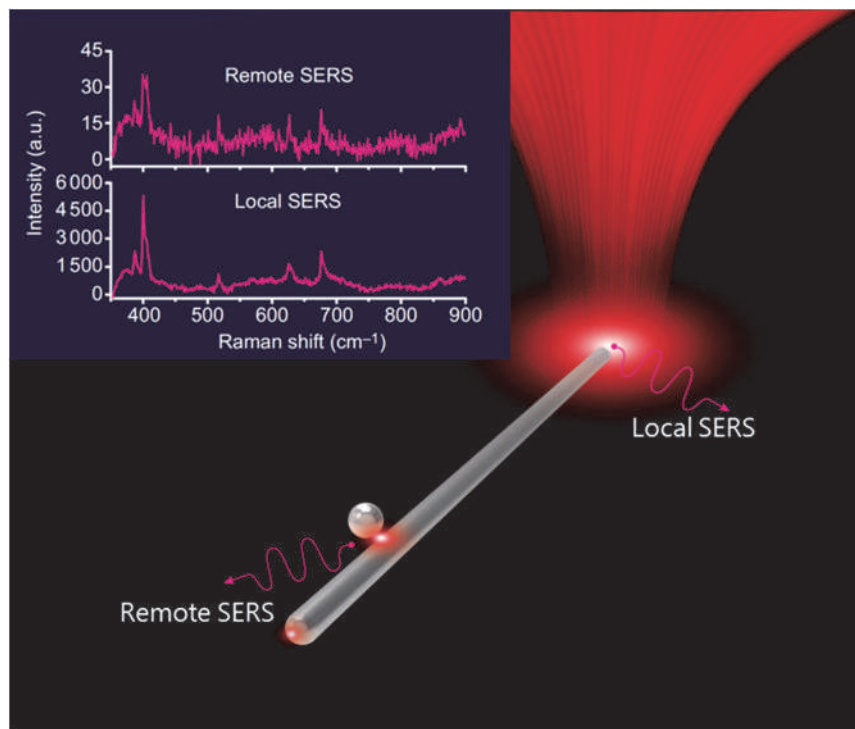


Figure I.33. Schema of a nanowire-nanoparticle system excited by light at one of its tips. Local SERS signal collected directly from the excitation point and remote SERS signal from the junction. Adapted from Huang et al.¹⁹³

An unusual remote configuration exploited a nanowire array with all-aligned nanowires in a porous template with the analyte located only at the upper side of the tips. (Figure I.34). The excitation and collection took place at the bottom tips of the nanowires and the SPP is transmitted back and forth. The excitation beam arrived to the bottom tips, being transmitted to the top tips via SPP. Then it excited the Raman active species and their Raman signal was transmitted via the SPP along $3.3 \mu\text{m}$.²⁶⁴

A more challenging development is the use of nanowires mounted on nanolithography movable probing tips, as remote TERS couplers. It was first developed by Berweger et al. in 2010, he used a monolithic Au conical tip (with a grating on its top part for the photon-SPP coupling) to get remote TERS effect from IR-125 and malachite green dyes deposited on gold substrates.²⁷⁵ He still did not use nanowires as remote TERS probes but in 2014, Lu et al. mounted a silver nanowire-nanoparticle system on a tungsten tip and were able to obtain remote Raman signals from a HeLa cell (Figure I.35).²⁷⁰ The main drawback of their system was the impossibility to exactly locate on the nanowire the nanoparticle that acted as nanoantenna. In 2016, Fujita et al. developed a dielectrophoresis-based method that allowed them to exactly position gold nanoparticles onto the silver nanowire probe. They succeeded in the remote TERS characterization of a benzenethiol covered Au surface.²⁷¹

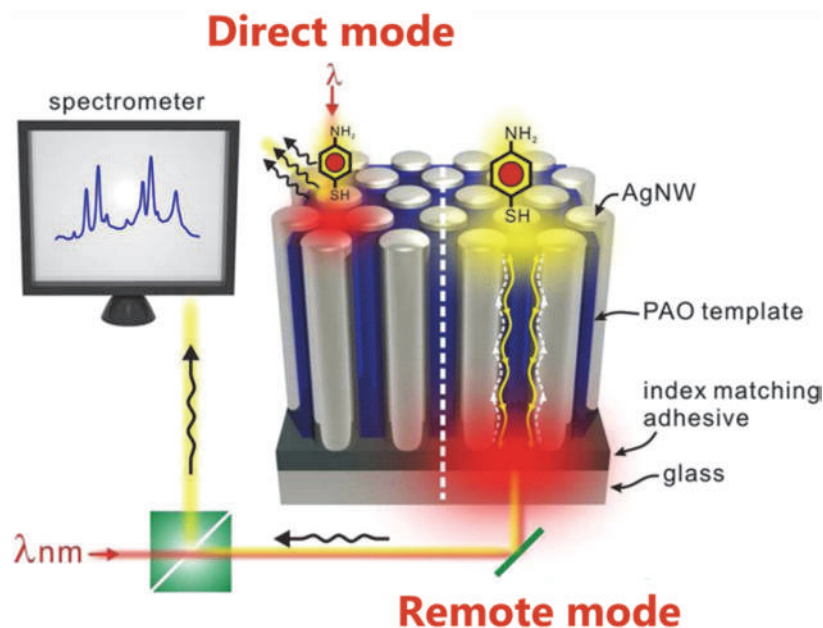


Figure I.34. Schema of the SERS sensor by remote plasmon. Both direct and remote (back and forth) modes are represented. Adapted from Huang et al.²⁶⁴

We considered that a step forward could be taken in this field if the tip of the nanowires were covered with a sensitive species, such as a polymer, possibly a molecular imprinted polymer, that would react with some specific analytes which could be trace detected by Raman.

Regarding the literature exposed before, it can be inferred that most of the authors use silver nanowires instead of gold. This choice seems motivated by the lower SPP propagation of Au in the visible range, as we exposed before. Nevertheless, a few authors, due to the higher robustness and chemical stability of gold decided to optimize their systems in order to use this material in their SPP remote Raman systems.^{208,216,275}

The analytes used to give proof of the different remote Raman experiments are the typical species used in Raman spectroscopy. Sulphur-containing species such as benzenethiol²⁷¹, 4-aminothiophenol (PATP)^{237,264,268,276}, malachite green isothiocyanate (MGITC)^{216,266} or poly(3,4-ethylenedioxythiophene) (PEDOT)²⁰⁸ have been widely used due to their affinity to noble metals. But non-sulphur-containing analytes with characteristics Raman signals are also great indicators for this remote Raman experiments.^{267,269,272,275,277,278}

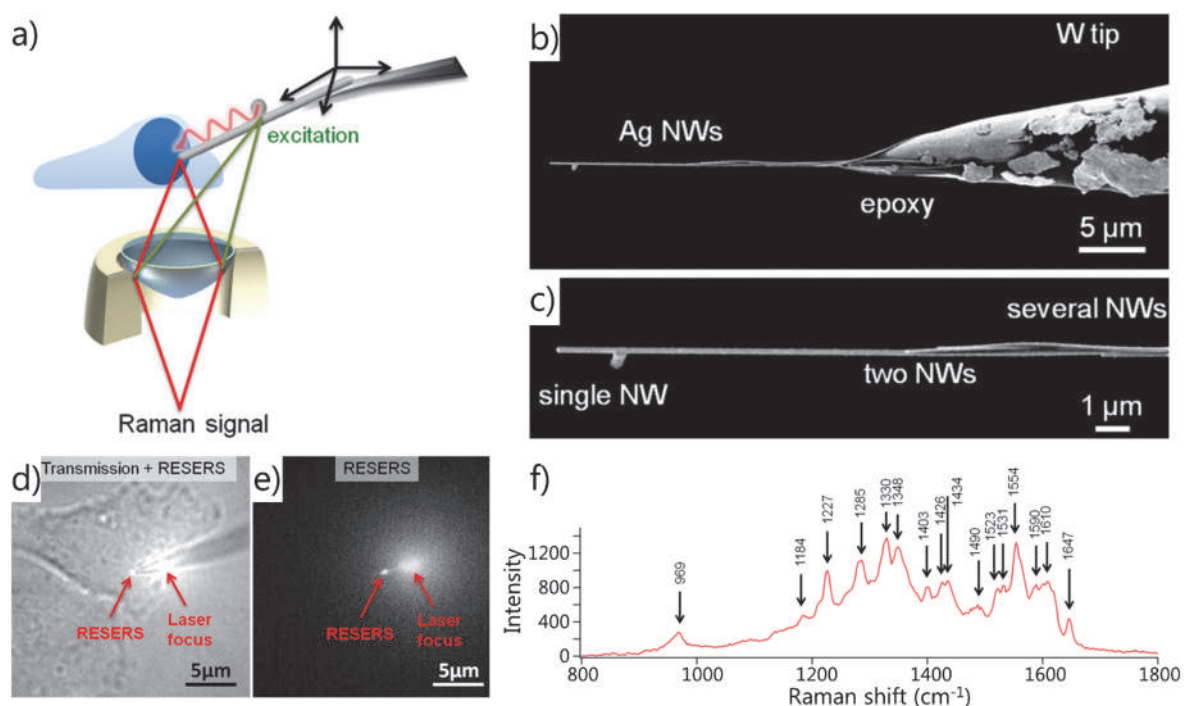


Figure I.35. a) Schematic illustration of plasmonic waveguide SERS endoscopy using a silver nanowire (Ag NW) – silver nanoparticle (Ag NP) probe in direct remote excitation mode. Raman signals are detected at hotspots inside the cell that are excited by the propagating SPP. b) SEM image of a typical tungsten tip with Ag NW attached and glued with conductive epoxy for endoscopic probing. c) Magnified image of the Ag NW probe tip showing a single nanowire at the end of a nanowire bundle. d) Remotely excited SERS (RESERS) endoscopy of a live HeLa cell by a Ag NW probe. Combination of optical transmission and remote excitation SERS imaging and e) remote excitation SERS only. f) A remote excitation SERS spectrum from the nucleus of the live HeLa cell. Adapted from Lu et al.²⁷⁰

The future applications of this technique in live non-damaging nanobiomedicine and nanoimaging are very promising. The use of these nanoprobes on movable stages allows the spatial nanocharacterization of microscopic samples in real time without radiating directly the sensitive areas with a laser beam. In order to achieve a more robust and reproducible technique, it is necessary to optimize their production and mounting process and use more durable materials, such as gold. The use of Au over Ag is also recommended when probing living cells due to the antiseptic characteristics of silver.²⁷⁹ Another possibility would be covering the nanowire probes by a non-fluorescent biocompatible layer, such as PEDOT.^{280,281}

I.1.4.2.2. Remote photoluminescence

Explored before the remote Raman effect,^{219,224,265,282} the remote photoluminescence via nanowires studies the coupling between the SPP and a photoluminescent species. A first approach, referred as nanosensors, is analogous to the remote Raman effect: the incoming SPP from the nanowire couples and excites a photoluminescent species placed in its surroundings, which decays radiatively (Figure I.36a).^{26,225,228,229,250,283} The second approach is related to the exciton-SPP coupling introduced before: an exciton from a photoluminescent species is excited in the surroundings of a SPP-supporting nanowire, then the exciton couples with the SPP which propagates until the other tip where it is emitted radiatively (Figure I.36b).^{219,224–229,250,265,283,284}

Similarly, a metallic nanowire was exploited to support long-range plasmon assisted energy transfer between two fluorescent emitters.^{229,283,285}

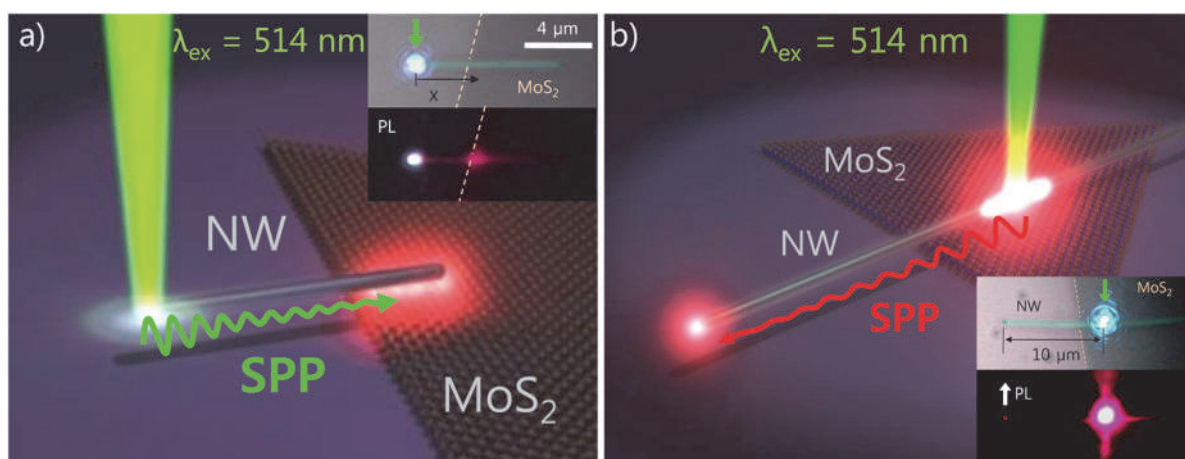


Figure I.36. a) Schema of a photoluminescence-plasmonic remote nanosensor. The laser-coupled SPP propagates along a Ag nanowire and couples with the excitons in the MoS₂ layer. Inset: optical microscopy images when focusing the laser on the left tip of the Ag nanowire. b) Schema of a photoluminescence-plasmonic remote nanosource. The excitons from the MoS₂ generated by the laser, couple with the SPP that propagates to the tip of the Ag nanowire that emits radiation. Inset: optical microscopy images when focusing the laser on the left Ag-MoS₂ interface.²²⁸

The first approach, has been mostly studied as a proof-of-concept of the SPP propagation and coupling with photoluminescent species, in order to study the nanosource or the energy transfer configuration in the same systems.^{225,228,229,250} It has also been demonstrated that this configuration promote two-photons remote photoluminescence.²⁵⁰ This nanosensor configuration could have great applications in non-destructive nanobiosensors for nanobiomedicine, analogous to the remote Raman nanosensors. Yan et al. reported in 2012 the use of SnO₂ nanowires as nanowaveguides for live single-cell endoscopy.²⁸⁶ We consider the replacement of

these non-plasmonic by plasmonic nanowires would allow the live study of several properties of the cell in a remote configuration (photoluminescence, Raman, index of refraction, conductivities).

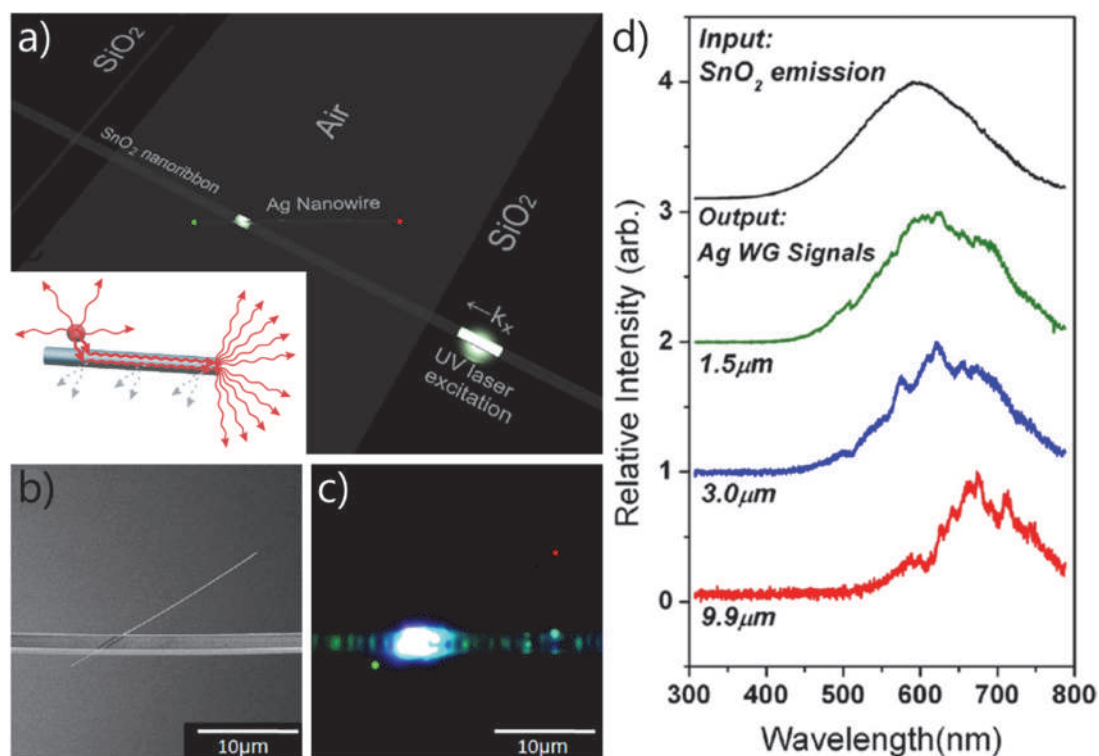


Figure I.37. a) Schema of the photonic-plasmonic routing device showing a Ag nanowire/SnO₂ nanoribbon cross-junction structure suspended between two SiO₂/Si wafers. Light scattered at junction was coupled into surface plasmon modes of the Ag nanowire, which then propagate along the wire and finally scattered back into free space photon at the two distal ends. A coupled photoluminescent species can either spontaneously emit into free space or into the guided surface plasmons of the nanowire.²¹⁹ b) SEM image showing the SnO₂ waveguide and the Ag nanowire in the actual photonic-plasmonic routing device illustrated in (a). c) Optical microscope image of the same device in (b). The large bright spot is the metal-dielectric junction where the photons in the SnO₂ nanoribbon couple into SPPs of the Ag nanowire waveguide. d) Dependence of Ag nanowire waveguide spectra on the propagation distance. Emission spectra of the Ag nanowire positioned with the micromanipulator in such way to get different propagation distances, and the PL spectrum of the SnO₂ ribbon (input signal, excited with low laser power) used in the experiment.²²⁶ Adapted from Akimov et al.²¹⁹ and Yan et al.²²⁶

The second approach describes an interesting way of coupling SPP into nanowires. An optical emitter located in the proximity of a noble metal nanowire can have three different emission decay channels: classical optical emission to the space; non-radiative

damping due to quenching as we explained before, and exciton-coupling of the spontaneous radiation into the SPP of the nanowire (Figure I.37). By finely tuning the emitter and nanowire materials and their location, this decay channel can be enormously enhanced and far exceed the classic radiative and non-radiative modes.^{219,224,265}

Important studies have been made in the nanosources field revealing the tuning of the emission spectra of the nanowire tip by changing the SPP travelled distance (Figure I.37).^{226,227} The SPP propagation length from metal nanowires is larger for wider wavelengths, due to the fact that the real part of the metal dielectric constant is more negative (Figure I.15a&b). This produces a higher damping for the shorter wavelengths as the SPP travelled distance is increased. For long distances, a red photoluminescence is observed in opposition of the broad/bluer from the short ones.^{226,227}

I.1.4.3. Other nanowire-SPP related applications and effects

Novel effects with new possible applications are being discovered in the last years. Ultimate nanosources could be plasmonic nanowire lasers. Their principle is similar to a normal laser but the gain media stimulates the emission of SPP instead of photons.^{64,287-290} We noted that the architecture of these nanolasers varies from one author to another. We discuss about the gain media and amplified emission in the next section. It has also been proposed the use of SPP in quantum cascade lasers but they are normal lasers where the SPP mode only plays a role as guiding mode.²⁹¹

It has been demonstrated that nanowires can perform as nanooptoelectronic circuits,^{25,29,292,293} such as logic gates by finely tuning the position of branched nanowires and nanoparticles²¹⁴ (Figure I.38a). Tuning the input polarization and the exact beam coupling, thus changing the coupling phase angle for a branched nanowire, it was demonstrated that the SPP could be selectively transmitted only to one of the branches of the nanowire (Figure I.38b).^{214,293}

Another exploitation of the remote configuration is the possibility to perform and monitor catalytic reactions at the opposite tip of nanowires. We already reported the monitoring of catalytic reactions by LSPR, which was performed on Ag roughened substrates.¹⁴⁵ It has also been demonstrated that a species that is positioned on the surrounding of a SPP waveguide can perform a catalytic reaction, if the conditions are met, due to the energy given by the incoming SPP.^{268,273,276}

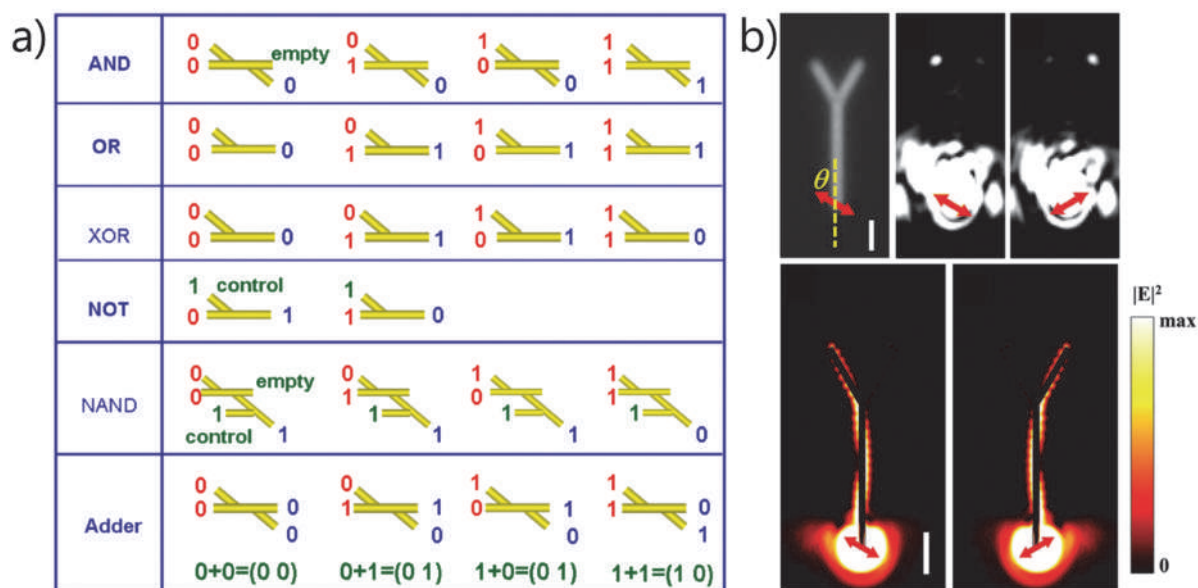


Figure I.38. a) All-optical logic operations based on nanowires networks. The terminals labelled with a red number are inputs and blue are outputs; control terminals require the input to be ON. Empty terminals are unused.²¹⁴ b) From top-left to top-right: Optical images of Y-shaped gold NW network and scattering images when the Y-shaped NW network is under linearly polarized illumination. The polarization of the incident light is marked by the arrows. From bottom-left to bottom-right: simulation results for the distribution of the electric field intensity in the Y-shaped NW network. The distributions are on the horizontal plane across the centre of the NW. The polarization of the excitation light is marked by the arrows. The length of the main wire is $3.4 \mu\text{m}$. The scale bars are $1 \mu\text{m}$, and also apply to the same row images.²⁹³

I.1.5. Improving the SPP propagation

As reported before, plasmonic nanowires could be an alternative to nanophotonic waveguides for the information technology chips and sensors exploiting light rather than electrons. But plasmons can propagate only up to a few tens of micrometres, that is much shorter than the propagation lengths of light within dielectric nanowires, which reach millimetric values.^{64,294,295} A promising approach to tackle this point consists in the improvement of the SPP propagation length by the coupling with a gain material surrounding the metal. Another important challenge deals with the efficiency of both the SPP excitation and the resulting emission of the system supporting the SPP. The use of nanoantennae to improve the light-SPP coupling is currently investigated by some groups to address this challenge. These two approaches are briefly reviewed in this part. The later one has been explored in my thesis project, as reported in Chapter IV.

I.1.5.1. Gain materials for SPP

Independently of defects, the short propagation of SPP comes mainly because of the high propagative losses, either by radiation into the surrounding dielectric media, or by resistive heating due to the electromagnetic field confinement.^{64,91,294} The study of gain materials for SPP is recent. During the last 15 years, theoretical^{211,287,294,296,297} and experimental^{288,290,297-303} studies in configurations and pump materials for “loss compensation” have been developed with promising results (Figure I.39). One of the milestones dates from 2003, when Bergman and Stockman proposed theoretically the Surface Plasmon Amplification by Stimulated Emission of Radiation (SPASER). It consists in an optically-active medium composed by two-level emitters, which should act as a laser cavity but with a surface plasmon resonance.²⁸⁷

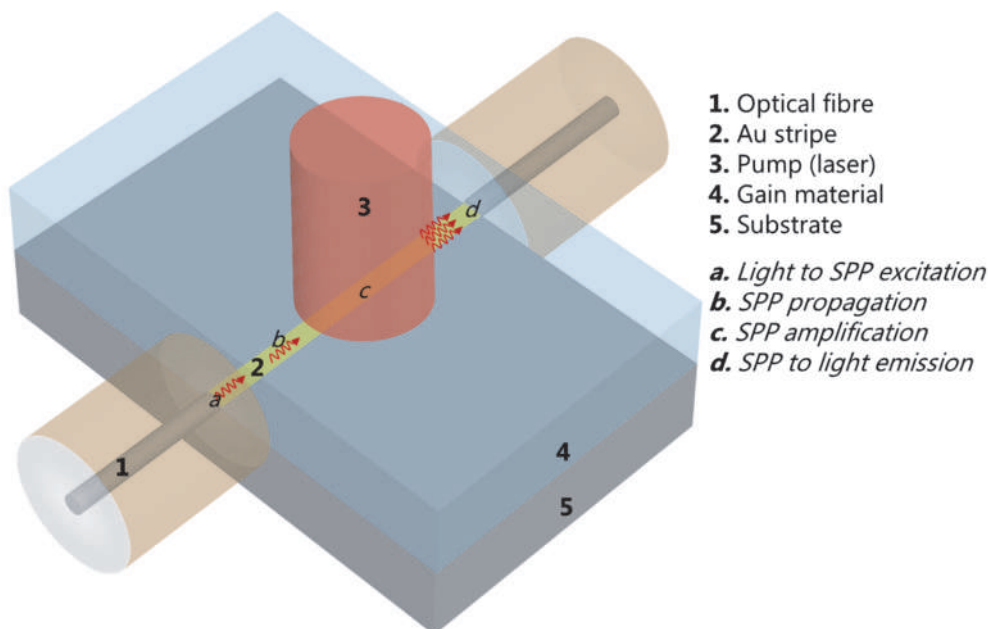


Figure I.39. Representative schema of a SPP amplifier. The pump (laser) is normally polarized along the gold stripe main axis. Adapted from Berini and De Leon⁶⁴

Different gain materials have been proposed, most of them are semiconductor compounds such as CdS²⁹⁹, CdSe^{290,297}, ZnO³⁰², quantum dots²⁹⁶, doped InP^{298,301}, GaAs³⁰³ or InGaAs^{298,301}. Some organic dyes have also been studied.^{288,300}

We should note that the architectures proposed by different authors not always follow the geometry of plasmonic nanowire/nanostripe deposited on a dielectric substrate and surrounded by the gain material. Some of them have followed that geometry,^{211,290,294,296,297,300} but others have been proposed. The most popular is the gain material nanowire deposited on a metal film covered by a thin dielectric layer.^{299,302} Nanoparticles protected by a dielectric layer with an outer shell that contains an organic gain-dye have performed well.²⁸⁸ The encapsulation of doped

semiconductors by the metal forming pillars has also been reported.^{298,301} Recently, the inclusion of a GaAs nanowire in an Au nanogroove performed well as nanolaser.³⁰³ Several reviews including information about this gain materials for SPP have been made in the recent years.^{64,194,289,292}

I.1.5.2. Antenna-coupled SPP

A coupler is required to get momentum matching for initiating the SPP propagation in metal films. The tips of a simple nanowire behave as nanoantennae, because they act as a surface discontinuity but their coupling efficiency is not controlled in general.^{154,164,304,305} Different systems have been proposed to improve this coupling by increasing the electromagnetic field at the tip. It consists in the introduction of a LSPR-supporting nanostructure, like a nanoparticle^{29,83,154,163,165,166,237,266,268,270,271,306} (Figure I.40), or lithographed antennae (Figure I.41) in the "coupling location" close to the tip of the nanowire.^{3,65,164,307}

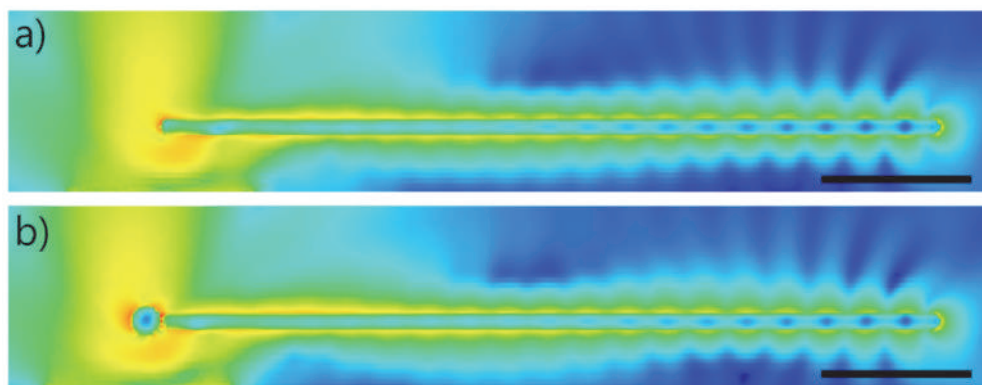


Figure I.40. Steady-state simulation image of electromagnetic near-field along a nanowire. a) An image of a free (uncapped) nanowire under the in-coupling light excitation (632.8 nm Gaussian source with the beam diameter of ~ 300 nm and linearly polarized along the long axis of the nanowire) focused on the left end of the nanowire. b) Case of a nanowire with a nanoparticle closely located to the tip under the same excitation conditions. (NW: 100 nm diameter, 5 μm length; NP: 200 nm diameter, attached to the NW the tip). Presumably, the black scale bars represent 1 μm). Adapted from Kenens et al.⁸³

Both theoretical^{83,85,87,162,164–166,306,308} and experimental^{29,83,85,154,163–166,220,237,266,268,270,271} studies of antenna-coupled nanowaveguides have been made during the last years with promising results. Most of them have been focused on the use of nanoparticles or lithographic bow-tie-alike nanostructures as nanoantennae.

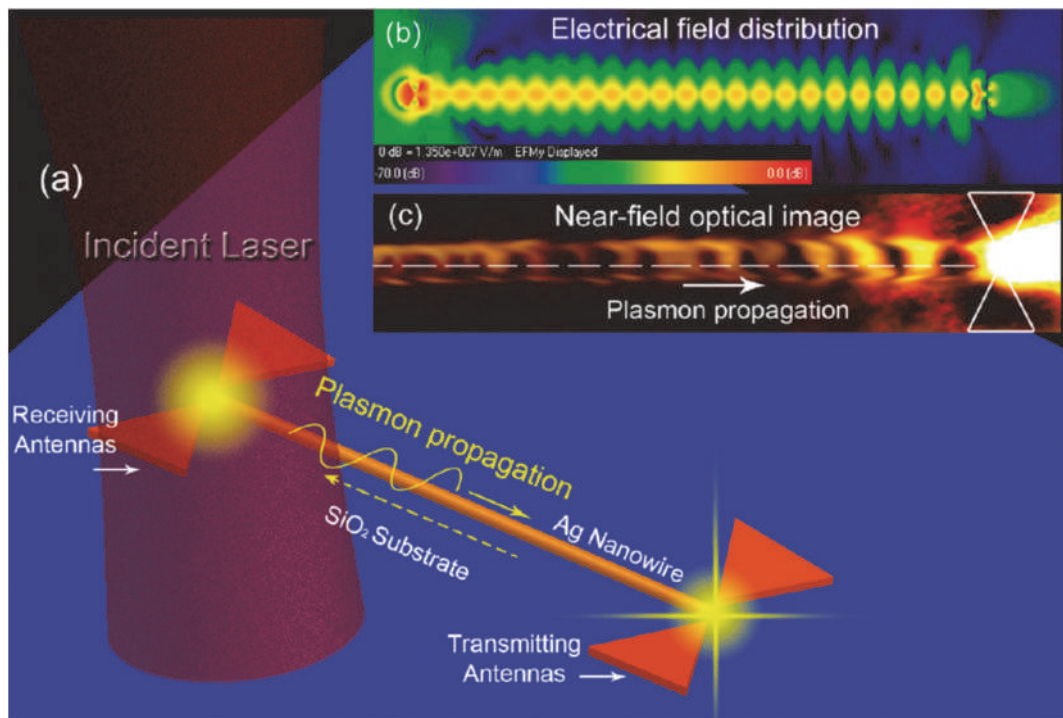


Figure I.41. a) Schema of a bowtie antenna-wire optical nanocircuit. The Ag nanowire is located at the feed gaps of both receiving and emitting bowtie antenna pairs. b) Finite difference time-domain (FDTD) simulated electric field distribution of the antenna-wire nanocircuit. c) SNOM image for the plasmon propagation along the nanowire and emission. Adapted from Fang et al.¹⁶⁴

Other original configurations have been also taken into account, in the theoretical study from Huang et al. where they proposed a two-wires SPP waveguide ended in antennas.³⁰⁸ Krenn proposed in 2007 a width-decreasing metal stripe coupled with a nanowire (Figure I.28e). In this configuration, a fundamental plasmon mode upcoming from a wide metal stripe adapted and propagated into the nano-stripe. This would allow the implement of nanowires in macrodevices.^{220,230}

Hao and Nordlander in 2006 made a theoretical study about the plasmon coupling between a metal nanowire and a metal nanoparticle, and they already introduced the concept of using this system as antenna-SPP propagation.³⁰⁹ It was in 2007 when Knight et al. made the first experimental demonstration of how the nanoparticles could act as nanoantennae for the SPP coupling in nanowires.¹⁶³ Once that effect was validated, some authors considered their use for remote Raman sensing as we reported before.^{237,266,268,270,271,276}

I.2. Synthesis of advanced 1D nanostructures for plasmonics

In order to achieve the plasmonic systems described before, it is necessary to produce reproducible and controlled nanostructures. Among them, nanoparticles^{3,5,48,71,81} and thin films, with or without a lithography process,^{18,86,152,168,310} have been produced and investigated. We restrain this short review to the one-dimensional nanostructures case, in agreement with our studies and with the results presented in this report.

I.2.1. Synthesis of 1D Nanostructures

In comparison to 0D nanoparticles, the bottom-up synthesis of 1D metallic nanostructures can be considered more challenging because it requires an anisotropic growth, while metal structures adopt mainly cubic structures. The research in the fabrication of nanowires developed rapidly in the 90s and their study became very intensive. The different approaches that have been taken depend mainly in the material of the nanowires and their desired properties.^{311,312} Here, after a short description of the main strategies and mechanisms involved in the synthesis of 1D nanostructures, a focus is proposed on the hard-template method exploited during my thesis project. The choice of this technique was motivated by the opportunity to design, with this method in a controlled and reproducible manner, the targeted morphologies (length, diameter) for long metallic nanowires and coaxial nanowires with a metallic core. A smooth nanowire surface and a good crystallinity of the metal core are other important features required to get long propagation length of SPP.

I.2.1.1. Main strategies

Nanolithography techniques referred as top-down approach have been widely used to fabricate nanowires. These techniques are generally classified depending on the parallel or serial processing that can be done. The serial ones, such as e-beam or ion-beam lithography, process micro- and nanostructures one-by-one. The in-parallel strategies allow to fabricate in the same process a big amount of micro- and nanostructures with very similar morphologies.³¹¹ Among the various top-down methods, the most used ones are the electron-beam (e-beam)^{43,57,313}, focused ion-beam (FIB)³¹⁴ and UV lithography^{315,316}, but stamping (embossing) technique is also attractive because of its lower cost. Near-field derivate techniques are particularly attractive to prepare nanowires with very small diameters, ultimately down to the atomic scale for the atomic manipulation by near-field microscopy.

Nanowires in-the-plane or perpendicular to the substrate can be achieved. However, it is important to note that the common cylindrical shape of a nanowire can be

processed for the case of etching perpendicular to the substrate, while nano-stripes with a non-circular cross-section are most usually obtained for a processing parallel to the substrate. Such a difference in the morphology can induce significant differences in their optical or magnetic behaviour.³¹⁷⁻³²⁰ A foremost advantage of many top-down techniques is the direct integration of the fabricated nanostructures into devices, while an assembly process is required to integrate nanowires synthesized by a chemical or an electrochemical bottom-up method.^{311,322}

The bottom-up routes in liquid phase, or by chemical vapour deposition (CVD) exploiting vapour-solid or vapour-liquid-solid mechanism, offer a lower synthesis cost, a higher volume of material and even novel structures that are more difficult or eventually impossible to get by top-down approaches.^{311,323}

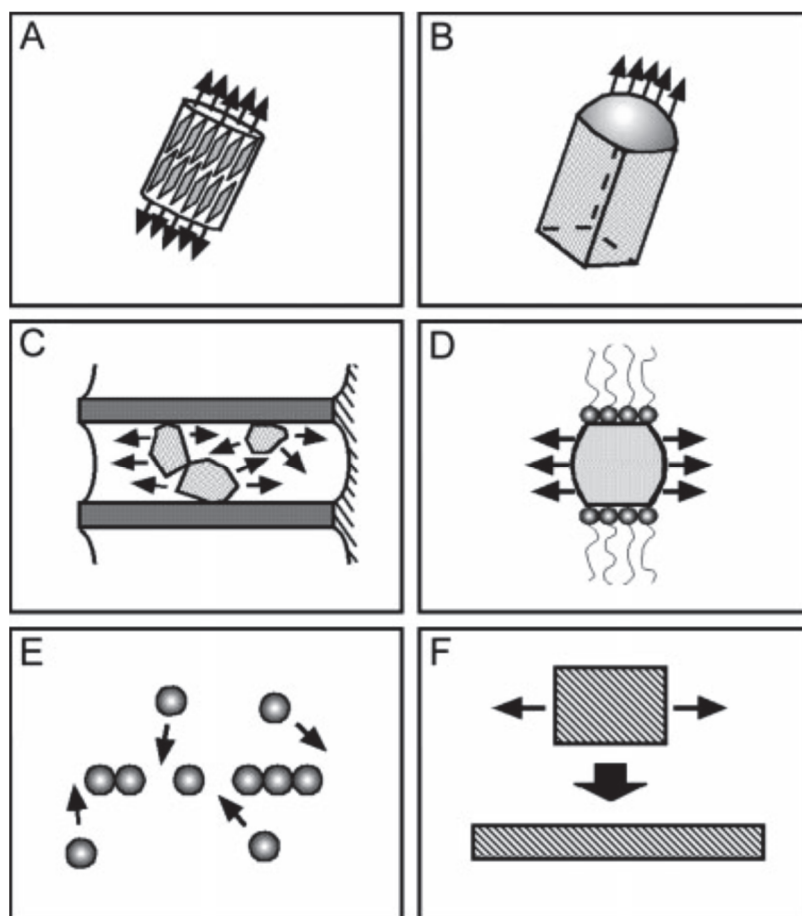


Figure I.42. Schema of the six main bottom-up approaches described in the literature for the synthesis of 1D nanostructures. a) Dictation by the anisotropic crystallographic structure of a solid. b) Confinement by a liquid droplet in the vapour-liquid-solid interface. c) Direction through the use of a hard template. d) Direction through the use of a soft template. e) Chain self-assembly of nanostructures. F) Size reduction of a 1D structure.³¹¹

The bottom-up methods described in the literature can be englobed in six main approaches.^{5,311} The anisotropy of a crystalline structure can dictate the preferential growth of a nanostructure (Figure I.42a).^{81,215,324–326} In a vapour-phase process (mainly chemical vapour deposition and derived techniques), the use, or not, of a metal catalyst nanoparticle can promote the growth of nanowires by vapour-solid or vapour-liquid-solid mechanism. (Figure I.42b).^{324,327–329} Alternatively, a hard template can act as a growth confiner and enforce the nascent nanostructure to acquire a nanowire shape structure (Figure I.42c).^{5,208,330–334} A soft template, i.e. a self-assembly of organic or biological molecules in solution can also enforce the growing nanostructure in a 1D shape (Figure I.42d).^{5,335,336} The self-assembly of pre-formed nanostructures can result in a chain-shape conformation, exploiting either the molecular design of the nanoparticle surface, or their physical interactions (electrostatic, magnetic) eventually under an electromagnetic field (electrophoresis, magnetophoresis) (Figure I.42e).^{337–340} The size reduction or uniaxial elongation of a structure, such as extrusion, can drive its transformation into a micro- or nanoscale wire (Figure I.42f).^{341–347}

These described methods can be combined between them in order to optimize the synthesis of certain required nanostructures.^{5,338}

I.2.1.2. Hard-template method and filling strategies

The hard-template method offers high versatility, reproducibility and time economy. It relies in a prefabricated nanostructured material that directs the distribution of building blocks, which can range from atoms and molecules (templated synthesis) to small nanostructures (templated assembly). This spatial restriction is achieved physically by the pores of a membrane and the growth is unforced to take place in a specific geometry.⁵ In the case of nanowires or nanotubes, the standard templates used are formed by cylindrical nanopores (Figure I.43a&b).^{323,348}

The nanowires template method was first developed by Possin in 1970 using an etched mica template to produce "metal wires with diameters as small as 400 Å and about 15 µm long" by electrodeposition.³³⁰ Continued by Williams and Giordano in 1984 that refined his method,³⁴⁹ and finally stablished by Penner and Martin during the 80s who started using track-etched polycarbonate membranes with micropores and nanopores oriented in direction perpendicular to the membrane surface, as promoted by the ion beam irradiation of the polymer film in a cyclotron (Figure I.43c)^{332,350,351}. It can be noted that many developments have been done to improve the quality of the nanopores in polycarbonate membranes (angular distribution, pore surface roughness, pore shape) and to partly control their location, which is intrinsically random, as each pore results from an ion track.^{352,353}

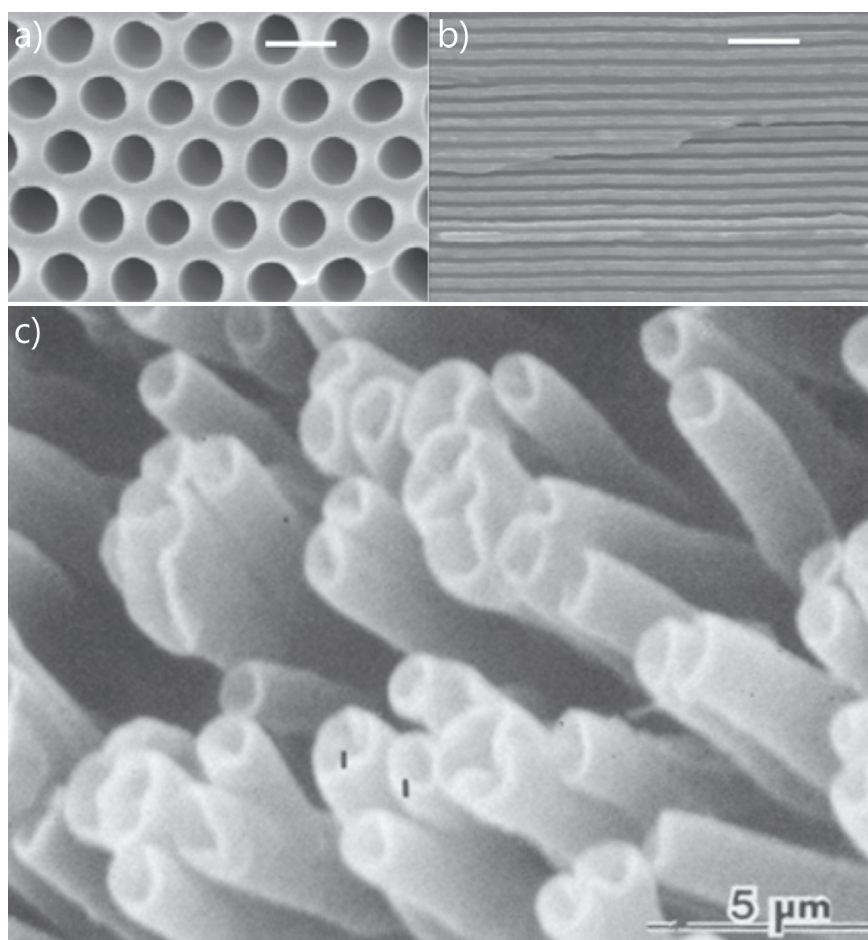


Figure I.43. Scanning electron micrographs of a) top view of an AAO membrane, b) side view of an AAO membrane,³⁴⁸ c) polypyrrole nanowires obtained after dissolution of Nuclepore membrane of 1 μm pore diameter.³⁵⁰ White scale bars are 100 nm in (a) and 500 nm in (b).

Dealing with anodic aluminium oxide (AAO) membranes, it has been reviewed first by Diggle, Downie and Goulding in 1969³⁵⁴. But it was not until 1990 that Liang and Martin used these AAO membranes to synthesize polyacetylene fibrils³³¹. Following their work, Wu and Bein,³⁵⁵ and Al-Mawlawi, Liu and Moskovits³⁵⁶ standardized the use of AAO membranes for template synthesis of nanowires. Nowadays, several groups exploit this method in order to fabricate reproducible organic and inorganic nanowires.^{24,27,208,323,334,357–359}

I.2.1.2.1. Electrochemical method

The combination of the template method with an electrochemical deposition/electropolymerization for the production of metal, semiconductor and polymer nanowires and nanotubes occurred since its first beginning. It requires the deposition of an electrode on one side of the template from which the nanostructures

will grow to fill the nanopores (Figure I.44).^{330,349,350} It allows a fine control of the nanowire structure and consequently of their physical properties by changing the electrochemical reaction time and conditions. The electrode can be deleted or kept to act as a support for the self-standing nanowires after template removal. This allows to create an environment free of surfactants and another pollutants, making this method an excellent candidate for the synthesis of plasmonic metallic nanowires.^{5,26,27,208,323,332,357,360}

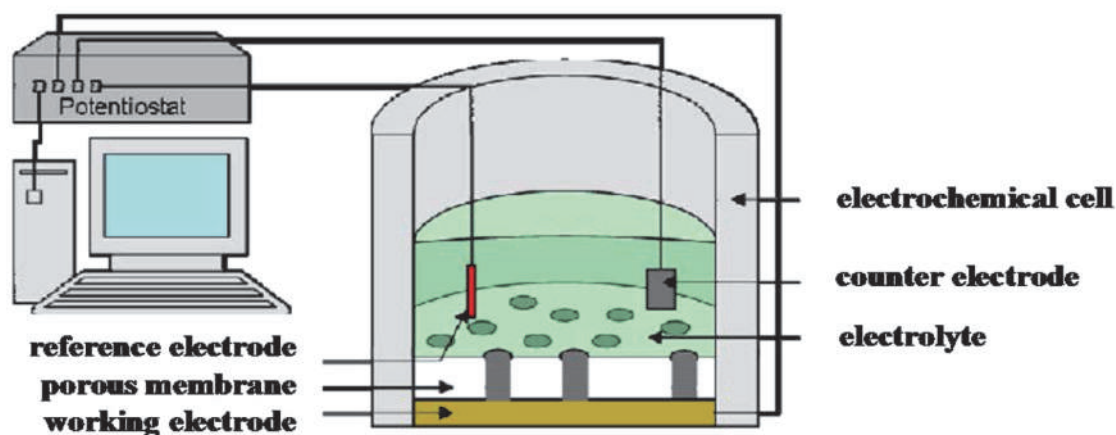


Figure I.44. Schematic of confined electrochemistry within a nanoporous membrane.²⁷

The first use of an AAO membrane as template for nanowires production was not combined with electrochemistry, but they were directly polymerized on the pore walls that were previously impregnated with a catalyst (electroless method).³³¹ The same author reported the use of AAO membranes in a templated electrochemical synthesis.³⁶¹ The group of Moskovits soon joined to the use of this alternative nanofabrication method.^{356,362}

I.2.1.2.1.1. Noble metals

The synthesis of noble metal nanowires by the templated electrochemical method was one of the first synthesis reported because of its simplicity.³⁴⁹ They can be deposited on the working electrode inside the pores by reduction of their salts.^{363,364}

An important interest of noble metals is their plasmonic properties in the visible range and their high stability and robustness relative to chemical and oxidation degradation. Ag have been mostly used because of its lower cost and its better SPP propagation in the visible range (Figure I.26b).^{43,44,67,157,365} But it presents an important drawback against Au and Pt, as it oxidizes and degrades in air.^{67,154,158,279,360} Ag nanowires must then be coated in order to protect them from environmental corrosion for a longer time scale.^{43,53,67,363,364} Furthermore, Ag is a bit less thermally stable than Au, something

possibly critical in its use in nanodevices or sensing applications.³⁶⁶ However, silver nanowires are much exploited for plasmonic studies. They are also a main alternative to indium tin oxide (ITO) as transparent conductive electrodes for photovoltaic devices and displays, where they are arranged in a percolating network.^{95–104}

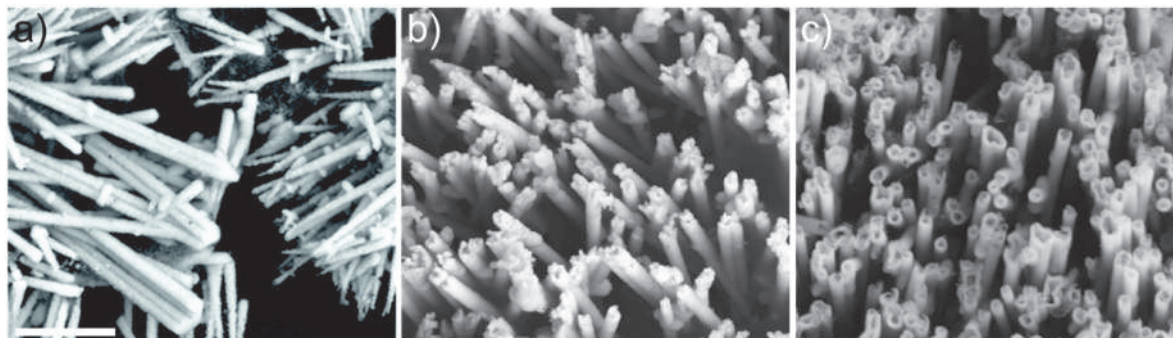


Figure I.45. SEM images of isolated a) Ag nanowires, b) Au nanowires, c) Pt nanotubes after template removal. The white bar corresponds to 2 μm and all the images are at the same scale.³⁶⁰

It has been reported that the direct electrodeposition of Au in a nanoporous template drives to the formation of Au nanowires under most electrochemical conditions (Figure I.45b), due to the stronger interaction between the reagent-product molecules (ions and native metal) themselves when they form the Au nanowires, than between the reagent molecules and the template pore walls, although under certain electrodeposition conditions they can form Au nanotubes³⁶⁷. This is analogous for Ag nanowires (Figure I.45a), but Pt has shown to form nanotubes due to a stronger interaction between its molecules and the pore walls (Figure I.45c). It can be noted that these experiments used the hard-template mounted between the two halves of a U-tube cell. In one half, they introduced the metal salt solution as in the conventional method but in the other half, instead of placing the cathode, they introduced a reductive agent and let the electrochemical reaction for a given time.³⁶⁰

Au nanowires have been synthesized by almost all the different methods that we introduced in the previous section: by top-down approaches such as electron-beam (e-beam),^{43,57,313} focused ion-beam (FIB),³¹⁴ UV lithography³⁶⁸ and stamping,³¹⁷ and by bottom-up techniques: anisotropic crystallographic growth (Figure I.42a),^{81,215,325,326} hard template (Figure I.42c),^{5,208,332,333,349} soft template (Figure I.42d),^{336,369} chain self-assembly of nanostructures (Figure I.42e)^{337,340,370} and uniaxial size reduction (Figure I.42f)^{311,341,342}.

Two important features in order to minimize the SPP losses are the crystalline structure of nanowires and the smoothness of their outer surface.^{25,154} Another important challenge deals with the synthesis of hybrid nanostructures including a plasmonic part.^{89,154} The templated electrochemical method proposes a good compromise.

Hybrid nanowires with different properties can be synthesized and the resulting Au has low polycrystallinity (few and big crystallites) with a smooth outer surface, thus acceptable for SPP propagation purposes.^{26,208,323,360,367,371}

It is now quite common to use the chloroauric acid as a greener source of Au(III) for gold electrodeposition. Indeed, it cannot release toxic agents such as CN^- and it is readily soluble in aqueous solution.^{208,363,364,367,371} The chloroauric acid is a strong acid and it deprotonates in aqueous media, giving rise to the stable and electroactive $[\text{AuCl}_4]^-$ complex. The cathodic reaction is as follows:^{363,364}



I.2.1.2.1.2. Conjugated polymers

A brief description of conjugated conductive polymers nanowires is proposed here, because hybrid metal-conjugated polymer nanowires have been synthesized and characterized, as reported later. Their synthesis is analogous to the metal nanowires, although the electropolymerization is normally oxidative. Among others, polythiophenes, polypyrroles and polyanilines nanowires have been synthesized (Figure I.46).^{146,361,372-377}

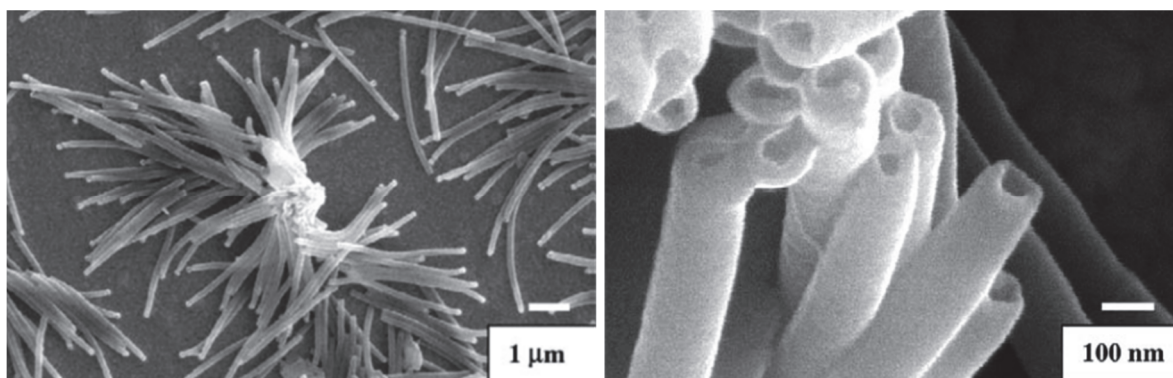


Figure I.46. SEM images of a bundle of 150 nm diameter PEDOT nanofibers (synthesis: 400 s at +0.80 V).³⁷⁴

The first electropolymerization was reported in 1862 by Letheby, although he did not attribute the new substance produced to an electropolymerization process.³⁷⁸ Since, then, the electropolymerization process has been widely studied for different polymers and under different conditions. It offers a fine tuning of the characteristics of the final polymer, their morphology, their structure and their doping level.^{375,379-385}

The first synthesis of polymer nanowires in a hard-template was reported by Penner and Martin in 1986.³⁵⁰ Their pioneer studies inspired other authors to use this technique to prepare polymer nanofibers. Nowadays this field is very active, due to the interesting

properties of conducting polymer nanofibers. Novel original structures with cutting-edge properties have also been studied and synthesized.^{5,311,323,361,373,375,377}

Among the different electropolymerizable polymers, the poly(3,4-ethylenedioxythiophene) (PEDOT) (Figure I.47) stands out because of its high stability, and its electronic and optical properties.³⁸⁶ In addition, PEDOT thin films³⁸⁷ and nanowires^{374,375,388,389} electropolymerized in aqueous medium have been extensively studied at the IMN in early 2000s. First synthesized by Jonas and Schrader³⁹⁰ and commercialized under the trade name Baytron[®], it is one of the most exploited polymers nowadays. It is involved in applications for conductive and antistatic coatings, biomedical devices, capacitors, and, combined with polystyrene sulfonate (PSS), in organic light-emitting diodes (OLED) and photovoltaic cells.^{280,281,383,391}

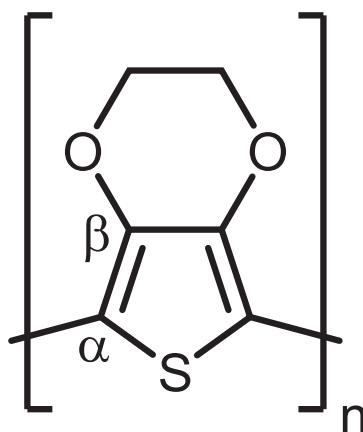


Figure I.47. Poly(3,4-ethylenedioxythiophene) structural formula with the C in α and β to the S emphasised.

PEDOT has a very characteristic Raman signal (Figure I.48b) that can be studied at different wavelengths. Its fluorescence is quenched due to the presence of the aliphatic cycle containing two O. This structure also forces the polymerization only at the α C, behaving as electron donors with a stabilized oxidized form.^{281,375,391}

The optical properties of PEDOT can be changed by tuning its oxidation level (Figure I.48a&b). Regarding the optical absorption spectra, a band at 595 nm dominates for the more neutral states. It is attributed to the π - π^* transition (gap of 1.6 eV). When increasing the doping level, the π - π^* band vanishes and another band at 880 nm comes into view, related to the polarons in the polymer. For higher oxidation levels, a wide band situated over 1350 nm arises, assigned to the bipolarons.^{374,375,392}

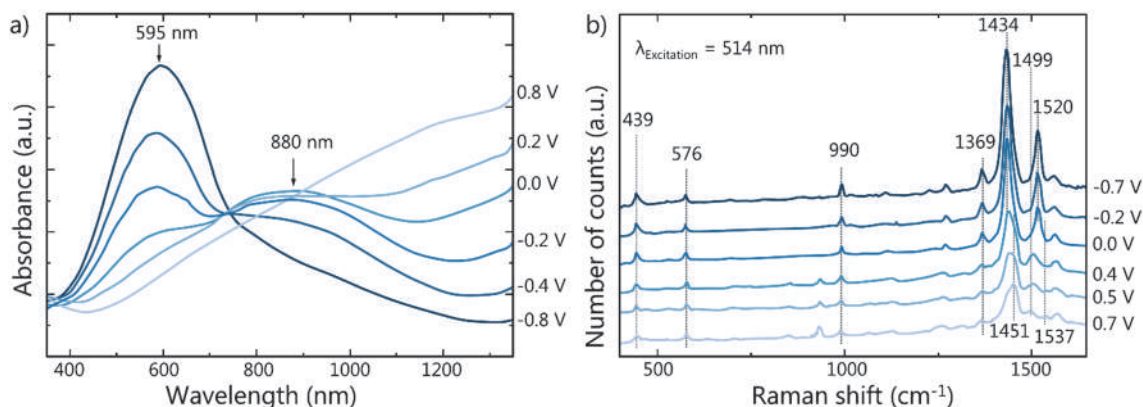


Figure I.48. Spectroelectrochemical study of PEDOT: a) absorption spectra and b) Raman spectra of a PEDOT film after application of a given voltage (vs SCE). Adapted from Retho.³⁷⁵

The modification of the Raman signal by the doping level was also studied at IMN (Figure I.48b). At higher oxidation levels, the band at 1434 cm^{-1} attributed to the C=C symmetric stretching shifts to 1451 cm^{-1} , while the C=C antisymmetric stretching band at 1520 cm^{-1} is replaced by two new bands at 1499 cm^{-1} and 1537 cm^{-1} .^{374,375,392}

Another interesting polymer that we briefly exploited during my thesis work for coupling photoluminescence with plasmonic nanowires was the poly(3-hexylthiophene-2,5-diyl) (P3HT). This choice was motivated by its ability to form nanostructures and by its absorption and fluorescence properties.^{120,146,377}

I.2.1.3. Core@shell nanowires

Beyond nanowires made of a single material, there is a huge interest for heterogeneous nanowires, as it permits to add different functionalities and/or to eventually promote original optoelectronic properties due to coupling or interaction at the interface between the different counterparts. However, lithography and conventional synthesis techniques meet constraints which limit their fabrication. Three kinds of multi-components organisation can be distinguished: (i) nanocomposite nanowires, where one of the species is randomly distributed in the matrix of another material, (ii) bi- or multi-segmented nanowires, with two (or more) species deposited alternatively along the wire axis, (iii) coaxial nanowires. The notation using the "@" symbol in A@B denotes A as core and B as shell. For instance, a metallic core allows the nanowire to behave as a SPP propagator, and an optical active shells permits the exploitation of that plasmonic behaviour for novel optical or optoelectronic applications.^{5,208,323} This coaxial morphology has been privileged in my thesis work. After a brief review of the general methods used for core@shell nanoparticles, the main strategies to synthesize coaxial nanowires with a metallic core are reported.

I.2.1.3.1. Main strategies for core@shell nanostructures

The synthesis and the study of core@shell nanostructures is quite recent, but already very extensive. Among the most reliable systems, one can mention core@shell quantum dots with highly tuneable photoluminescence properties and nanoparticles grafted with functional groups. Here, we just briefly mention the strategies developed for the synthesis of the metal-containing nanostructures due to their plasmonic properties.

In the literature, the general approach for the production of core@shell nanostructures is the construction of the shell around an already synthesized core, at least one of them being a metal.^{5,27,393,394} Their synthetic approach normally relies in the shell deposition by a chemical reaction that selectively occurs on the core surface: direct chemical reaction,²⁸² sol-gel,³⁹⁵ hydrothermal,³⁹⁶ thermal decomposition,³⁹⁷ radiolytic,³⁹⁸ electrochemical,^{208,399} or plasmon-mediated^{143,400}.

More rarely, it is described the one-step production of core@shell nanostructures in special conditions, such as in the organic-aqueous interface.^{326,401}

I.2.1.3.2. Hard template method

A well-adapted method for the synthesis of core@shell nanowires due to its high versatility, production and reproducibility is the hard template method. It is normally proceeded by electrochemistry, in order to finely control the morphology of the coaxial nanowire.^{27,120,208,323,333,402,403}

The first reports were made in the group of C. R. Martin during the late 90s.^{402,403} They described the synthesis of different core@shell hybrid nanowires. Although each material was deposited inside the nanopores by a different reaction, the methodology was similar: first, they produced nanotubules of the outer material, normally by electroless plating, direct electropolymerization or CVD on the pore walls. The next step, to produce the core, involved the application of an external potential, performing an electropolymerization or electrodeposition.

Beyond this quite straightforward method, more complex strategies termed as coaxial lithography (COAL)³³³ have been extended, notably by the group of C. A. Mirkin and nowadays COAL has been used to produce exotic 1D nanostructures with all their dimensions controlled (Figure I.49).^{208,323,333}

Some groups reported a first step consisting in the deposition of the core^{24,208,333,376} and some others first produced the shell⁴⁰²⁻⁴⁰⁵. The use of a hard template allows this steps inversion.

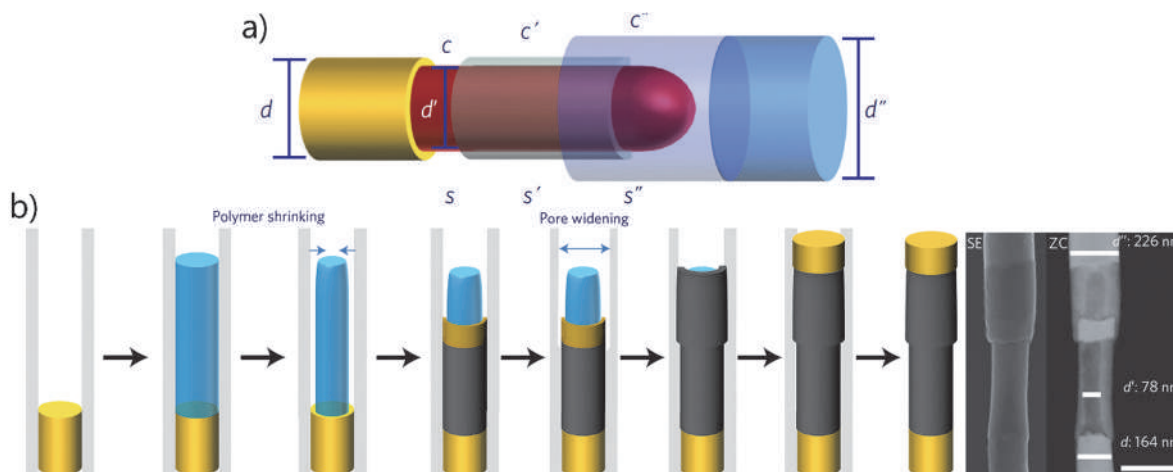


Figure I.49. a) Scheme illustrating the geometrical and compositional parameters that can be controlled by COAL: diameters (d , d' and d'' : from 20 nm to 400 nm), segment lengths (s , s' and s'' : from 8 nm to a few micrometres) and compositions (c , c' , c'' , polymers; metals; inorganic semiconductors). b) Synthetic steps of COAL: electrochemical deposition within the AAO membrane of a metal segment (yellow), followed by deposition and shrinking of a polymer segment (blue) under vacuum. Deposition of a multi-segmented shell (Au, yellow; Ni, grey) around the polymer segment. Control of the shell diameter via pore widening. This allows for synthesis of core/shell/shell nanowires, as shown by the scanning transmission electron microscopy (STEM) images in SE (secondary electrons) and ZC (z-contrast) modes of a polyaniline (PANI) core/Au ring/Ni shell nanowire composed of segments that have three different diameters after dissolution of the AAO template. Scale bar on SEM images corresponds to 250 nm. Adapted from Ozel et al.³³³

As an example of first deposition of the shell an electroless method was used to plate gold on the pore walls and faces of the membrane.⁴⁰⁶ First, a “sensitiser” (Sn^{2+}) was adsorbed to the substrate surface. Then, the membrane was thoroughly rinsed with methanol. The next step was an activation by immersion in an aqueous ammoniacal solution of AgNO_3 resulting in the formation of nanoscopic Ag particles on the pore walls and membrane faces.⁴⁰⁷ The membrane was then again thoroughly rinsed twice with methanol and with water. Finally, the Ag-coated membrane was immersed into a gold plating solution and Au nanotubes were obtained.

The fine control of the nanowire dimensions is achieved by introducing additional steps, such as the polymer shrinking under vacuum or hydrophobic collapse^{54,333,376,408} (in the case of polymer cores) and the pore widening,^{46,208,333,408} in order to create a space for the shell around the core. We exploited the later method to synthesize our coaxial nanowires.

The pore widening of AAO membranes consists basically in the wet-chemical etching of the pore walls of porous anodic aluminium oxide membranes, normally with

H_3PO_4 .⁴⁰⁹ When this process takes place, a gap is created around the core (Figure I.49b) where the shell will be deposited.³³³ The selective etching of the pore walls among the rest of the AAO membrane is believed to happen mainly because of the higher concentration of anionic impurities present in this part (Figure I.50a&b).^{359,410} By tuning the etching time, different pore openings can be obtained^{359,409} (Figure I.50c) in order to produce thinner or thicker shells⁴⁶ (Figure I.50d).

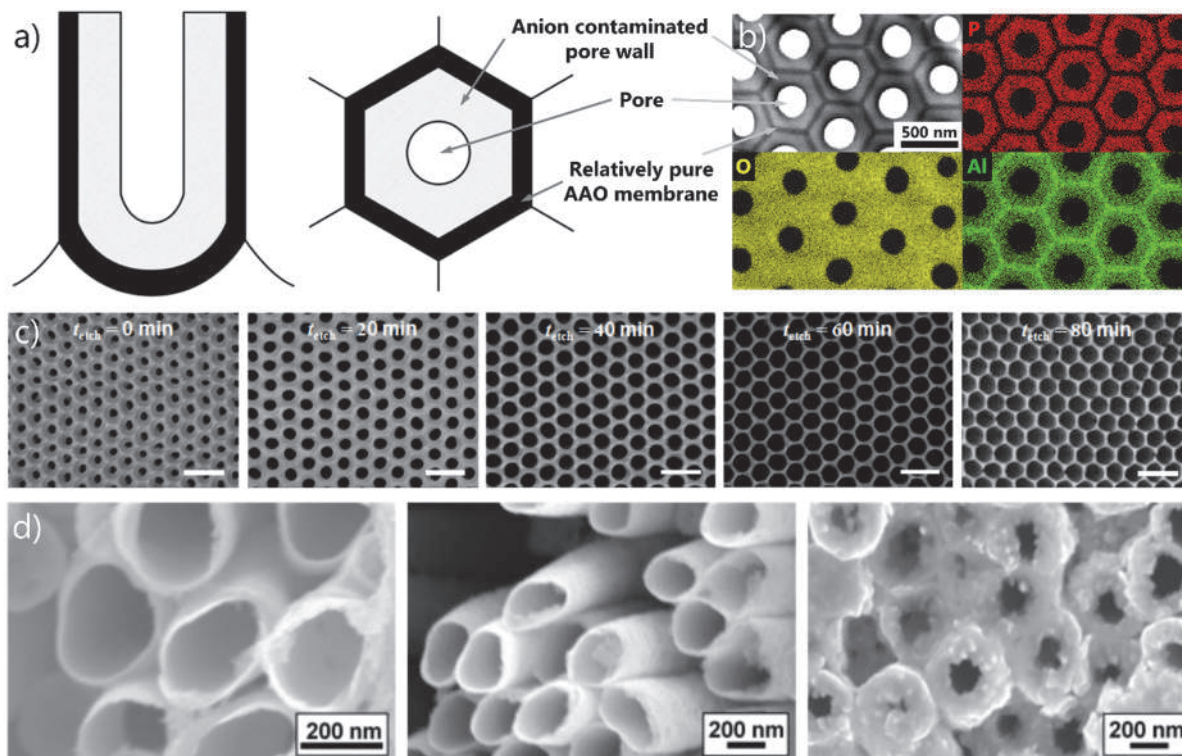


Figure I.50. a) Schema illustrating the duplex structure of pore walls of porous AAO: vertical (left) and transverse (right) cross-sections.³⁵⁹ b) TEM plane view of AAO anodized with H_3PO_4 and the corresponding X-ray maps of the elements: phosphorus (red), oxygen (yellow), and aluminium (green).⁴¹⁰ c) SEM micrographs showing the morphological evolution of top surface of AAO as a function of etching times (t_{etch}) in 5 wt % H_3PO_4 at 29 ± 0.2 °C. Scale bars are 200 nm.⁴⁰⁹ d) From left to right SEM images of gold nanoshells, after core removal, deposited after AAO pore widening in 8.5 wt % H_3PO_4 for 15, 30, and 60 minutes.⁴⁶

I.2.1.4. Direct optical nanolithography of polymers

The optical lithography is the transfer of a pattern to a sample by means of light. It normally requires a photoresist material that is deposited on the sample, selectively removed by the use of light and a mask (development), and then the unprotected sample is removed (etching step) leaving the same pattern.

The downsizing of masks allowed the fast transfer of nanopatterns (optical nanolithography) onto substrates, very useful for big scale production.^{411–413} One of the main constraints for decreasing the size of the patterns is the etching step. The less expensive and more common wet etching process uses a compound (developer) that removes the sample isotropically, resulting in a lower resolution. The dry etching, normally costly, removes the sample anisotropically, resulting in a higher resolution.

One of the most balanced dry etching methods for the creation of nanopatterns, in terms of economic cost and resolution, is the laser dry etching. In addition, by fine control of the laser position, it does not require the use of a mask. It basically consists in the use of a laser in order to ablate patterns on a sample. It has been reported that PEDOT:PSS films can be patterned by this method (Figure I.51).⁴¹⁴

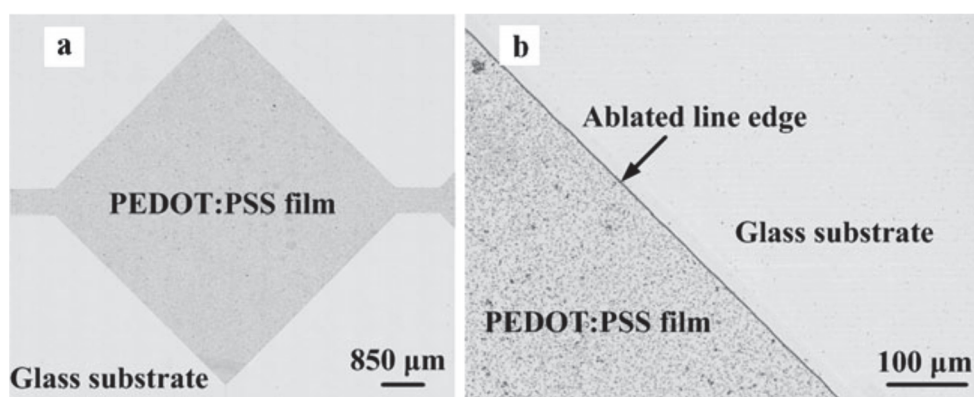


*Figure I.51. Microscopy photographs of a PEDOT:PSS electrode after laser dry etching. The dark area was the un-ablated region in the PEDOT:PSS film, and the light area was the laser ablated region.*⁴¹⁴

Alternatively to polymer etching, the photobleaching of photoluminescent polymers by laser irradiation has also been exploited to induce a modification of the emission at the nanoscale. An example is reported (Figure I.52) in metal nanowires covered with fluorescent dyes.^{238,239}

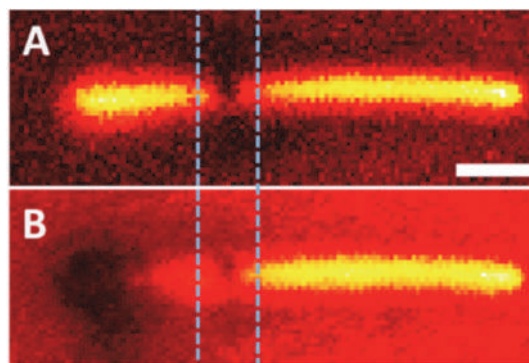


Figure I.52. a) Sample-scanned fluorescence image of a Cardiogreen-coated gold NW with a gap in the dye fluorescence response near the middle of the NW, created by direct laser photobleaching with $12 \mu\text{W}$ of power for 2 min. b) Fluorescence image taken after excitation of the same NW at the left end with $20 \mu\text{W}$ of 785 nm laser light for 20 min. The laser power for the image acquisition was $0.07 \mu\text{W}$. The scale bar corresponds to $2 \mu\text{m}$.²³⁹

I.2.1.5. Coupling antennae with nanowires

The combination of nanoantennae with plasmonic nanowires in order to improve the photon-SPP coupling has been briefly mentioned in a previous part. Further information is proposed here, as this topic will be directly addressed in the Chapter IV of this manuscript.

Experimentally it was first reported by Knight in 2007 when he observed a nanoparticle-mediated light coupling of light into nanowires.¹⁶³ Since then, different synthesis techniques and antennae geometries have been studied by several authors.

I.2.1.5.1. Main strategies

A first point dealing with antenna coupling is the optimal geometry of the antennae: sharp tips and features,^{154,415} nanoparticles,^{26,29,74,83,85,163,165,166,229,237,266,306,416}, bowties^{162,164}, triple bow-ties¹⁶⁴ and more complex geometries^{87,308,417} have been revealed as optimal candidates.

The second point deals with the precise placement of the antenna in the light-SPP input or/and outputs of the waveguide. Focused ion-beam^{165,304} and electron-beam lithography^{85,164,417} are the techniques mostly used, as previously illustrated (Figure I.41). Another strategy consists in synthesizing both nanowaveguides and nanoantennae separately and assembling them afterwards on a suitable substrate. The main drawback of this method is due to the randomness to get the desired nanoantenna-nanowaveguide arrangement.^{29,163,266,270} Alternatively, grafting of complementary functions on the nanoantenna and on the waveguide can improve the

yielding of successful coupling.²⁷⁵ The optical trapping of nanoparticles^{74,418–420} and nanowires^{74,421} is also an extensively used method to precisely locate micro and nanoparticles on a substrate. The use of nanomanipulators as atomic force microscope tips⁸³ or optical nanofibers (Figure I.53)¹⁶⁶ to move the nanoantennae to the optimal position have been found as a suitable option. Fujita et al. proposed a method to anchor nanoparticles on the desired part of nanowires by applying a voltage between a tip and the nanowire in a nanoparticles-containing dispersion.²⁷¹ An exotic technique proposed by Wiley and based in the nanoskiving of gold microplates could be used in order to get a good number of nanowire-nanoparticle systems.¹⁵⁴

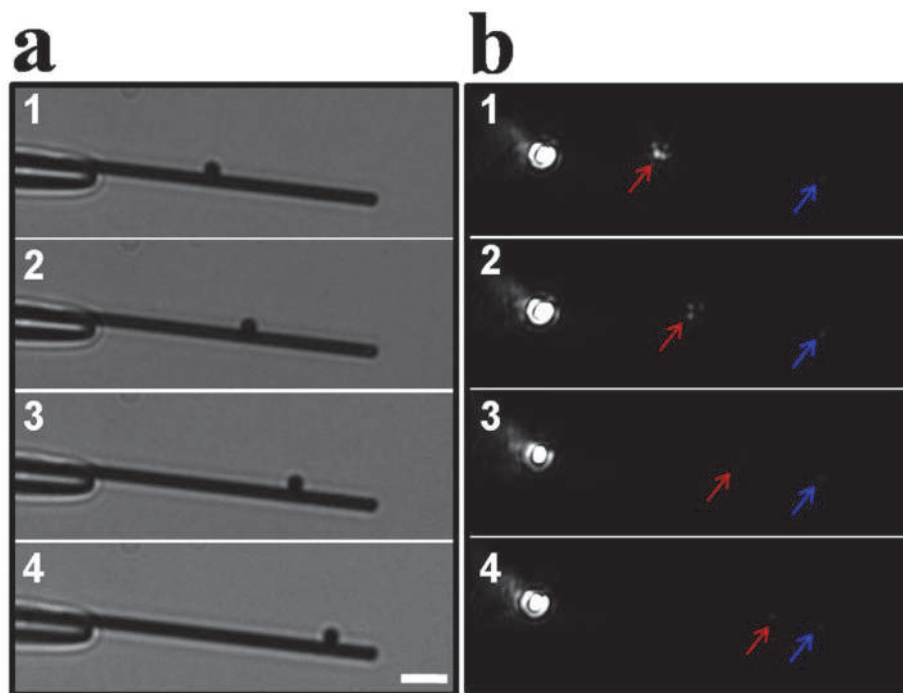


Figure I.53. Characterization of emissions at an Ag NP-NW waveguide for different locations of the NP manipulated by a tapered optical fibre. a) Bright-field optical images collected by a 50× objective (N.A. = 0.80, Olympus). b) The corresponding dark-field optical images. Emission spots at Ag NP and NW end are indicated by red and blue arrows respectively. The white scale bar corresponds to 5 μm .¹⁶⁶

I.2.1.5.2. Metal etching by thermal or laser treatment

Besides lithographic and nanomanipulation techniques, an interesting strategy for coupling an antenna to a nanowire supporting SPP consists in transforming the metallic nanowires tips into metallic nanoparticles by laser treatment. Regarding the literature, we realized that converting Ag and Au nanowires, or a part of them, into nanoparticles have been realized during the last decade. Such a modification of a gold nanowire was already reported but it has never been used as antennas for SPP-photon coupling. We

exploited this method to fabricate antenna-improved nanowires, as reported in Chapter IV.

The selective and precise modification of metal nanostructures, particularly nanowires, can be performed by high energy methods such as ion-beam,^{165,242} electron-beam,^{164,422} thermal treatment^{98,366,423–425} or photolithography^{99,426–431}.

For thermal or laser assisted treatments, the mechanism normally consists in the melting of the metal due to the increase of its temperature.⁴³¹ The melted metal generally tends to form droplets, rather than wetting the substrate surface. The resulting more stable shape is roughly spherical. After shutting down the irradiation, the rapid freezing helps maintaining this nanoparticle morphology.^{98,366,423,424}

Under thermal treatment, some authors have reported the full transformation of nanowires in chains of nanoparticles by a thermal process the whole nanowire (Figure I.54a).^{98,366,423,424}

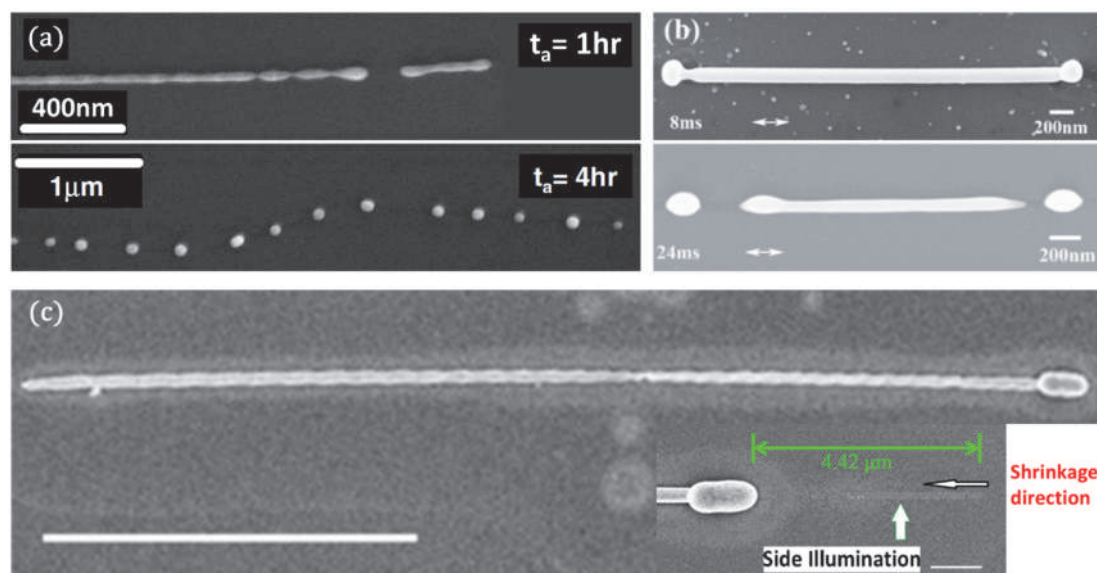


Figure I.54. Effects of different post-treatments on the morphology of Au or Ag nanowires (SEM images). a) 50 nm diameter Au nanowires annealed at 500 °C for 1 or 4 hr.⁴²³ b) Ag nanowires following femtosecond laser irradiation for 8 and 24 ms. (laser pulses at a repetition rate of 1 kHz gave a laser fluence of $\sim 130 \text{ mJ cm}^{-2}$; laser wavelength: 800 nm). Double arrows show the direction of the laser polarization.⁴²⁸ c) Ag nanowire after irradiation with a continuous-wave laser (150 mW, wavelength: 532 nm, 1 s, circular polarization). Scale bar is 1 μm . Inset: enlarged image of the nanorod-shaped terminal. The green arrow denotes the position of the beam centre (scale bar: 200 nm).⁴²⁹

In order to better control the position of the nanoparticles, it was reported that irradiating a sample with a pulsed laser induced the transformation of the tips of the nanowires into nanoparticles when they were aligned parallel to the electric field of the

incident radiation. This was attributed to the longitudinal surface plasmon resonance, i.e. parallel to the nanowire axis. It has been shown that longer irradiation times have a similar effect than a specific thermal treatment at 500°C under vacuum ($\sim 5 \times 10^{-6} \text{ mbar}$) of the whole sample (Figure I.54b).^{99,427,428} Further research revealed that focusing the laser beam at those tips could selectively perform the same transformation without affecting the rest of the sample (Figure I.54c).⁴²⁹ Also, focusing the laser on an arbitrary point of the nanowire created a gap and, in some cases, a nanoparticle at each side of this gap.⁴³⁰

I.3. Strategy and methods selected for my thesis project

The above parts introduced the main notions required to understand plasmonic behaviour of 1D nanostructures. The state-of-the-art of the corresponding recent advances permits to identify some important challenges of this research field, also promising for a new generation of nanodevices (sensors, integrated light nano-sources,...) exploiting plasmonic effects. Among them, we selected to address three challenges:

- Controlling the nano-architecture of hybrid nanowires to promote an optimal plasmonic-based effect
- Studying these hybrid nanowires as single nanostructures once dispersed on a solid substrate.
- Improving the coupling of an external source (a laser in our approach) with the plasmonic nanowire.

The first objective was to design the optimal nanowire-based nanostructures that could support SPP. The inclusion of Au backbone was a must have, as it would act as plasmonic 1D structure. The choice of Au over other plasmonic metals such as Ag or Cu was mainly motivated by its high chemical stability when kept in air that permit to avoid to deposit a protecting shell. Gold is also a standard electrode for electrochemistry, a technique used in our template synthesis. The plasmonic properties of Au nanowires had been already largely studied, revealing that the plasmonic nanowires should be over 100 nm to improve the SPP propagation length. We combined this background knowledge with our capability of finely tuning their properties and the possible formation of hybrid nanowires by using the electrochemical hard-template method. Furthermore, this method avoided the use of surfactants and other possible pollutants that could complicate the Raman signature analysis. In order to give to our nanowires an original function or optical behaviour, we worked on the design and synthesis of coaxial (or core@shell) nanowires, composed by a plasmonic active core of Au and a shell with characteristic optical or spectroscopic properties. There is a dual goal to this coaxial design: the shell material should reveal the plasmon propagation by coupling with the SPP, and its coupling with local electromagnetic field should promote a modified or amplified spectroscopic or optical signature.

We considered different materials as promising candidates, such as fluorescent thiophene-based polymers or photoluminescent clusters embedded in inert and transparent polymers, in relation with previous studies performed in the group of J.L. Duval on the photonic and emissive properties of fluorescent and phosphorescent

nanowires.^{24,358,387,432,433} Our final choice was on a Raman active species, because the Raman signal is much less intense than a fluorescent one and it thus could strongly benefit from a field enhancement and antenna effect. Additionally, our group has a strong expertise in Raman spectroscopy and it is well-equipped with a recent Raman spectrometer coupled to a microscope and a nanopiezoelectric-stage, a set-up designed for Raman mapping with a resolution of about 110 nm. For the Raman scattering source, the conjugated polymer poly(3,4-ethylenedioxythiophene) (PEDOT) is an excellent candidate, as it can be easily electropolymerized, it is fairly stable in air and under laser irradiation and it gives a characteristic Raman spectrum rich of information on the molecular and supramolecular structure. Moreover, this polymer has been much investigated in the 2000s at IMN, with the attribution of the Raman bands through a theoretical approach, the study of its spectroelectrochemical behaviour and the synthesis of PEDOT nanowires with evidence of improved electrical properties due to the confined synthesis.

We achieved the synthesis of Au@PEDOT nanowires with PEDOT located all along the nanowire (Figure I.55c), only at the tips (Figure I.55d) and just at one tip (Figure I.55e). We also synthesized pure PEDOT and pure Au nanowires in order to master the full-synthesis techniques and as comparison with the more complex nanowires. Furthermore, we were able to disperse them on a variety of solid substrates obtaining isolated nanowires that we could fully locate by different techniques. In Chapter II, their synthesis and characterization are detailed.

The extreme confinement for PEDOT growth provided by the template synthesis lets expect an unusual supramolecular ordering of this few nanometres thick shell. It has been carefully explored by Raman spectroscopy on Au@PEDOT nanowires, as reported in Chapter III.

We finally propose to improve the local optical coupling on a part of the nanowire by forming Au nanoparticles at the tip(s) of a gold nanowire (Figure I.55f&g). We discovered by serendipity that we could transform the tips of the nanowires into nanoparticles by fusing them with the laser beam. When modifying just one tip we created the half dog-bone nanowire (Figure I.55f) and when modifying both, the dog-bone nanowire (Figure I.55g) which we could couple with PEDOT particles after a dispersion step. In order to analyse the plasmonic behaviours of these different nanowires, some developments of the micro-Raman spectrometer have been done to settle the remote configuration and to perform signal maps with few nanometres steps. The direct nano-reflectance of the laser, the remote nano-reflectance and the remote Raman spectroscopy study of these novel hybrid nanowires are presented in Chapter IV.

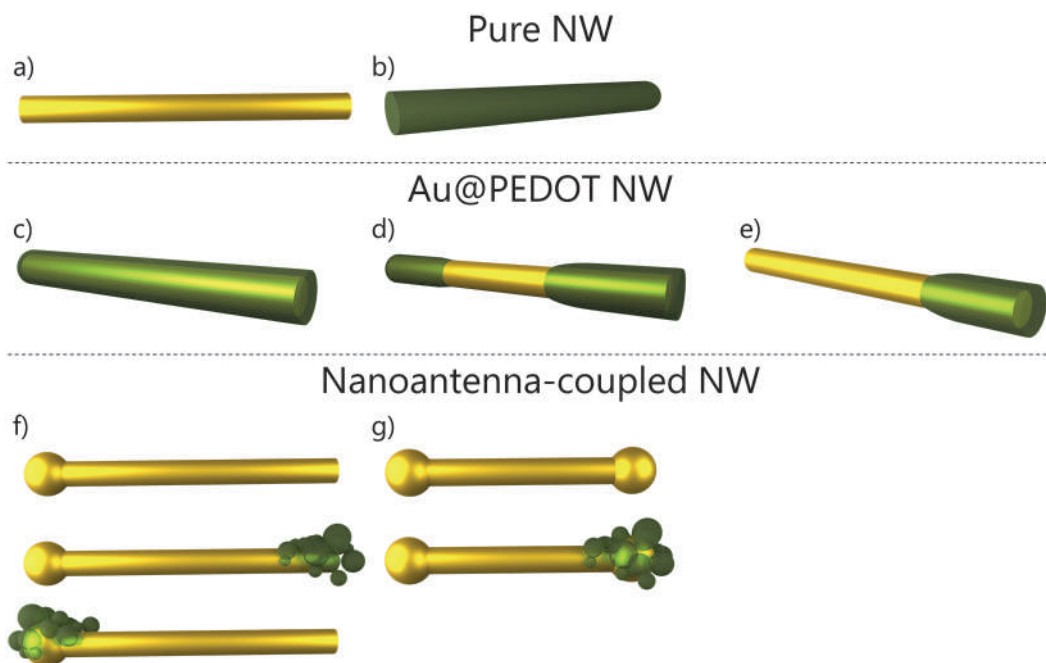


Figure I.55. Schema representing all the different designed nanowires during my thesis work. a) Pure Au nanowire, b) pure PEDOT nanowire, c) fully-covered-PEDOT Au@PEDOT nanowire, d) Au@PEDOT nanowire with PEDOT shell only at the two tips and e) only at one tip, f) half dog-bone Au nanowires without and with PEDOT particles and g) dog-bone Au nanowires without and with PEDOT particles.

CHAPTER II

Synthesis & Characterization

II. Synthesis & Characterization

II.1. Introduction

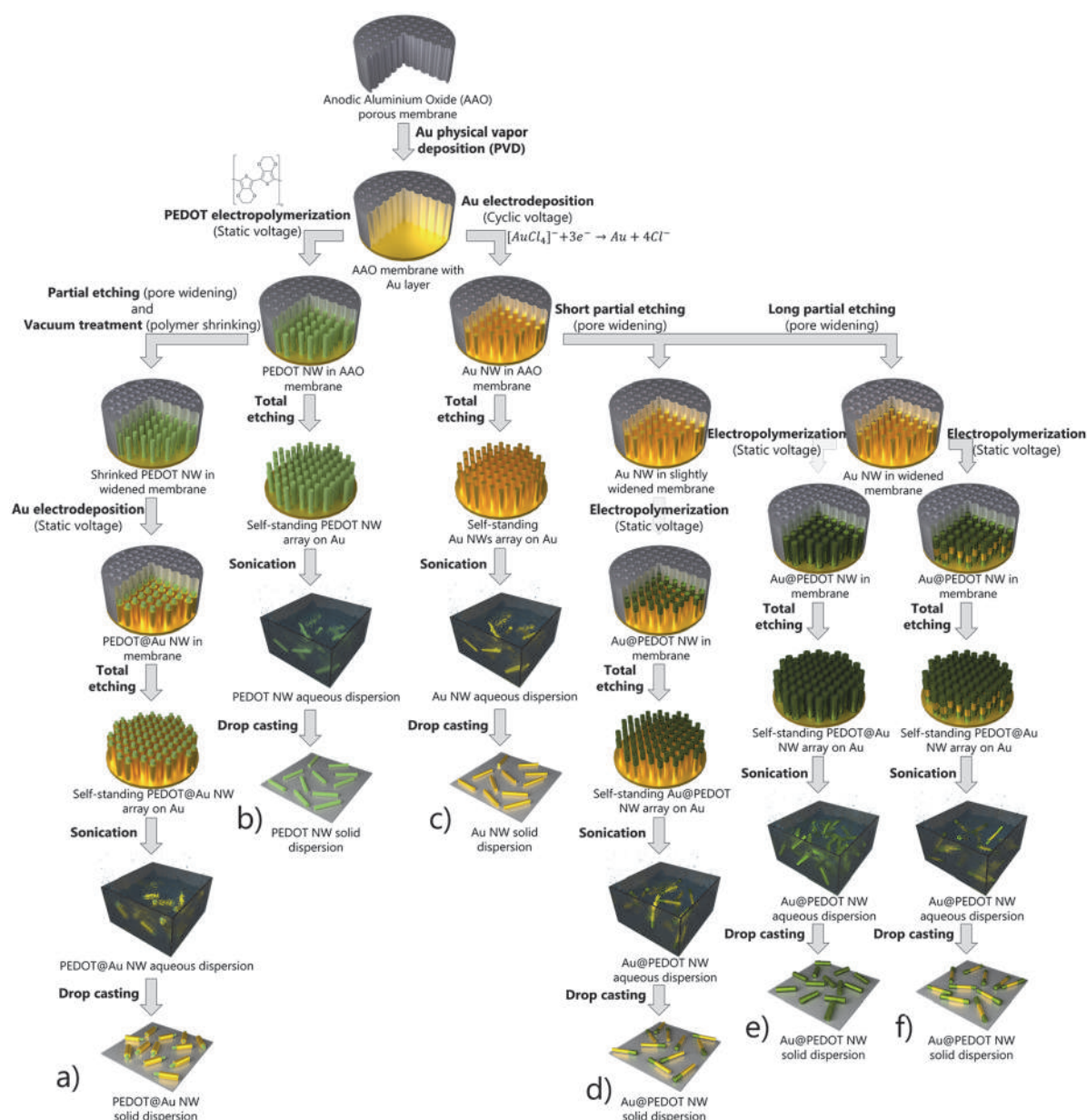


Figure II.1. Schematic description of the processes developed for the synthesis of coaxial nanowires with template methods using AAO membrane.

In this Chapter, we first present the preparation of the nanoporous templates and their characteristics. Then, the synthesis and characterization of Au nanowires and PEDOT nanowires is reported. Finally, the fabrication of various kinds of coaxial Au@PEDOT nanowires is presented, with the PEDOT shell placed in a controlled way on different

parts of the Au core: all along, just at the tips or just at the top tip. A morphological and chemical study of the nanowires is systematically reported in order to demonstrate the successful synthesis and to get structural information.

It can be noted that the synthesis of Au@PEDOT nanowires requires many process steps (Figure II.1). In particular, the pore widening method can be tuned and it opens the way to control and modulate the position of PEDOT along the gold nanowire. By modifying all the synthesis parameters we could prepare the different hybrid nanowires described in the end of Chapter I (Figure II.1).

Additionally, the modification of such as-prepared nanowires has been achieved by post-synthesis processes using laser treatment. First, the laser etching aims at removing the PEDOT with a spatial control at the sub-microscale. Second, the laser heating aims at modifying the tips of Au nanowires to promote large balls for an improved optical coupling, either at the excitation, or at the emission.

II.2. Template-based synthesis

First specifications for a template-based strategy deal with the choice of nanoporous membranes. The choice of AAO membranes rather than polycarbonate ones was motivated by different required characteristics. Although PC is less expensive and fragile, the AAO membranes allow us to prepare coaxial nanowires because the alumina pores can be chemically widened at the nanometric scale in a well-controlled manner, a key-step in our process. Additionally, it is possible to totally etch the AAO and eliminate the etching agent on the nanowire surface, while the total removal of polycarbonate surrounding the nanowires is hardly achieved.²⁰⁸ This last point could alter the physical behaviour or be critical for further synthesis step.

The electroplating of gold within the nanopores was exploited because it fills totally the nanopores with a good crystallinity and the resulting nanowire surface is very smooth, as it replicates the pore surface. These two points meet the criteria for promoting a good propagation of SPP.

II.2.1. AAO membranes

For the templates, we evaluated the AAO membranes purchased from InRedox and Synkera. They are 50 μm thick with a porosity usually ranging between 10% and 20%. The PC membranes could have porosities up to 50%. They are consequently very fragile and need to be carefully manipulated with tweezers. We also exploited a vacuum pick-up system for helping in manipulation. The nominal pore sizes of the membranes given by the manufacturers were 20, 40, 55, 80, 100, 120, 150 and 200 nm, that respectively corresponded to a pore size distribution centred on 22, 42, 55, 75, 114, 140, 160 and

200 nm with a size distribution of about 15% of the diameter, as determined by SEM and TEM.

Because of their anodizing synthetic process which forms the nanopores, AAO membranes are non-symmetric, i.e. they have two different sides (Figure II.2). The side called "solution layer" is where the anodization is initiated (on the aluminium foil), as it is in contact with the anodizing solution during the entire process. In non-optimized conditions, it can result in poorly self-organized nanopores perpendicular to the surface. Consequently, its appearance is duller and matte. Once the anodization process is ended, the AAO membrane is separated from the Al foil, making apparent the "barrier layer" side. As the self-ordering of the pores distribution improves with anodization depth, the "barrier layer" side appearance is smoother, shinier and more reflective.

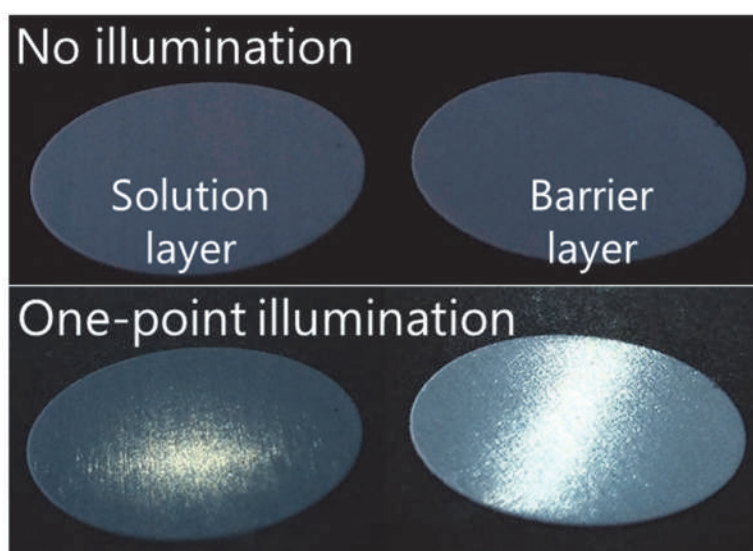


Figure II.2. Optical images of both sides, solution and barrier layers, of anodic aluminium oxide porous membranes. Without illumination (up), it is difficult to observe the difference between them but under one-point illumination (down), the higher reflectivity of the barrier layer side is easily observable. $\Phi_{pore} = 140 \text{ nm}$.

It has also been proposed that this anodization process of the aluminium foil results in a pore surface made of a thin amorphous alumina layer partially hydrated and anion-rich, while the core is almost pure alumina. This difference can be exploited to perform anisotropic acid etching of the AAO membrane (once the nanowires are synthesized inside of it), which preferentially removes the superficial layer all along the nanowires. Additionally, in the synthesis of Au nanowires described in a later section, some H^+ from the electrochemical solution could evolve into H_2 , increasing locally the pH and making the pore walls more reactive against acids.^{359,409,410,434}

II.2.2. Gold electrode on AAO

Prior to start with the electrochemical hard-template based synthesis, a gold layer was sputtered on the barrier layer face by physical vapour deposition (PVD) in a radiofrequency magnetron sputtering system (Figure II.1). This Au layer acted as a working electrode in the electrodeposition of nanowires. The sputtering deposition was made by Franck Petitgas in charge of this equipment at the Institute. The gold target was placed in a vertical position.

The optimal conditions found for the Au sputtering on these AAO membranes were the following:

Au radiofrequency magnetron sputtering system conditions

Membrane side exposed	Barrier layer
Target disposition	Axial (vertical)
Au thickness	5 times the pore diameter
Voltage	334 V
Current	90 mA
Sputtering power	30 W
Deposition pressure	$<5 \times 10^{-3}$ mbar
Argon flow	50 SCCM
Deposition rate	10 nm/min

Table II.1. Optimal conditions found for the Au metallization of AAO membranes by PVD in the radiofrequency magnetron sputtering system.

If the Au layer was too thin, the electrochemical solution impregnating the membrane would leak through it. If it was too thick, there would be a major risk of delamination and separation from the AAO membrane.

We observed that, once metallized with gold, the colour of the membranes in a reflexion mode changed depending on their pore diameter (Figure II.3). For the pore diameter varying from 10 to 160 nm, the colour progressively changed from goldish to reddish for 35 and 55 nm, and then to clear blue for larger diameters. It has to be noted that, in reflexion mode, the membranes before metallization were almost transparent for the smaller pore diameters and tended to white for larger pore diameters, due to the light scattering at the alumina/air interface all along the pores.



Figure II.3. Au metallized AAO porous membranes of different pore diameters.

This colour variation should be a combination of different characteristics, which can change from one kind of metallized membrane to another: the pore diameter, the membrane thickness, the gold layer thickness. As the gold layer was systematically thicker than 100 nm (except for the 10 nm pore diameter), the latter hypothesis could be rejected because no light can be transmitted through it.⁴³⁵ A key point was observed when PEDOT nanowires were characterized by SEM and TEM. This study evidenced the presence of gold nanoparticles located at their bottom tip, where the electroplating began in contact with the working electrode. Such gold nanoparticles at the bottom of the nanopores resulted from the sputtering process, with some gold atoms penetrating and depositing on the pore surface along few hundreds of nanometres. This observation suggests that gold atoms tended to aggregate preferentially than to form a continuous film under an almost perpendicular (grazing) incidence. The mechanism responsible for the reddish coloration is thus attributed to the plasmonic behaviour when the nanoparticle diameter was few tens of nanometres.

II.2.3. Supporting materials for studying individual nanowires

Another key point of the methodology was the choice of the support to disperse the different kinds of nanowires for further characterization and studies. We had to characterize the morphology (SEM, TEM), the composition (EDS-HRTEM, Raman) and the optical and spectroscopic response (reflectance, Raman, EELS-STEM) of a given nanowire dispersed on a substrate. The characteristics of the supporting system were thus crucial to develop our project (Table II.2). A main specification concerned its optical behaviour under laser excitation. It should give, neither a Raman signal in the PEDOT Raman region of interest ($1000 - 1800 \text{ cm}^{-1}$), nor a fluorescent signal in order to avoid parasitic signals in spectroscopic studies. Regarding the previous literature concerning the substrate and SPP propagation in metallic nanowires, we should use a substrate with a low dielectric constant, in order to restrain plasmonic losses.²⁰³ But this is in conflict with another characteristic: in order to perform SEM and EELS-TEM measurements and to avoid the metallization of the sample (to prevent modifying its optical and plasmonic properties), the substrate should be conductive. In order to be

in agreement with both features, very thin dielectric substrates mounted on TEM grids were positively considered, despite their extreme fragility.

Substrates specifications					
Type of substrate	(a)	(b)	(c)	(d)	(e)
SiO ₂ slab (Non-fluorescent)	✓	✓	✗	✗	Transparent, bad size
Boron-doped Si wafer	✓	✗	✓	✗	Available for patterning
C-based TEM grid	✗	✗	✓	✓	For first TEM characterization
SiO _x TEM grid (50 nm thick)	✓	✓	✓	✓	Fragile, too thick for EELS
SiO _x TEM grid (20 nm thick)	✓	✓	✓	✓	Very fragile

Table II.2. Key properties of several solid substrates explored for the dispersion of nanowires. Positive (✓) or negative (✗) specifications are indexed for (a) parasite spectroscopic Raman or fluorescence signal, (b) dielectric properties for plasmon propagation, (c) conductivity for SEM studies and (d) electron transparency for TEM studies, (e) other important features. Only the SiO_x TEM grids did meet the basic criterion for their choice in our advanced studies.

Referenced substrates for correlated techniques

In order to be able to find the same nanostructures when changing between techniques or making experiments in different days (passing from macro to sub-micro), it was necessary to have a referenced system. Taking into account the substrates exposed we present different designs.

Our first design, easier to product and more economic, was to laser ablate a predefined pattern on a boron-doped Si substrate (Figure II.4a). This process was made by Sebastian Nufer in M-Solv Ltd, partner of the ITN project. Thanks to it, we could correlate optical/Raman microscopy and SEM (Figure II.4b&c & Figure III.12).

The main drawbacks of this kind of substrates were their high dielectric constant (they are quite conductive), avoiding the SPP on gold nanowires, and the impossibility of making TEM studies with them. They allowed us to make a first approximation and full characterization of our nanowires, but for the next step of the project we used more advanced but expensive substrates.

The use of patterned SiO₂ slabs was not even tried. We could have SPP propagation on Au nanowires but we were not going to be able to characterize them by SEM without metallization and therefore changing their properties.

We thus choose very thin (20, 50 nm) SiO_x TEM grids commercially available (Figure II.5). We thought that these could be our optimal substrates if we were able to correlate different techniques on them. We tried them and the results were outstanding. All our requisites were fulfilled. To prevent charges effect during SEM imaging, it was necessary to work at low acceleration voltages (< 2.00 kV).

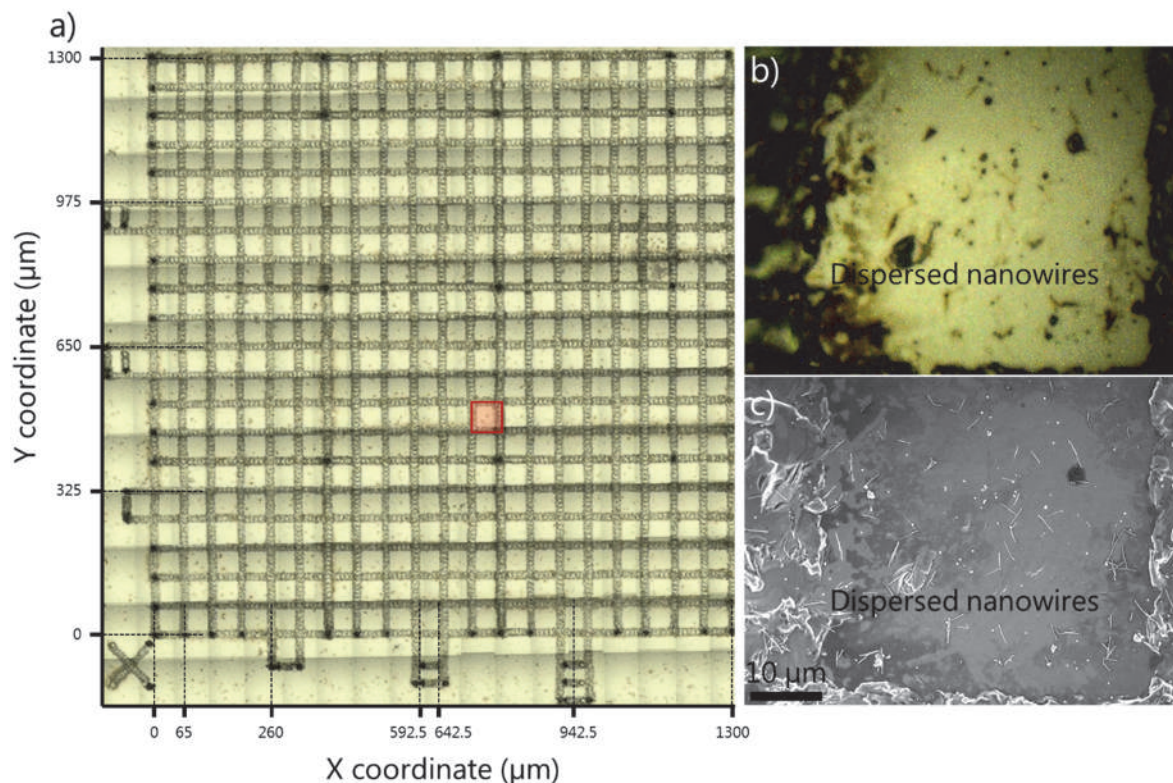


Figure II.4. a) Optical microscopy image of a boron-doped Si substrate with a laser ablated pattern. The lateral dimension of the squares is 50 μm and the width of the tranches 15 μm . In red, a square with interesting nanowires is marked. b) Optical microscopy and c) SEM images of the same marked-in-red square. It can be observed the very good correlation of optical and e-beam images.

Once the nanowires were dispersed on the SiO_x TEM grids, we could locate them by using the optical microscope coupled with the Raman set-up (Figure II.5). The contrast given by the thin SiO_x layer was so high that we could even locate $\text{Ø } 20 \text{ nm}$ Au nanowires by optical microscopy.

The critical point when using these TEM grids as substrate was the drop casting of the nanowires dispersion on them. The fragility of these substrates could cause their break and collapse during this step. It should be done carefully, taking no more than 3 μl of the dispersion with a micropipette and making the drop casting step as closer to the substrate as possible but without touching it. Once the drop was on the TEM grid, we allowed it to dry for one day in a protected environment.

The main differences between both SiO_x TEM grids were experienced while working with them. The 50 nm thick grids are significantly less fragile and possess a larger useful surface than the 20 nm thick ones. But the 20 nm thick offer a more homogeneous flat surface, a key-point for realizing the maps and they are thin enough to minimize the interaction with the electron beam for TEM-EELS study, as envisaged.

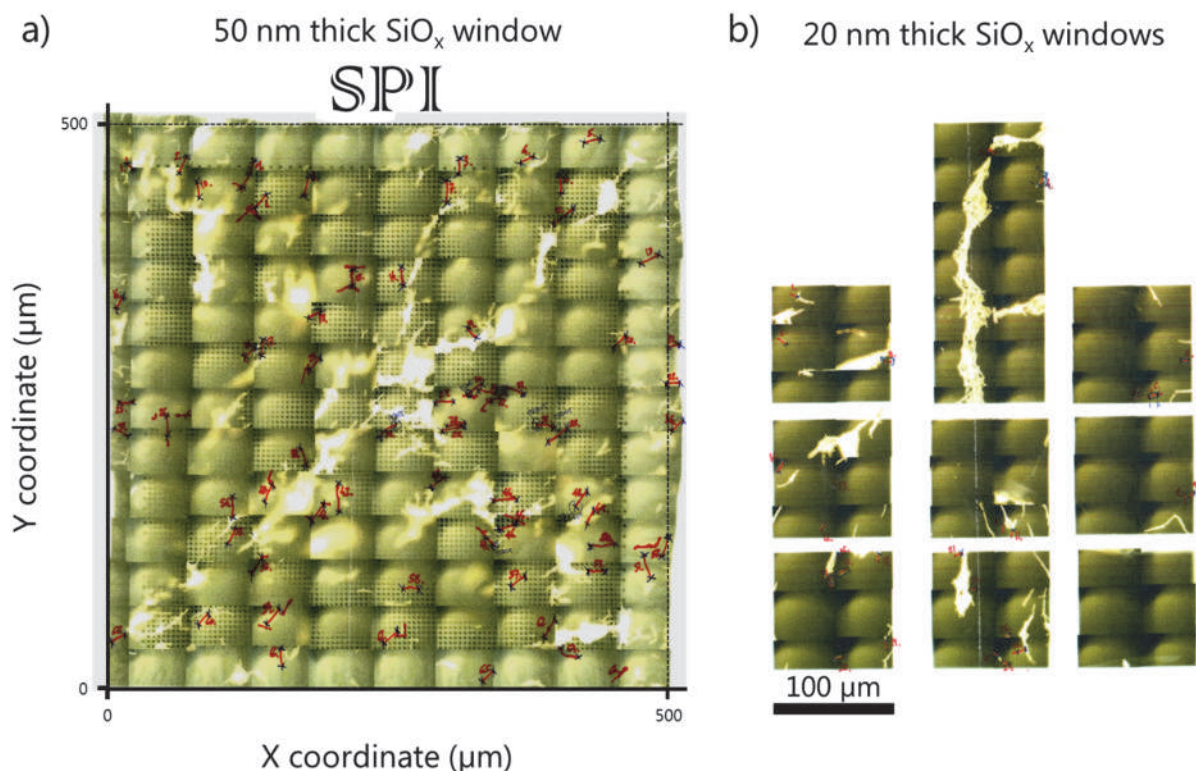


Figure II.5. Optical microscopy images of a) 500 x 500 μm, 50 nm thick SiO_x window in a TEM grid. The window is microperforated with 2 μm holes separated 5 μm between their centres. "SPI" (the brand of the manufacturer is etched next to one of the sides of the window, permitting a fast orientation of the grid. b) 100 x 100 μm and 100 x 250 μm, 20 nm thick SiO_x windows in a TEM grid. The presence of a window of different dimensions allows a fast orientation within the sample. We should note that the distance between the windows is larger than it appears in the image, but it was hidden as the nanowires placed on that space cannot be studied. We draw the interesting nanowires in red.

II.2.4. Other key aspects to perform reproducible synthesis and dispersion processes

Among all the synthesis tricks, we should note the use of Teflon labware against glass. We noticed that Pyrex[®] glass, presumably during the concentrated H₃PO₄ etching treatment could release SiO₂ nanoparticles (Figure II.6). Since we started using polytetrafluoroethylene (PTFE) glassware, we did not observe anymore the presence of these nanoparticles.³⁴⁹ It must be noted that ultrapure water (resistivity > 18.2 MΩ.cm) has been used in all the steps of the process to get reproducible process and to prevent

from external pollutants such as NaCl. We relied on it in order to avoid any kind of impurity or pollution deposited on or close to the nanowires.

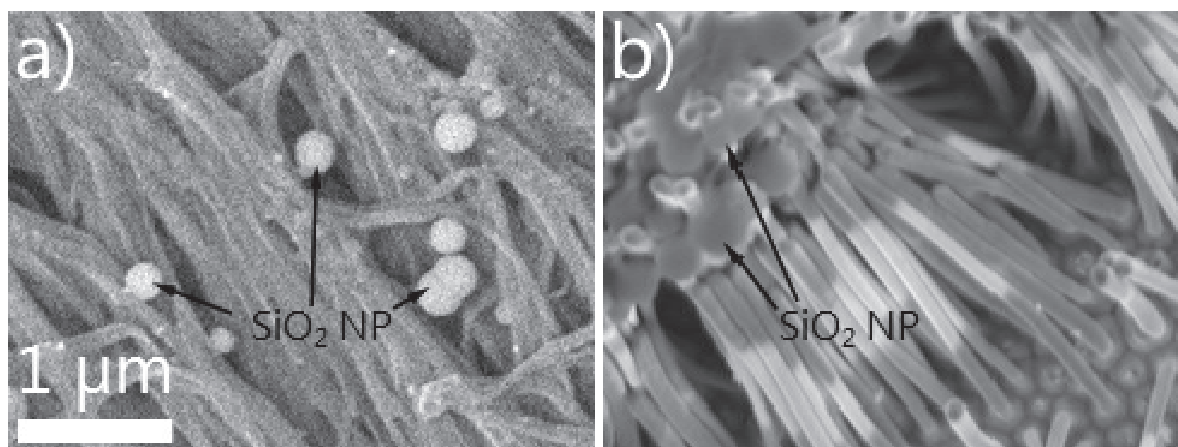


Figure II.6. Examples of SiO₂ nanoparticles pollution in samples. a) Back-scattered electrons-SEM image of an array of \varnothing 55 nm PEDOT nanowires. b) SEM image of an array \varnothing 140 nm Au@PEDOT nanowires.

In order to eliminate any possible impurity from this Teflon container and for the non-TEM substrates, we performed several consecutive hard-cleaning processes.^{436,437}

To remove eye visible organic or inorganic deposits, the labware were cleaned with soapy water first and then rinsed with acetone. This process should be repeated until the pollution was no more visible, then rinsing with Milli-Q[®] water. Normally, this process was not necessary because dedicated labware was used.

In order to remove any micrometric and nanometric metallic impurities, we prepared an aqua regia mixture (HNO₃:HCl 1:3). We rinsed the labware and the substrates with it and allowed to react for 15 minutes. We then rinsed with Milli-Q[®] water 3 times.

The next step was used to remove any organic pollutant, non-visible by eye. We prepared a piranha clean (H₂SO₄:H₂O₂ 10:1) and we rinsed the labware and the substrates with it. We allowed to react for 15 minutes. We then rinsed with Milli-Q[®] water at least 3 times.

We observed that the Teflon labware could “trap” the acid molecules in their surface to release them later. After cleaning them with the acid treatment described before, we rinsed thoroughly with water and we filled the glassware with water. In the beginning, the pH was 7, but after 5 minutes, we observed a lower pH (red universal indicator paper). For this reason, the last step of the cleaning process was to fill the labware with Milli-Q[®] water and heat it to 80°C with stirring. The water was changed every 10 minutes up to 3 changes.

The use of strong acids is not a trivial topic. They must be handled by an expert chemist in a controlled environment wearing the required personal protective equipment (PPE)

in order to avoid undesired chemical reactions, overheating or release of toxic gases. Before disposal they must be neutralized, normally with sodium carbonate.

In order to dry the glassware, we put the material in a clean oven at 130°C for 1 hour.

II.3. Synthesis and characterization of Au nanowires

In my thesis project, the role of the Au nanowires was to act as plasmonic building blocks supporting SPP. As described in this part, their easy and fast electrochemical synthesis makes them very attractive. However, dispersing them and getting them individually is not trivial because a billion of similar nanowires are synthesized simultaneously in the membrane and the template has to be removed. Micrometre-long gold nanowires normally collapse and stay in bundles from two to hundreds of nanowires. The synthesis of the gold nanowires and their characterization is reported below.

II.3.1. Synthesis and dispersion of Au nanowires

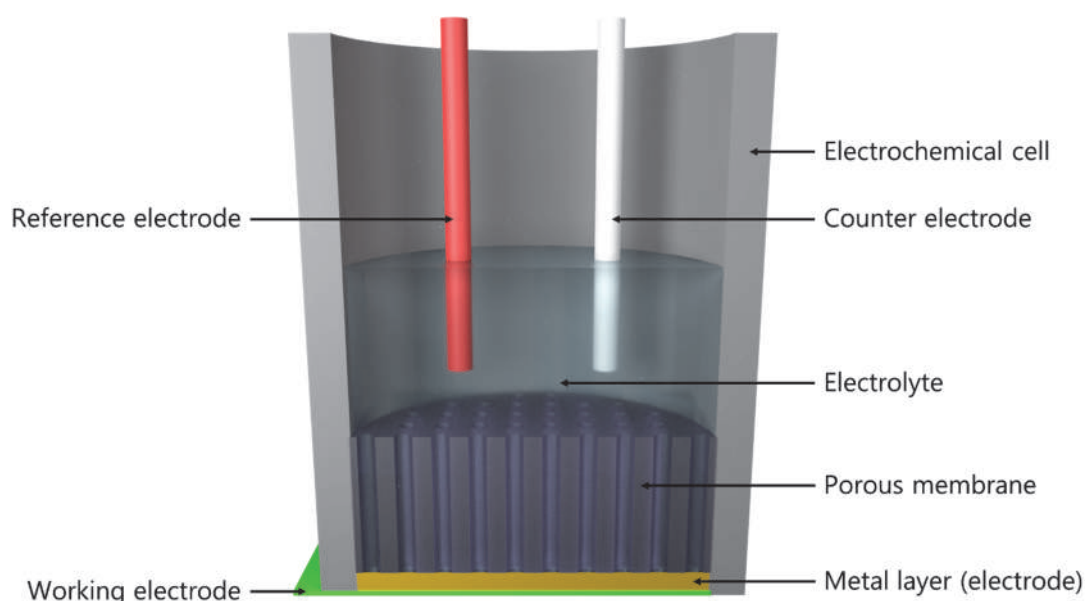


Figure II.7. Schematic of confined electrochemistry within a nanoporous membrane.

The synthesis of the Au nanowires was made following the electrochemical template-base method (Figure II.1c & Figure II.7). First, the metallized membrane was introduced in a three-electrode home-made electrochemical cell, with the Au layer onto the working electrode and the opposite side in contact with an aqueous solution of

chloroauric acid (Table II.3) that penetrated the membrane pores (PC and AAO in the case of pure Au nanowires).

A platinum foil was used as a counter-electrode. For gold electroplating, a cyclic voltammetry was performed in the range 0.75 - 0.00 V against saturated calomel electrode (SCE) at a sweeping rate of 50 mV/s causing the reduction of $[\text{AuCl}_4]^-$ ions into Au^0 that was first deposited at the bottom of the pores to form nanowires (Figure II.8).^{208,367,371}

Electrochemical aqueous solution for Au electroplating

Species	Concentration	Role
HAuCl_4	0.03 M	Electrolyte to reduce
K_2HPO_4	0.1 M	Buffer at pH = 7.6
KCl	0.1 M	Enhances the conductivity of the solution

Table II.3. Composition of the electrochemical solution for Au plating prior to mixing.

The standard reduction potential of the chloroaurate ion versus SCE is around 0.75 V. It means that the reaction should be spontaneous. But this is kinetically hindered by the complexation of the Au cation by the chlorides, preventing its spontaneous reduction. The sweeping starts at 0.75 V vs SCE, the equilibrium potential, in order to ensure that no reaction happened in the beginning of the cycle. The mixture is in a metastable state and the current was 0 (Figure II.8). Going towards less positive potentials made the environment more reductive and promoted the reduction of the chloroaurate into native gold. At 0.46 V, there is a peak followed by a plateau, meaning that an overpotential of -0.29 V should be overcome in order to deposit the native gold. The applied potential is reversed at 0.00 V/SCE up to 0.75 V/SCE to allow the replenishment of the electrolyte inside of the nanopores. In that moment, a new cycle starts and the electrodeposition of gold inside of the nanopores carries on.^{363,364}

The number of cycles determined the length of the nanowires in a proportional relationship, we measured it for the case of PC membranes with a nominal pore diameter of 100 nm (Figure II.9). The growth rate could thus be deduced. It was equal to about 4.7 nm/s. Under these conditions and for the AAO membranes of 114 nm pore size, we measured that 120 cycles produced 12 μm long gold nanowires, corresponding to a growth rate of 3.3 nm/s. This lower growth rate could be due to the larger pore density in AAO than in PC (about five times larger electrode surface accessible to the electrolyte), while the same concentration of chemicals is used in both synthesis or due to a lowering of the growth rate when the nanowires have already grown above a critical length. After synthesis, Au nanowires embedded in the membrane were rinsed thoroughly with ultrapure water to remove any residue of the Au saline solution.

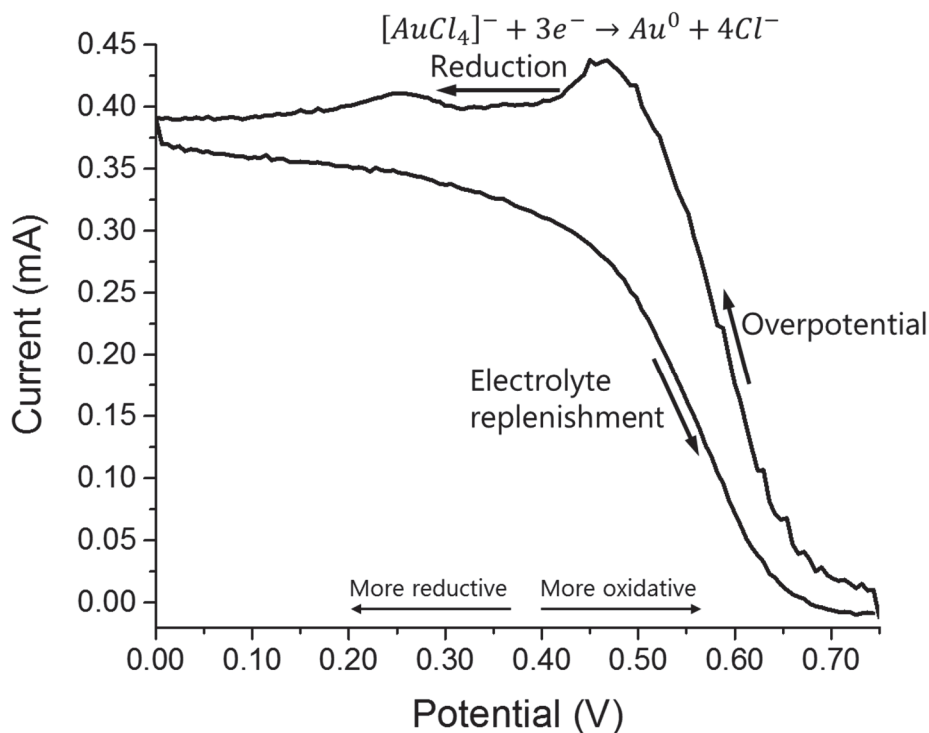


Figure II.8. Typical cyclic voltammetry of $[AuCl_4]^-$ reduction in a pH = 7.6 aqueous solution in a nanoporous metallized alumina membrane. In this particular case, the pore size of the membrane was 75 nm and its porosity 11%.

There are two main reasons because we performed these length-to-electrodeposition time experiments in PC and not in AAO. The first reason is because these were one of the first systematic and reproducible experiments that I did perform during my thesis project and in the beginning we utilized PC membranes rather than AAO. The second reason is for the SEM measuring method used. Indeed, nanowires synthesized into PC membranes disperse after template removal in a better manner than from AAO membranes. It is due to the smaller pore density (typically $1-5 \cdot 10^8 \text{ cm}^{-2}$ in PC and $1-3 \cdot 10^9 \text{ cm}^{-2}$ in AAO), which help preventing nanowires aggregation into bundles.

For the case of the AAO template, the full membrane removal was achieved by immersion in a 4.9 M H_3PO_4 solution for 48 hours. The remaining fragile gold film supporting the nanowire array was then rinsed with ultrapure water several times. It was stored with some water drops into small sealed glass. By sonicating it during 0.5 s, the nanowires were separated from the gold film and dispersed in ultrapure water just before drop-casting 100 μL of the dispersion on the substrates exposed in the previous section. One day was required for a slow drying of water to restrain aggregation of the nanowires.

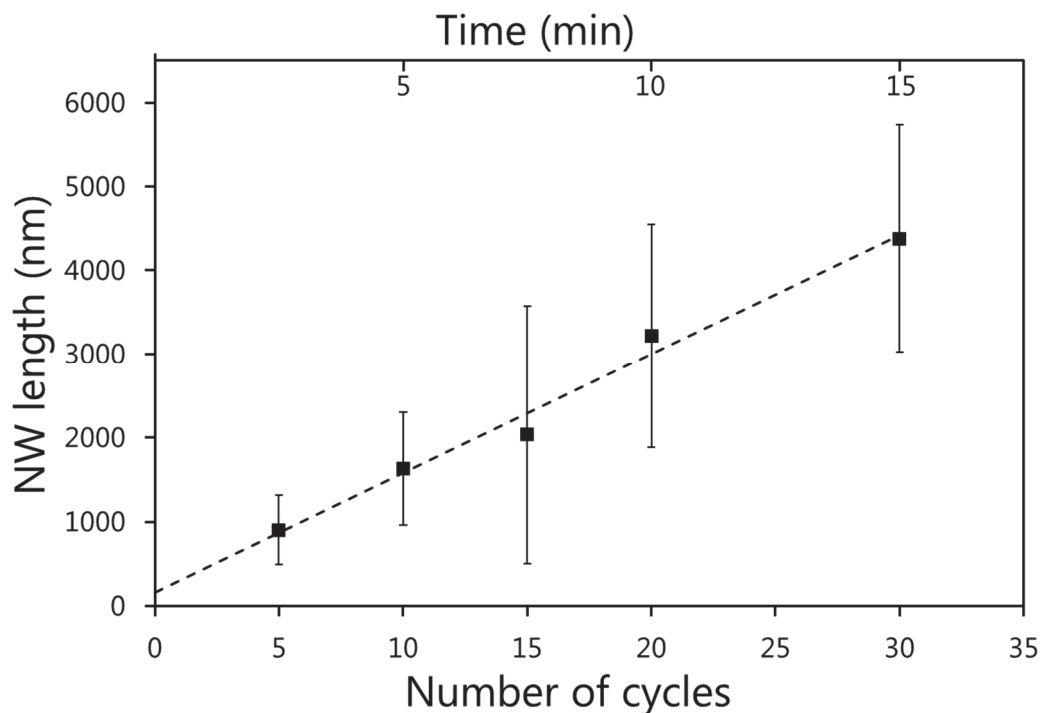


Figure II.9. Relationship between the number of cycles/electrodeposition time and the length of the produced nanowires. These synthesis were made in a 100 nm pore size PC membranes at a sweeping rate of 50 mV/s between 0.75 – 0.00 V vs SCE.

In the case of the polycarbonate membrane, dichloromethane was used to remove it. Because of the fast etching rate of dichloromethane to polycarbonate, the gold nanowires were separated from the gold film at the same time than the membrane was removed. For that reason, this process was performed directly on the substrate.

II.3.2. Characterization

The first characterization was made with the naked eye, with a colour change in the membrane after the Au nanowires electrodeposition. In order to quantify this colour change, near IR-UV-vis measurements were made for membranes with different Au nanowire lengths. These measurements were correlated with scanning electron microscopy images of the same nanowires after membrane removal and dispersion on boron-doped silicon substrates. We would like to note that the light scattering of these nanowires with a micrometric length can be observed with an optical microscope.

II.3.2.1. SEM and TEM study of Au nanowires

SEM images of both Au nanowires arrays on the Au electrode after template removal and Au nanowires solid dispersions after sonication and drop casting were taken for

different diameters and lengths. HR-TEM images were also made revealing the good crystallinity of the gold (Figure II.10c).

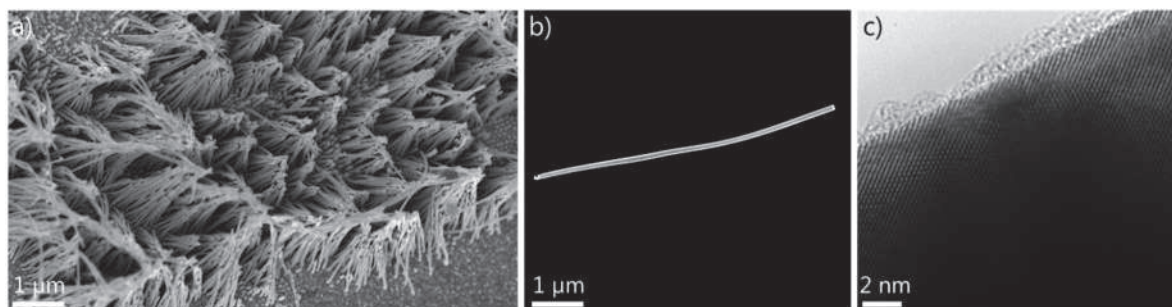


Figure II.10. SEM images of a) an array of \varnothing 35 nm Au nanowires on the Au electrode after template removal, b) a single \varnothing 105 nm Au nanowire on boron-doped Si substrate after sonication and drop casting. c) TEM image of the edge of a \varnothing 114 nm Au nanowire with traces of pollution at the surface. The crystallinity of gold can be clearly seen where the thickness is small enough.

Making a systematic SEM and TEM study of a series of nanowires with different electrodeposition times (i.e. number of cycles) and the same diameter, we established a simple relationship between the electrodeposition time and their length (Figure II.9).

II.3.2.2. NIR-UV-vis spectroscopy

We propose to address the mechanisms responsible for the observed colour change of the membranes after Au nanowires electrodeposition, besides the effect of the porous template. Indeed, alumina template or polycarbonate appears white when in air, while it is almost transparent in water. For well-ordered nanopore array (not the case here), metamaterial-like effects could also take place.

The main mechanism supposed to be responsible for the colour change deals with plasmonic resonance effects, which depends directly on the nanowire dimensions. This plasmonic origin and its relation with advanced studies reported in Chapter III and IV encourage us to make a quantitative analysis. We carried out reflectance studies of the filled membranes in the near infrared-ultraviolet-visible range and correlated the obtained spectra with the length measured (Figure II.11). For a detailed study, we chose a series of arrays of \varnothing 100 nm (nominal pore diameter) nanowires in PC, because it is the diameter of interest exploited in the coaxial nanowires and antenna-modified nanowires investigated in the next Chapters of my thesis project. It has to be noted that AAO membranes containing gold nanowires are not suitable for different reasons: (i) the very high density of nanowires induces a light trapping and is expected to promote plasmonic coupling between neighbour nanowires, (ii) the strong scattering of the incident and reflected signal by the nanoporous AAO located above the gold

nanowires. It is the reason why polycarbonate membranes have been exploited for this study. Very few similar studies have been reported previously, mainly with shorter nanowires, i.e. with a much shorter aspect ratio. Anthony Désert as a postdoctoral student in the group also explored the reflectance study of similar arrays of nanowires. We studied the as-measured diffuse reflectance spectra (incident light at 8° relative to the normal to the membrane) for five lengths of Au, from 900 to 4380 nm and for a membrane with a gold electrode attached (Figure II.11a).

The reflectance spectrum of the metallized membrane without nanowire is flat in the nIR range down to 600 nm and it is dominated by a minimum of reflectance at 490 nm. This absorption is attributed to the interband transitions in gold⁴³⁸ and it is responsible of the golden colour of a smooth gold film in reflexion and to the blue colour in transmission when the gold thickness is smaller than 50 nm, typically. In presence of the gold nanowires, an important decrease of the reflectance above 500 nm is measured and a second band appears, which extends from 550 to 700 nm, depending on the NW diameter. A regular oscillation of the spectra can be noted in the IR range. This interference signature certainly comes from interaction between the incoming light and the reflected one on top of the nanowires. So, it suggests that the distribution of nanowire lengths is quite narrow at the wavelength scale, a condition for getting interferences. The new band responsible for the main loss of reflectance is now analysed. Based on previous works in the literature and confirmed by further study on individual nanowires, the new band is attributed to the transversal localized surface plasmon resonance (T-LSPR) of the gold nanowires.^{43,77,89,90,439,440} The small incidence angle (8°) of the light on the membrane, i.e. on the nanowires, is the right configuration to excite the transversal plasmon. A red shift of this T-LSPR band is observed when increasing the NW length. In order to analyse the precise position of this band, the signal from the PC membrane attached to an Au film is subtracted (Figure II.11b). The minimum of this T-LSPR band is well revealed.

Finally, we investigated the relation between the position of the T-LSPR band (minimum of the normalized reflectance) with the Au nanowires length and the aspect ratio (Figure II.11c). Only a small redshift of 15 to 20 nm was obtained, while the spectral changes with the length on the raw reflectance spectra are more pronounced. It could certainly be attributed to a broadening of the T-LSPR band with the NW length. Such a broadening effect can be an intrinsic mechanism of the plasmonic resonance^{441,442} but it can also partly come to a distribution of the nanowire lengths resulting from the electroplating. It is important to note that the previous study made at the laboratory by A. Désert gave similar results.

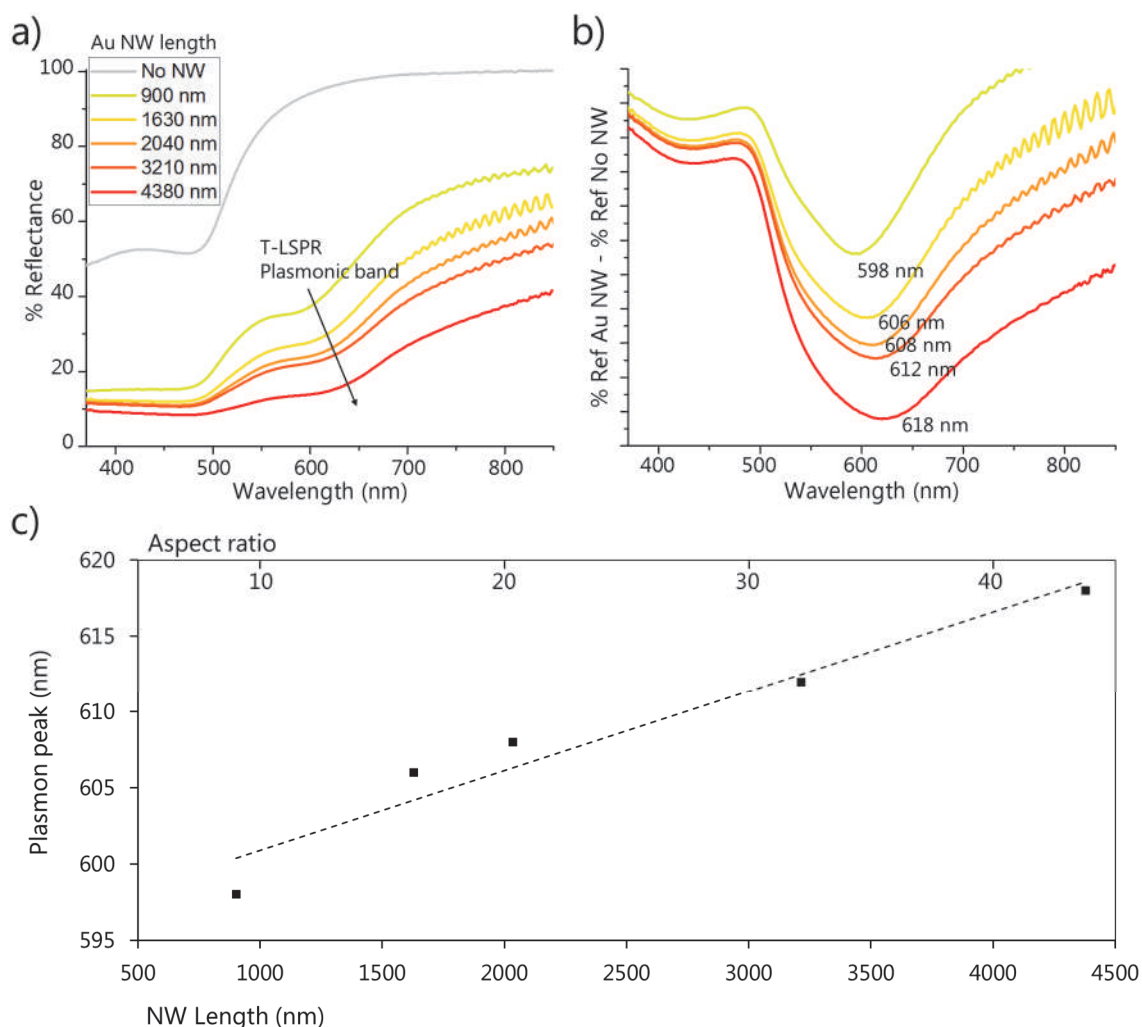


Figure II.11. a) Raw diffuse reflection spectra of the metallized $\varnothing_{\text{pore}}$ 100 nm porous PC membranes containing nanowires of different lengths. "No NW" corresponds to the signal from a $\varnothing_{\text{pore}}$ 100 nm porous PC membrane directly attached to a gold film and was considered as blank. b) Same spectra after blank subtraction and normalization. c) Relation between the length of the nanowires inside the previously described PC membranes and their found T-LSPR band.

The dependence of the T-LSPR with the nanorod length and the aspect ratio has been extensively studied.^{43,77,89,90,439,440} However, it concerns generally extinction studies of colloidal dispersion of nanorods with diameters smaller than 100 nm and lengths smaller than few hundreds of nanometres, corresponding to aspect ratio smaller than 10.^{36,62,77,81,92,93,325,439,442} In our study, the aspect ratio went up to 44. For nanorods with aspect ratio smaller than 5, the group of El Sayed reported no change in the T-LSPR position,⁴⁴⁰ while their modelling predicted a small blue shift for individual nanorods.⁴³⁹ The group of C.A. Mirkin has much investigated plasmonic nanorods, with length up to 3 μm .^{62,94,443} No shift in the resonance was observed for extinction study of colloidal dispersion of the nanorods.

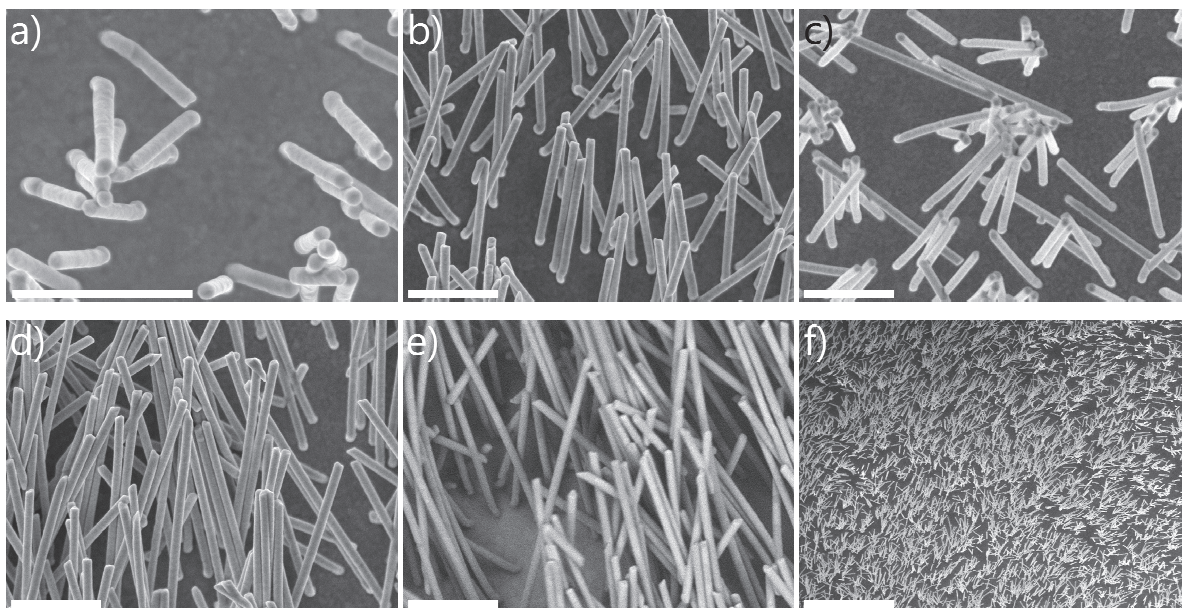


Figure II.12. SEM image (top view) of Au nanowires after removal of the PC template. Nominal pore diameter: 100 nm. Pore density: $6 \cdot 10^8 \text{ cm}^{-2}$. Average length = a) 900 nm b) 1630 nm c) 2040 nm d) 3210 nm e) 4380 nm (back-scattered electrons). f) Same sample than in (b) but from a further view. Scale bars correspond in all the cases to 1 μm except in (f) that it is 10 μm .

The main difference between these studies and ours deals with the measurement configuration. In the case of colloidal dispersion, the nanorods are far from the others and no interaction is expected. In our case, the NW are quite well-aligned in an array with a pore density of $6 \cdot 10^8 \text{ cm}^{-2}$ and a random location of the pores due to the cyclotron irradiation in the track-etching process (Figure II.12). So the distance between nanowires can be smaller than 100 nm to allow a resonant coupling between T-LSPR of near-by nanowires. Additionally, a small angular distribution for the nanopore axis results from the irradiation process (much weaker than the bundling effect observed in after PC removal (Figure II.12)). It can also contribute to a plasmonic coupling between juxtaposed nanowires. Such a coupling was shown to be responsible for a red-shift of the T-LSPR similarly to the one measured in our experiments.^{82,88}

II.4. Synthesis and characterization of PEDOT nanowires

In order to optimize the synthesis conditions, prior to the fabrication of the coaxial nanowires, we synthesized electropolymerized PEDOT films and PEDOT nanowires. Poly(3,4-ethylenedioxythiophene) was an excellent candidate for our purpose because it can be easily electropolymerized in an aqueous electrolyte, it is stable in air and under

low power laser irradiation. Importantly, as for many conjugated polymers, its Raman signal gives information on its conformation, its conjugation and its doping level. Our group at IMN benefits from a strong background for the analysis of the Raman spectra of PEDOT electropolymerized in identical conditions, with reference studies to attribute the Raman bands.^{374,375,388}

II.4.1. Synthesis of PEDOT nanowires

The synthesis of PEDOT in nanoporous membranes was analogous to the Au nanowires, except the electrolyte and electrochemical parameters. The configuration of the three-electrode homemade cell was the same but the membrane was in contact of an aqueous solution of the monomer 3,4-ethylenedioxythiophene (EDOT) (Table II.4) that penetrated the membrane pores. In order to perform the oxidative electropolymerization of EDOT into PEDOT, a fixed potential of 0.80 V vs SCE was applied. The nascent PEDOT nanowires grew from the Au electrode at the bottom of the pores. Because of the good conductivity of oxidized, thus doped PEDOT, the growth of the nanowires was not blocked. This oxidized PEDOT was positively charged, the different anions present in the solution could act as counter ions. Dodecyl sulphate anions and ClO_4^- have been shown to be involved in the doping of PEDOT synthesized with this electrolyte acting as these described counter ions.^{146,383}

Electrochemical aqueous solution for PEDOT electropolymerization

Species	Concentration	Role
EDOT	0.05 M	Monomer to be oxidized in the oxidative electropolymerization
Sodium dodecyl sulphate (SDS)	0.1 M	Acts as a surfactant to form micelles and maintain the solubility of EDOT in aqueous solution; contributes to the doping with DS^- anions
LiClO_4	0.1 M	Enhances the conductivity of the solution; contributes to the doping of PEDOT with ClO_4^- anions

Table II.4. Composition of the electrochemical solution for PEDOT electropolymerization.

The electropolymerization of PEDOT is oxidative. At a fixed potential of 0.80 V vs SCE, we synthesized the PEDOT nanowires inside AAO membranes of different pore sizes (Figure II.13). The mechanism of electropolymerization has been much investigated in early 2000s.^{379,384} The dominant mechanism proposed is reported here. When applying the 0.80 V vs SCE potential, the EDOT molecules situated in close proximity of the Au

electrode lose one electron to the gold surface and attach to it.^{381,386} These positively charged EDOT molecules could react with a near neutral EDOT molecule, withdrawing an electron and liberating a proton. It thus forms a monocationic dimer, or a hole is transferred from the Au electrode to that neutral EDOT molecule and it forms a bicationic dimer. This dimer reacts analogously to form an oxidized trimer and successively. The doping counterion compensates the excess of positive charge. In the counter electrode, the formation of bubbles is observed, indicating the reduction of the liberated protons.

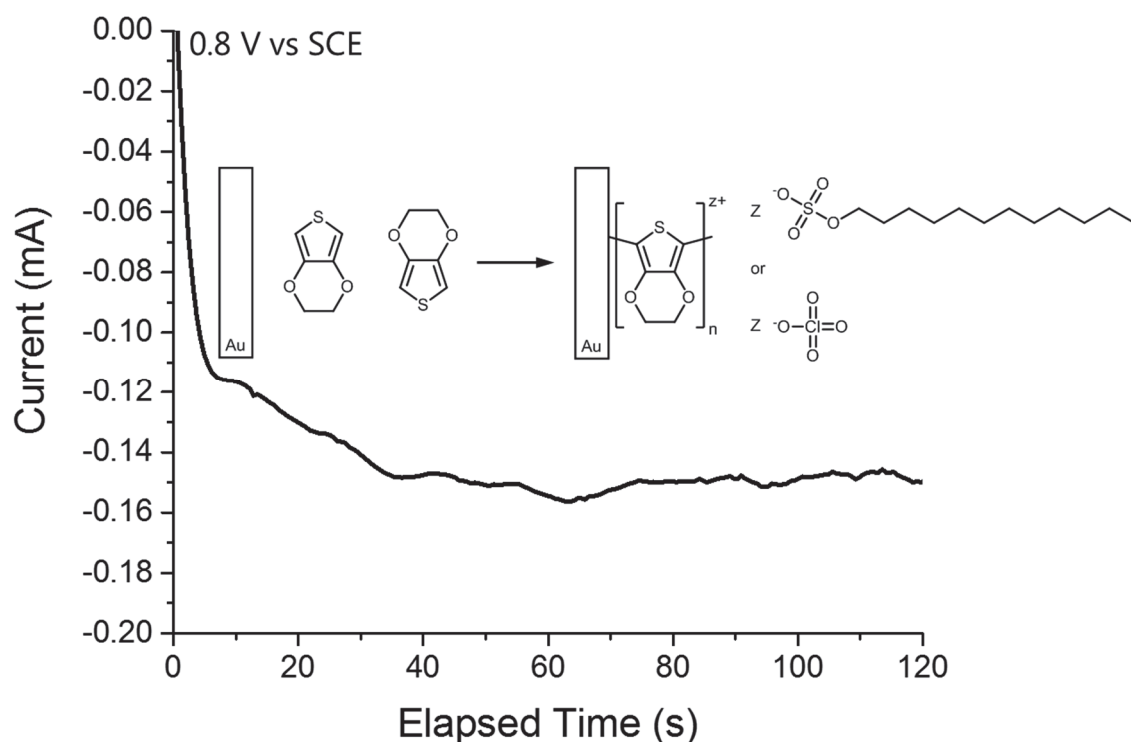


Figure II.13. Typical current vs time smoothed plot of PEDOT electropolymerization from an EDOT aqueous solution in a metallized nanoporous alumina membrane. In this particular case, the pore size of the membrane was 114 nm and the membrane porosity about 15%. Inset: schema of the electropolymerization proposed mechanism.

A first rise of the current is measured during about 10 seconds, followed by a less abrupt rise and a final stabilization of the current after 30 seconds (Figure II.13). This can be attributed to the initiation of the electropolymerization on the Au electrode, thus consuming EDOT oligomers and doping cations (ClO_4^- , DS^-), and the replenishment of the electrolyte inside the nanopores by species diffusion and by the driving force on the ions due to the electric field. This transient regime was followed by a stationary regime characterized by a current which remained almost constant, as expected for an anode with a fixed surface.

P. Rétho reported that the length of the PEDOT nanowires was directly related to the electropolymerization time with a growth rate of 8.5 nm/s at 0.8 V vs SCE, in a membrane of 73 nm of pore diameter and for the same electrolyte.³⁷⁵ We estimated a similar growth rate although we did not perform an exhaustive and systematic study as we did with the Au nanowires.

The PEDOT nanowires embedded in the membrane were rinsed thoroughly with ultrapure water to remove any residue of the electrolytic solution. Finally, in order to remove the template, the same process than with the Au nanowires was followed to obtain an array of self-standing PEDOT nanowires on a fragile thin Au film. By a very short sonication time in ultrapure water, they could be separated from the gold layer and dispersed prior to be drop-casted on different kinds of substrates.

The synthesis of the PEDOT films was carried out under the same conditions but using a Pt foil as a working electrode. A homogeneous deep blue PEDOT layer was obtained after an electropolymerization time of 500 s (Figure II.14). But if the electropolymerization time is increased up to 3600 s, we got a thick black rough film of electropolymerized PEDOT and a powder like aspect.



Figure II.14. PEDOT film electropolymerized on a Pt foil during 500s at 0.80 V vs SCE.

II.4.2. Characterization of PEDOT nanowires

The change of the colour of the membrane is also observable in the case of the PEDOT nanowires. It becomes progressively greyish blue and black, darker with the length of the nanowires.³⁷⁵

A systematic characterization of these nanowires by SEM, TEM, NIR-UV-vis reflectance and Raman spectroscopy was carried out. The larger diameter nanowires could be even seen individually when lying on a silicon surface by optical microscopy.

II.4.2.1. Characterization by SEM and TEM

We studied arrays and isolated nanowires by SEM and TEM. The synthesized PEDOT nanowires were normally homogeneous and smooth with an almost constant diameter along their main axis. This was found for the PEDOT nanowires synthesized with different diameters (Figure II.15). After dispersion, they remain attached in bundles although some isolated PEDOT nanowires could be found. The apparent morphology at the top is tubular in some of our nanowires synthesized in PC (Figure II.15d). This tubular morphology was often described in the literature for different conjugated polymers. It was attributed to a preferential electropolymerization on the pore wall, due to the interaction with cationic species^{374,388}. Previous experiments made in our group have shown that PEDOT electropolymerized in the same conditions turn into nanowires due to a thickening of the pore wall.

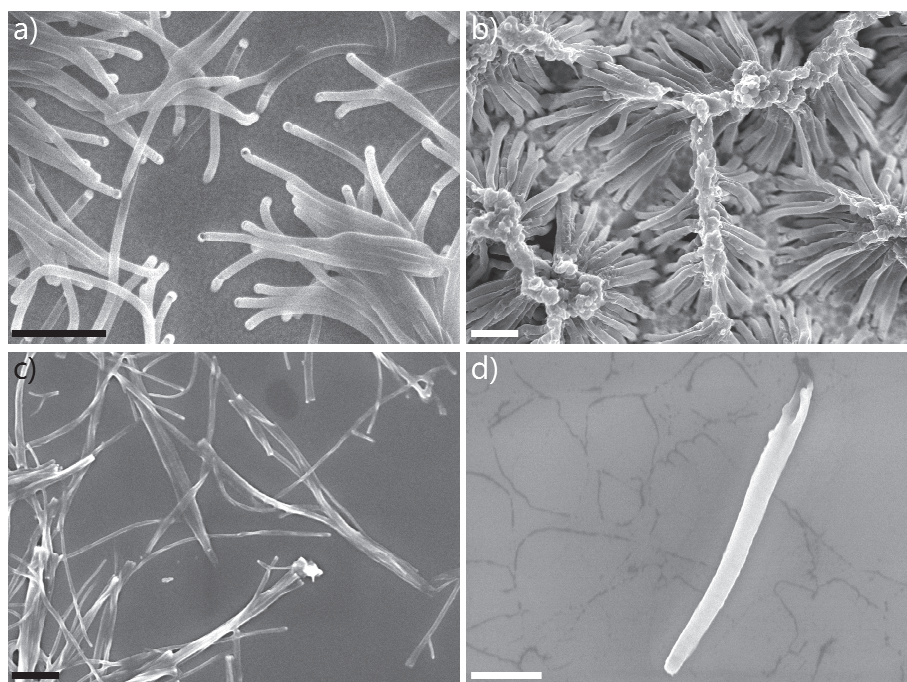


Figure II.15. SEM images of a) an array of PEDOT nanowires on the Au electrode after PC template (nominal pore diameter was 100 nm) removal, b) array of \varnothing 160 nm PEDOT nanowires on the Au electrode after AAO template removal, c) bundles of \varnothing 42 nm PEDOT nanowires on a boron-doped Si substrate after sonication and drop casting and d) a single PEDOT nanowire on a boron-doped Si substrate after PC template (nominal pore diameter was 200 nm) removal with dichloromethane. Scale bars correspond in all the cases to 1 μ m.

Some nanoparticles embedded in the polymer and concentrated at the bottom tip of the nanowires could be easily observed, while the PEDOT was almost transparent in these conditions of study with backscattered electrons (Figure II.16). We checked that

it was not due to a contamination by the chloraurate electrolyte. The strong white contrast in the images obtained with the backscattered electrons SEM suggested they were metallic. We observed that their presence was recurrent in all the samples, even from previous students that used the same sputtering conditions. The TEM images showed some nanoparticles along 100-150 nm typically, with a progressive decrease of the NP size. We can thus conclude that the Au nanoparticles come from the Au sputtering of the AAO membranes prior to the PEDOT electropolymerization, as it was reported before in the literature.⁴⁴⁴ The presence of such gold NP could be exploited for example for SERS studies. It must be noted that for gold nanowires, the sputtered NP were obviously embedded in the electroplated gold and could not be observed.

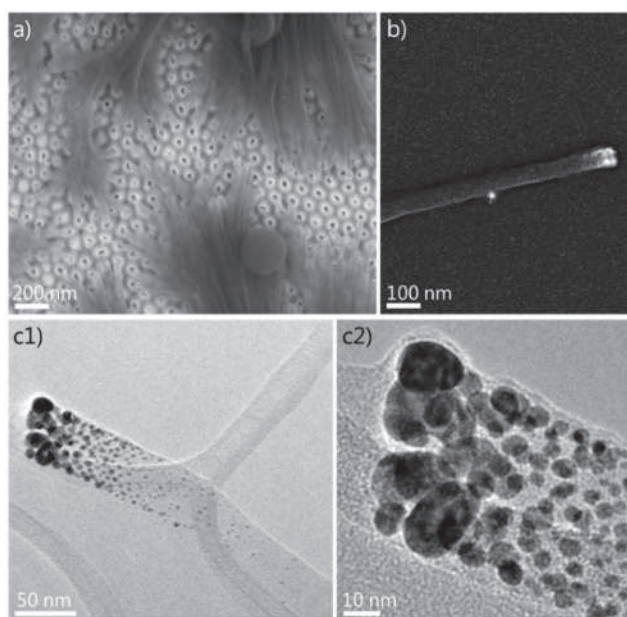


Figure II.16. SEM-backscattered electrons (BSE) images of a) an array of PEDOT nanowires on the Au electrode after complete membrane etching, b) bottom tip of an isolated PEDOT nanowire. c1 & c2) TEM images of the bottom tip of an isolated PEDOT nanowire. The average diameter of the nanowires shown in the images are 55 nm.

II.4.2.2. NIR-UV-vis spectroscopy study

Important information on the doping level of PEDOT can be obtained from the optical spectroscopy study. Our nIR-UV-Vis spectroscopy equipment required a macroscopic sample. Thus, the PEDOT nanowires were maintained in the template with the gold film to get a 1 cm² sample. As it was a non-transparent sample, the reflectance configuration had to be used. We measured both the reflectance spectra before and after the PEDOT NW electropolymerization (Figure II.17).

The reflectance spectrum of the metallized AAO membrane exhibits the same shape than the one measured for the PC with an attached Au layer, except that the main drop of reflectance is around 600 nm, instead of 490 nm, as expected for inter-band transitions of gold. It can be attributed to the plasmonic behaviour of the gold nanoparticles partly covering the bottom of the pore surface, as identified in the previous section.

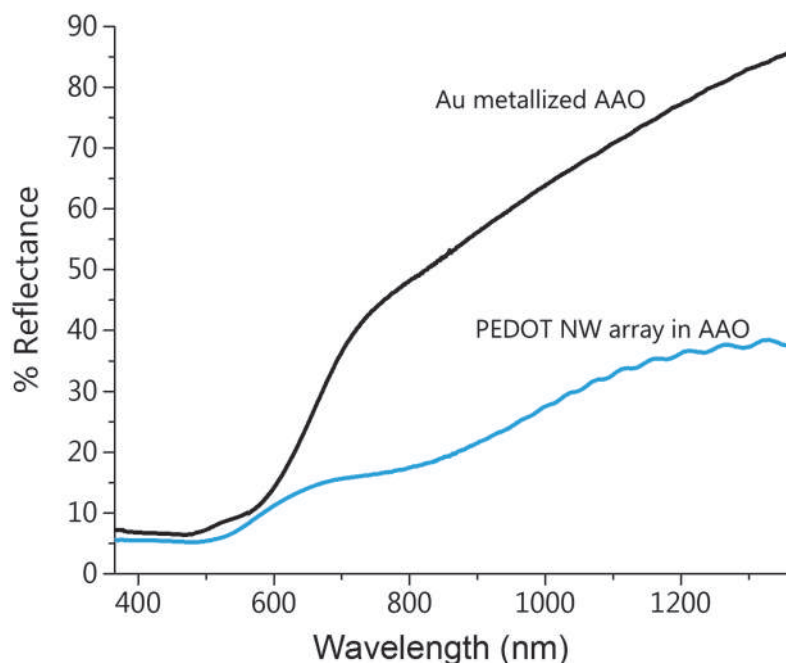


Figure II.17. NIR-UV-vis reflectance spectra of a metallized porous AAO membrane before (black) and after (light blue) electropolymerization of PEDOT nanowires in it. $\varnothing_{\text{pore}} = 160 \text{ nm}$; PEDOT nanowires expected length: $\sim 400 \text{ nm}$ (50 s electropolymerization time).

In order to analyse the PEDOT spectrum, it was thus required to subtract the reflectance spectrum of the metallized AAO membrane to the spectrum of the PEDOT NW embedded in it. Then, it could be compared with the spectra measured in a spectroelectrochemical study of PEDOT nanowires and films synthesized in similar conditions.^{375,445} PEDOT in the reduced state (undoped) is characterized by a broad absorption band with a maximum between 550 and 600 nm attributed to $\pi-\pi^*$ transitions, while this band vanishes in the doped state and is replaced by an increasing absorption from 600 nm to the near IR, due to (bi)polaronic bands (Figure I.48).³⁷⁵

Here, with respect to the reflectance of Au metallized AAO, the spectrum of PEDOT NW is dominated by a drop of the reflectance at wavelengths larger than 600 nm with an inflexion around 800 nm. It indicates the presence of polaronic and bipolaronic bands when PEDOT is well doped.

II.4.2.3. Raman spectroscopy study

One of the main purposes of studying pure PEDOT nanowires was to analyse and compare their Raman signal with the one coming from PEDOT synthesized in the coaxial nanowires, as reported later in this Chapter and further investigated in Chapter III. In this part, we thus restrain our study to identify an eventual effect of the following points on the Raman spectrum of PEDOT: chemical treatment with phosphoric acid, film versus nanowire (confined synthesis), laser excitation wavelength.

II.4.2.3.1. Attribution of the main Raman bands of PEDOT

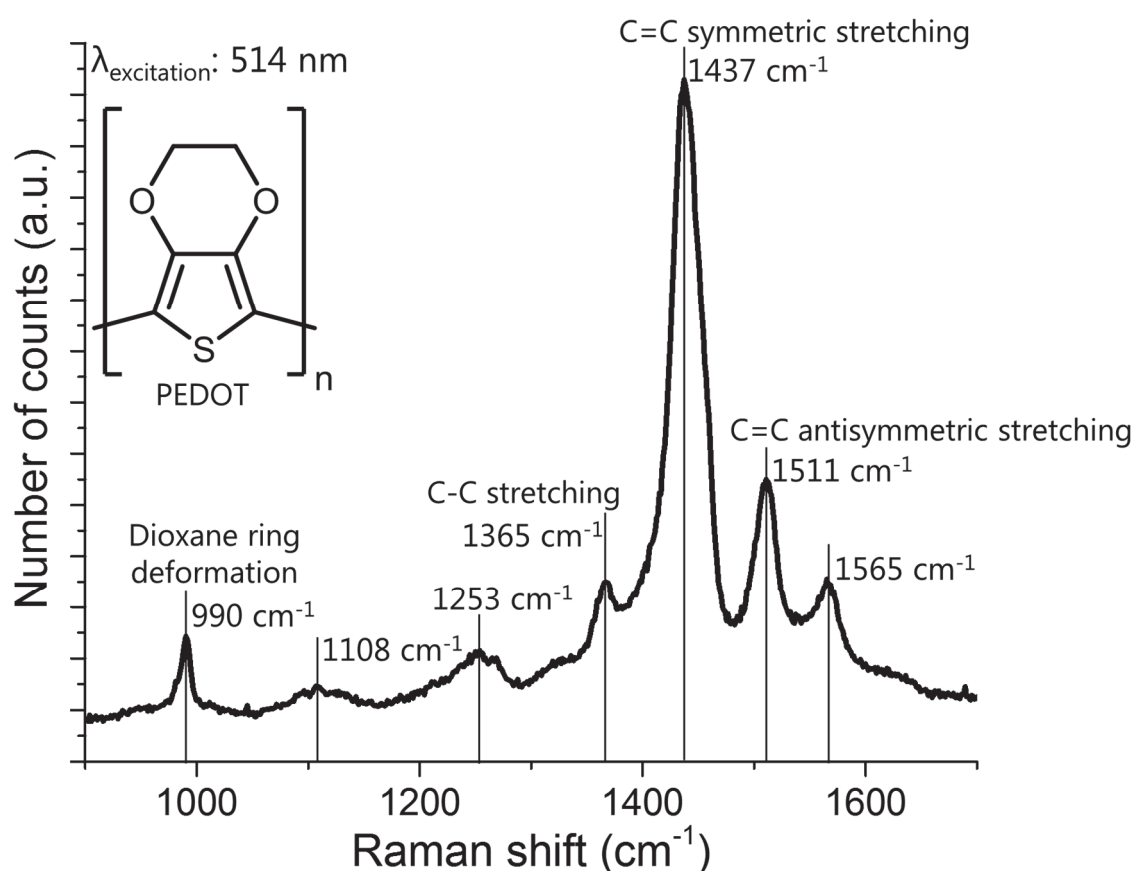


Figure II.18. Characteristic Raman spectra of a single PEDOT nanowire synthesized in a $\varnothing_{\text{pore}} 160 \text{ nm}$ AAO membrane. The excitation wavelength was 514 nm.

This attribution was proposed on a PEDOT nanowire with a diameter of 160 nm (Figure II.18). Based on previous theoretical and experimental studies, the most intense band at 1437-1441 cm^{-1} is attributed to the C=C symmetric stretching, the band at 1511 cm^{-1} corresponds to the C=C antisymmetric stretching and the C-C stretching band appears at 1365 cm^{-1} . The characteristic band found at 990 cm^{-1} corresponds to the dioxane ring deformation. The band at 1253 cm^{-1} results from a contribution of the C-H₂ twisting and the inter-cycle C-C stretching. The smaller and broader band at 1108 cm^{-1}

could be formed by a combination of the superior part of the dioxane deformation and the thiophene ring deformation. The origin of the band around 1565 cm^{-1} has not been clearly identified in previous theoretical studies.^{374,375}

The main band at 1437 cm^{-1} is particularly interesting, because its intensity depends on the length of conjugated segments through resonant effect and on the conjugated segment orientation relative to the excitation polarization.

II.4.2.3.2. Effect of the treatment with phosphoric acid

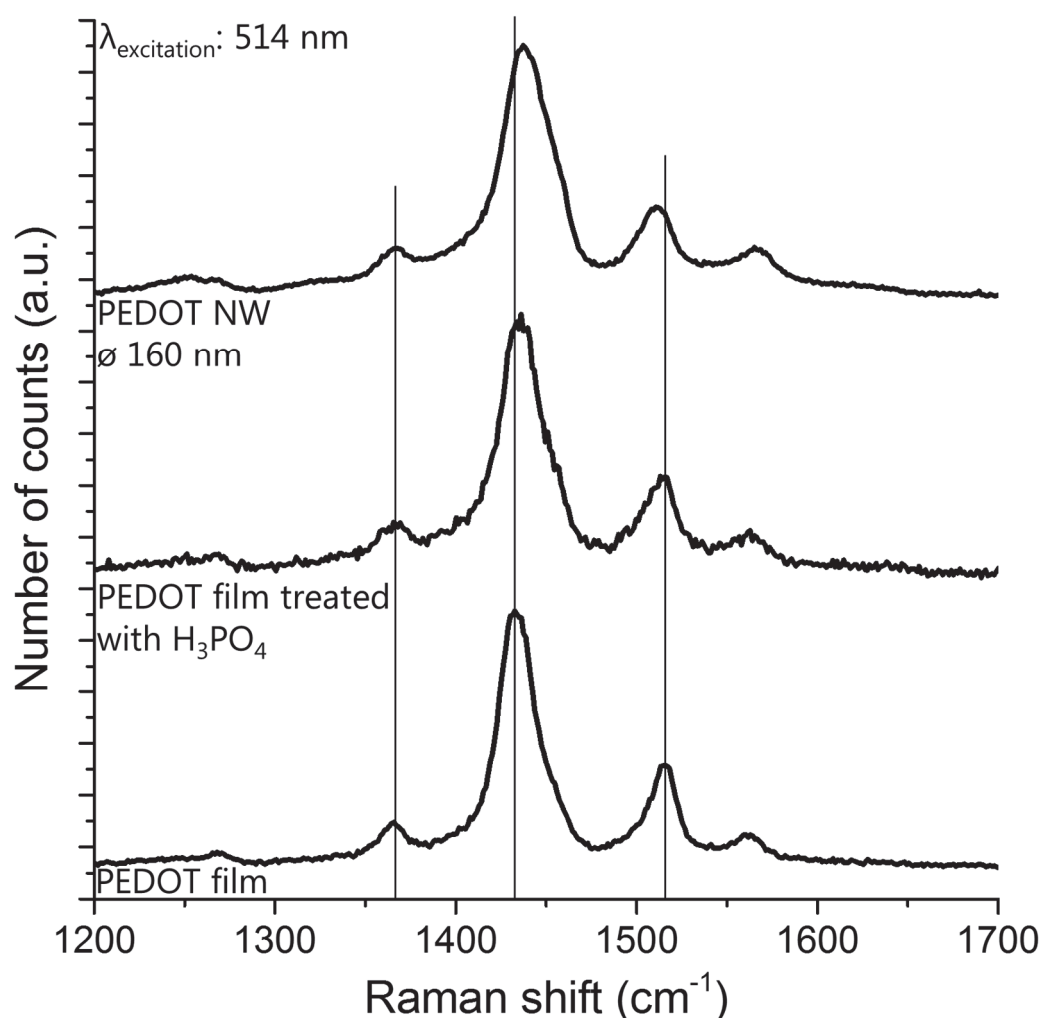


Figure II.19. Comparison of normalized Raman spectra from a PEDOT film electropolymerized on an Au electrode, the same film after treatment with phosphoric acid for 48 h, and a single PEDOT nanowire on a boron-doped silicon substrate. Excitation wavelength: 514 nm.

The Raman spectroscopy on a single nanowire requires to remove the AAO membrane in a concentrated phosphoric acid bath followed by several rinsing with water. Additionally, the PEDOT and the coaxial nanowires were kept in water before the

dispersion on a substrate or TEM grid. The study reported here aimed to evaluate an eventual effect of this treatment on the PEDOT. Other authors have reported the treatment of PEDOT:PSS composites with phosphoric acid resulting in an enhanced conductivity.^{446–448} We compared the Raman spectra of a PEDOT film before and after a chemical treatment with phosphoric acid (Figure II.19). No significant change appeared in the Raman spectrum, suggesting that the etching of the AAO membrane did not affect the PEDOT chains.

II.4.2.3.3. Effect of the confined electropolymerization

Many studies on different conjugated polymers have demonstrated that the confined electropolymerization promotes molecular and supramolecular improvements when the nanopore diameter is smaller than 60 nm. We have already reviewed this point in Chapter I and it will be further explored in Chapter III. In the case of a 160 nm diameter PEDOT nanowire (Figure II.19), only a slight shift toward higher wavenumbers was observed, suggesting very weak changes in the supramolecular configuration. This result agreed with previous studies, where significant changes were obtained only for PEDOT nanowire diameters smaller than 60 nm.³⁷⁵

II.4.2.3.4. Effect of the laser excitation wavelength on the Raman spectrum

It is well-known that the excitation wavelength strongly affects the Raman spectra of conjugated polymers. The excitation-dependent changes are due to resonant effects, mainly related to the doping level, the length of conjugated segments and the chain (conjugated segment) ordering which impact the molecular and supramolecular structure of the conjugated polymer. It is important to remind that the absorption band of undoped conjugated segments is related to the π - π^* transitions. When the conjugated segments increases, this band progressively shifts towards higher wavelengths, due to the delocalisation of the charges along the conjugation length.⁴⁴⁹ Another important resonant dependence of Raman signal deals with the doping level, because it fully changes the absorption spectrum, as described before. To summarize, when referred to the absorption of PEDOT, the blue and green excitation lines probe mainly the shorter and/or poorly doped conjugated segments, while the red and nIR lasers are more sensitive to the longer and doped conjugated segments.

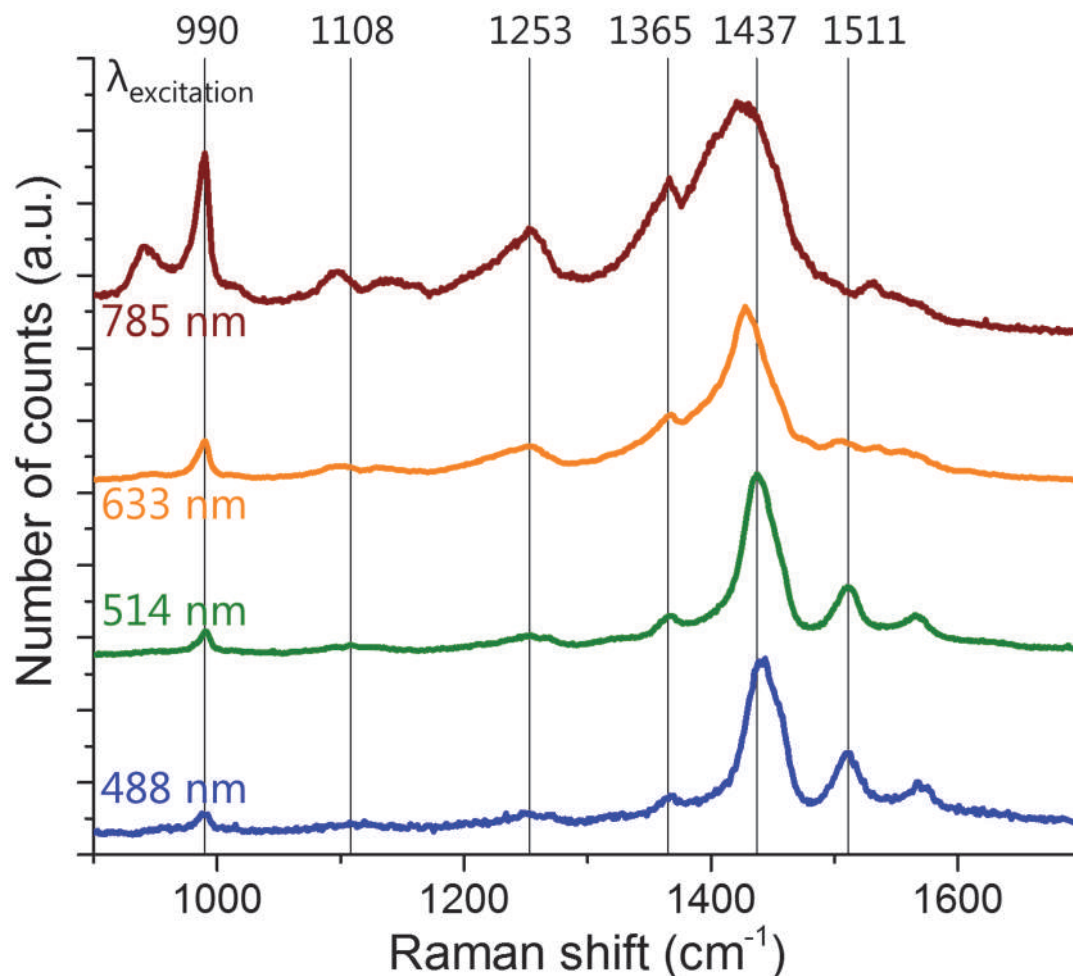


Figure II.20. Normalized Raman spectra of a single pure PEDOT Ø 160 nm nanowire excited at different wavelengths: (from top to bottom) 785 nm, 633 nm, 514 nm and 488 nm.

Here, we present a Raman spectroscopy study of a single nanowire at four different excitation wavelengths 488, 514, 633 and 785 nm (Figure II.20). It is clear that the Raman spectrum for 785 nm was different to the ones at shorter wavelengths. To explain these differences, it must be mentioned that the measured signal was much weaker for the 785 nm case, as shown by the relatively more intense band at 990 cm^{-1} than the main one at 1437 cm^{-1} . The dioxane ring deformation (990 cm^{-1}) is supposed not to be very sensitive to the excitation wavelength. It could thus serve as a reference for the intensity. So, the changes in the shape of the main band could be explained by a strong decrease of the C=C stretching band intensity combined with a shift of -7 cm^{-1} (in comparison with the green excited spectra), placed at 1430 cm^{-1} in the 785 nm case. It resulted in an apparent broadening, as it superposed with the 1365 cm^{-1} band. The reduced contribution of the C=C antisymmetric stretching was also noted. Combining these results with the reflectance study and previous absorption study, our research

suggested that PEDOT chains electropolymerized at + 0.80 V/SCE in the 160 nm pore diameter were quite heavily doped but they exhibited a distribution of conjugation lengths. It will be useful for comparing with the PEDOT Raman spectrum for Au@PEDOT nanowires.

II.4.2.3.5. Raman intensity study along single nanowires

We also performed micro-Raman analysis along different individual nanowires. Here, we only focus on the spatial changes of the intensity of the main band at 1437 cm^{-1} . We observed that for many nanowires, in one of the tips of the nanowires the PEDOT Raman signal increased by a factor larger than 10 (Figure II.21). This effect can be attributed to a SERS effect for the PEDOT in contact with Au nanoparticles located only at the bottom of the nanopores, i.e. of the nanowires. These Au nanoparticles resulted from the sputtering of the gold layer on one side of the template, as shown before.

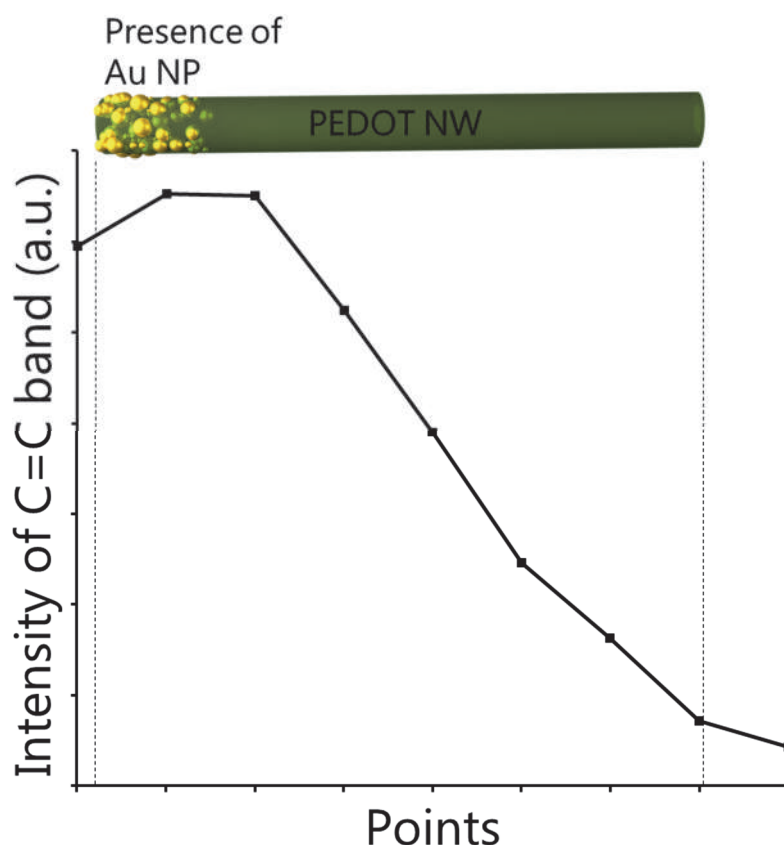


Figure II.21. Optical image of a \varnothing 160 nm PEDOT nanowire under a $\times 100$ objective. Correlated intensity of the C=C symmetric stretching Raman band at different points along the nanowire. On top possible schema of this nanowire containing Au nanoparticles in its left tip that enhance the Raman signal.

II.5. Synthesis and characterization of Au@PEDOT nanowires

It was crucial to perfectly locate the active species at different places along the nanowire, in order to get unequivocally results from the plasmon propagation and remote Raman excitation. This point will be further explained later. Our work is among the first ones that achieved such a controlled morphology of coaxial nanowires, with application to plasmon propagation studies.²⁰⁸ Alternatively, another group have presented a different approach using a micropipette system in order to locally place the active species, once the nanowires were already deposited on the substrate.²⁵⁰

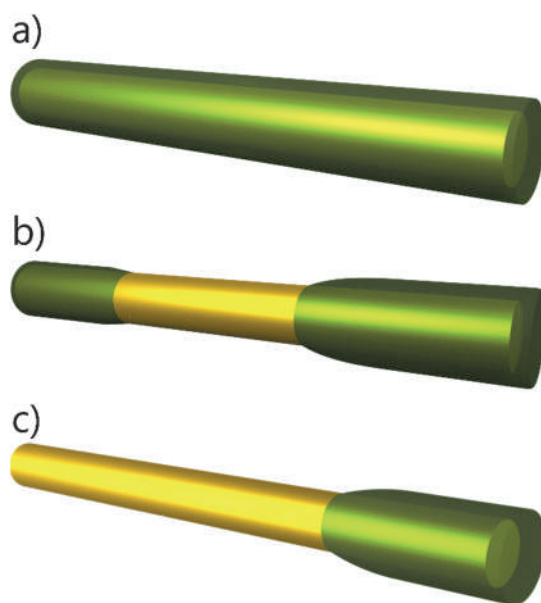


Figure II.22. Schema of the three kinds of Au@PEDOT NW prepared by the electrochemical hard-template method: a) PEDOT shell all around the gold core, b) PEDOT shells at the two extremities of the gold NW and c) PEDOT shell only at one extremity.

In our work described here, three original kinds of coaxial nanowires were synthesized, following a multi-step hard-template electrochemical method.

- PEDOT shell all around the gold core (Figure II.22a)
- PEDOT shells at the two extremities of the gold NW (Figure II.22b)
- PEDOT shell only at one extremity (Figure II.22c).

Such different geometries have been achieved by a careful engineering of the template process. Alternatively to as-grown coaxial nanowires, a post-treatment by laser dry etching of the polymer also permits to get the same arrangements, but with a better control of the length of the PEDOT shell segments.

II.5.1. Synthesis and morphological characterization

The whole process is a combination of the processes described before for synthesizing the Au nanowires and the PEDOT nanowires, but with an additional pore widening intermediate step (Figure II.23).

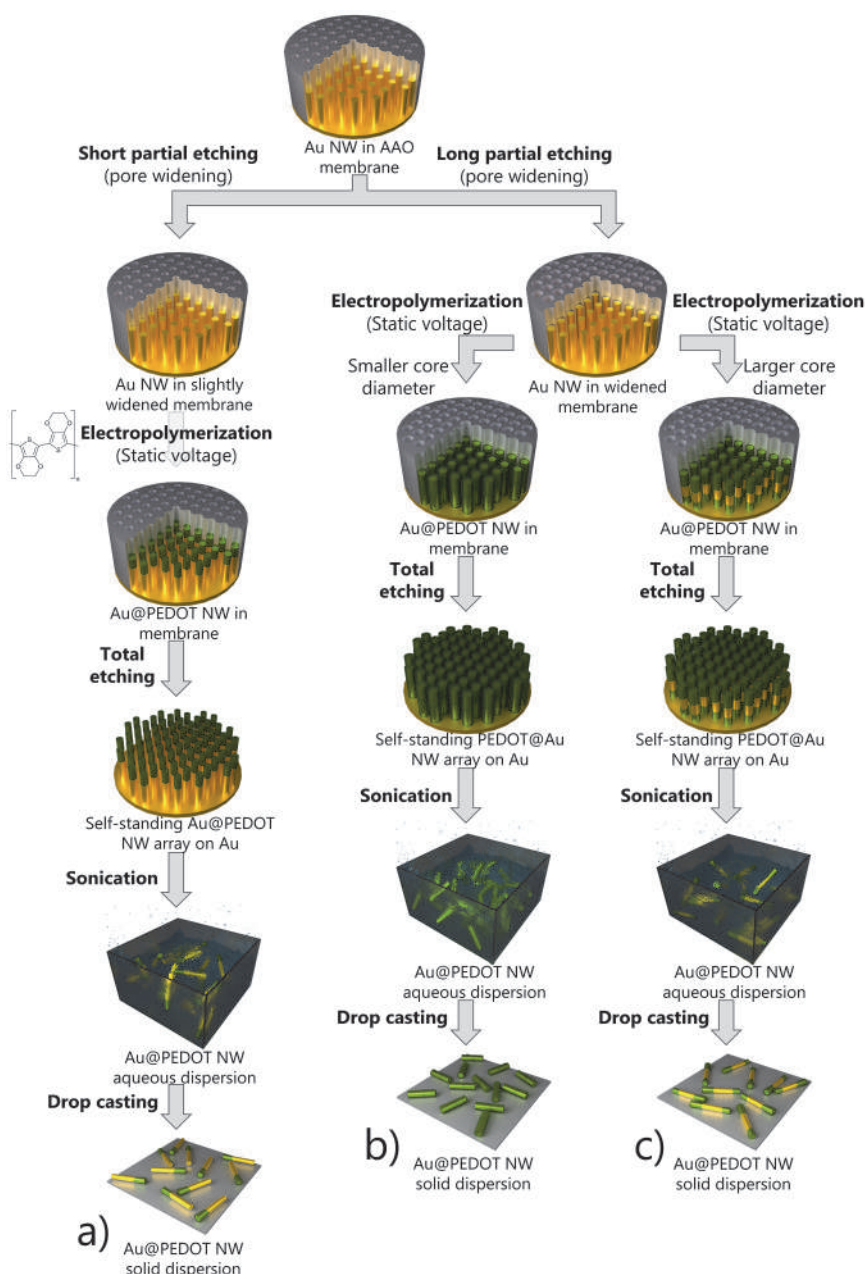


Figure II.23. Schematic description of the processes developed for the synthesis of coaxial nanowires with template methods using AAO membrane. a) Au@PEDOT NW with PEDOT located only on one tip, b) Au@PEDOT NW with full PEDOT shell and c) Au@PEDOT NW with PEDOT located only at the tips.

The first step is the synthesis of the gold nanowire core, as it was described before. The second step is the partial etching of alumina surrounding the metal by immersion of the membrane in an aqueous solution of H_3PO_4 (0.87M). In the typical case, the etching step lasted 90 minutes. The pores of the alumina membrane are widened and gaps are created around the nanowires. The very selective and anisotropic etching of the pore walls among the rest of the alumina template was believed to result from the following factors: (i) the pore walls in direct contact with the etching solution was necessarily firstly removed; (ii) a non-uniform composition of the alumina membrane.

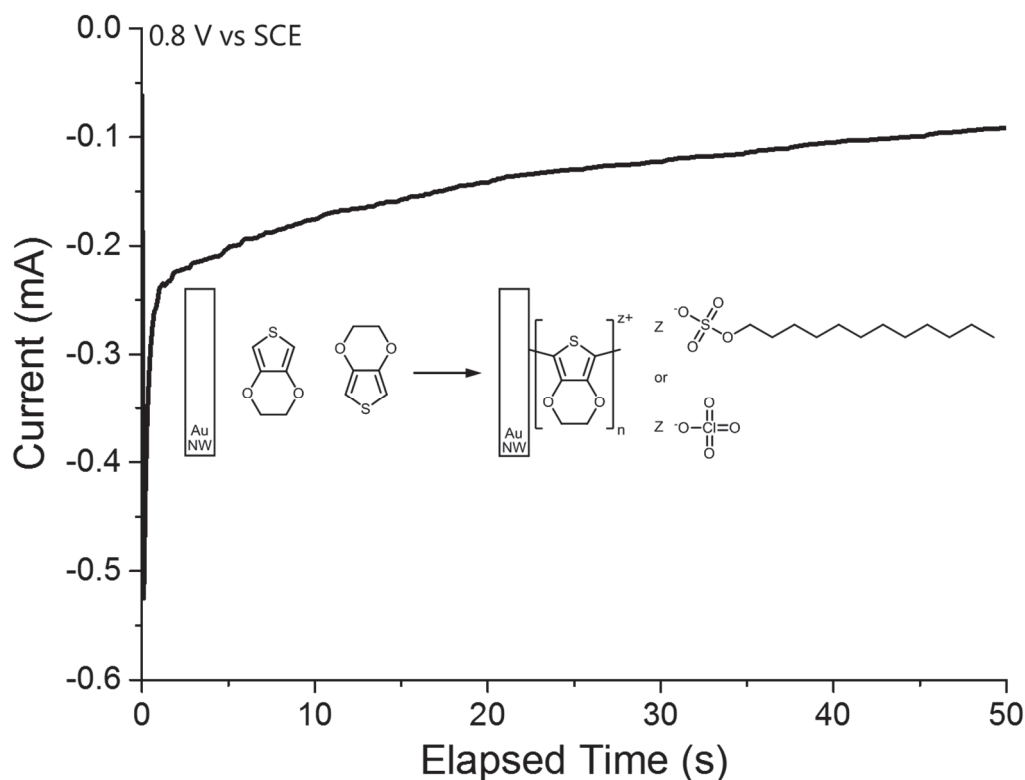


Figure II.24. Typical current vs time smoothed plot of PEDOT electropolymerization from an EDOT aqueous solution on gold nanowires in a widened nanoporous metallized alumina membrane (pore size: 114 nm prior to pore widening; porosity 16%). Inset: schema of the electropolymerization proposed mechanism. The smooth of the plot was made in order to eliminate the noise by the Savitzky-Golay method with a polynomial order 5.

In a third step, after rinsing the sample with ultrapure water, an aqueous solution containing the 3,4-ethylenedioxythiophene (EDOT) monomer is dropped to fill the freed space between the Au nanowires and the partially etched AAO pores. Then, the oxidative electropolymerization is carried out at a fixed potential of +0.80 V vs. SCE for 50 s (Figure II.24).^{146,374,380} The electropolymerization started with a strong current (about an order of magnitude larger than for PEDOT synthesis in a similar membrane) which rapidly dropped, then followed by a progressively decreasing current toward

values similar than in the pure PEDOT nanowires. The growth mechanism proposed is that the EDOT monomers confined between the gold nanowire and the alumina shell are first electropolymerized. This nano-3D active surface is much larger than the gold electrode localized at the bottom of the pores when depositing PEDOT nanowires. The initial very sharp drop of the electropolymerization current could be attributed to a closing of the upper part of the narrow channel by PEDOT preferentially deposited at the upper tip, thus limiting or eventually inhibiting further diffusion of species to restrain the electropolymerization along the lateral surface of the nanowire, characterized by a continuous decrease of the deposition current. This explanation can address the configuration of PEDOT placed on one or both tips (Figure II.23a&c), but it cannot explain the case of homogeneous PEDOT shells all along Au@PEDOT nanowires. Another possible explanation for this current decrease would be that once the first chains of monomers are attached to the gold nanowires surface, the current starts to decrease as the oligomeric EDOT chains conductivity is smaller than the gold nanowires. The simple mechanism above-mentioned has to be improved, as proposed below in view of additional results.

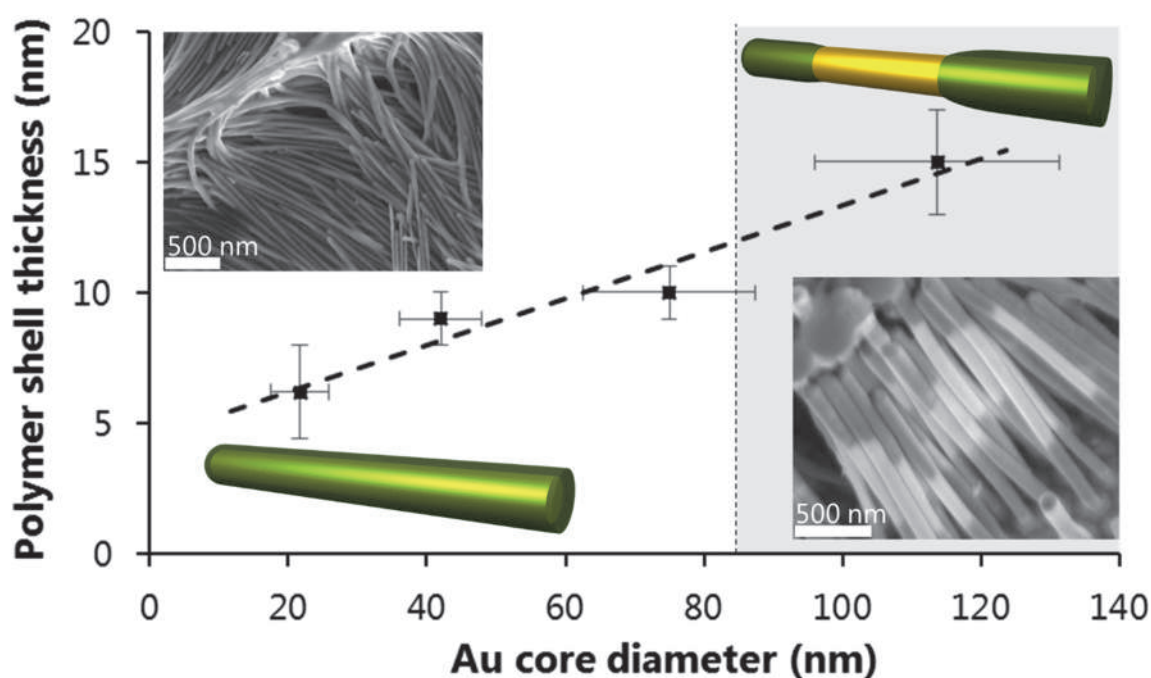


Figure II.25. Plot of the PEDOT shell thickness versus the Au core diameter for identical synthesis conditions. Inserts show typical SEM images (initial pore diameter: 42 nm left, 114 nm right) and the corresponding artistic schemes of the nanowires with two distinct morphologies: PEDOT (in green) surrounding all the Au (yellow) nanowire for 22, 42 and 75 nm initial pore diameters ; PEDOT surrounding only the extremities of the Au nanowires for 114 nm initial pore diameter.

Finally, the membrane was treated with concentrated phosphoric acid for 48 hours to totally remove the alumina template. A thin and fragile layer of Au underlying an array of Au@PEDOT nanowires was obtained. To disperse the nanowires in water or ethanol, a brief sonication (half a second typically) was applied. The versatility of this process allowed to disperse these nanowires on any kind of surface, such as boron-doped silicon substrates and transmission electron microscopy grids.

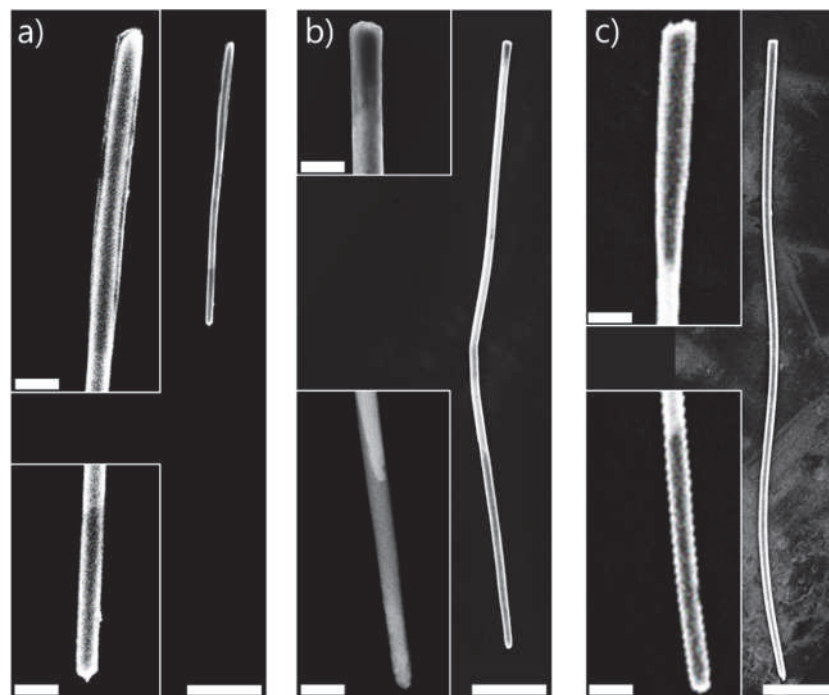


Figure II.26. SEM images of single Au@PEDOT nanowires with PEDOT only at their tips synthesized in \varnothing 114 nm AAO membranes for a) length $L = 4 \mu\text{m}$, $t_{\text{electropolymerization}} = 50 \text{ s}$, b) $L = 8 \mu\text{m}$; $t_{\text{electropolymerization}} = 50 \text{ s}$, c) $L = 8.5 \mu\text{m}$, $t_{\text{electropolymerization}} = 150 \text{ s}$. Scale bars of a), b) and c) are $1 \mu\text{m}$ (main images) and 200 nm (insets).

The H_3PO_4 concentration and the etching time make possible to tune the widening size of the pores around the nanowires. The PEDOT electropolymerization time allows to control the synthesis of the polymer shell, in order to produce the nanowires with different shell distributions. For an etching time of 90 minutes, a pore widening of about 5 to 15 nm was obtained depending on the initial pore size. Importantly, it was observed that the smaller diameter gold nanowires were fully covered with PEDOT, while the larger diameter nanowires were covered only at the extremities (Figure II.25). These observations also supported the hypothesis that the PEDOT shell grown at the upper tip could block the 5-15 nm wide channel surrounding the gold cylinder, thus inhibiting further growth of PEDOT at the bottom and on the lateral size when all the monomers remaining in the closed cavity have been electropolymerized.

Another possible growth mechanism to explain the preferential electropolymerization at the extremities of the nanowires deals with a tip effect, i.e. an electric-field enhancement which takes place at the top extremity of a strongly anisotropic conducting object connected to an electrode. The larger the aspect ratio (length/diameter), the stronger the electric field enhancement at the tip. Such a local field enhancement could contribute to the overpotential promoting a faster oxidation of the monomers, thus obtaining a faster electropolymerization on the top extremity, rather than on the lateral surface.

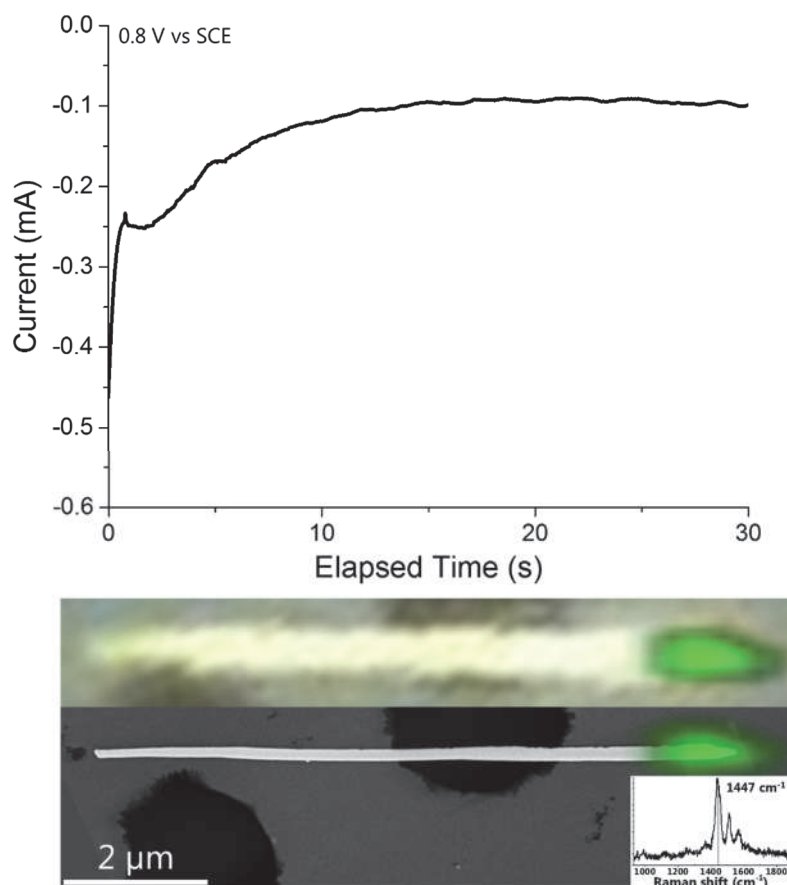


Figure II.27. Top) Typical current vs time smoothed plot of PEDOT electropolymerization from an EDOT aqueous solution on gold nanowires in an asymmetrically widened nanoporous metallized alumina membrane. In this particular case, the pore size of the membrane was 140 nm (prior to pore widening) and its porosity 16%. Bottom) Optical microscopy view (objective x100 LF) and SEM image with superposed Raman spectroscopy mapping (intensity at 1447 cm^{-1} appears green) of a single gold nanowire synthesized in a nanopore 140 nm AAO membrane (length: 9 μm , diameter: 100 nm at left tip, 230 nm at right tip) covered with PEDOT close to the right tip.

The synthesis of the previously introduced asymmetric coaxial Au@PEDOT nanowires with PEDOT only at the upper tip was achieved by controlling the synthesis parameters

(Figure II.27). A partial asymmetric opening around the gold nanowire was achieved by shortening the pore widening to 5 minutes. The oxidative electropolymerization time was reduced to 30 seconds (Figure II.27top) and we utilized AAO membranes with a larger average pore diameter (140 nm) in order to maximize the preferential growth at the upper tip, as described above.

We should emphasize that this kind of asymmetric Au@PEDOT nanowires were found optimal for investigating the remote Raman excitation, as reported in Chapter IV. The lack of PEDOT at the nanowire tip where the laser is focused makes possible to exclude the possibility of any parasitic Raman signal due to a direct excitation, and not in a remote way.

II.5.2. Characterization of the Au@PEDOT NW

The first observation was the darkening of the membranes after the PEDOT electropolymerization.

SEM and TEM

We already presented in the previous sections a SEM and TEM analysis that we performed on these Au@PEDOT nanowires. In this section, a further detailed study show univocally the composition of these nanowires. The SEM and TEM images gave us a clear idea of the morphology of the nanowires. A comparison of the secondary electrons (Figure II.28a) and the backscattered electrons (Figure II.28b) images is proposed. In the first case, nanofibers are closely packed, in contact with each other. In the latter case, only the gold cores were observed due to its higher atomic number. Nanofibers do not contact each other, due to the PEDOT shell that surrounds them and can slightly appear as a dark shell.

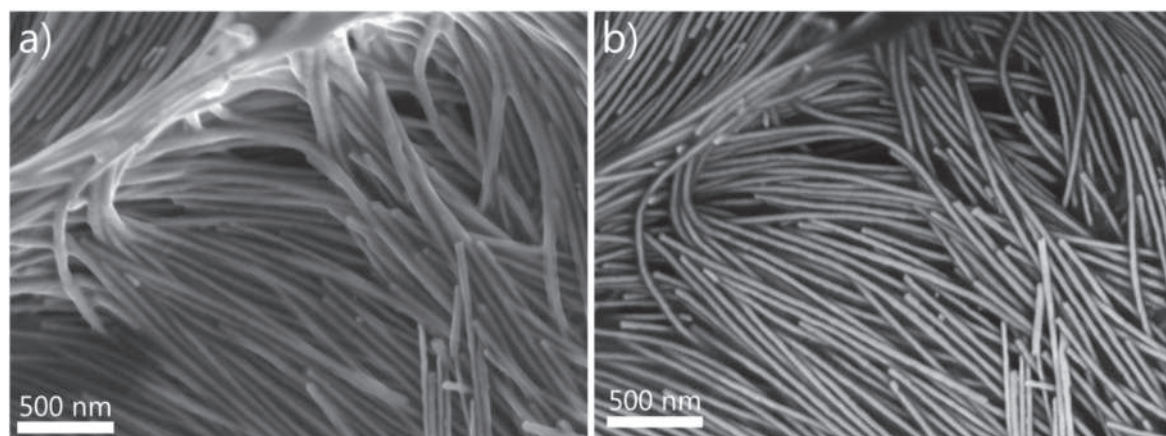


Figure II.28. SEM images of Au@PEDOT nanowires array of the a) secondary electrons and b) backscattered electrons. \varnothing core: 42 nm Length: 6 μ m.

In a TEM study made with Raul Arenal at UNIZAR (Zaragoza, Spain), we performed both imaging and electron energy loss spectroscopy in order to get an elemental analysis. The results were as expected: the nanowire was formed by a gold core and a homogeneous PEDOT shell (Figure II.29a) that contained both carbon and sulphur (Figure II.29c).

We performed a systematic analysis of the SEM and TEM images from nanowires of different diameters synthesized with the same conditions. It confirmed that the PEDOT layer was only deposited at the tips for the larger diameter nanowires as we presented before. Furthermore, we observed that the PEDOT shell thickness increases with the gold core diameter for the same synthesis conditions (Figure II.25).

The nanowire length is an additional parameter that could interplay with the growth mechanisms. For longer nanowires and an average diameter of 114 nm, the selective growth of PEDOT at the tips of the nanowires was still present even more pronounced. By increasing the electropolymerization time of PEDOT, longer covered segments of the gold nanowire tip were achieved (Figure II.26).

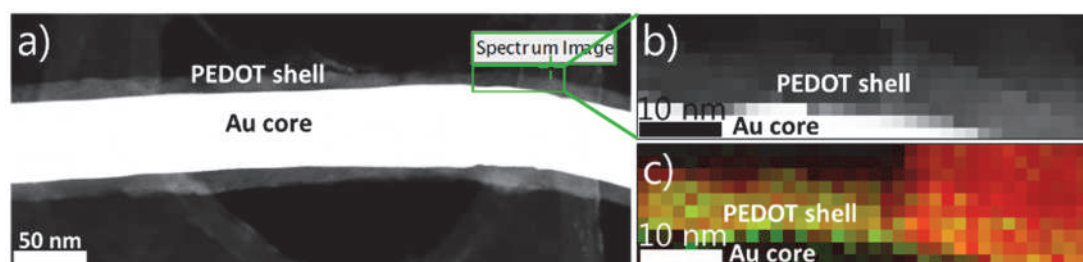


Figure II.29. a) STEM-HAADF of an Au@PEDOT nanowire. b) Higher magnification view and c) STEM-energy electron loss spectroscopy image of the same portion of the nanowire highlighted in (a). Carbon is in red and sulphur is in green.

II.6. Post-treatment: Laser dry treatments and PEDOT particles

Depending on the nanopore, i.e. the nanowire diameter, the asymmetrical nanowires with PEDOT at just one tip also had some PEDOT at the opposite tip. For the Raman studies with a remote excitation, the presence of PEDOT on the two opposite tips could make ambiguous the effects measured. It is the reason why we developed a method to selectively eliminate the undesirable PEDOT from that tip. It relied on the direct optical nanolithography of PEDOT by laser dry etching.

In addition, the introduction of an antenna in the metal system is required to improve the photon-SPP coupling. It is the reason why we performed laser dry heating treatment to form small gold particles at the tip(s) of the gold nanowires.

The fine placement of the Raman active species on these kind of nanowires seemed a more complicated task. In these cases, we could not perform an electropolymerization directly on the nanowires, although one of our options was the photopolymerization via a laser source. In order to couple the modified Au nanowires with Raman-active species we drop casted polymer nanoparticles on the substrate with nanowires that randomly dispersed and could end on their tips.

II.6.1. Laser dry etching of PEDOT

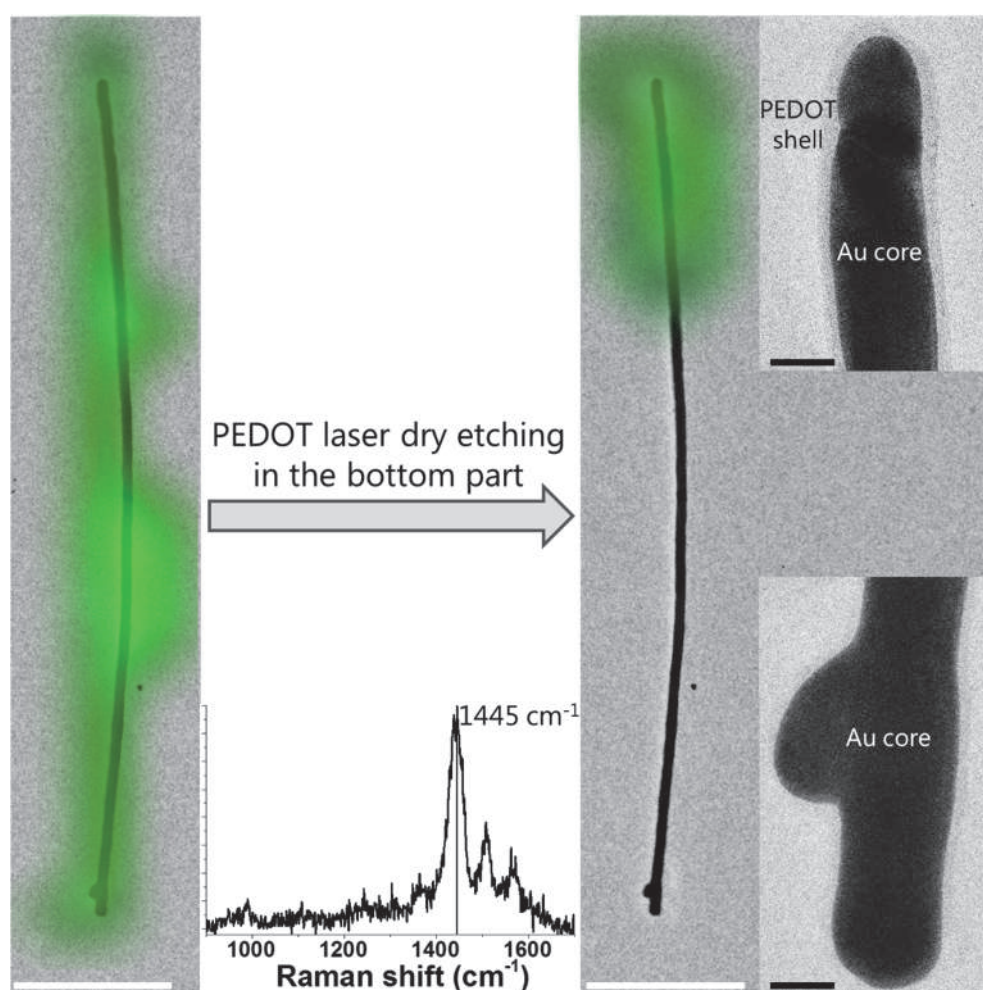


Figure II.30. Superposed Raman mapping signal and TEM image of a \varnothing 31 nm Au@PEDOT nanowire before (left) and after (right) laser dry etching of the bottom half-part of the nanowire. The PEDOT shell is clearly seen in the magnified TEM image of the untreated part. White and black scale bars are 500 nm and 20 nm respectively.

In our Raman studies with PEDOT nanowires once dispersed on a substrate, we observed that at certain laser powers the PEDOT signal vanished after several measurements and the nanowire disappeared. The trivial explanation for this phenomena was the degradation and etching of PEDOT due to the laser

irradiation.^{25,239,414} By a careful control of the laser features (wavelength, power, duration of exposure), we thus performed a selective PEDOT laser dry etching at specific parts of the Au@PEDOT nanowires. We found that, for our experimental set-up (Renishaw InVia spectrometer), the optimal conditions were the 488 nm laser at a power of 1.5 mW during 120 seconds with a x100 objective and a numerical aperture of 0.8 (radiant exposure of 4.14×10^{13} J/m²).

As a proof of concept, we tried the laser etching process on a Au@PEDOT nanowire fully covered with PEDOT synthesized in a 42 nm pore diameter AAO membrane (Figure II.30). We then measured its Raman mapping, which confirms the gold nanowire is fully covered with PEDOT (Figure II.30left). Then, the laser dry etching of PEDOT from part of the nanowire was achieved by focusing the laser on one of its tips and making a sweep process with the etching conditions mentioned above in the area where we wanted to remove the polymer. Another Raman mapping confirmed that the PEDOT signal completely disappeared and a TEM study confirmed that no PEDOT remains along the treated area (Figure II.30right).

II.6.2. Laser-induced formation of Au nanoparticles

The controlled location of Au nanoparticle on one or both tips of a nanowire is a challenging process. Here, we discovered accidentally the possibility of transforming the tips of our Au nanowires into Au nanoparticles when focusing an intense laser beam at one of the tips of a nanowire (Figure II.31). We then realized that in the literature, this transformation process had already been reported but not for enhanced propagative plasmonic prospects.^{427-429,431}

In order to make a reproducible process, we tried several gold laser dry etching conditions until we found the optimal ones. We used a laser source of 488 nm with a power of 15 mW during 3 seconds with a polarization parallel to the main axis of the nanowire and through a x100 long focal objective with a numerical aperture of 0.8. After the laser treatment of one of its tips we obtained a half dog-bone like nanostructure. We could then treat the opposite tip in order to create a new nanoantenna and obtain a dog-bone like nanostructure.

These experiments were performed in a Renishaw InVia™ Raman spectrometer in most of the cases. It allowed a good spatial stability and high reproducibility. In some moments during my thesis, this spectrometer broke down and we had to use a Jobin Yvon T64000 spectrometer that did not perform at the same quality standard. Due to this reason, the reproducibility of this step was reduced (instead of a nanosphere we just obtain a shortened nanowire) and we had to prepare more samples in order to obtain the desired nanostructures.

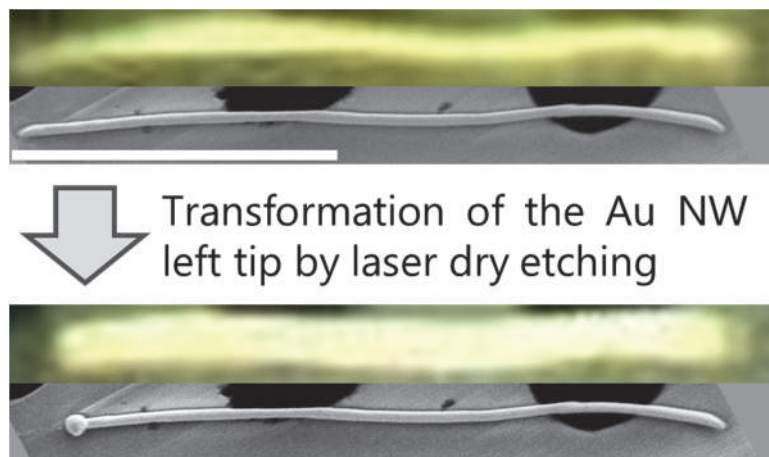


Figure II.31. From top to bottom: Optical microscopy and SEM of a Au nanowire before any treatment and after laser treatment on its left tip (half dog-bone). The white bar corresponds to 5 μm .

II.6.3. PEDOT nanoparticles synthesis and dispersion

We drop casted polymer nanoparticles on the dog-bone and half dog bone nanowires solid dispersion. Some of them attached to the nanowire – nanoparticle end, being an excellent platform to perform remote Raman studies. In the case that the polymer nanoparticles arrived on undesired segments of the nanowire we removed them by laser dry etching as described before. In order to continue in the same line we relied on the PEDOT as Raman active material.

Commercial nanoparticles

We believed that commercially available PEDOT nanoparticles would allow us to save time as we could skip the synthetic step. But we soon discovered that they were embedded in an undesirable surfactant (Figure II.32a). The PEDOT counterion/dopant was indicated to be dodecylbenzenesulfonic acid (DBSA), we considered that the surfactant was actually an excess of this substance. After centrifugation, redilution and fast sonication we could remove this surfactant and obtain a solid dispersion of PEDOT nanoparticles, without a high fluorescent baseline and a small shift of the Raman peaks (Figure II.32b&c). Another point that we should note is that the Raman spectra of these commercial PEDOT nanoparticles was different from the Raman spectra of PEDOT nanowires described before (Figure II.32c). Presumably that was due to their doping level or the presence of a different counterion.

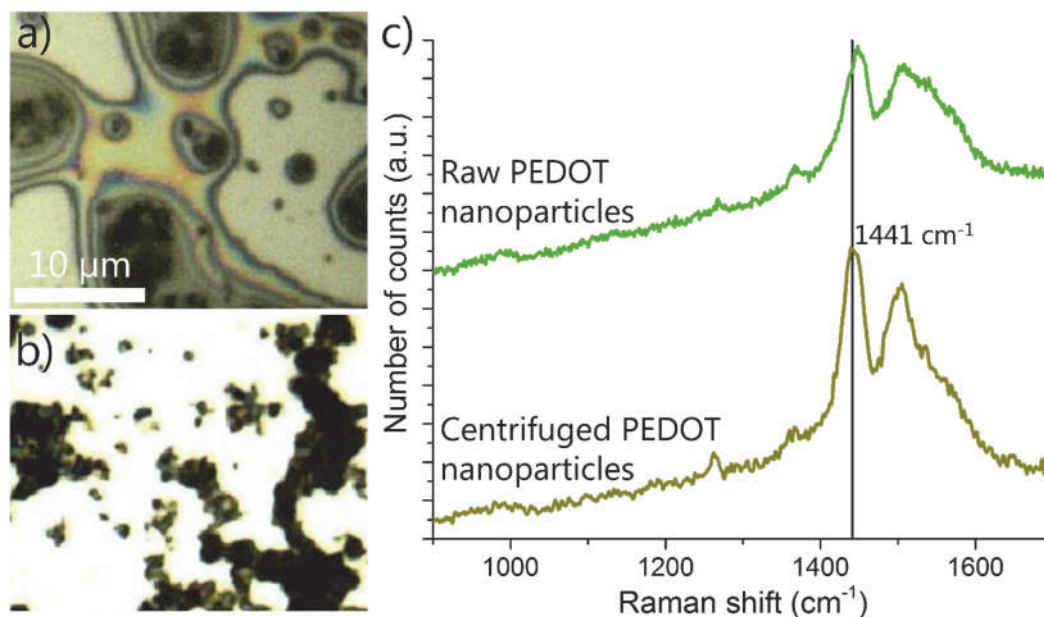


Figure II.32. Optical images of commercial PEDOT nanoparticles solid dispersions on *p*-doped Si a) without and b) with centrifugation-redispersion treatment prior to drop casting. c) Raman spectra of these PEDOT nanoparticles dispersions at an excitation wavelength of 514 nm.

After confirming that these PEDOT nanoparticles could couple with treated Au nanowires (Figure II.33), we successfully removed them by laser dry etching from the undesirable places by the method described before.

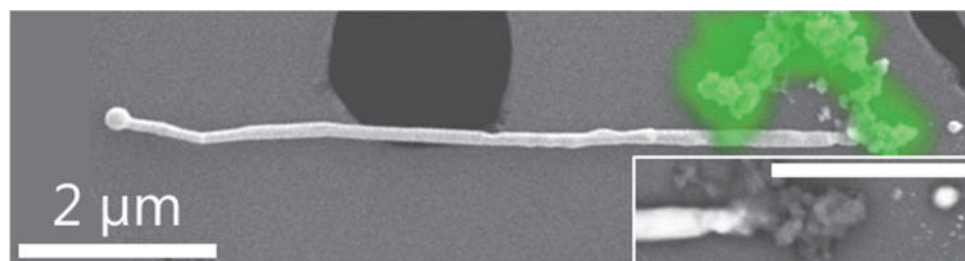


Figure II.33. SEM image with superposed Raman mapping signal for the C=C symmetric stretching PEDOT band of a half dog-bone Au nanowire with PEDOT particles on the non-nanoantenna tip. Inset: Zoom backscattered electrons image of the PEDOT particles containing tip. Scale bar in the inset corresponds to 1 μm.

The main drawback of these nanoparticles was their lower photostability. At low intensity laser powers they degraded, making very difficult to perform reproducible remote micro-Raman experiments.

II.7. Conclusions

We have effectively designed, synthesized, dispersed on solid substrates and characterized different kinds of plasmonic-active nanowires. From pure Au and pure PEDOT nanowires that served us as starting point, passing through the Au@PEDOT with the PEDOT shell perfectly located, which deeply study in Chapter III, and finally to the hybrid Au nanowire – Au nanoantenna coupled with PEDOT particles. Their synthesis by the electrochemical hard-template method allowed us to finely tune their morphology, and the post-synthesis steps permitted the creation of more complex gold-based structures, whose plasmonic role will be studied in Chapter IV.

CHAPTER III

Supramolecular ordering in
PEDOT and Au@PEDOT nanowires

III. Supramolecular ordering in PEDOT and Au@PEDOT nanowires

Organic optoelectronics is nowadays a very important and active domain of research and development, with commercial devices in displays and flexible devices including photovoltaics. Major challenges have been tackled during the last decade. One can cite the improvement of the organic dyes photostability and the encapsulation methods, the design of new molecules and polymers altogether with the development of processing techniques in order to exploit self-assembly and supramolecular ordering for improved charges mobility and management into multi-layered systems, among others. In this context, the template method has notably been used as a platform for exploring the mechanisms, the benefits and the drawbacks on the electric and optical properties of the confinement at a sub-micrometric scale of functional molecules and polymers. The resulting organic nanowires and nanotubes have also been considered individually as nano-sensors, nano-sources or well-organised in arrays for example in photovoltaic devices.

During my thesis project, the management of the supramolecular ordering of π -conjugated systems has been investigated through a novel confinement geometry resulting from the coaxial morphology. This study is reported in this Chapter.

First, a brief review of the supramolecular ordering induced by the synthesis in a template is proposed to identify the novelty of the present study. Second, the specifications of the experimental set-up and the measurement protocol are described. Then, the comparative study of the supramolecular ordering of the PEDOT chains within pure PEDOT and Au@PEDOT nanowires is reported.

III.1. Short review of supramolecular ordering in polymer nanowires

The management of the supramolecular ordering of π -conjugated systems is a central point to improve devices performances. Controlling changes in the polymer supramolecular orientation inside the nanowires can induce enhanced or novel optoelectronic and physical responses, due to modified carrier mobility, exciton dissociation, junction morphology and profile, etc.^{347,450–454} For more than two decades, processing conjugated polymers with nanotemplates have been shown to promote

such an improved organisation of the chains into nanowires and nanotubes. Different mechanisms have been proposed to explain this improved ordering, depending on the filling method of the nanopores: electropolymerization, solvent-assisted of a polymer in solution, confined polymerization. Here, we briefly review that topic.

In 1989, Aldissi studied the polymerization of polyacetylene in fibres, with an ordering induced by a nematic liquid crystal solvent in a magnetic field. They used polarized infrared absorption spectroscopy (PIRAS) and conductivity measurements to determine that the polyacetylene oriented along that magnetic field.³³⁵ The group of C.R. Martin during the same and next years reported a similar supramolecular preferential orientation along the fibres in hard-template synthesized polymer nanowires and nanotubes using the same type of characterization methods.^{331,455} It was also supported by a X-ray diffraction (XRD) study, and soon discovered that the supramolecular order of the polymer chains increased for smaller nanowires diameter.⁴⁵⁶ They attributed this effect to the preferential interaction between the pore walls (rich in anions) and the conjugated polymer chains with a cationic character due to the oxidative electropolymerization. While the core of the nanowires, not in contact with the pore walls, were considered disordered (amorphous) (Figure III.1). The higher surface to volume ratio when the nanowire diameter decreases made this effect more notable in small diameter nanowires. The nanotube morphology is thus optimal.

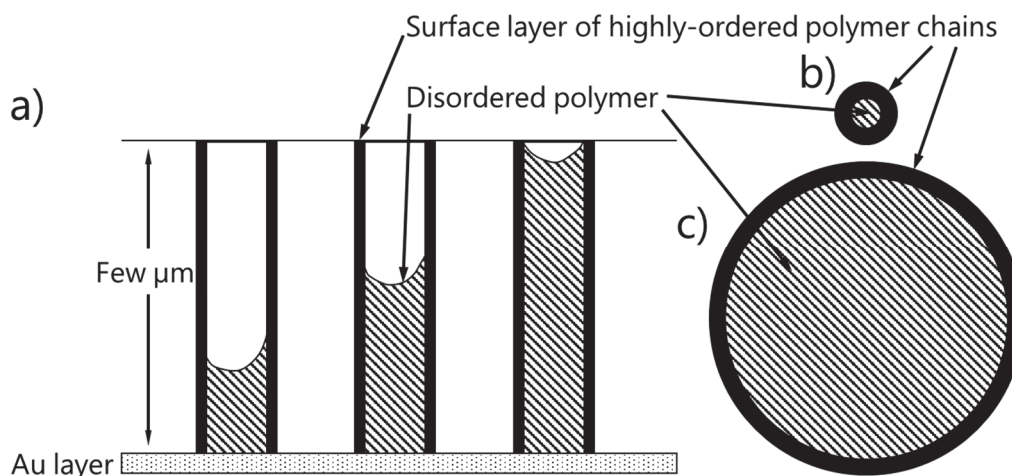


Figure III.1. Schematic cross-sectional views of template-synthesized conjugated polymer nanowires a) inside the membrane,⁴⁵⁷ b) small diameter nanowire and c) large-diameter nanowire.⁴⁵⁸

The explanation for the preferential supramolecular ordering of the polymer chains along the nanowire main axis is that these polymer chains follow an epitaxial growth respect the pore walls.⁴⁵⁶ Granström and Inganäs in 1993 and 1995 obtained similar results for several kinds of templated-synthesized conjugated polymer nanowires such as polypyrroles, polythiophenes which supported that theory (Figure III.2a).^{450,459} It can

be noted that in their most recent reports, the group of Martin showed that the preferential ordering of the polymer chains can be perpendicular to the nanowire main axis because the polymer chains were growing from the pore walls (perpendicularly to the pore walls) and not along them (parallel to the pore walls) (Figure III.2b).^{458,460–462} However, most of the reports about hard-template synthesized nanowires made to date with advanced techniques allowing the study of single nanowires, have defended the initial theory of the supramolecular orientation along the main axis.^{208,450,453–457,463,464} The studies made with PEDOT nanowires have supported the supramolecular orientation of the polymer chains along the main axis of the nanowires.^{450,453}

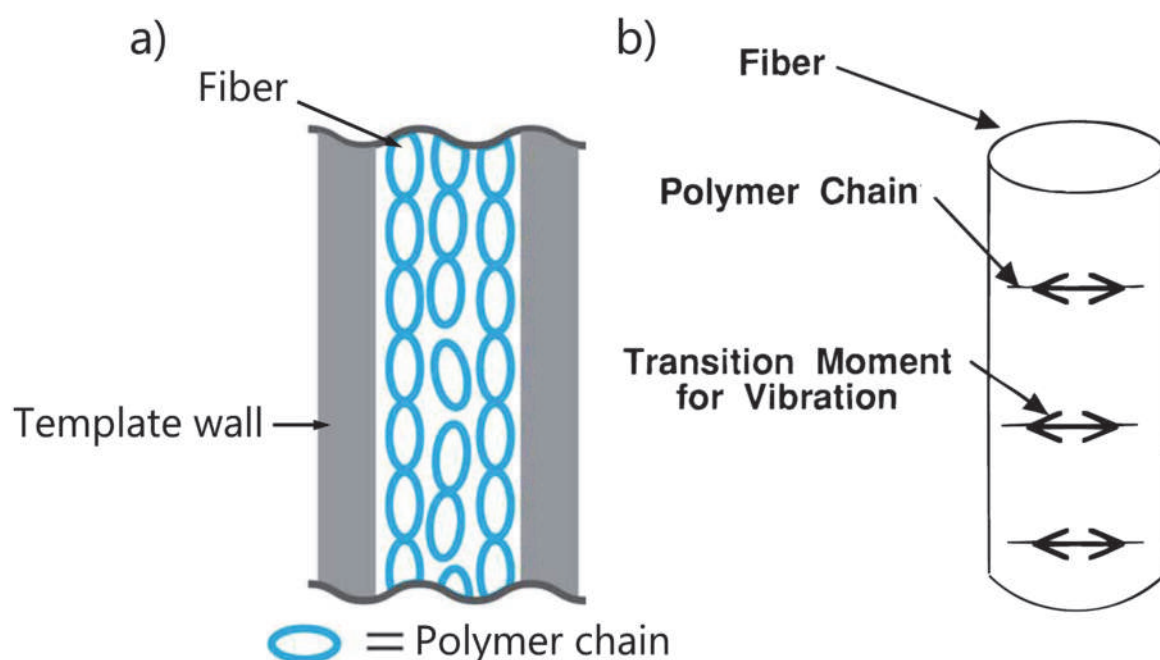


Figure III.2. a) Parallel⁴⁵³ and b) Perpendicular^{460,462} disposition of the polymer chains inside the nanowires respect to its main axis proposed by different authors.

Many characterization methods have been used to determine the supramolecular ordering. It can be noted that for conjugated polymers, such an ordering means generally a preferential orientation of the chains because of the intrinsic 1D nature of a conjugated segment and of π -stacking between chains. A supramolecular improvement is often shown with a comparative methodology between a disordered and an ordered polymer obtained by changing a synthesis or processing parameter. Furthermore, these characterization methods must include an anisotropy parameter, in order to distinguish between the different possible orientations. Preferential orientation of conjugated segments has been investigated mainly by PIRAS,^{331,335,454,456,460,462,465} and polarized Raman spectroscopy^{465–467} while XRD^{450,456,459} gave satisfying results in a few cases, because it requires a larger amount of material, i.e. billions of well-ordered nanowires. Alternatively, other techniques such as X-ray

photoelectron spectroscopy (XPS)^{453,462} or UV-vis absorption^{452,462}, electrical^{335,389,450–453,455,456,458,459,463,464} and thermal^{451,454} conductivities have been used to evaluate the ordering and the packing without considering the polymer orientation. More recent quantification of the mechanical properties of a single nanowire (Young's modulus) has also been shown as suitable for measuring the order degree of polymer nanowires.³⁴⁷ It has also been discovered that in some cases, small crystalline domains can be found inside the polymer nanowires.^{346,450,451,459,465}

The electrons placed in connected p molecular orbitals can delocalize, forming conjugated systems. The length of this connected p orbitals is called conjugation length and, in conjugated polymers in particular, is responsible for their conductivity and optical response. A larger conjugation length in polymers is also normally related to a higher chain order.⁴⁶⁸ Regarding the vibrational spectroscopy techniques some groups have correlated the conjugation length in polythiophenes with the intensity ratio between the symmetric and the antisymmetric C=C stretching bands.^{374,468} The higher the $I_{\text{antisymmetric}}/I_{\text{symmetric}}$ ratio, the longer the conjugated segments. We should note that by Raman spectroscopy some authors have reported the study of the degree order of polymer chains, specifically polythiophenes, by means of the full-width-at-half-maximum (FWHM)⁴⁶⁹ and the intensity ratio (in height) between the antisymmetric and the symmetric C=C stretching bands.^{374,468} The lower the FWHM the higher the "crystallinity" and thus a lower amount of disordering. The higher the $I_{\text{antisymmetric}}/I_{\text{symmetric}}$ ratio, the longer the conjugated segments and the better their coplanar ordering.

In this Chapter, the study of the supramolecular ordering of PEDOT synthesized in two different templated configurations is reported. A main achievement is the proof of a totally original orientation of the conjugated segments when ultra-confined in the unusual nano-reactor geometry promoted for the coaxial nanowires. The experimental methods and protocol are first detailed. Then, the supramolecular configuration within PEDOT nanowires is reported, to serve as a reference system. The third part presents the full Raman spectroscopy study of PEDOT shell surrounding the gold core of Au@PEDOT nanowires with a detailed spectral analysis. A growth mechanism based on the ultra-confined electropolymerization is proposed in the fourth part to explain the structural improvements measured in the coaxial case, in comparison to the usual nanowire case.

III.2. Methods and measurement: polarized nano-Raman spectroscopy

The fabrication of the samples was already detailed in the previous Chapter. Here, we motivate and describe the experimental set-up configuration, and we describe the experimental methodology exploited to get reliable and accurate measurements.

Among the different techniques that permit the study of the polymer supramolecular ordering in nanowires, we chose the polarized Raman spectroscopy for the following reasons:

- Study of single nanowires (rather than an array of millions/billions required for some characterization techniques) permitted by the laser excitation coupled with an optical microscope
- High response and stability of the PEDOT Raman signal for small radiation powers
- Possible surface enhanced Raman scattering due to the presence of the Au plasmonic core in Au@PEDOT coaxial nanowires
- Controlled polarization of both the excitation and the emitted light
- Simple preparation of the sample
- Opportunity to characterize the same nanowire also by SEM and TEM, by using an adequate substrate or grid
- Possibility to make future advanced remote nano-Raman measurements as we will reveal in Chapter IV

We utilized a Renishaw InVia™ Raman spectrometer that is coupled with a confocal microscope (Appendix I). The presence of Renishaw plc located in Wotton-under-Edge, United Kingdom, as a partner in our European Training Network project allowed us to have a powerful feedback from the company for optimized configurations and further developments. This equipment is managed with a great expertise by Dr. Jean-Yves Mevellec, who trained me to exploit it at its maximum.

Our system is equipped with five different laser lines: 457 (2.71 eV), 488 (2.54 eV) and 514 nm (2.41 eV) from an Argon laser, 633 nm (1.96 eV) from a Helium/Neon laser and 785 nm (1.58 eV) from a diode laser. Two gratings are available: 2400 gr/mm (grooves per millimetre) for the visible laser lines and 1200 gr/mm for the red-infrared ones.

A nanometric piezo-stage was installed recently on the sample holder, a non-standard equipment that permits to get x-y-z steps as small as few nanometres for mapping Raman signal with a great spatial accuracy. The spectrometer was mounted on an anti-vibration table. It made possible to measure Raman and laser (monochromatic) reflectance maps using the nanometric piezo-stage for up to 5 hours without any disturbances.

One of the crucial issues during the use of this spectrometer was the control of the confocality. We used a x100 long focal objective with a numerical aperture of 0.8 in order to optimize the optical configuration for studies with polarized light. Second, the Renishaw software, WiRe™, has the option to work in confocal mode, which closes the slit opening to 20 μm and the CCD camera width to 3 pixels. Ultimately, In order to get an ultimate precise spatial resolution, it was possible to close the slit up to 10 μm and set the CCD camera width to 1 pixel but the Raman signal hugely dropped. Nevertheless, for the laser nano-reflectance measurements that we introduce in Chapter IV we utilized that configuration.

Using the conditions described above we could estimate the laser spots diameter on the sample by the following formula:^{470,471}

$$Laser_{diameter} = 1.22 \frac{\lambda}{NA} \quad (III.1)$$

Where λ is the laser wavelength and NA is the numerical aperture of the objective (0.8), which is defined as the half angle of the light focused by the objective on the sample.⁴⁷⁰ The calculated laser spot diameters are the double than the Rayleigh resolution (in x and y) which corresponds to the maximal resolution achieved by an objective under a certain wavelength or by the radius of the first diffraction laser spot or Airy disk (distance between the centre of the spot and the border).⁴⁷⁰ It can be easily inferred that the laser spot is larger for larger wavelengths, whose values we calculated for the four wavelengths exploited during my thesis project (Table III.1).

Wavelength	Laser spot diameter	Laser power (max)	Irradiance (max)
488 nm	0.74 μm	15 mW	34 mW/μm ²
514 nm	0.78 μm	15 mW	31 mW/μm ²
633 nm	0.96 μm	10 mW	14 mW/μm ²
785 nm	1.20 μm	50 mW	44 mW/μm ²

Table III.1. Estimated laser spot diameters when focused on a flat perpendicular surface. The taken laser power is the one provided by the manufacturer at 100% laser power and the irradiance is calculated by dividing the laser power by the spot surface. The numerical aperture of the x100 long focal objective is $NA = 0.8$.

The sample, consisting of a solid dispersion of nanowires on a flat surface (normally a Si wafer or a SiO_x TEM grid), was mounted horizontally. The laser excitation arrived perpendicularly to the substrate surface and then to the nanowires. The collected beam came perpendicularly from the substrate and the nanowires, thus in the opposite sense to the excitation beam (Figure III.3). We could use both polarizers for the excitation and collection beams in order to make advanced polarization studies. In the studies presented in this Chapter, the polarizers for both the excitation and collection light

were always parallel between each other: (i) excitation: vertical – collection: vertical (ii) excitation: horizontal – collection: horizontal. To determine if there were any effect of the optical pathway and orientation of the grating on the polarized intensity, a study of the Raman signal of benzene molecules in liquid was made. It showed that no correction of the measured intensity is required for the (i) and (ii) configurations with a better than 5% accuracy.

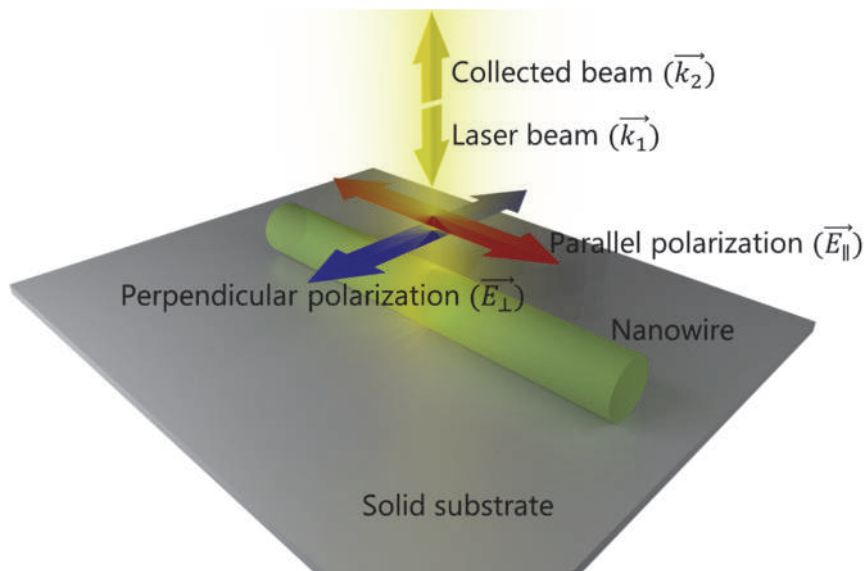


Figure III.3. Schema representing the Raman excitation and collection of a nanowire placed on a solid substrate with a perpendicular laser beam. The laser beam (\vec{k}_1) and collected beam (\vec{k}_2) propagation vectors are represented, as well as the electric field vectors for the parallel (\vec{E}_{\parallel}) and perpendicular (\vec{E}_{\perp}) polarizations.

It can be noted that getting reproducible measurements in the confocal configuration required a quite long training to make optimal optical alignment for each wavelength. As it is often the case in advanced experimental work, I met some technical failures or problems: the Argon laser not available for more than half a year, the automatic laser filters worked arbitrarily, some issues for high accuracy measurements due to vibrations transmitted from the CCD camera fan. All these, combined with some “noises” from other persons using other set-up in the same room and perturbing hour-long Raman spectroscopic maps on our nanowires.

The detailed experimental protocol used to get reliable measurements is described in detail in the Appendix 1.

III.3. PEDOT and Au@PEDOT nanowires

Raman comparison: Wavelength effect

We performed systematic micro-Raman mapping spectroscopy studies on the Au@PEDOT nanowires in order to fully characterize them, analyse their optical properties and detect possible anisotropies. Here we present a basic study of their spectra and their comparison with pure PEDOT nanowires. The more advanced micro-Raman measurement dealing with the polymer chains alignments will be treated in Chapter III.

III.3.1. Optimal Raman conditions for the study of PEDOT-containing nanostructures

Degradation studies permitted to quantify the maximum laser power supported by these hybrid nanowires (Table III.2). The protocol that we designed was simple: first we measured the Raman signal of a single PEDOT-containing nanostructure with a very low laser power ($<1.0 \mu\text{W}$) for 100 seconds. If the signal to noise ratio was not enough we then increased the laser power until we got a reproducible signal. In that moment we began the degradation step: we applied a laser beam of the same power than in the previous measurement for 500 seconds. After that step we measured again the PEDOT signal under the same conditions described before. We then repeated the degradation step with a higher laser power and after that we measured again the PEDOT signal. We repeated this steps until we observed significant changes in the Raman signal (bands shift and/or intensity decrease) (Figure III.4).

It can be noted that the irradiation power was the same for home-made PEDOT nanowires and Au@PEDOT nanowires at 488 and 514 nm laser excitation, but it was five times larger at 633 and 785 nm. It was complex to quantitatively evaluate the role of the gold on the Raman intensity, because it could both increase the Raman intensity, due to the electric field enhancement and tip effects, or decrease the Raman intensity, due to a shadowing effect of the PEDOT located in contact with the substrate. These two effects also depended on the laser wavelength. An alternative explanation concerned the resonant or non-resonant Raman signal, which resulted in orders of magnitude changes of the Raman intensity. This is related to the absorption by the PEDOT, and thus by the conjugation length. In other words, the observed difference in the polymer degradation could reveal changes in the conjugation length. No degradation at a larger power could thus reveal a reduced efficiency of the Raman effect, i.e. different conjugated lengths.

Laser maximum power before PEDOT degradation in different nanostructures:

Wavelength	PEDOT NW/NP	Commercial PEDOT NP	Au@PEDOT NW
488 nm	15 μ W	1.5 μ W	15 μ W
514 nm	15 μ W	1.5 μ W	15 μ W
633 nm	10 μ W	1.0 μ W	50 μ W
785 nm	50 μ W	25 μ W	250 μ W

Table III.2. Maximum laser power applied in home-made PEDOT nanowires and nanoparticles, in commercial PEDOT nanoparticles and in Au@PEDOT nanowires before changes appear in the PEDOT Raman signal, indicating a degradation. Circularly polarized laser beam and $\times 100$ long focal objective ($NA = 0.8$).

It should also be noted that for the commercial nanoparticles, the PEDOT was significantly less stable and it required a 10 times smaller laser power. Acquisition times were normally 200 seconds in the case of single point measurements and up to 10 seconds per point when mapping.

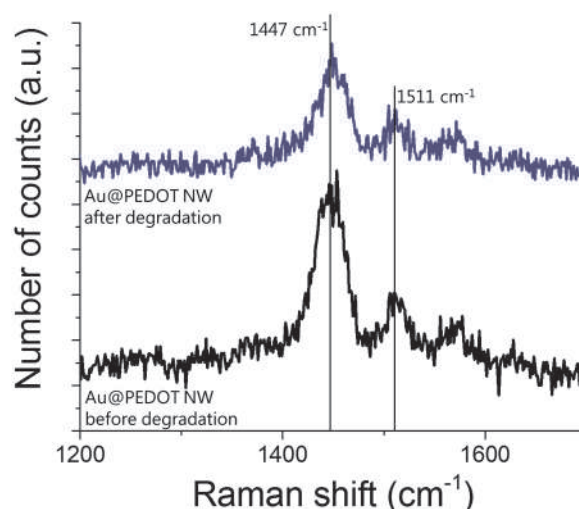


Figure III.4. Example of PEDOT signal before and after degradation in an Au@PEDOT NW ($\varnothing_{\text{core}} = 140$ nm, Shell thickness = 15 nm). The circularly polarized laser power used for the measurements before and after the degradation process was 7.5 μ W with an acquisition time of 100 s. The laser power used for the degradation was 150 μ W and was applied for 500 s. $\lambda_{\text{exc}} = 514$ nm.

It is important to note that a smaller quantity of PEDOT gives a smaller Raman intensity. We have shown that the thickness of the PEDOT shell could range between 6 and 15 nm, depending on the pore diameter of the membrane used, of the duration of the alumina etching for the pore widening step of the process and of the time of electropolymerization to fill the shell. For the larger diameter, the quantity of PEDOT was always smaller in the coaxial morphology, thus resulting in a lower Raman intensity.

III.3.2. Spectral comparison for Au@PEDOT and PEDOT nanowires

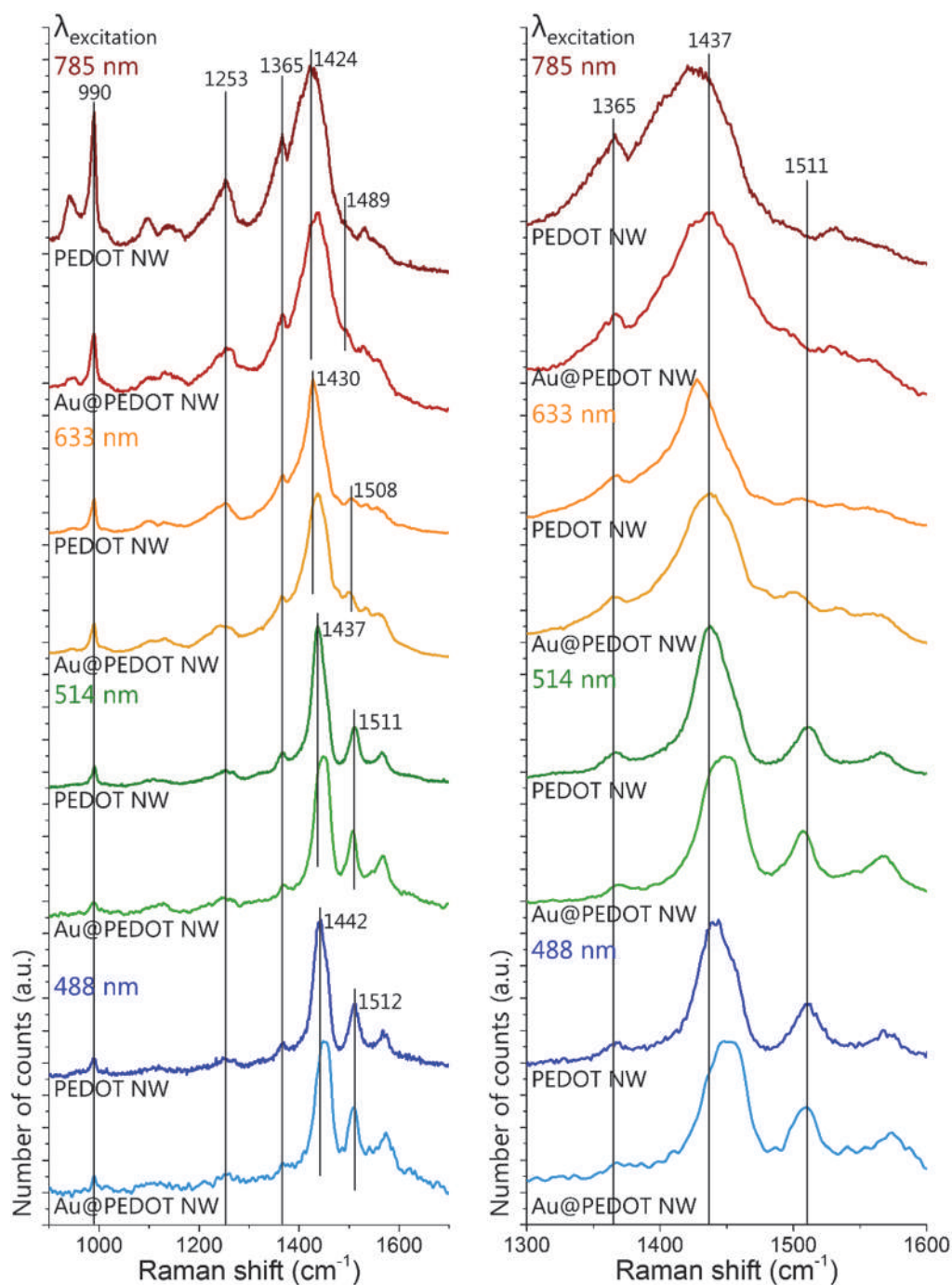


Figure III.5. Raman spectra (left) and enlarged spectral range of interest (right) of PEDOT nanowires (darker colours) and Au@PEDOT nanowires (lighter colours) at different excitation wavelengths. From top to bottom: 785 nm, 633 nm, 514 nm and 488 nm. The average diameter of the PEDOT nanowires was 160 nm. The diameter of the Au@PEDOT nanowires core was 140 nm with a PEDOT shell of 15 nm.

In a first study, the Raman spectra of the coaxial Au@PEDOT nanowires were measured at different excitation wavelengths (488 nm, 514 nm, 633 nm and 785 nm) with circular polarization in order to not to induce anisotropic behaviours and compared with the spectra measured for pure PEDOT nanowires under the same conditions (Figure III.5).

It should be noted that the experimental data shown below for the Au@PEDOT nanowires were measured close to the top tip of the nanowires, where the PEDOT thickness is larger. The position of the main bands was referred at its maximum. However, as the measured Raman bands are quite large and partly asymmetric. It can induce some discrepancies in the reported values. That is the reason why we mainly comment the main tendencies measured.

For conjugated polymers, different wavelength excitations predominantly probe conjugated segments with different conjugated lengths, due to resonant effects. So, for larger excitation wavelengths, the shift toward smaller values of the position of the main band (C=C symmetric stretching vibrations) and of the C=C antisymmetric stretching vibrations band (Table III.3 & Figure III.6) can be explained by the fact that longer conjugated segments are probed.

Raman shifts for the C=C stretching bands (cm^{-1}): symmetric | antisymmetric

Wavelength	Treated PEDOT film	PEDOT NW	Au@PEDOT NW
488 nm		1442 1512	1449 1509
514 nm	1436 1525	1437 1511	1447 1507
633 nm	1425 1530	1430 1508	1437 1501
785 nm		1424 1489	1434 1486

Table III.3. Raman shifts obtained experimentally for the C=C symmetric stretching and C=C antisymmetric stretching bands of PEDOT for different structures (film after acidic treatment, nanowires and shell surrounding Au nanowires). Four different excitation wavelengths were used for the analysis. Circular polarization at the excitation and no polarization at the collection were selected in order to not induce any anisotropic effects. The total average diameter of both PEDOT and Au@PEDOT nanowires was 160 nm.

The comparison between the Raman spectra of the PEDOT NW and the Au@PEDOT NW showed a systematic change, whatever the excitation wavelength. There is an up-shift (toward higher wavenumbers) of the main band attributed to the C=C symmetric stretching band, and conversely a down-shift (toward smaller wavenumbers) of the C=C antisymmetric stretching band for the Au@PEDOT nanowires (Table III.3 & Figure III.6). A similar tendency is also observed when comparing the PEDOT film and a PEDOT nanowire. It results from the confined growth and its impact on the ordering of the polymer chains. In the case of Au@PEDOT, the growth is much more confined (a 15-20

nm wide shell around the gold nanowire) and an improved molecular ordering is expected, as confirmed later.

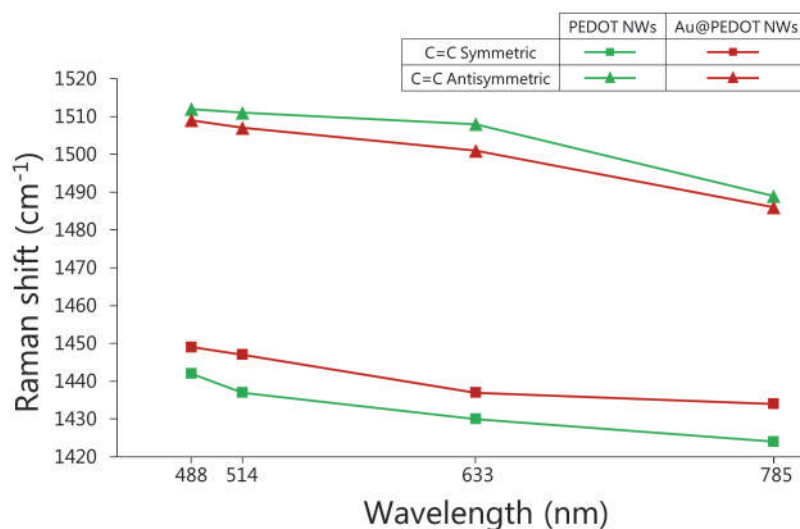


Figure III.6. Graphic representation of the Raman shifts indicated in (Table III.3).

The intensity ratio between the bands of the C=C antisymmetric stretching and symmetric stretching bands ($I_{[\text{antisymmetric C=C stretching}]} / I_{[\text{symmetric C=C stretching}]}$) has been identified as a good indicator of the conjugation length and the supramolecular ordering (Figure III.7).

It is observed that the intensity ratio is significantly larger for the Au@PEDOT nanowires than for the PEDOT nanowires (Figure III.7). It is an additional result suggesting an improved ordering of the conjugated polymer chains and longer conjugation length in the shell of the Au@PEDOT nanowires than in PEDOT nanowires.

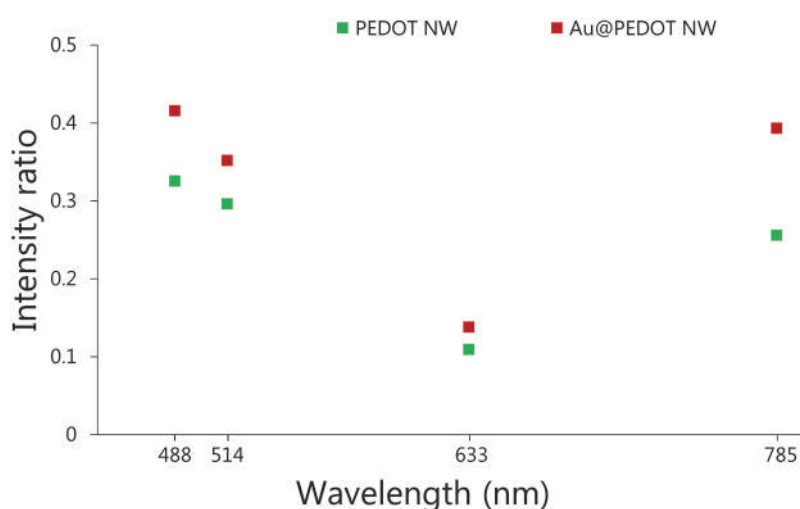


Figure III.7. Graphic representation of the intensity ratio $I_{[\text{antisymmetric C=C stretching}]} / I_{[\text{symmetric C=C stretching}]}$.

It is important to note that the 785 nm intensity ratio could not be analysed in the same manner as the others. Meanwhile we could clearly extract and fit both peaks symmetric and antisymmetric for the shorter wavelengths Raman signals, we could not extract the antisymmetric one for the 785 nm as it partly overlaps the symmetric one. We just took its intensity-to-baseline. Thus the comparison for this wavelength should be made just between the Au@PEDOT NW and the PEDOT NW intensity ratio, which followed the same pattern as in shorter wavelengths and not between the 785 nm and the other excitation wavelengths.

III.4. Supramolecular polymer ordering in nanowires analysed by polarized Raman spectroscopy

III.4.1. PEDOT nanowires: Effect of the diameter on the supramolecular structure

The synthesis, the morphological and spectroscopic characterization of PEDOT nanowires has been reported in Chapter II. A preliminary Raman spectroscopy study was shown. Here, a systematic polarized Raman study of different nanowires with different diameters and at different excitation wavelengths is detailed in order to investigate the molecular and supramolecular structure of the PEDOT electropolymerized in nanoporous templates.

It was crucial to first determine the maximum laser power at which the PEDOT nanowires do not degrade, i.e. optimal conditions to get the larger and more reproducible Raman signal. This optimal conditions, quite reproducible for a given system, were determined by measuring Raman spectra for different laser powers and measurement times (by changing the optical filters positioned on the incoming pathway before the sample). We used these optimal conditions (laser power, measurement time) for our next studies (Table III.2). In addition, the same area of the nanowire was systematically measured after several irradiations with different polarizations to check that no degradation was initiated.

We analysed the spectra measured from polarized Raman spectroscopy at different wavelengths (514 and 785 nm) and for different nanowire diameters (42, 160, 200 nm). In order to prevent from optical-geometrical effects due to the relative orientation of the nanowire, the polarizers and the spectrometer grating, we looked for nanowires that were positioned either totally vertical or totally horizontal on the screen. Then, we

performed the polarized Raman studies with polarized light both parallel and perpendicular to the main axis of the nanowire.

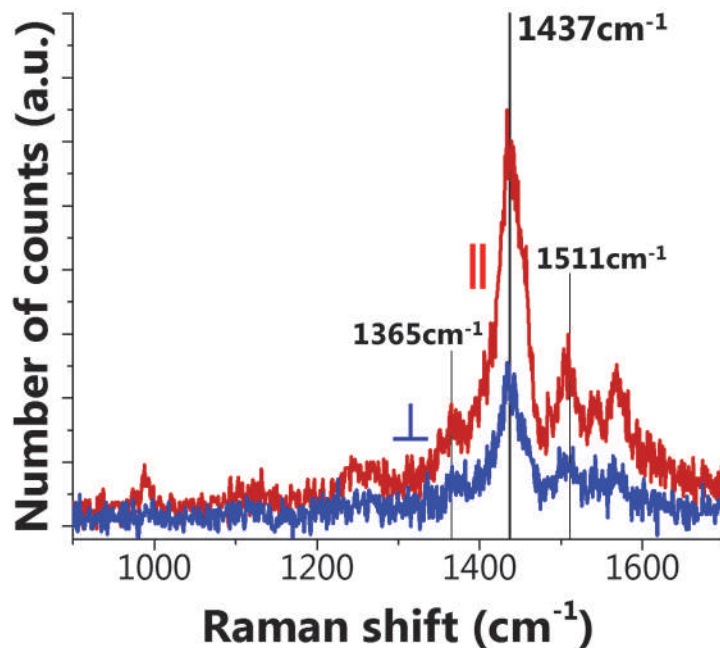


Figure III.8. Polarized Raman spectra measured for a single PEDOT nanowire (diameter: 42 nm) with light polarized parallel (red spectrum) and perpendicular (blue spectrum) to the nanowire main axis. ($\lambda_{excitation} = 514 \text{ nm}$, Laser power = $15 \mu\text{W}$, $t_{acquisition} = 4 \text{ s}$)

More intense Raman bands were measured in the case of the parallel polarization (Figure III.8). In order to quantify the difference between both polarizations in a reproducible manner, we calculated the dichroic ratio R (Equation (III.2)). The PEDOT band to calculate R was the main band corresponding to the C=C symmetric stretching.

$$R = \frac{I_{\parallel} - I_{\perp}}{I_{\parallel} + I_{\perp}} \quad (\text{III.2})$$

I_{\parallel} (I_{\perp} respectively) was the intensity of the C=C symmetric stretching band for excitation and detection in parallel (perpendicular, respectively) polarization. A fully oriented system would give a dichroic ratio of 1 for chains aligned parallel to the nanowire axis and -1 for chains aligned perpendicular to the nanowire axis.

Further information could be obtained on the conjugation length by measuring the dichroic ratio for two different excitation wavelengths: 514 nm and 785 nm. Indeed, it has been shown that the resonant Raman of conjugated segments strongly depends on the excitation, because of the absorption of conjugated segments which progressively red-shifts when the conjugation extends over longer segments (from 2 to 10 C=C, typically): the longer the wavelength, the longer the conjugation length.^{374,375}

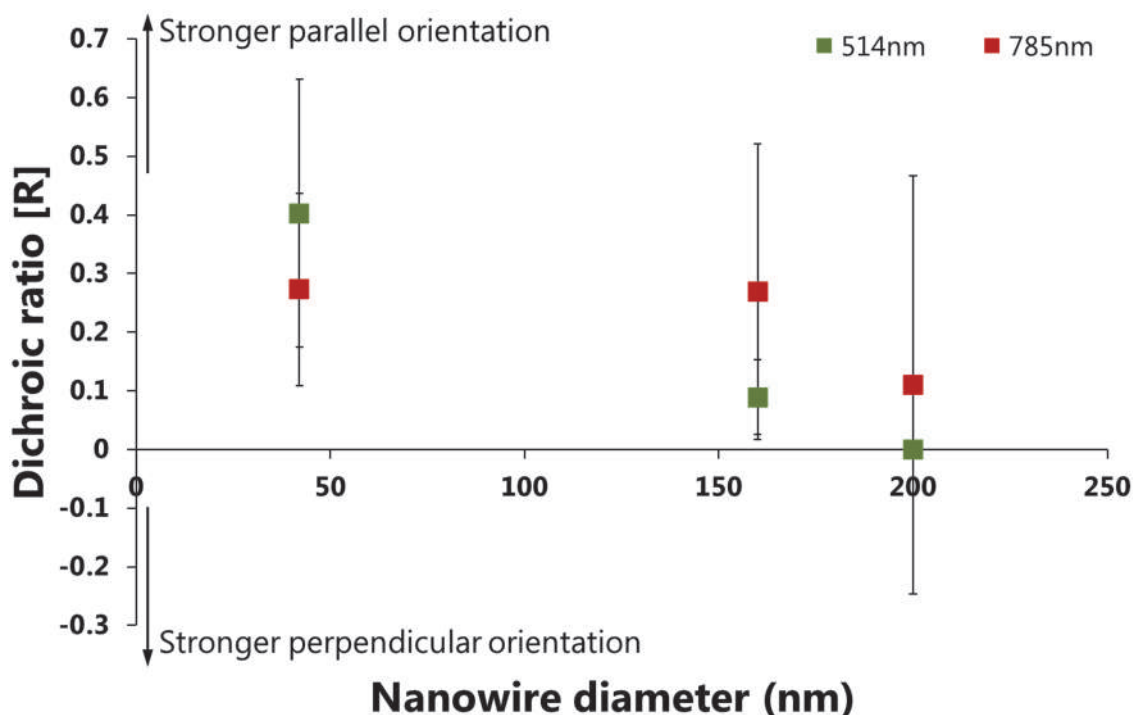


Figure III.9. Variation of the dichroic ratio with the nanowire diameter (40, 165 and 200 nm) from the study of polarized Raman spectroscopy for pure PEDOT nanowires of different diameters and at different $\lambda_{excitation}$.

It could be observed that the dichroic ratio increased for the smaller diameters, up to $R \approx 0.4$ for $d = 42$ nm, while no preferential orientation ($R \approx 0$) was found for $d = 200$ nm) when analysing the sample under a green laser (514 nm).

The same behaviour, was observed for the 785 nm case, but in this case, its dichroic ratio value was lower for smaller diameters ($R \approx 0.27$). Nevertheless, the dichroic ratio did not decrease so abruptly for higher diameters, it was even constant up to 150 nm and at 200 nm its value was not 0 ($R \approx 0.1$).

The first point to outline was the evidence of a preferential alignment of the PEDOT chains parallel to the nanowire axis. Such a preferential alignment was improved for the nanowires with the smaller diameter. It was in agreement with the confined electropolymerization mechanism proposed in previous studies, assuming an anisotropic growth on the lateral pore surface which promoted an ordered polymer shell, while disordered polymer thickened the shell to form nanowires (see beginning of this Chapter). The proportion of ordered versus disordered polymer chains thus progressively decreased when the diameter increased.

These results could be further discussed, considering the wavelength dependence of the C=C symmetric stretching Raman intensity.^{374,375} This study showed that in the 40 nm nanowires, both longer and shorter conjugated chains were aligned along the nanowire main axis, while for the larger diameters, there were a preferential alignment

only for the longer conjugated chains. In addition, the dichroic ratio was larger for the short segments at 40 nm diameter, while it was the reverse for the 165 and 200 nm diameter nanowires. A possible explanation was that the proportion of long conjugated segments progressively increased when the diameter increased, in relation with the shell thickening to form nanowires, rather than nanotubes.

In order to make a more complete study, other nanowire diameters should be studied. But as this behaviour was already reported in the literature,^{450,453,472} we decided to move on to the next milestone of our project.

III.4.2. Au@PEDOT nanowires

An analogous study was made for the Au@PEDOT nanowires, but the number of experiments that we performed was higher, as these nanowires had not been synthesized and characterized previously. They are also the relevant nanostructures for our future experiments on the remote excitation and detection discussed in Chapter IV.

III.4.2.1. Effect of the diameter on the supramolecular structure

We first made a broad study to observe the general behaviour of the Au@PEDOT nanowires with different diameters (22, 42, 55, 75 and 140 nm) in comparison with the PEDOT nanowires. The first results revealed that the Raman signal was usually more intense when the laser was polarized perpendicular to the nanowire, contrary to the PEDOT nanowires case (Figure III.10).

The analysis of the results in this case was more complex than for the pure PEDOT nanowires.

A first reason was that the smaller quantity of PEDOT under the laser beam gave a lower Raman signal: the PEDOT shell in the Au@PEDOT nanowires was no thicker than 20 nm, against 42 to 200 nm for the PEDOT nanowire diameter. We could partly overcome this issue by working at slightly higher laser powers (Table III.2) or/and by increasing the acquisition times, while taking care of any degradation of the PEDOT (i.e. change in the shape and the intensity of the Raman spectrum).

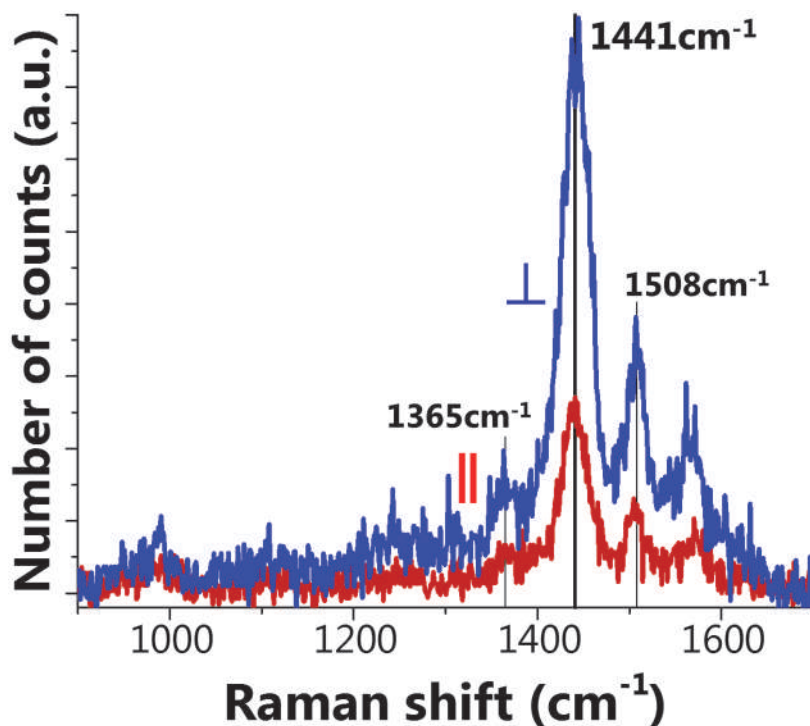


Figure III.10. Polarized Raman spectra measured for a single Au@PEDOT nanowire (core diameter = 42 nm) with light polarized parallel (red spectrum) and perpendicular (blue spectrum) to the nanowire main axis. ($\lambda_{excitation} = 514 \text{ nm}$, Laser power = $15 \mu\text{W}$, $t_{acquisition} = 8 \text{ s}$).

Another point had to be considered: the PEDOT shell structure could significantly change from the upper tip to the bottom tip, which would impact the Raman signal. The morphological study reported in Chapter II has shown that different morphologies and thicknesses could be obtained depending on the nanopore diameter, the pore widening step and the electropolymerization time: a continuous PEDOT shell from bottom to top, a PEDOT shell only close to the two tips, and a PEDOT shell only close to the top tip. For that reason, we propose a distinct analysis for the top and bottom tips.

III.4.2.2. Effect of the diameter and the morphology on the supramolecular structure

As we previously described, we observed a higher PEDOT Raman signal in the case of perpendicularly polarized light (both at the excitation and collection) to the main axis of the nanowire. But when we studied in more detail these Au@PEDOT nanowires we could notice that this behaviour did not happen on both tips in the same manner (Figure III.11).

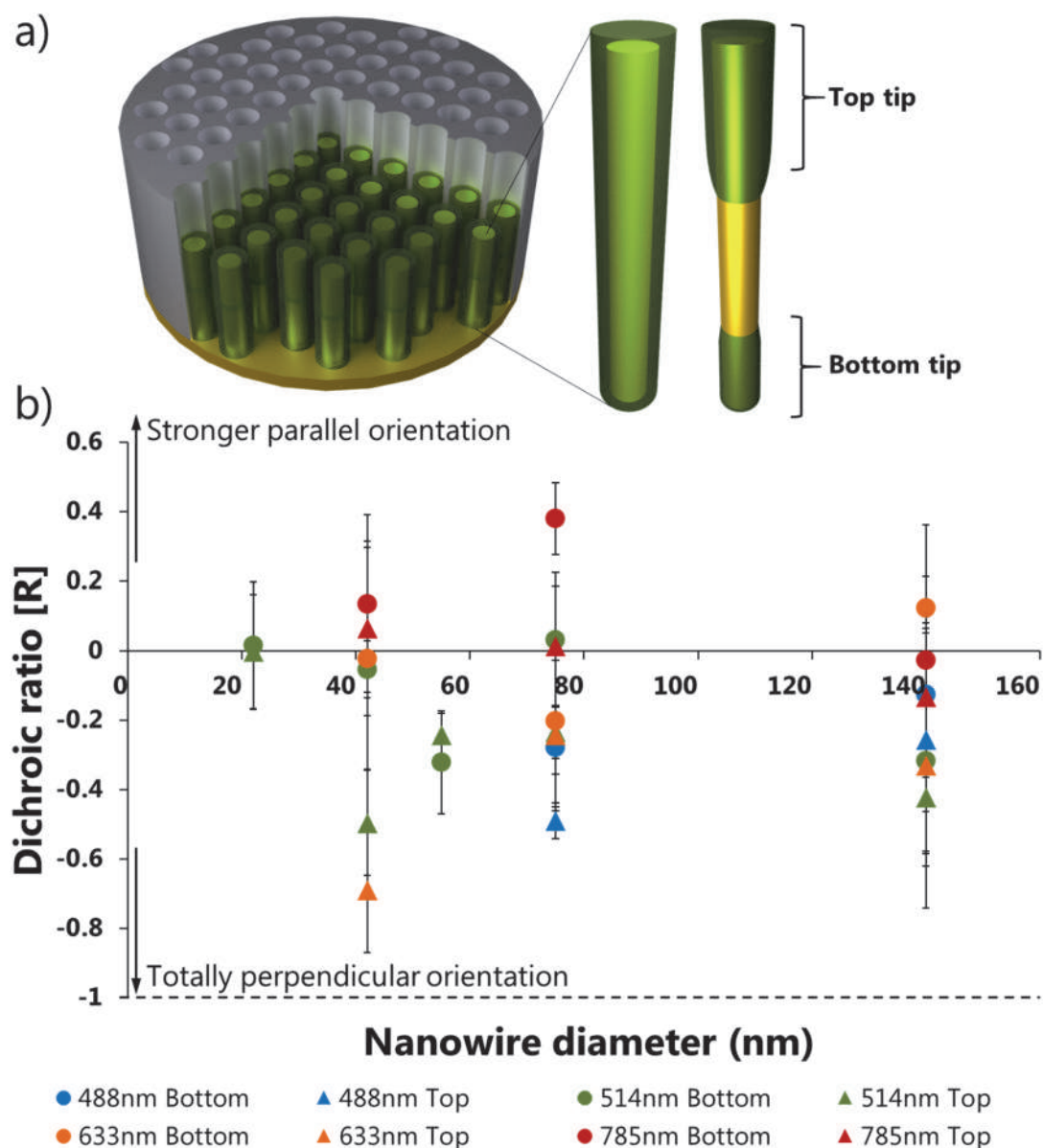


Figure III.11. a) Schema showing the location of bottom and top tip for a Au@PEDOT nanowire. b) Dichroic ratios measured for different Au@PEDOT NW diameters and at different $\lambda_{excitation}$. The polarized Raman spectroscopy study distinguished the measurement at their bottom tips (circles) and at their top tips (triangles).

The complete and detailed study of the polymer shell by polarized Raman spectroscopy in the Au@PEDOT nanowires reveals that in most cases the dichroic ratio is more negative for the top tip than for the bottom tip of the nanowires, being even positive in some cases of the second case. Following the explanation that we adopted for the pure PEDOT nanowires, we could correlate these observations to the preferential ordering of the polymer chains in the polymer shell in a determined direction. In opposition to the pure PEDOT nanowires we did not find significant differences in the polymer chain alignment regarding the core diameter.

In this case, the preferential orientation of the polymer chains, more pronounced on the top tip, would be perpendicular to the main axis of the nanowires. It can be observed that on the bottom tip, the alignment is less perpendicular ordered or even parallel in some cases. Regarding the excitation wavelengths, the blue and red laser obtained higher perpendicularly-aligned responses. The infrared studies shown lower perpendicular oriented results or even parallel oriented. The explanation for these phenomena could reside in the different chain growth on the bottom and the top tips that we discuss at the end of this Chapter.

Furthermore, we observed that the dichroic ratio in the asymmetric Au@PEDOT nanowire case (PEDOT only at the top tip) was more extreme ($R = -0.5$ for $\phi_{core} = 140 \text{ nm}$ and $\lambda_{exc} = 633 \text{ nm}$). We could relate this to a more pronounced ordered perpendicular disposition of the PEDOT chains in the small PEDOT shell at the tip. To confirm this phenomena we should perform more studies at different wavelengths and with different core diameters.

III.4.2.3. Correlated studies: micro-Raman and SEM

As we presented in Chapter II, by the use of the referenced substrates, we had the possibility to found and characterize exactly the same nanowire by different correlated nano-resolution techniques (Raman, SEM, TEM, EELS). Going a step beyond, we made polarized micro-Raman mapping of the same nanowire that we studied later by SEM (Figure III.12). We studied the variation of intensity of the Raman C=C symmetric stretching band along the nanowire for the two polarizations (parallel and perpendicular) and for excitation wavelengths at 488, 514, 633 and 785 nm. It has been shown for conjugated polymers that the Raman bands intensity strongly depends on the excitation wavelength in the visible and near infrared range. It was attributed to resonant Raman effects, which depend on the conjugation length and the doping level.^{374,392} Indeed, the absorption spectrum of conjugated polymers varies with both the distribution of conjugation lengths and the level of doping.⁴⁷³

For this correlated study, the Raman spectra was measured all along a 95 nm diameter single Au nanowire covered with PEDOT at the two ends and at different excitation wavelengths and for both polarizations parallel and perpendicular. We reported the variation of the most intense Raman band along the nanowire for each polarization (Figure III.12). The morphological information was obtained by SEM using a specific boron-doped silicon substrate with marks and grids to localize the nanowires. The parts of the gold nanowire covered by PEDOT appears darker on the SEM image. They fit well with the parts where we measure the characteristic PEDOT Raman signal. The matching results show that we could precisely correlate both techniques and that the perpendicular polarized signal obtained is stronger than the parallel one (Figure III.12).

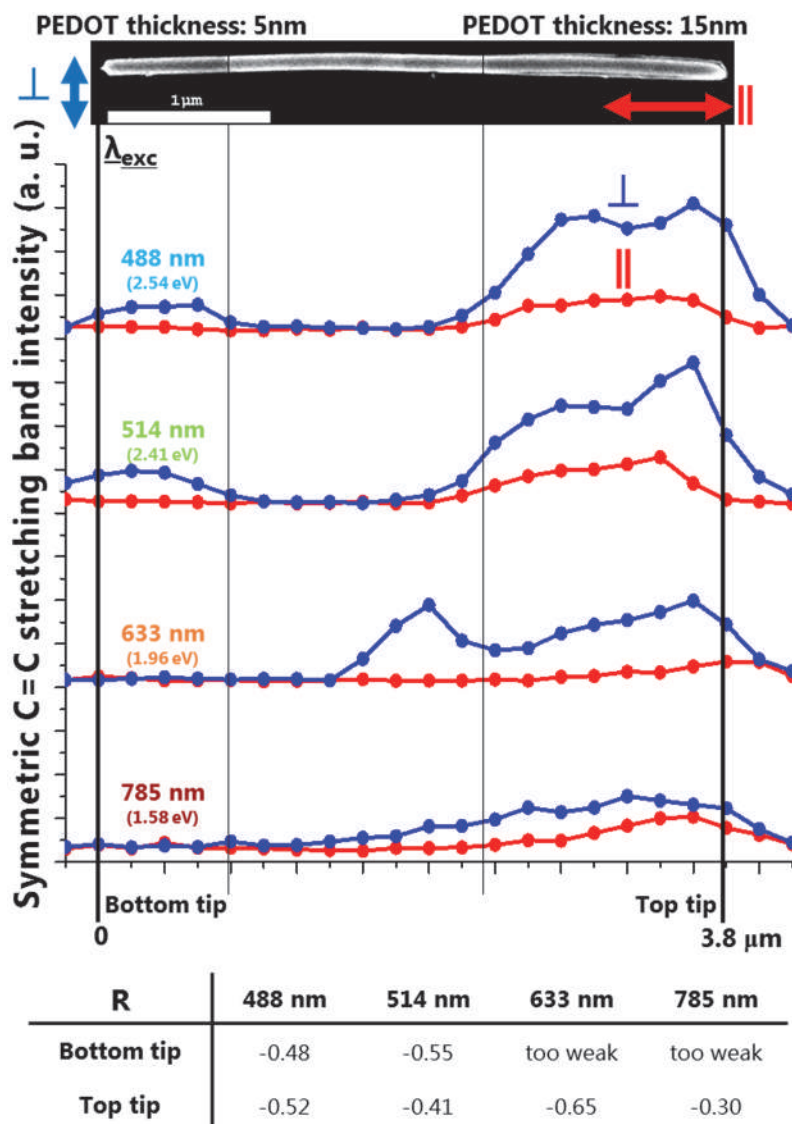


Figure III.12. Scanning electron microscopy (SEM) image and plot of the Raman intensity corresponding to the symmetric C=C stretching of PEDOT along the Au@PEDOT nanowire with PEDOT only at the tips. The intensity mapping is shown for light polarized parallel (red) and perpendicular (blue) to the nanowire main axis (analyser always parallel to $\vec{E}_{excitation}$). The diameter of the Au core is 95 nm and its length is 3.8 μm . The table reports the averaged values of the dichroic ratio R (Equation (III.2)) for the symmetric C=C stretching band located at the bottom or at the upper side of the gold nanowire for four excitation wavelengths: 488, 514, 633 and 785 nm.

The distinction between the bottom tip and the top tip could be done with respect to the thickness of the PEDOT layer, which was thicker at the top tip (as expected by the partial etching of alumina and the comprehensive PEDOT growth mechanism around gold nanowire). Therefore, a stronger Raman signal intensity was expected, as the intensity is roughly proportional to the amount of material probed.

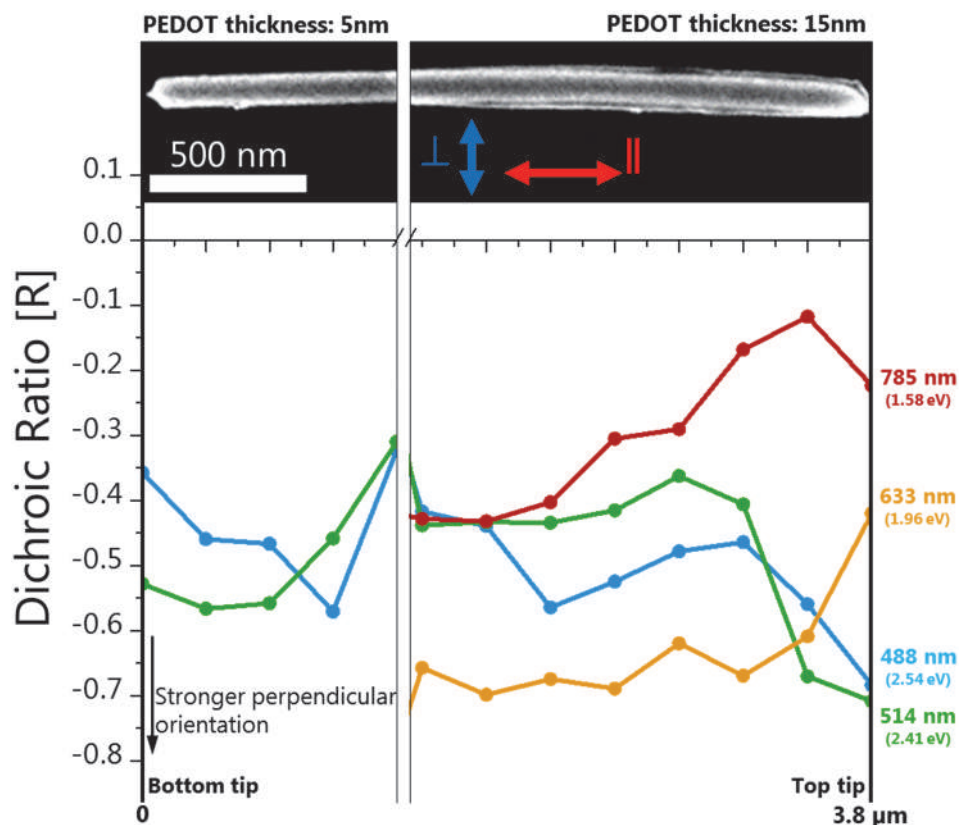


Figure III.13. SEM image and plot of the dichroic ratio R (Raman symmetric $C=C$ stretching for PEDOT) measured at the tips covered with PEDOT for the Au(95 nm)@PEDOT nanowire studied previously (Figure III.12). The dichroic ratio was calculated for each point using the Raman data from the parallel and perpendicular polarizations (Equation (III.2)). Four different excitation wavelengths were studied: 488, 514, 633 and 785 nm.

For this coaxial nanowire, the corresponding values of the dichroic ratio for each point of the mapping (Figure III.12) and averaged over the 0.8 – 1.5 μm long PEDOT shell covering the two nanowire extremities were reported (Figure III.13). Negative values of R corresponded to the perpendicular orientation of the conjugated chains. For the thicker PEDOT shell (10 to 15 nm thick) at the upper side of the nanowire, similar values of R (≈ -0.4 ; -0.5) were measured at $\lambda_{\text{exc}} = 488$ nm (2.54 eV) and 514 nm (2.41 eV). It reaches -0.65 at 633 nm (1.96 eV) but only -0.35 at 785 nm (1.58 eV). In the near infrared domain (785 nm) probing predominantly the longer conjugated segments, the negative dichroic ratio weaker than for other excitation wavelengths could be attributed to a weaker chain alignment perpendicular to the wire axis.

It is interesting to combine these result with the observation that both 633 and 785 nm excitation wavelengths did not detect any contribution of PEDOT at the bottom side of the nanowire, in contrast with the Raman characterization by the 488 and 514 nm excitation wavelengths, as well as with the SEM studies showing a thinner PEDOT

layer (5 to 10 nm). These results strongly suggested that the conjugated segments were very short when grown at the bottom of the gold nanowire, oppositely located to the electrolyte reservoir. This aspects will be discussed in the following section.

This first micro-Raman experiment was also used as preliminary study for the novel nano-Raman and nano-reflectance mapping that we will explore in Chapter IV.

III.5. Proposed mechanism

First, we compared the non-polarized Raman spectra of case of both PEDOT and Au@PEDOT nanowires. The intensity ratio between the C=C antisymmetric stretching and the C=C symmetric stretching bands, is in relation with the length of the conjugated segments: a relatively more intense antisymmetric band corresponds to longer conjugated segments.^{374,468,469} Our results strongly suggest that the PEDOT chains in Au@PEDOT nanowires are more conjugated and ordered than in PEDOT nanowires.

Then the study under polarized light has shown that the polymer chains are weakly ordered with a preferential orientation parallel to the main axis, while for Au@PEDOT nanowires, a very pronounced preferential orientation is perpendicular at the top tip and mixed at the bottom tip.

The case of the PEDOT nanowires is similar to what it has been already reported in the literature. Some authors supported that the negatively charged pore walls act as a preferential electropolymerization sites where the polymer chains grow acquiring a preferential orientation, while a random orientation takes place with the thickening of the tube thickness (Figure III.14left).

The case of the Au@PEDOT nanowires is different. Our results strongly suggest that the conjugated segments are shorter when grown at the bottom of the gold nanowire, oppositely located to the electrolyte reservoir. It makes sense that this part is less accessible to the diffusion of the EDOT monomer, dodecyl sulfate and perchlorate anions from the above reservoir than the upper side. Such a mechanism can also explain the reduced electropolymerization rate (thinner layer), which should result in shorter polymer chains and correspondingly shorter conjugated chains for PEDOT at the bottom side than at the upper side. Ultimately, the PEDOT shell at the upper tip can block the 10-15 nm wide channel surrounding the gold cylinder, thus inhibiting further growth of PEDOT at the bottom and on the lateral size when all the monomers remaining in the closed cavity have been consumed. Another possible growth mechanism to explain the preferential electropolymerization at the extremities of the nanowires deals with a tip effect, i.e. an electric-field enhancement which takes place at the top extremity of a strongly anisotropic conducting object connected to an electrode. The larger the aspect ratio (length/diameter), the stronger the electric field

enhancement at the tip. Such a local field enhancement could contribute to the overpotential and then promote a faster oxidation of the monomers and thus a faster electropolymerization on the top extremity, rather than on the lateral size. However, such a tip effect cannot account for the growth initiated at the bottom of the nanowire, because no tip effect takes place due to the proximity of the planar electrode on the bottom side of the porous membrane.

So, the proposed mechanism for the PEDOT growth in coaxial nanowires is analogous to the PEDOT nanowires case, but with the electropolymerization starting from the gold nanowire, which acts as a nanoelectrode. Then the alumina walls blocks the perpendicular extension of the PEDOT chains, possibly reorienting longer chains, or possibly stopping the electropolymerization (Figure III.14right). This mechanism can explain both the preferential orientation perpendicular to the nanowire axis evidenced in most cases, but also the less perpendicular or even a preferential longitudinal orientation observed in some cases at the bottom tip when exciting with red-infrared lasers (633 nm and 785 nm), i.e. probing the longer conjugated segments.

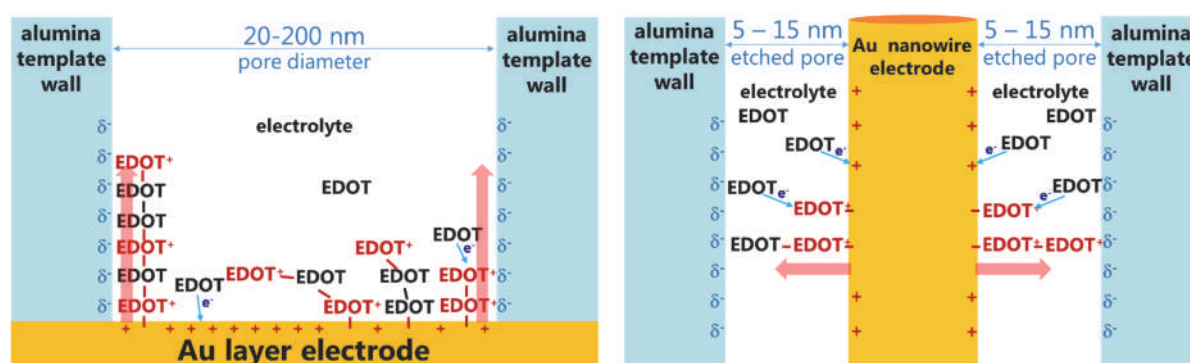


Figure III.14. Simplified schemes of the confined electropolymerization of EDOT in the two geometries. Left: from the Au layer anode, right: from the Au nanowire.

We emphasize that these unique conditions of electrodeposition in an ultra-confined channel and strongly anisotropic nano-electrodes give opportunities to tune standard and unusual mechanisms involved in the growth of 1D-nanomaterials. A direct exploitation is proposed in the next part to investigate the plasmon-mediated remote Raman excitation.

III.6. Conclusions

We have demonstrated an enhanced supramolecular ordering of the PEDOT polymer chains in the shell of Au@PEDOT nanowires. While the PEDOT chains preferentially align parallel to the main axis of the nanowire in pure PEDOT nanowires, they adopt a preferential perpendicular orientation in the case of Au@PEDOT ones. The Raman spectroscopy study also suggest that their conjugation length and their ordering is improved in Au@PEDOT NW. A growth mechanism has been proposed, which is in accordance with some of the previous literature reports described in the beginning of this Chapter.

We have also introduced the possibility of correlating different nano-techniques by the use of the referenced substrates that we presented in Chapter II. We have perfectly correlated the polarized micro-Raman spectra taken along a Au@PEDOT nanowire with PEDOT only at their tips with its SEM image. This feature will be further explored in Chapter IV.

CHAPTER IV

Advanced optical and remote
plasmonic study of individual
nanowires

IV. Advanced optical and remote plasmonic study of individual nanowires

IV.1. Introduction

The ultimate goals of my thesis was i) the enhancement of the plasmon propagation in nanowires by the design of antenna-coupled nanowires and the study of their optical and plasmonic properties; ii) the proof of concept of the utilization of these systems for plasmon-mediated remote Raman spectroscopy.

We reported in previous Chapters the fabrication of these plasmonic structures and their characterization, mainly by micro- and nano-Raman, SEM and TEM. In this Chapter, we investigate the optical and plasmonic properties of single dog-bone and coaxial nanowires by Raman spectroscopy and laser reflectance with a spatial resolution better than 200 nm by coupling these studies with electron microscope images.

First, it is proposed a presentation of the plasmonic systems selected among the numerous nanowires fabricated for their characteristics in relation with the targeted optical behaviour. We detail the methods developed for correlating the optical study with the morphological study. The accuracy of this correlation is required for a proper analysis of the results.

We then present the study of the laser nano-reflectance (in a configuration normally named Rayleigh scattering, i.e. at a given wavelength and in direct mode, following the ordinary disposition of the spectrometer described in the previous Chapter) of gold nanowires with different morphologies.

Finally, the very unusual measurement configuration, called "remote", is explored. For our 1D systems, it consists in an excitation at a different place than the collection. This remote configuration has been used for studying the remote laser reflectance of dog-bones nanowires and the remote Raman spectroscopy of the coaxial Au@PEDOT nanowires.

IV.2. Selection of plasmonic systems

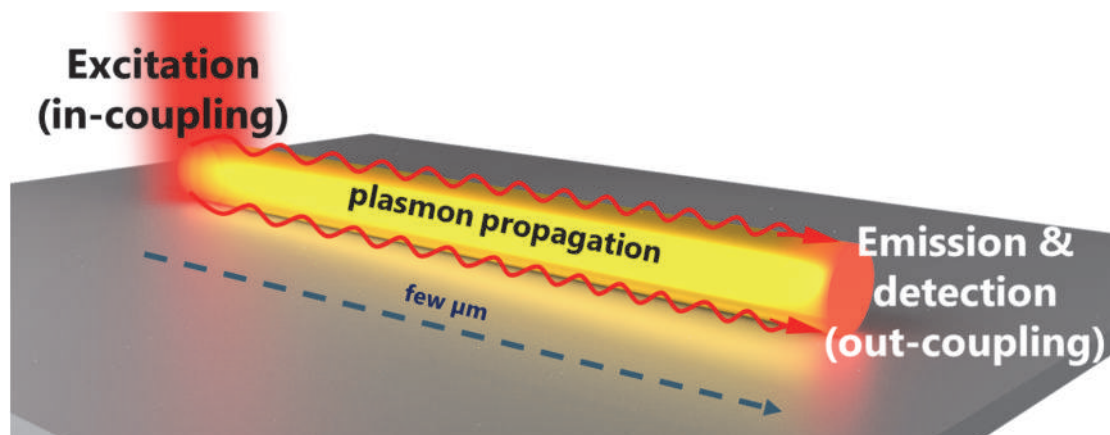


Figure IV.1. Schema of a remote nanospectroscopy experiment. The SPP-supporting nanowire is excited locally at one of its photon-SPP coupling active sites (tip). It propagates the plasmon that is coupled again, emitted and locally detected at the opposite tip, separated some μm from the excited one.

A first objective deals with the enhancement of surface plasmon polariton excitation by a laser micro-probe, i.e. improving the coupling between the incident laser and the surface plasmon to promote SPP ("in-coupling"), and the re-emission of light at another point of the nanowire ("out-coupling") (Figure IV.1). Three kind of systems were selected: a basic isolated Au nanowire (Figure IV.2a), a gold nanowire with a gold nanoparticle at one of its tips (half dog-bone) (Figure IV.2b) and a gold nanowire with a gold nanoparticle at each of its tips (dog-bone like structure) (Figure IV.2c).

We then considered that the study of these systems should be completed by the introduction of a photoactive species at one of their tips, in order to evaluate if they could be used as remote nanosensors and nanosources. We reported the synthesis of Au@PEDOT nanowires with PEDOT shell at only one of their tips (Figure IV.2d). The other systems were achieved by the dispersion of PEDOT particles on one of the Au nanowire-nanoparticle tips (Figure IV.2e&f). The choose of PEDOT particles instead of the PEDOT shell or a thin PEDOT film covering all the systems was motivated mainly by two reasons: the PEDOT shell of a Au@PEDOT nanowire completely disappears after the laser dry heating treatment to produce gold nanoparticles, a PEDOT shell that covers all the system could give ambiguous results in the remote configuration, making hard to distinguish between the Raman signal coming from the direct excitation and then mediated by the SPP, from the Raman signal excited remotely by the SPP. It can be noted that the PEDOT particles could be deposited in random places of the nanowires because we can destroy the nanoparticles deposited at undesirable places.

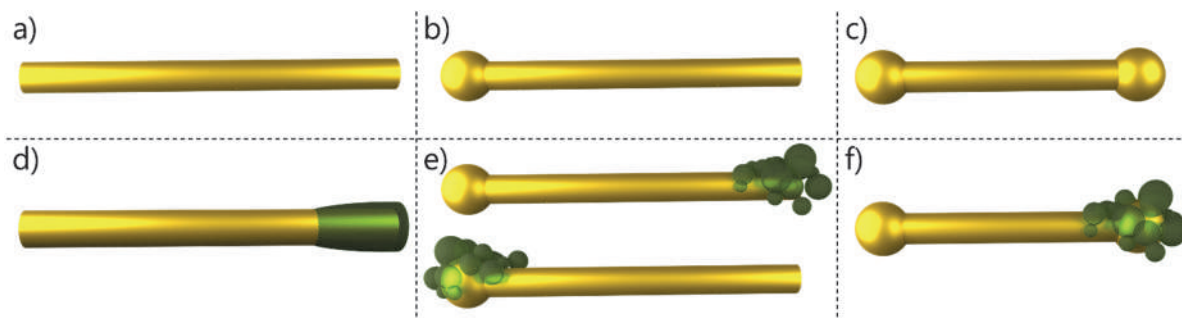


Figure IV.2. Schema of the different gold-based nanowire-nanoantenna systems proposed: a) Au nanowire, b) half dog-bone: Au nanowire with a Au nanoparticle at one of its tips, c) dog-bone: Au nanowire with a Au nanoparticle at each of its tips, d) Au@PEDOT nanowire with PEDOT shell only at one of its tips, e) half dog-bone from (b) with PEDOT particles top) on the nanowire tip, and bottom) on the Au nanoparticle, f) dog-bone system from (c) with PEDOT particles on one of the nanoparticles (tips).

IV.2.1. Methods for correlated optical, spectroscopic and morphological study

We relied in our electrochemically templated synthesized nanowires. In order to get good solid dispersions, we used Au@PEDOT nanowires, but with the PEDOT only at one of the tip in order to avoid possible complications.

Once the Au@PEDOT nanowires were prepared and dispersed in water by the methods described in Chapter II, we drop casted 3 μL of that dispersion on a TEM grid with thin SiO_x windows. For the samples to be studied by low-energy EELS studies (carried out by our partner in UNIZAR, Zaragoza, Spain), we used the 20 nm thick SiO_x grids. In the case we were not going to perform that characterization, we used the 50 nm thick SiO_x ones, as they were less fragile and their surface was larger. This drop casting step should be done using a micropipette and very close to the substrate but not making contact, in order to minimize the risks of breaking it.

For the best samples after dispersion, we found more than 60 nanowires that seemed homogeneous, smooth, straight and long enough (at least 4 μm). This observation was achieved by mapping the total surface of the grid by successive optical microscopy images. At this point, our sample contained Au@PEDOT nanowires (Figure IV.3). One of these nanowires could be easily transformed in a single Au nanowire by dry etching the PEDOT shell from the tip of the targeted nanowires (Figure IV.3). From one Au@PEDOT nanowire, the "half dog-bone" Au nanowire-nanoparticle (Figure IV.3) and the "dog-bone" Au nanoparticle-nanowire-nanoparticle (Figure IV.3) could also be

produced by laser dry etching (heating) of one or both Au tips, respectively. In order to get the more complex hybrid systems including the Au nanowire-nanoantennae and the PEDOT particles, it was necessary to drop cast the PEDOT particles and perform laser dry etching of the undesirable ones (Figure IV.3).

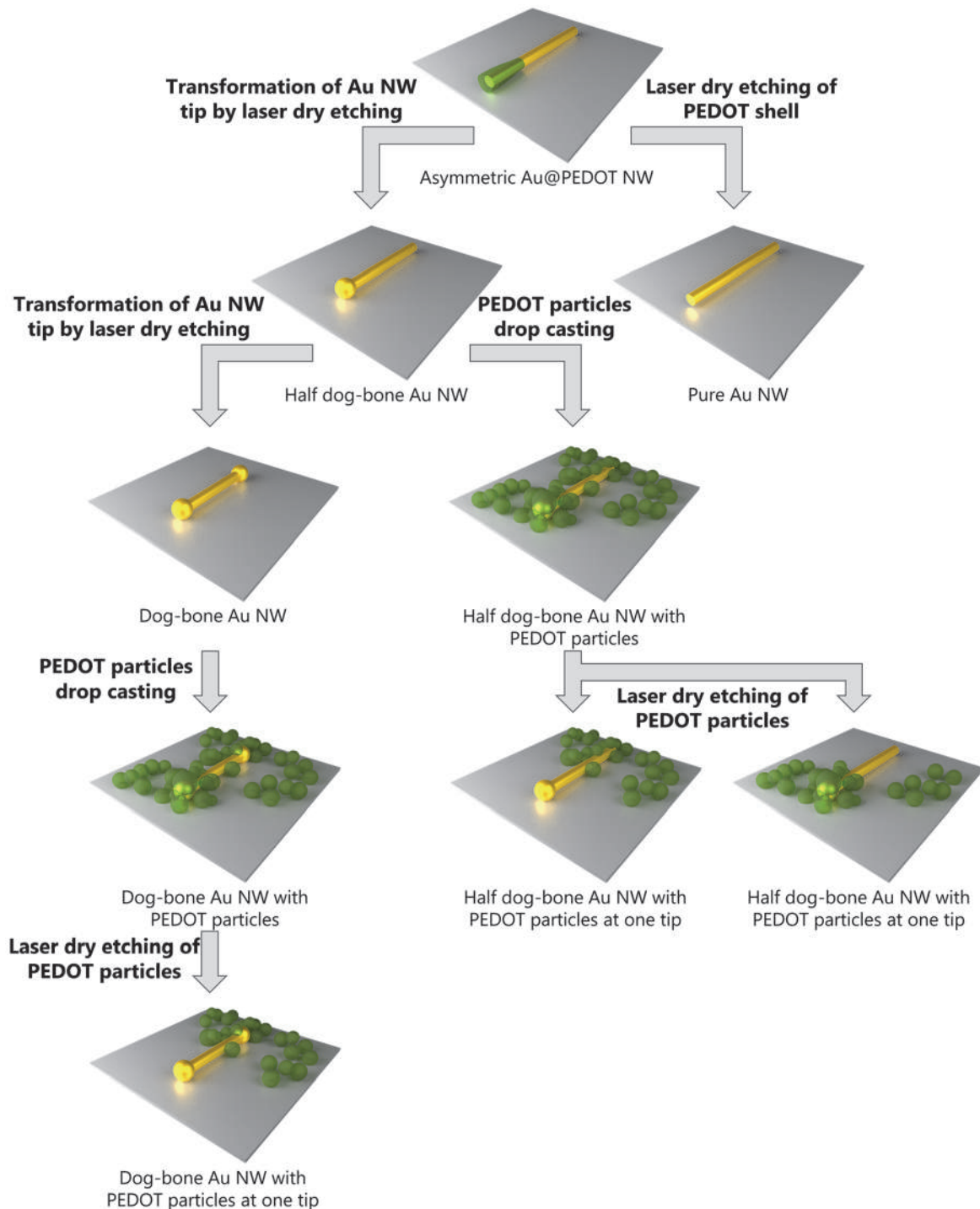


Figure IV.3. Schematic description of the post-synthesis processes developed for the production of advanced gold-based nanowires by laser treatments and dispersion of PEDOT particles.

Once all these processes were done, we characterized by Raman spectroscopy the PEDOT containing systems and by a SEM study with a low acceleration voltage (500 V) and a low magnification the non-containing ones, in order to not damage them or change their properties (Figure IV.4). Indeed, we checked that the electron beam can strongly modify the Raman spectrum of the PEDOT, as it is usual for conjugated polymers.

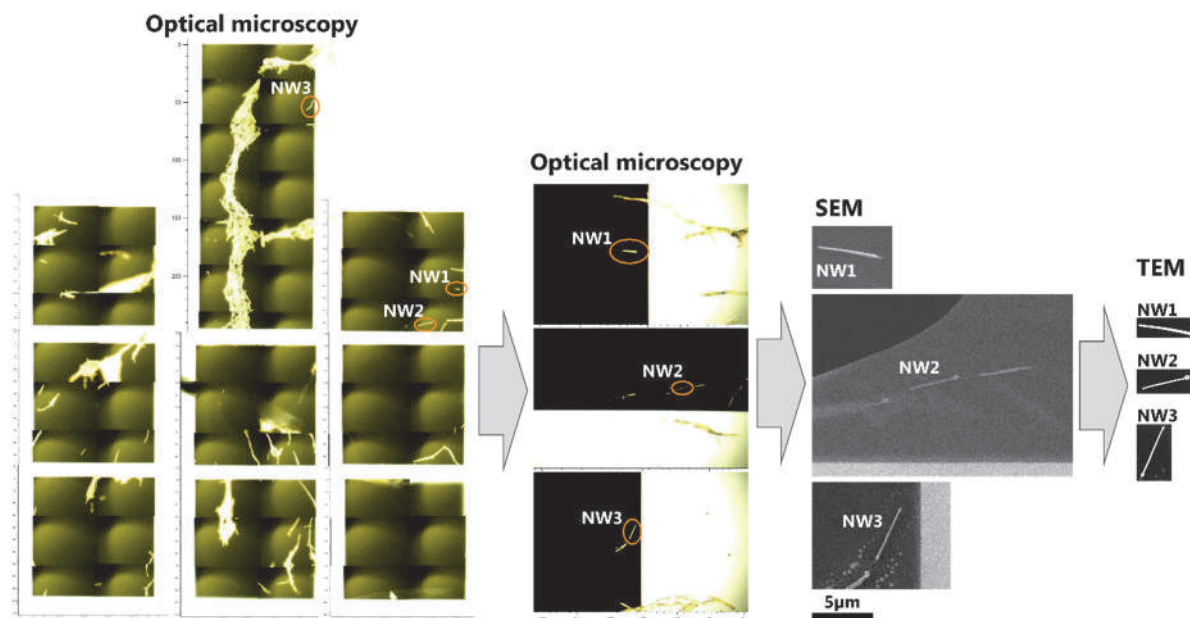


Figure IV.4. Example of the correlated localization of the nanowires on the windowed TEM grid. From their first localization by optical microscopy (left) to their ultimate analysis in the TEM (right).

The handling of the samples was crucial. During their production steps, they were mounted and stored in Gel-Pak[®] antistatic boxes with retention level X4 (Figure IV.5a). This permitted a safe handling and avoided the deposition of dust or other ambient pollutants.

Once the different plasmonic systems were produced, the samples were mounted in special metallic SEM holders for TEM grids (Figure IV.5b). This permitted an easy rotation of the sample inside the Raman spectrometer, a safe transport between techniques and their study by SEM. In order to perform the TEM and EELS studies the samples should be mounted in the normal TEM holders.

We should remark that the critical handling step was when changing between holders (Gel-Pak[®] box, SEM holder and TEM holder). If the TEM grid fell down, there was a high probability of break of the SiO_x windows, something that rendered the sample and all the previous work made with it useless. We used a vacuum pick-up system and tweezers in order to minimize the risks.

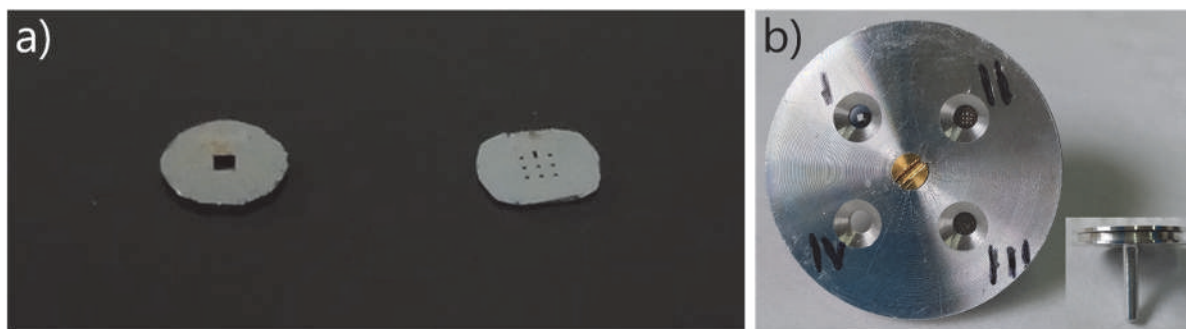


Figure IV.5. Pictures of a) TEM grids with SiO_x windows of 50 nm (left) and 20 nm (right) thick on Gel-Pak[®] antistatic box. b) TEM grids with SiO_x windows of 50 nm (I) and 20 nm (II and III) in SEM holder for TEM grids. Inset: Lateral view of the SEM holder.

About experimental and time management

Finally, we could study experimentally 6 of the 7 different systems proposed (Figure IV.6). We should note that the study of the systems including the PEDOT particles was not as complete as the others because of a problem of stability for the commercial PEDOT particles. They were embedded in a surfactant and they were less stable than our electropolymerized PEDOT, forcing us to use lower laser powers and then longer acquisition times to get enough Raman signal. We decided to use the proposed electropolymerized PEDOT particles and we prepared the samples, but the lack of time and the breakdown of the lasers in the Raman spectrometer prevented us from performing the desired experiments.

Some additional remarks can be done by comparing the images presented (Figure IV.6). First, the pure Au nanowire (Figure IV.6a) has a less homogeneous structure (its diameter changes along its longitudinal direction) than the Au@PEDOT ones (Figure IV.6d). This fact comes from the alumina membranes used in their synthesis. While the Au@PEDOT nanowires correspond to older samples, the Au nanowire comes from a new batch of commercial alumina membranes whose properties were significantly worse. For these Au@PEDOT nanowires, we can observe that the left tip of the longer one (Figure IV.6d2) is partially hidden by some cover. This thin covering layer was part of the SiO_x window that broke and bend over that area. We attributed that to the vacuum pumping of the SEM, as we did not observe it by optical microscopy.

We also remark that in both cases of Au nanowire-nanoparticle systems (Figure IV.6b&e), both tips were laser dry heated but one of them (right tip) instead of producing the characteristic Au nanoparticle just volatilized and shortened the nanowire as we described in Chapter II. In one of them (Figure IV.6e), a gold nanoparticle was produced but at a certain distance of the nanowire tip.

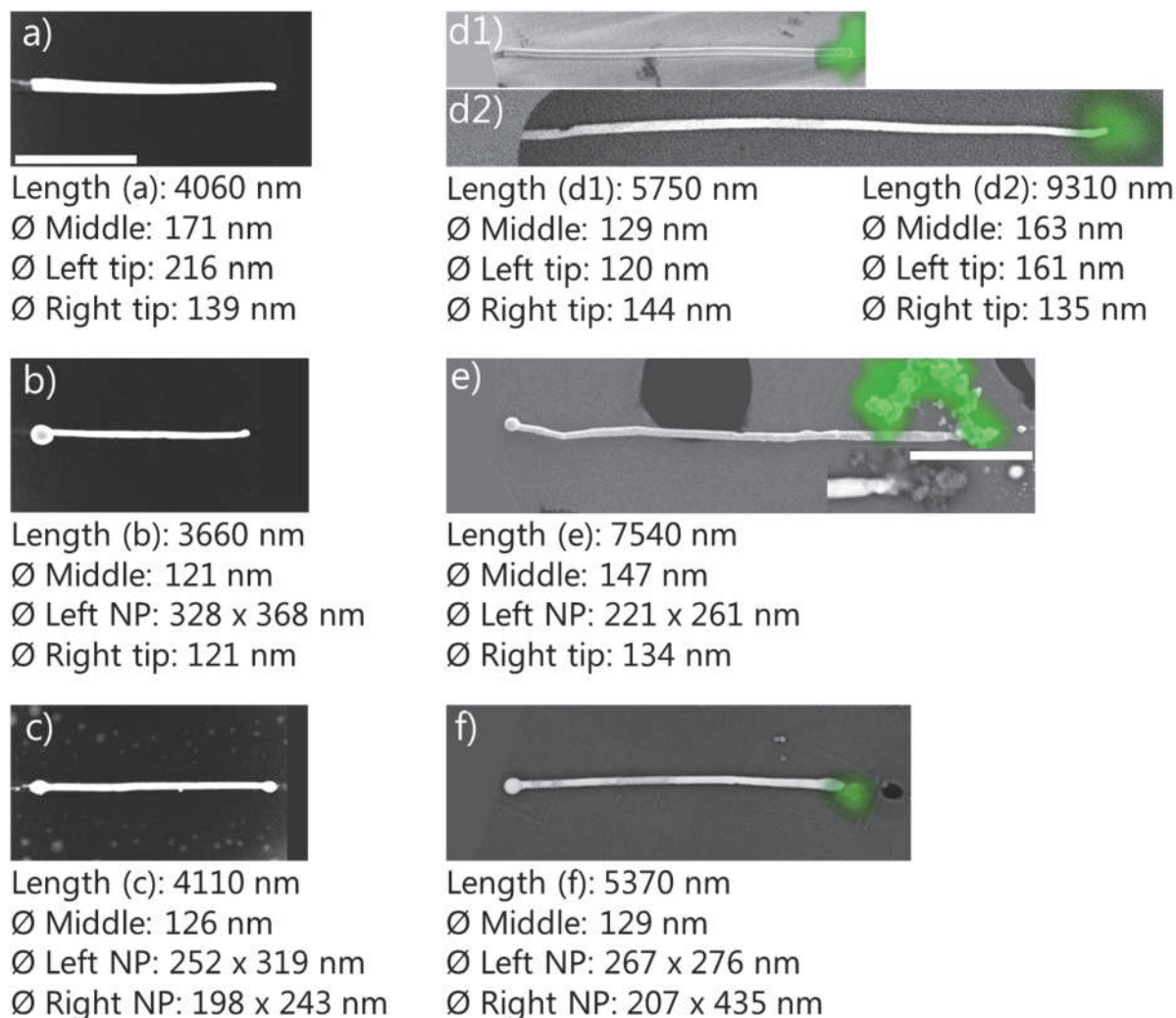


Figure IV.6. Characterization of the nanowires of interest with their characteristic sizes. TEM images of a) single Au nanowire, b) half dog-bone system, c) dog-bone system. SEM images superposed with a Raman mapping of the C=C symmetric stretching PEDOT band of d) Au@PEDOT nanowires of different lengths with PEDOT shell only at one of its tips, e) half dog-bone system with PEDOT particles on the nanowire tip. Inset: Backscattered electrons image of the nanowire tip without Au nanoparticle covered with PEDOT particles. f) Dog-bone system with PEDOT particles on one of its nanoparticles. Scale bar is 2 μ m and is effective for all the images unless for the inset where the scale bar is 1 μ m.

The last important remark concerns the PEDOT particles-containing dog-bone system (Figure IV.6f). First, when mapping this nanosystem we observed the signature of PEDOT both at one of its tips and in the middle of it. We then performed a PEDOT laser dry etching at the undesirable PEDOT particle that should be located in the middle of it. The PEDOT signal then disappeared and afterwards by SEM we did not observe any PEDOT particle in that area. Secondly, in some cases, the Au laser dry heating process

concentrated so highly the energy in one point that even the SiO_x support could be degraded, as we can see in this case where a hole was produced.

IV.3. Laser nano-reflectance of advanced gold nanowires

Measuring the reflectance of individual nano-objects is quite challenging. Reflectance spectroscopy requires to sweep the wavelength of the excitation probe. White sources are generally used, not lasers. Our objective was to exploit our experimental set-up conceived for Raman mapping coupled to a nano-piezoelectric stage to measure the reflectance cartography of individual nano-objects at a given wavelength. This technique can be called nano-reflectance or laser nano-reflectance to explain the monochromatic nature of the source.

In this Part, we describe the system and the procedure to make such measurements. Then, the laser nano-reflectance study of a Au nanowire, a half dog-bone nanowire and a dog-bone nanowire are reported. The analysis of the reflectance mappings allowed to reveal specific optical behaviours of the nanowires and to qualify the benefits of the gold nanoparticles located at one tip, or the two tips of the nanowire. Another objective consists in comparing our results with the ones obtained by a low-loss EELS study of the same nanowires to get complementary information about their plasmonic behaviour.

IV.3.1. Methodology

The nano-reflectance experiments were carried out in the Renishaw InVia™ Raman spectrometer that we described in Chapter III for the characterization of PEDOT-containing nanowires (Figure IV.7a). Some changes were required to get access to this configuration: the Rayleigh rejection filters were changed by a block containing mirrors and filters that allowed the pass of the Rayleigh signal (Figure IV.7b&c). In this block, instead of two edge filters, there is first a beam splitter. After this beam splitter, there is a neutral optical density filter that protects the CCD camera from the incoming reflectance signal, as it would be too intense.

The optical alignment of the instrument in Rayleigh mode was analogous than for the Raman mode explained in Chapter III. The main difference resides that in this case, there is only one block for all the wavelengths and the left and manual mirrors should be realigned and optimized for each laser wavelength.

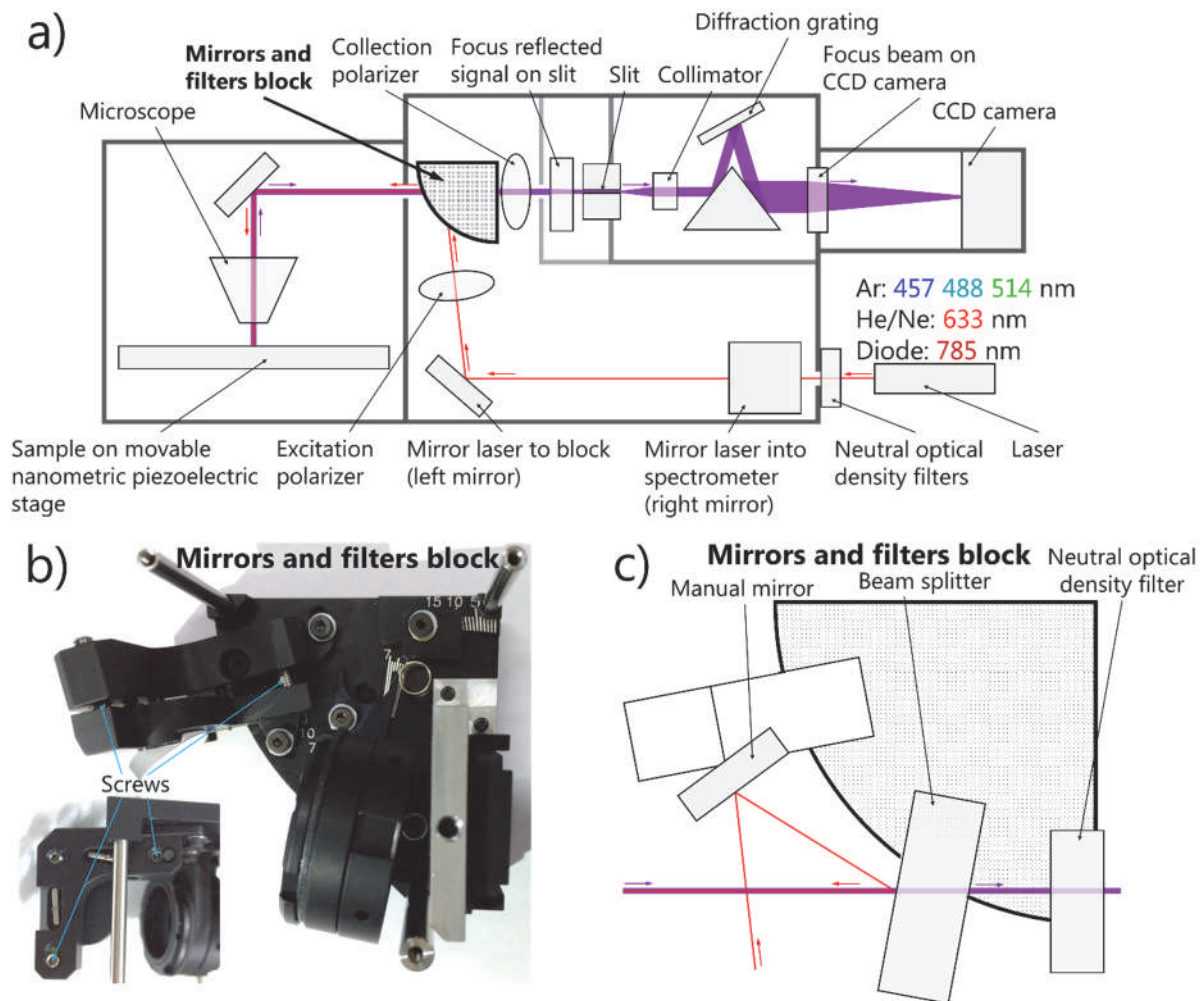


Figure IV.7. a) Schema of Renishaw InVia™ micro-spectrometer in Rayleigh configuration. b) Open mirrors and filters block and c) schematic view of b).

We should note that in order to perform more reproducible experiments and to avoid sources of error, we performed the different polarization measurements by rotating the nanowires 90 degrees and not by introducing in the beam path a half-wave plate. This could be easily done thank to the SEM holder for TEM grids that was mounted in a hole covered with an antivibration foam of the piezoelectric stage and could be rotated around its axis.

The measurement conditions were the following. A long frontal distance objective x100 with a numerical aperture of 0.8 has been used for all the study. For the 633 nm laser excitation, 10 nW were allowed to reach the sample by using neutral optical density filters and 0.1 second was needed as an acquisition time with "orthogonal" polarization. In the case of the 785 nm laser, the power allowed to arrive to the sample was 0.025 nW with a similar acquisition time (0.1 second) with "normal" polarization. The "orthogonal" and "normal" polarizations are the two different polarizations that we could set for the excitation beam. The "orthogonal" polarization arrived with a beam

polarized vertically when regarding the sample form above and the “normal” with a horizontal polarization. The polarization was maintained for all the experiments for a given wavelength and we rotated the nanowires as described before. Thus, the measured intensity for both polarizations can be compared straightforwardly. The intensity map was obtained with measurements achieved every 30 nm in x and y axis to get 10000 to 20000 points, typically.

We described in Chapter III some drawbacks related to this Raman spectrometer. The principal one that we should take into account when performing these nano-reflectance experiments was the spatial drift that could be caused by different environmental factors. We observed this drift in all the three directions, being more common in z. This drift was minimized by installing the piezo-stage the day before and by a warm-up period of the system for at least one hour before the measurements.

We could consider the long duration of every mapping experiment (around 4 hours) as another drawback. This forced us to use the spectrometer for full weeks in order to be under similar conditions. The prototype state of the piezoelectric control and WiRe coupling software developed by our Renishaw partner (Dominik J. Winterauer, Tim Batten) made that sometimes, a bug appeared and the mapping experiment suddenly failed. Our discussion and great feedback from the developers allowed us to minimize this problem.

IV.3.2. Results

The signal measured by this method is a narrow peak centred at the same wavelength than the excitation beam. We focused our analysis on the intensity of this peak.

The experiments consisted in mapping the laser nano-reflectance of our nano-systems. A laser excited the sample and a piezoelectric stage moved it simultaneously, while a CCD camera recorded the reflectance signal for each point. By fitting the signal with a Lorentzian curve at each point and studying its intensity, we could build a 3 dimensional map with the x and y spatial dimensions and the intensity of the reflectance signal.

It is important to mention that the number of nanowires measured in each case was not large enough to make a complete statistic study. In order to explain the results that we obtain. From a broader point of view, it would be required to study more nanowires with similar characteristics to confirm this exploratory work.

We must note that the results obtained with the 785 nm laser excitation can be perfectly fitted with a Lorentzian curve. But for the 633 nm excitation line the Lorentzian fitting could partly fail, so their analysis consisted in measuring the signal to baseline.

An important point for this analysis was the spatial correlation between the TEM imaging and the nano-reflectance map. The size of the maps was strictly respected

with the step in x and y directions and put in relation with the size of the SEM/TEM images. We observed that intensities maxima correspond to a larger Au nanoparticle or a larger diameter. We then used it as a mark to correlate and place the maps. We observed that all the other nanowire features fitted well with the intensity map.

Twelve individual maps were measured, corresponding to 3 kind of nanowires, 2 wavelengths (633 and 785 nm) and to parallel (longitudinal) and perpendicular (transversal) polarization for each nanowire (Appendix II). In these experiments, only the excitation beam was polarized and no polarizer was placed at the collection beam. These results are presented and analysed to determine the effect of:

- The morphology of the nanowire
- The polarisation of the excitation and the collection
- The excitation wavelength.

IV.3.2.1. Effect of the morphology

Here, the profile of the maximum reflectance intensities measured along the nanowires is shown for allowing a precise analysis (Figure IV.8).

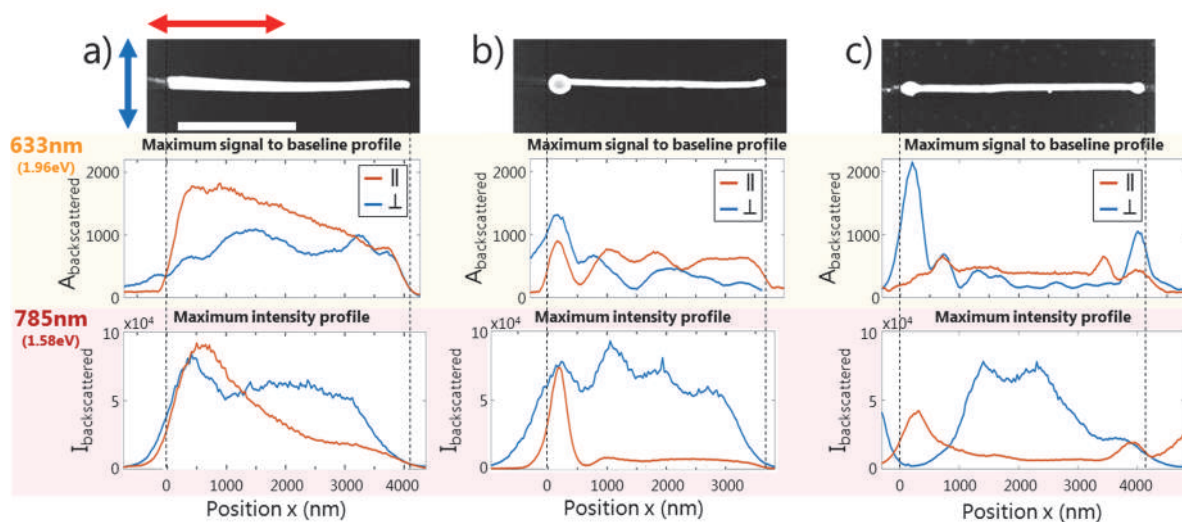


Figure IV.8. TEM images and maximum intensity (signal to baseline for 633 nm and Lorentzian fit for 785 nm) longitudinal profiles for parallel (red line) and perpendicular (blue line) polarization at 633 nm or 785 nm as excitation wavelengths. a) Single Au nanowire, b) half dog-bone Au nanowire, c) dog-bone Au nanowire. White scale bar corresponds to 2 μ m.

An overview (Figure IV.8) shows a good agreement between the nanowire length and the intensity profile for most cases, considering the overlap of the laser spot with the nanowire. However, a more precise analysis reveals some “apparent” incoherence between the profiles for the two polarizations. While the length has been checked by

a calibration of the piezoelectric stage before running the experiments, the lateral adjustment of each profile with the SEM image can be questioned. For this reason, the analysis proposed at this moment cannot be precisely quantitative. However, the good agreement of the intensity maximum with the centre of each nanoparticle for the dog-bone nanowire suggests an accuracy of about 100 nm along the nanowire axis. Except for the left NP of the dog-bone measured at 785 nm and transversal polarization. This later profile is in fact highly questionable as an intensity maximum is measured at the left-hand side out the nanowire.

A second comment deals with the spatial changes of the intensity measured along a nanowire. They all have the same range of magnitude. This is in apparent contradiction with our observation on the display of a much higher reflection when the laser beam was focused on the Au nanoparticles than on the nanowires. This can be explained by an extreme spatial resolution due to the almost closed slits and CCD camera collected width (Figure AI.2 in Appendix I) which we implemented for these laser nano-reflectance experiments. For the image on display of the optical microscopy, the light scattered in all directions by the nanoparticle appears, while in the performed experiments, only the signal coming from a fraction of the nanoparticle is collected.

In summary, a first analysis indicate that the nanoparticles effectively act as strong scatterers in most cases, but some curious intensity profiles suggest there are additional effects .

IV.3.2.2. Effect of the polarization and the wavelength

A more detailed analysis can be proposed when regarding in details the effect of the polarization for each wavelength and each nanowire. Maps of the signal to baseline has been additionally plotted (Figure IV.9 & Figure IV.10).

Parallel polarization (red line): we can observe that, at 785 nm, the signal intensity appears often related to the size of the metallic area irradiated by the laser beam, as expected. A quantitative analysis gives additional information. In the simple nanowire case, there is a decrease of the diameter from left tip to right tip by a factor ~ 1.6 , while the local intensity maximum decreases by a factor $\sim 5-6$ at 785 nm (Figure IV.9a). For the half dog-bone nanowire, from the left nanoparticle tip (368 nm x 328 nm) to the right tip (diameter), the intensity drops by a factor >7 (Figure IV.9b). For the dog-bone nanowire, from left NP (319 nm x 252 nm) to right, the intensity drops by a factor $\sim 3-4$ (middle, 126 nm diameter) then ~ 2 (right NP: 243 nm x 198 nm) (Figure IV.9c). Thus, a simple analysis based on the irradiated metallic area cannot explain quantitatively such intensity changes. It is still more evident for the measured intensity profiles of the (half) dog-bone nanowires in the parallel polarization for the 633 nm laser probe (Figure IV.10b), while the profile for the simple nanowire is in good relation with the spatial change of its lateral section. At least, the cylindrical shape and the roughly

spherical shape should be considered to include the angular distribution of the reflection which is affected by the size and the shape.

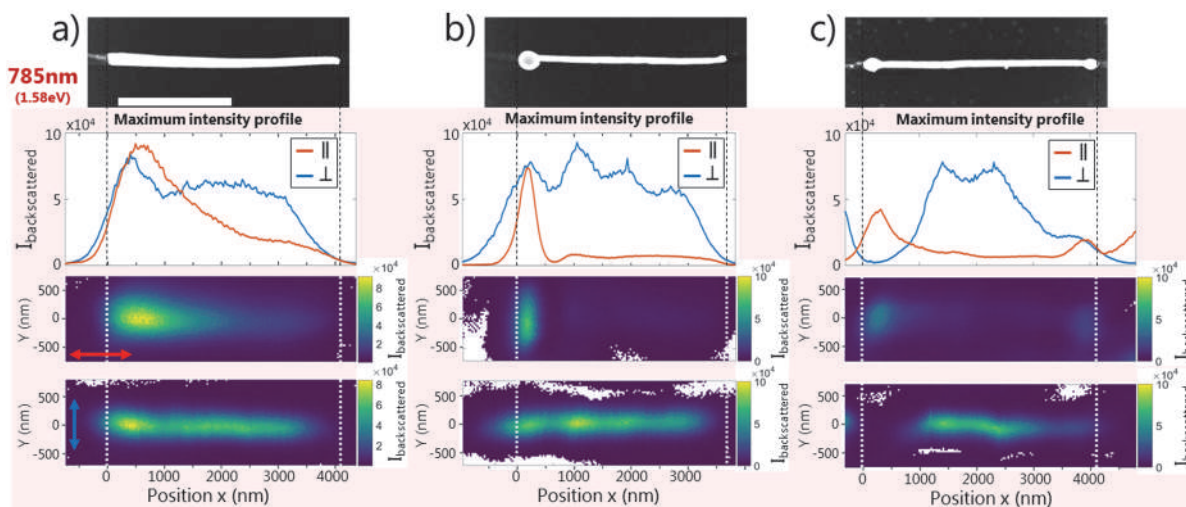


Figure IV.9. $\lambda_{exc} = 785 \text{ nm}$. TEM images, maximum intensity (Lorentzian fit) profiles and intensity heat maps for parallel and perpendicular polarization. a) Single Au nanowire, b) half dog-bone Au nanowire, c) dog-bone Au nanowire. White scale bar corresponds to $2 \mu\text{m}$.

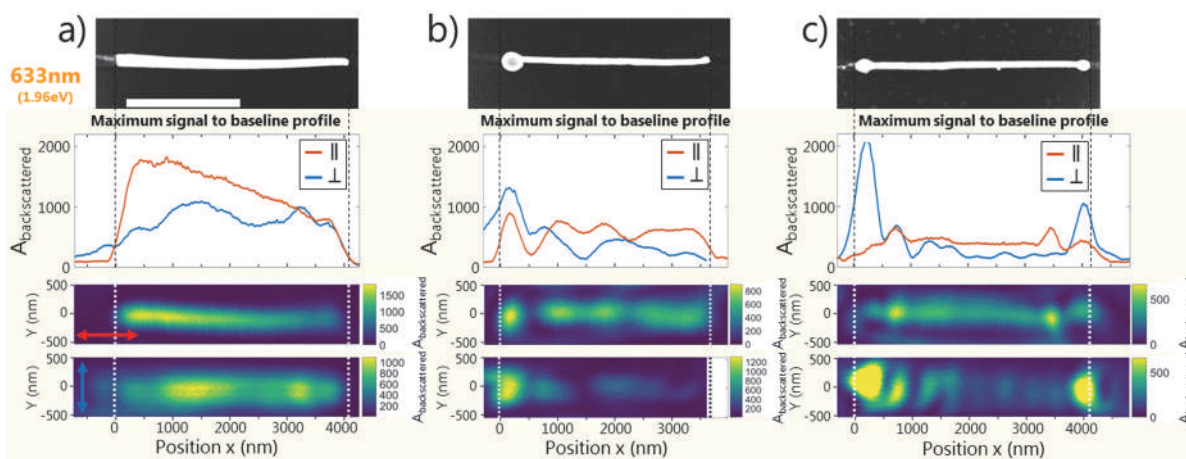


Figure IV.10. $\lambda_{exc} = 633 \text{ nm}$ TEM images, maximum intensity (signal to baseline) profiles and intensity heat maps for parallel and perpendicular polarization. a) Single Au nanowire, b) half dog-bone Au nanowire, c) dog-bone Au nanowire. White scale bar corresponds to $2 \mu\text{m}$.

Perpendicular polarization (blue line): the intensity profiles do not replicate at all the relative changes of the nanowire and nanoparticle shapes. A general tendency is the presence of many intensity variations along the nanostructure, suggesting some

oscillations but no clear period can be identified all along any system. These observations suggest that the excitation of the transversal and longitudinal plasmon modes depends on the polarization of the light. Such modes resonances are directly related to the nanostructure size. In Chapter II, we determined the transversal localized surface plasmon resonance of gold nanowires with resonant wavelength equal to 600 – 620 nm with an average diameter of 100 nm and a length up to 4.4 μm , quite comparable sizes with the three systems investigated here. Thus, the 633 nm excitation laser is expected to get a strongly different behaviour depending on the polarization, with a stronger absorption in parallel than in perpendicular, and hence a smaller reflectance. The comparison of the intensity range for the two polarizations at 633 nm doesn't show a pronounced difference, whatever the system. A first explanation could be that the reflectance measured for this systems is not dominated by T-LSPR. But the difference in the nature of the excitation light (full field non-coherent white lamp versus coherent laser spot focused on a small part of the nanowire) has also to be considered, as it may induce a different interaction with the nanowire.

Clearly, the non-perfect shape of the nanowire (varying diameter) and the presence of non-perfectly spherical nanoparticle(s) at the tip(s) make these systems complex in comparison to the perfect cylinder modelled, as reported in the literature.^{83,85,87,164,165,308}

In summary, the experimental nano-reflectance set-up recently developed in our group has been tested by the first study reported here. The very good signal/noise ratio makes possible to show the richness of the measured behaviours, with a great ability to evidence reflectance variation at a scale much below the micrometric scale. However, the complexity of the real systems investigated here make complicate a clear analysis of the physical mechanisms responsible of the effects measured. The possibility to couple this new system with an atomic force microscope (AFM) or a STM could still improve this powerful nanocharacterization tool.

IV.4. Remote configuration for laser reflectance and Raman spectroscopy

The ultimate goal of my thesis was the study of the plasmon propagation in the systems described before. In order to get a full understanding of their plasmonic behaviour, we performed remote nano-Raman and remote nano-reflectance sensing on the gold-based nanowires, eventually incorporating PEDOT.

The remote techniques for SPP-based systems consist in the excitation of SPP through plasmon-photon coupling on an active site of the sample (the tip of the nanowire or a nanoparticle) and the collection of the signal coming from another active site (the opposite tip or another nanoparticle), while the signal is mediated by SPP along a

waveguide (the nanowire) (Figure IV.1). It is crucial to avoid any parasitic signal coming from other areas of the sample, as the measured signal is expected to be significantly smaller than when excited in direct configuration.

These experiments in remote configuration were performed in the Renishaw InVia™ Raman spectrometer. The switch between the remote laser nano-reflectance and the remote nano-Raman spectroscopy was simply done changing the block, as described before. Thanks to the presence of Renishaw plc in our research network and their constant support and feedback, we could perform this kind of experiments in a rigorous and reproducible manner. We proposed them our suggestion of separating the collection and excitation areas and they proposed us two distinct procedures: either shifting the collection area and remaining unchanged the excitation area, or the opposite, shifting the excitation area and remaining unchanged the collection one (Figure IV.11). We opted for this second option because in that manner, we could optimize in direct mode the more delicate collection area in order to get the signal only from a very narrow point. Such a configuration has been exploited recently by some other groups.^{193,208,228,264,274,278} Afterward we could shift the laser excitation to another point and this optimized collection area would be at the same position. It is emphasized that the off-optical axis shift is small enough to prevent the excitation from a spatial distortion.

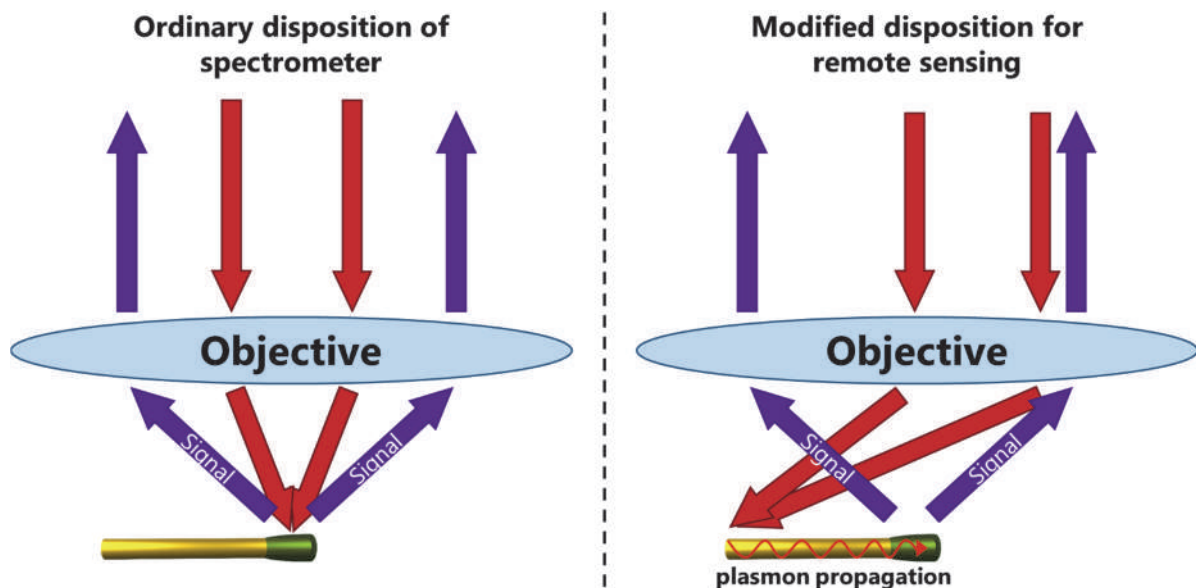


Figure IV.11. Schematic view of the optical configuration (laser source, objective, sample and collected light) for measuring a) the standard and b) the remote signals for the case of the Au@PEDOT nanowire system.²⁰⁸

IV.4.1. Laser excitation shifted from the collection area

First, we proceed as in Chapter III for optimizing both, the laser beam path and the collection area. Once this was done, we should decide where we wanted to shift the laser (normally to the opposite tip of the nanowire) and place the collection zone in the exact position where we will want to collect when offsetting the laser beam. In order to offset the laser point we used first the manual mirror, shifting it twice the desired distance. At this point the laser point has lost its perpendicular incidence respect to the sample. In order to regain it, we should use the left mirror until its verticality is optimal (we noted the position values of the left mirror prior to this step in order to easily put back in direct mode the spectrometer once all our experiments were finished). If the laser point was now placed on the desired area, the offset was successfully done. If not, the previous steps should be repeated until a vertical laser beam is achieved on that area. In order to make an ultimate fine alignment, tiny movements of both left and manual mirror are done until a maximum photon-SPP coupling is observed on the optical image.

One of the most challenging steps was to find the optimal SPP-photon in-coupling position with the excitation beam and, at the same time, be in the optimal SPP-photon out-coupling position for the collection. We first performed this optimization by regarding the live optical microscope video and trying to find the maximum coupling, i.e. intensity with the naked eye. In order to make a more quantitative and reproducible optimization, we then performed this step but in remote nano-reflectance mode: the remote spectra was measured every 0.1 seconds and at the same time, we performed very small movements in the mirrors as described in the previous paragraph and on the sample position with the piezo stage (5 nm steps). The optimal position was found when the intensity of the reflectance signal was maximal.

All these manual operations should be done while minimizing the interaction with the spectrometer as even the process of closing and opening its protective door could change the laser beam path.

We consider important to remark that, in order to get a signal with a high spatial resolution and minimize all the parasitic signals coming from parts of the sample near to our acquisition area, we closed to slit to 20 μm and took only an area of 1 or 2 and 3 pixels wide from the CCD camera for the reflectance and the Raman configurations, respectively. The optimization of this parameters was done prior to the offset of the laser. By closing both the slit and the CCD camera width, we could achieve a very narrow area of collection that should be centred in the collection point represented in the optical image (Figure IV.12).

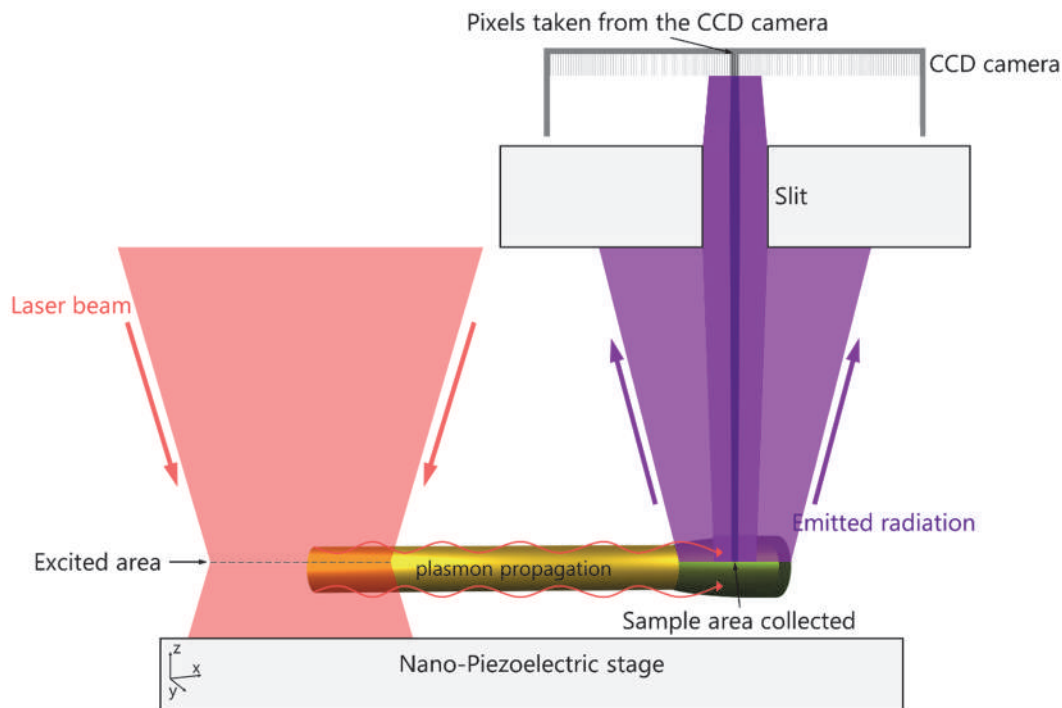


Figure IV.12. Schema of the relation between the customizable parameters of a remote nano-spectrometer and the sample spatial resolution. A Au@PEDOT nanowire is under remote laser excitation (laser beam in red) that irradiates a given area (excited area). The Raman signal produced (emitted radiation in purple) at the opposite nanowire tip is collected on the CCD camera. The spatial resolution (sample area collected) of this collected signal can be tuned by the slit opening and the pixels taken from the CCD camera.

One of the main challenges to overcome was the weakness of the Raman signal. The laser power was restricted to not degrade the PEDOT. Then, in order to obtain strong enough signals due to the very small quantity of PEDOT and the drastic optical configuration, an acquisition time of 200 seconds was required. For the nano-reflectance experiments on pure gold nanostructures, an acquisition time of 0.1 seconds with a much lower laser power was enough to get a strong signal. The main issue that we found concerning the remote laser nano-reflectance experiments deals with some parasitic collected signal coming from the diffracted light by the sample. It is the reason why the slit and the width of the CCD camera were reduced as much as possible, to collect the signal coming from the smaller area and to reject photons coming from elsewhere.

We should remark that in the case of the non-PEDOT containing nano-systems, the desired polarizations parallel or perpendicular to the nanowire was executed by maintaining the same beam polarization and rotating the nanowire. For the PEDOT containing nanosystems we maintained the nanowire alignment and polarized the light

by the use of half-wave plates that could be placed at both the excitation and the collection beam paths. After the introduction of the corresponding correction factors in the second case, both techniques should perform equally.

We first present a qualitative and exploratory study by regarding the optical microscopy images when exciting on one tip of the nanosystem at different wavelengths without the microscope back light (Figure IV.13).

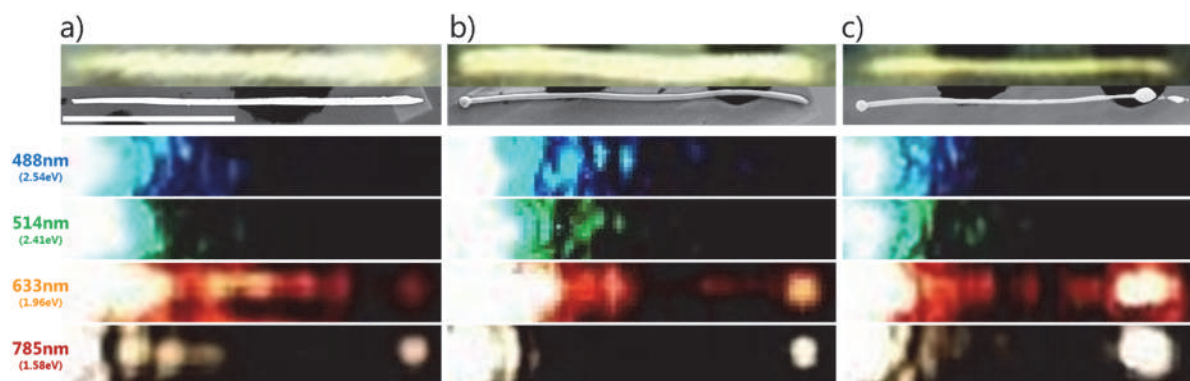


Figure IV.13. From top to bottom: Optical microscopy images, SEM images and optical microscopy images without back light when exciting on the left tip of the nanowires with a parallel polarized laser beam with a wavelength of 488 nm, 514 nm, 633 nm and 785 nm. a) Single Au nanowire system, b) half dog-bone system and c) dog-bone system. All the images of the same excitation wavelength were taking under the same laser and camera conditions. Scale bar is 5 μm and is the same for all the images. Colours are false for the 785 nm case.

Regarding these optical images (Figure IV.13), we could support that the plasmon propagation increases at higher wavelengths. It can be easily observable that in the blue (488 nm) and the green (514 nm) there is no evidence of propagation for any of the systems (no spot at the opposite tip). For the red laser (633 nm), a spot appears at the opposite side from the excitation, an evidence of SPP mediated signal. This remote spot intensity is increased for the infrared exciting laser (785 nm) for a given system. A comparative analysis of the remote spot intensity for the 3 systems shows a more intense spot in presence of a gold nanoparticle at the excitation, and still more intense with a nanoparticle at the out coupling. However, such a comparison can be criticised because it assumes that the optimal position for the excitation, i.e. SPP coupling has been achieved. In practical, the measurements were done for the coupling position that gives the more intense remote signal, in the limit of the lateral positioning.

IV.4.2. Remote laser nano-reflectance

A more quantitative experiment was required in order to univocally study the effect of these gold nanoparticles for the coupling with SPP and the propagation toward the

opposite tip. By means of the remote nano-reflectance, we measured the intensity of light that arrived to the opposite tip of the nanowires. All the experimental parameters were kept equal for the three nano-systems and for the parallel and perpendicular polarizations of light (polarizer at excitation, no polarizer at the collection). Each reflectance intensity was measured at least three times on the same point in direct and in remote configuration. No change was observed for all the cases.

In order to always maintain the same referential system, we label a the left tip of the nanowire, and b the right tip (Figure IV.14, Figure IV.15 & Figure IV.16). For a set of comparison, the intensities measured in direct and remote modes are reported on the left part of the figures. In direct mode, we measured the reflected intensity when exciting and collecting at the same point, a or b . In the remote configuration (right part of the figures), the excitation was applied at a , and then the collection measured at b ($a \rightarrow b$) or the opposite, excitation at b and collection from a ($b \rightarrow a$). We performed this experiments with a unique excitation source, the 785 nm diode laser. The laser power was 0.025 nW and the acquisition time 0.1 second for both direct and remote configurations. The reflectance scale of the three figures below is strictly the same for the three kinds of nanowires in the direct configuration (maximum at 3.7×10^4) or in the remote configuration (maximum at 0.7×10^4).

Simple nanowire case (Figure IV.14)

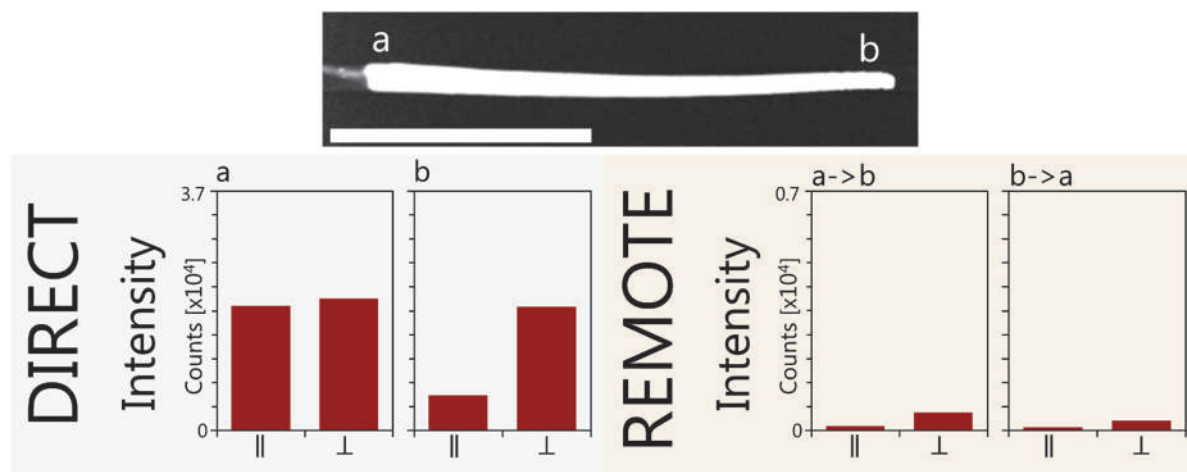


Figure IV.14. Remote nano-reflectance experiments. TEM image of the simple Au nanowire studied. Left: nano-reflectance measured in direct mode for the two polarizations of the excited light. Right: nano-reflectance measured in remote mode for the two polarizations of the excited light ($a \rightarrow b$: exciting on a and collecting on b ; $b \rightarrow a$: exciting on b and collecting on a). $\lambda_{exc} = 785 \text{ nm}$; polarization only at the excitation; scale bar = $2 \mu\text{m}$.

Half dog-bone nanowire case (Figure IV.15)

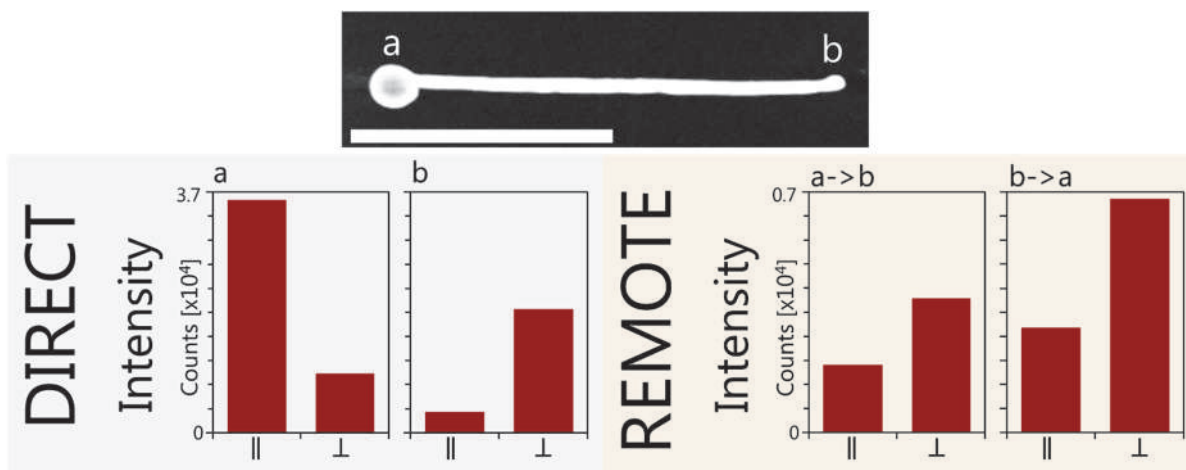


Figure IV.15. Remote nano-reflectance experiments. TEM image of the gold half dog-bone nanowire studied. Left: nano-reflectance measured in direct mode for the two polarizations of the excited light. Right: nano-reflectance measured in remote mode for the two polarizations of the excited light (a → b: exciting on a and collecting on b; b → a: exciting on b and collecting on a). $\lambda_{exc} = 785 \text{ nm}$; polarization only at the excitation; scale bar = $2 \mu\text{m}$.

Dog-bone nanowire case (Figure IV.16)

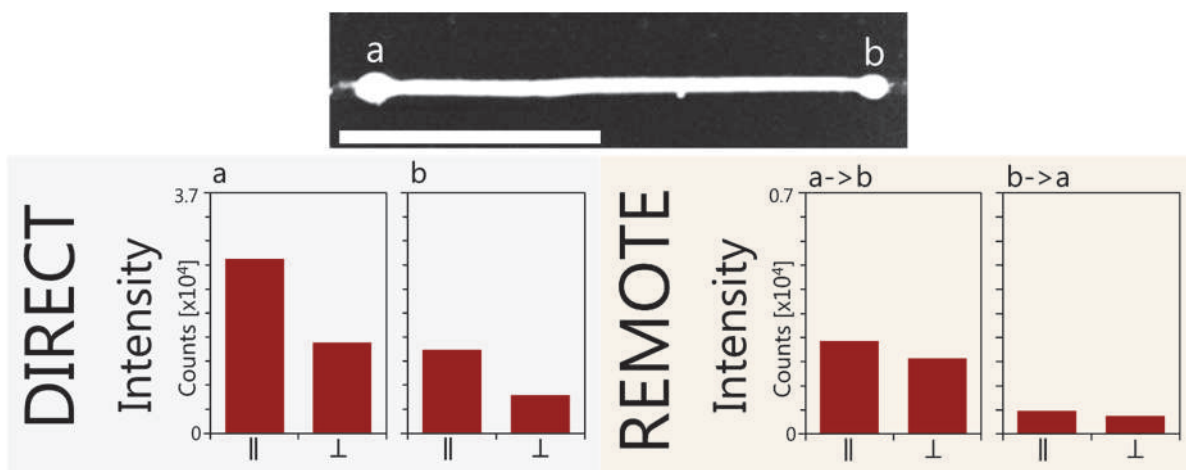


Figure IV.16. Remote nano-reflectance experiments. TEM image of the gold dog-bone nanowire studied. Left: nano-reflectance measured in direct mode for the two polarizations of the excited light. Right: nano-reflectance measured in remote mode for the two polarizations of the excited light (a → b: exciting on a and collecting on b; b → a: exciting on b and collecting on a). $\lambda_{exc} = 785 \text{ nm}$; polarization only at the excitation; scale bar = $2 \mu\text{m}$.

IV.4.2.1. Analysis for the Direct configuration.

A general comment can be done by comparing the measured reflectance intensities for the direct configuration with the reflectance intensity profiles measured and reported in the previous part. As it was also measured in the direct configuration, we could expect a similar proportion between the intensity measured with a parallel (I_{\parallel}) and with a perpendicular (I_{\perp}) polarization. The direct measurements were done at the position at the nanowire tip where the maximum of signal was transmitted to the opposite, i.e. the maximum in-coupling (adjustments made regarding the display as in this configuration it is impossible to know quantitatively the remote signal). We could suggest that for this reason in some cases, as in the dog-bone nanowire, the proportion between I_{\parallel} and I_{\perp} between both studies differs.

Considering that the measurement was done at the position where the maximum of scattered signal was observed, we could consider the intensity maximum close to each tip for the maps. On one hand, a similar proportion between I_L and I_T between both studies can be obtained for the simple nanowire in position a and for the half dog-bone on position b . For the four other positions, a strongly different proportion between the two polarizations is obtained. This comparison suggests that our hypothesis to consider the intensity maximum close from each tip on the maps (previous study) as the I_{\max} position in this second study is wrong.

IV.4.2.2. Analysis for the Remote configuration

- For the simple nanowire (Figure IV.14), the remote signal is systematically much weaker than the one measured in a direct configuration. This result was expected and it can be attributed to two mechanisms: (i) the coupling efficiency at the excitation and the out-coupling with the SPP, and (ii) the losses of SPP along the $4\mu\text{m}$. The small difference between the parallel and perpendicular polarization is considered as too small to be further analysed.

- For the half dog-bone nanowire (Figure IV.15), the remote signal is very strong in the four configurations, which contrasts drastically with the simple nanowire case. Despite an enhancement factor cannot be estimated, it is interesting to compare the intensity ratio between the intensity measured on the same point (a or b) in remote configuration over the one measured in direct. The direct reflectance indicates the ability to irradiate for the tip considered, depending on its size and shape and of course of the size of the incident beam. The remote intensity depends on the coupling efficiency at the opposite tip, the propagating losses of SPP, and the geometry of the tip which acts for the out-coupling. It gives the following values:

Position a :

Parallel $I(b \rightarrow a)/I(a) = 0.31/3.6 = 0.086$

Perpendicular $I(b \rightarrow a)/I(a) = 0.68/0.91 = 0.75$

Position b :

Parallel $I(a \rightarrow b)/I(b) = 0.20/0.33 = 0.61$

Perpendicular $I(a \rightarrow b)/I(b) = 0.39/0.19 = 0.21$

In these conditions, it seems remarkable to get so large intensity ratios, while the values estimated for the simple nanowire are no larger than 0.03. It can thus be deduced that the large gold nanoparticle at a tip of the nanowire strongly enhances the in- and the out-coupling with the SPP. More precisely, the gold nanoparticle enhances much more the out-coupling for the transverse polarization and the in-coupling for the longitudinal polarization.

- For the dog-bone nanowire (Figure IV.16), a first observation on the intensity values shows that they are intermediate between the very low remote signal for the simple nanowire and the strong remote signal for the half dog-bone. In addition, the left nanoparticle (position a : a little bit larger than the right b nanoparticle) gives a larger scattered light in direct mode than the right one, whatever the polarization. In remote configuration, the same tendency is observed considering the excitation, with the measured reflectance intensity at the remote position. It is larger for an excitation in the left one and the collection on the right one $a \rightarrow b$ than for $b \rightarrow a$. This result contrasts with the study of the half dog-bone.

To summarize, this study has shown that the half dog-bone is the more efficient system, among the three ones, to get a more intense signal in the remote configuration when exciting on its nanowire tip and collecting on the nanoparticle. The addition of a second nanoparticle did not apparently improve the out-coupling. The effect of the polarization of the excitation beam is not trivial, depending on the system. Previous experiments and modelling on cylindrical nanowires have shown that a longitudinal polarization permits to obtain a larger remote intensity than a perpendicular one.^{91,155,195,205,213,243} Such a phenomenon can be attributed to a more efficient coupling with the SPP propagating along the nanowire, while a transversally polarized excitation interacts preferentially with non-propagating transversal localized plasmons. The presence of a nanoparticle with a diameter larger than the nanowire diameter at a tip may open new opportunity for momentum matching, a required condition to excite SPP.

As a conclusion, a nanoparticle located at a tip acts as a special antenna which seems to open multidirectionality to the in- and out-coupling with SPP. It can also modify the effect of the polarization behaviour of the nanowire. A modelling of our system by a

finite element method solving the Maxwell equations is required to further explain these effects. Indeed, our systems have an unusual morphology. If we assume the gold nanoparticle (roughly spherical with the same diameter) as isolated from the nanowire, the absorption of light at the resonance is expected to be weak in comparison to the scattered light, according to Mie theory. It is proposed that dipolar and multipolar plasmon modes could coexist in these systems, thus promoting complex configuration depending on the polarization. It is also important to remind that the excitation point was chosen by looking for the coupling and propagation maximum and it could not always totally correspond with the exact tip of the nanowires. A better set-up should require to move independently the laser probe objective (or optical fibre) and the collecting lens with nanometric steps, in order to optimize the finding of the maximum coupling and propagation spot. This would allow of making remote intensity mappings and thus the correct finding of the optimal coupling spot. Our colleague J.Y. Mevellec has developed during my thesis such an experimental set-up on a Jobin-Yvon spectrometer. However, different preliminary experiments in remote configuration have shown that some vibrations produced instabilities and a drift of the sample - laser relative position. No solution has been identified up to now.

Finally, we consider that the modelling of these systems by finite elements would greatly enhance our understanding. It could validate the possible hypothesis considered in view of the experimental plasmonic behaviour.

IV.4.3. Remote nano-Raman spectroscopy

The last exploration of the SPP coupling and propagation in nanowire systems is related to the remote nano-Raman spectroscopy. This technique is analogous to the remote nano-reflectance spectroscopy developed in the previous Chapter, but the signal analysed in a remote place comes from a Raman emission instead of a reflectance one.

IV.4.3.1. Proof of concept

The nanowires developed to explore this phenomenon includes a Raman active species at one of the SPP-photon coupling points. If the Raman active species is placed at the opposite side from the laser excitation, it can interact directly with the enhanced field at the tip, or indirectly through a photon emitted by the out-coupling tip. It thus presents some analogies with the SERS effect. The objective utilized was the same as in the nano-reflectance experiments, a long focal objective with an optical aperture of 0.8. The laser power used depends on the laser excitation source and the nature of PEDOT as reported in Chapter III (Figure AI.1), and the acquisition time was fixed at 200 seconds, in order to have an intense enough signal.

We carried out the preliminary studies of remote nano-Raman always using parallel polarized light with a wavelength of 785 nm, which gives the longer SPP length in gold than the other accessible laser wavelengths. The excitation is provided at the gold tip, which do not possess PEDOT, i.e. the Au@PEDOT nanowire with PEDOT only at one of the tips (Figure IV.2d & Figure IV.17a).

In order to validate our analysis and prevent from a parasitic PEDOT Raman signal, we used systematically the same method, consisting in focusing the laser at four different positions and measuring the Raman signal, while maintaining the collection area on the PEDOT containing tip as we already proceeded in the remote nano-reflectance measurements (Figure IV.17a): 1) excitation at the PEDOT-containing tip (standard direct measurement configuration), 2) excitation on the SiO_x grid at a distance equal or lower than the nanowire length (about 9.2 μm) from the coaxial tip, 3) excitation of the nanowire at around 2 μm from the Au tip onto the nanowire, 4) excitation precisely at the gold tip.

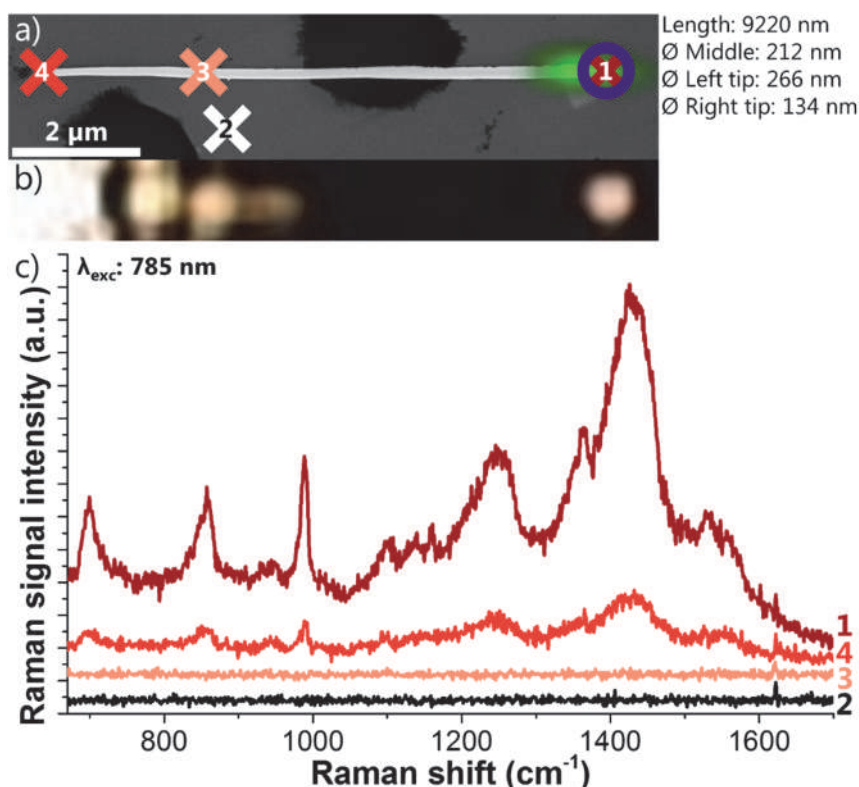


Figure IV.17. a) SEM view with superposed Raman spectroscopy mapping (intensity at 1447 cm⁻¹ appears green) of a single gold nanowire partially covered with PEDOT close to its right tip and four excitation configurations (X symbol labelled 1 to 4) and maintained collection area (O) of the Raman signal plotted in (c) at 785 nm. b) Optical microscopy image without back light when exciting in position 4 with a laser at 785 nm (objective x100 LF). c) Raman spectra measured in the position 1 for the 4 different excitation positions.

The positions (2) and (3) allowed to discriminate the remote plasmon-mediated effect from a parasitic excitation of PEDOT, coming directly from the laser beam or by its scattering by the nanowire (position (3)), or from the supporting silica grid (position (2)). A fifth measurement (spectrum not shown) in the direct mode was systematically done in order to check that the PEDOT signal did not suffer any degradation.

In the first configuration (direct mode), the typical PEDOT spectrum was measured, with the main C=C symmetric stretching band around 1420 - 1430 cm^{-1} . In the fourth position (remote geometry), a similar spectrum was measured but with a smaller intensity, as expected due to the coupling efficiency of the laser with the gold nanowire to excite SPP, to plasmonic losses when propagating along the nanowire, and possibly to the excitation of the Raman scattering. The latter case could be source of enhancement, rather than quenching of the Raman intensity, as further discussed later. No signature of PEDOT was detected, neither in the second, nor in the third configuration of measurement. These results unambiguously showed that the Raman signal detected when exciting the Au tip is due to a stimulation of PEDOT via the surface plasmon polaritons after their propagation along the gold nanowire, i.e. remote Raman signal (Figure IV.17). This preliminary study opened us the way to investigate longer nanowires and design the new architectures (half dog-bone and dog-bone nanowires).

We then carried out remote nano-Raman experiments with the four different PEDOT-containing systems obtained, under the four available laser wavelengths (488, 514, 633 and 785 nm) and with light polarized perpendicularly or parallel to the main axis of the nanowires. With this equipment, we could separately polarize the excitation and collection beams, in order to get a full understanding of the optical and plasmonic anisotropy of our systems. Nevertheless, we performed crossed polarization studies only with the PEDOT containing systems and in some cases the Raman signal was so weak that we could not get any reproducible results. For this reason, we could not make a complete study of the crossed-polarization phenomena.

The analysis of the Raman bands was done by fitting the Raman signal to Lorentz curves. The effect of the parameters (wavelength, polarization) was determined by comparing the intensity of the symmetric C=C stretching band with its maximum between 1420 and 1450 cm^{-1} (depending on the excitation wavelength). Because of the somehow weak signal measured in some cases, we could not perform a spectral analysis comparison of the shape and position of the different Raman bands, but just compare the intensity of the main band.

In the reflectance study, the signals measured for the different systems always have the same order of magnitude. For this reason we could analyse, treat and compare directly the raw signals. In the case of the Raman signal, it depends on the quantity of active species (PEDOT) in the nanosystem and on plasmonic assisted interactions. The

difference of the Raman signal between the different systems could thus differ in orders of magnitude. This effect was increased due to the utilization of two different PEDOT species: the electropolymerized PEDOT and the commercial PEDOT particles. The laser power used for the experiments containing these different species was not the same in order to not to destroy the PEDOT particles.

For these reasons we always normalized the PEDOT signal obtained dividing it by the sum of the PEDOT signals in direct mode for parallel and perpendicular configurations for that wavelength and that system (Equation (IV.1)):

$$I_{n\lambda}^{Normalized} = \frac{I_n^\lambda}{I_{direct\parallel}^\lambda + I_{direct\perp}^\lambda} \quad (IV.1)$$

where I_x^λ is the symmetric C=C stretching band height of a experiment n (which can be remote or direct, or parallel or perpendicularly polarized) performed at a given wavelength λ and in a given system and thus $I_{direct\parallel}^\lambda$ and $I_{direct\perp}^\lambda$ are these intensities for the direct parallel and direct perpendicular polarization modes, respectively, at this λ_{exc} and in the same position.

The systematic remote nano-Raman studies of the four nanostructures were performed analogously to the remote nano-reflectance spectroscopy defined before. We placed the nanowires in a perfect horizontal disposition with the PEDOT-containing tip on the right and defined its left tip as a and its right tip as b . Then, we carried out the distinct direct and remote configurations. In this mode, we only analysed as direct the direct nano-Raman on b , as in a there is no PEDOT and if we got any signal there would be due to the remote detection of the PEDOT in b . Then, the three remote modes were, exciting on the non-PEDOT containing tip a and detection from the PEDOT containing b , excitation on b and collection from a and excitation, and collection in a , in order to see if any back-an-forth signal could be recovered.

We should note that the intensities for 488 nm and 514 nm are never plotted in remote mode in any of the cases as we never obtained remote nano-Raman signal when exciting at those wavelengths.

It is also important to note that in these experiments, we did not present the enhancement factor as conclusion in the end as in the remote laser nano-reflectance experiments due to the different characteristics of the nanowires presented (length, PEDOT shell vs PEDOT particles, kinked and bent tips) and the fact that in some cases the Raman signal was 0. For that reason we analysed the nanowires one per one as we present in this section.

Final remark, such experiments were done and even repeated in different days and similar results were measured. It confirms the robustness of the results reported here.

IV.4.3.2. Simple gold nanowires of different lengths

The first system studied was the short Au@PEDOT nanowire (5.8 μm) with PEDOT only at one of their tips (Figure IV.18). We expected to get a higher remote relative signal than in the preliminary case, as the SPP would propagate less distance and thus its losses would be minimized.

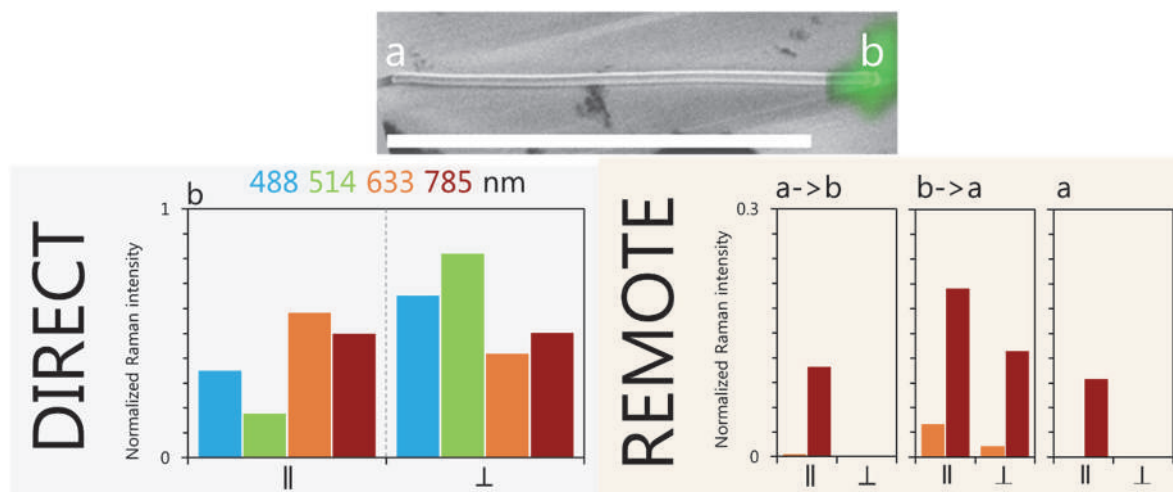


Figure IV.18. Study of a 5.8 μm long Au(\varnothing 120 - 144 nm)@PEDOT nanowire. Top: SEM images with superposed Raman mapping signal for the C=C symmetric stretching PEDOT band. Point a corresponds to the left tip (no PEDOT) and point b to the right tip (PEDOT). Scale bar is 5 μm . Bottom: Normalized Raman intensity (defined in (Equation (IV.1))) of the C=C symmetric stretching PEDOT band in different configurations. Direct on b for 4 different λ_{exc} wavelengths 488 nm (blue), 514 nm (green), 633 nm (orange) and 785 nm (dark red). Remote on b (a->b), remote on a (b->a), direct on a (suggesting a->b->a) for λ_{exc} = 633 nm (orange) and 785 nm (dark red). No signal was obtained in remote mode for 488 nm and 514 nm. Polarization parallel (||) or perpendicular (\perp) only at the excitation.

We first analyse the results of the study in the direct configuration for the four laser wavelengths. A larger normalized intensity is measured for excitation at 488 nm and 514 nm, while no clear preferential orientation is evidenced when the excitation at 633 nm and 785 nm. This result is quite similar with the detailed study of other coaxial nanowires reported in Chapter III. The preferential orientation of the shorter PEDOT chains perpendicular to the nanowire axis, as induced by the ultra-confined electropolymerization, can explain this result.

For the remote configuration, no signal is observed when exciting at 488 nm and 514 nm in any case. But at 633 nm some interesting features start to appear. For (a->b): a tiny Raman signal is measured when irradiating in the non-PEDOT-containing tip (position a) with a parallel-polarized laser and collecting at the tip covered with PEDOT

(position b). This signal is thus mediated by the SPP. For ($b \rightarrow a$) and parallel polarization at excitation, when exciting on the PEDOT-containing tip and collecting at the opposite tip, the measured normalized signal was more than 12 times larger than for ($a \rightarrow b$). We even obtained PEDOT signal when exciting with perpendicular polarization.

For the excitation at 785 nm, the normalized intensities obtained for the remote configurations are much larger than for the 633 nm case (Figure IV.18). The intensities are larger for $b \rightarrow a$ than for $a \rightarrow b$. Most spectacularly, for the parallel polarization, a Raman signal was measured in the direct configuration on a , while there is no PEDOT at this place. So, it strongly suggests a back-and-forth SPP-mediated process, i.e. excitation of SPP at a , propagation of SPP toward b , excitation of Raman signal of PEDOT, coupling with SPP that back-propagate the Raman signal to a . Such a phenomenon has been previously evidenced.²⁶⁴

We propose that the above-described effects are possible because of the wavelength dependence of SPP propagation. Indeed, although the excitation wavelength is at 633 nm (same mechanism can be transposed for the 785 nm case), the Raman Stokes shift signal emitted at 1430 cm^{-1} is actually at 696 nm. It is known that a SPP in gold better propagates for a larger wavelength above 500 nm. So the SPP propagation length of this 1430 cm^{-1} Raman band is larger at 696 nm than the one for the 633 nm laser. It can thus contribute to a recorded more intense Raman band. The stronger remote intensities measured for laser excitation at 785 nm than at 633 nm, as well as the back-and-forth signal measured in the position a only for 785 nm strongly support this mechanism.

The next structure studied was a similar but longer (9.3 μm) Au@PEDOT nanowire with PEDOT only at one tip (placed on the right) (Figure IV.19). A smaller remote Raman signal due to SPP propagation losses is expected. The SEM analysis shows a kink near the left tip and a curvature of the right tip, that could create hotspots and impact the SPP propagation and so the emitted signal.

For the direct configuration, a stronger signal was measured in transversal than in longitudinal polarization for the four laser wavelengths. When exciting and collecting directly on the tip b at any of the excitation wavelengths, we observed the typical preferential PEDOT chains perpendicular orientation described in Chapter III.

In the remote configuration, as in the previous nanowire, no signal was detected when exciting with 488 or 514 nm lasers. This means that the propagation losses along the nanowire at those wavelengths are too large. The same mechanism can explain that, at $\lambda_{\text{exc}} = 785 \text{ nm}$, the $a \rightarrow b$ remote signal appears 14 times smaller than the direct measurement in b , instead of a decrease by a factor 5 for the shorter NW.

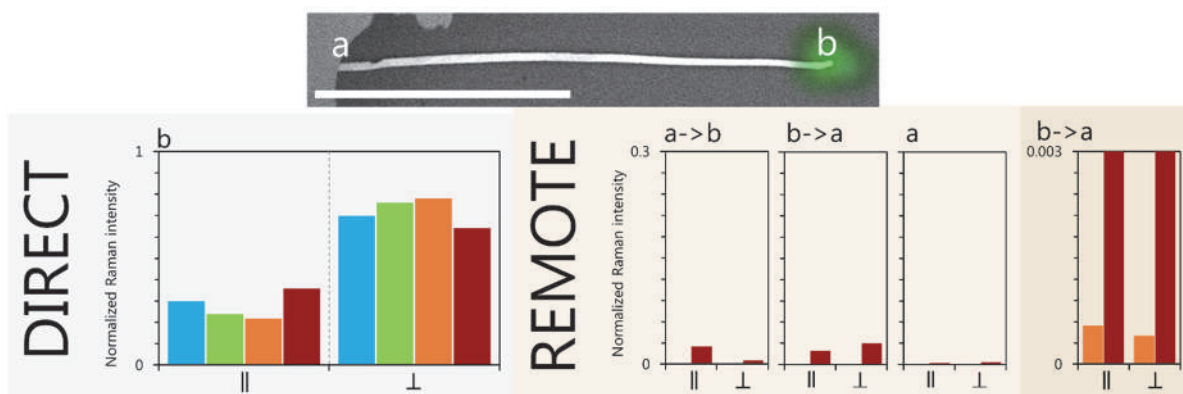


Figure IV.19. Study of a 9.3 μm long Au(\varnothing 161-135 nm)@PEDOT nanowire. Top: SEM images with superposed Raman mapping for the C=C symmetric stretching PEDOT band (PEDOT appears green). Point a corresponds to the left tip (no PEDOT) and point b to the right tip (PEDOT). Scale bar is 5 μm . Bottom: Normalized Raman intensity (defined in (Equation (IV.1))) of the C=C symmetric stretching PEDOT band in different configurations. Direct on b for 4 different λ_{exc} wavelengths 488 nm (blue), 514 nm (green), 633 nm (orange) and 785 nm (dark red). Remote on b (a->b), remote on a (b->a), direct on a (suggesting a->b->a) for λ_{exc} = 633 nm (orange) and 785 nm (dark red). Right: modified vertical axis for the b->a case. No signal was obtained in remote mode for 488 nm and 514 nm. Polarization parallel (||) or perpendicular (\perp) only at the excitation.

It can also be noted that a signal was measured for the perpendicular polarization for $a \rightarrow b$, in contrary to the previous NW. Moreover, the $b \rightarrow a$ signal is larger in perpendicular than in parallel polarization. The later effect suggests that the curved tip b helps for exciting the SPP with a perpendicularly polarized excitation.

IV.4.3.3. Half dog-bone nanowire with PEDOT particles on one tip

The next system is the half dog-bone 7.5 μm long Au nanowire with commercial PEDOT particles dispersed around and on the right tip (no Au nanoparticle), as PEDOT cannot be electropolymerized after dispersing the NW (Figure IV.20). The effect of the gold nanoparticle on the remote Raman signal is investigated. But the partial break of the NW close to the left tip should significantly affect the plasmonic behaviour and consequently the Raman scattering. Because of the degradation of these PEDOT nanoparticles under direct excitation with 488 and 514 nm lasers, we only show experiments with the 633 nm and 785 nm excitation wavelengths, and in remote mode with the 633 nm laser.

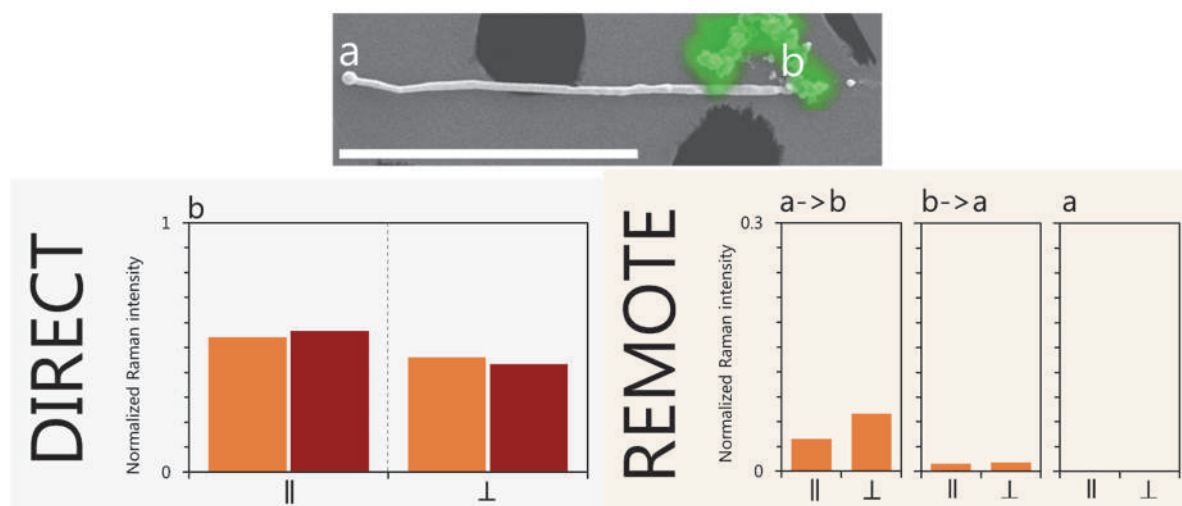


Figure IV.20. Study of a $7.5 \mu\text{m}$ long half-dog-bone $\text{Au}(\varnothing 147 \text{ nm})$ with PEDOT particles on the right tip (without Au nanoparticle). Top: SEM images with superposed Raman mapping for the C=C symmetric stretching PEDOT band (PEDOT appears green). Point a corresponds to the left tip (gold NP, no PEDOT) and point b to the right tip with commercial PEDOT particles. Scale bar is $5 \mu\text{m}$. Bottom: Normalized Raman intensity (defined in (Equation (IV.1))) of the C=C symmetric stretching PEDOT band in different configurations. Direct on b for 2 different λ_{exc} wavelengths 633 nm (orange) and 785 nm (dark red). Remote on b (a->b), remote on a (b->a), direct on a (suggesting a->b->a) for $\lambda_{\text{exc}} = 633 \text{ nm}$ (orange). Polarization parallel (||) or perpendicular (\perp) only at the excitation.

For the direct excitation of the right tip, a slightly stronger signal is measured for the polarization parallel to the nanowire, but we don't further discuss this result because PEDOT in these commercial nanoparticles is randomly oriented.

It is also complicated to establish the effect of the gold NP on $\lambda_{\text{exc}} = 633 \text{ nm}$ by comparing with the two simple NW, because of the difference in the PEDOT (its supramolecular structure and its location). Comparing the a->b and b->a Raman signals measured here, a much stronger signal is obtained for the excitation on the gold NP, than on the b tip. Additionally for a->b, the signal is stronger for the perpendicular than for the parallel polarization, while PEDOT chains are randomly oriented. On the left tip, the gold NP with a diameter larger than the NW diameter could explain these two effects by promoting a stronger excitation of SPP, whatever the polarization as it is roughly spherical. However, it is not a clear demonstration of an eventual enhanced antenna effect by the gold NP.

IV.4.3.4. Dog-bone nanowire with PEDOT particles on one tip

The last system proposed was the dog-bone structure with PEDOT particles at its right tip (Figure IV.21). Its length is 5.4 μm , the Au nanoparticle on the left is quite spherical and the one on the right is elongated. As important remark of this dog-bone nanowire, apart from its slightly bent geometry, we should note that it contained a PEDOT particle deposited on its middle zone that was successfully removed by laser dry etching.

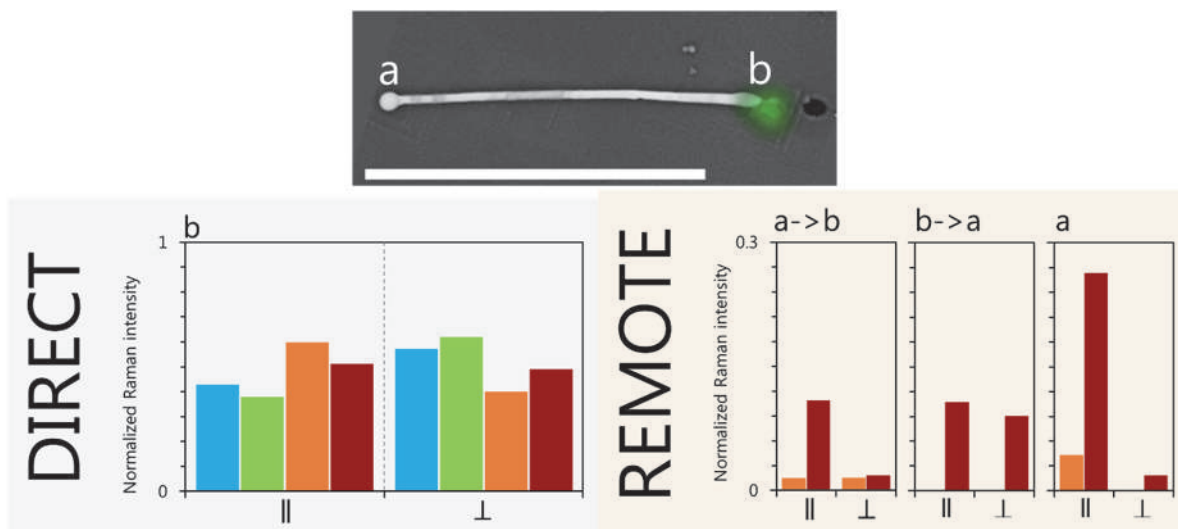


Figure IV.21. Study of a 5.4 μm long dog-bone Au(\varnothing 129 nm) nanowire with PEDOT particles on the right tip. Top: SEM images with superposed Raman mapping for the C=C symmetric stretching PEDOT band (PEDOT appears green). Point a corresponds to the left tip (gold nanoparticle, no PEDOT) and point b to the right tip with commercial PEDOT particles. Scale bar is 5 μm . Bottom: Normalized Raman intensity (defined in (Equation (IV.1))) of the C=C symmetric stretching PEDOT band in different configurations. Direct on b for 4 different λ_{exc} wavelengths 488 nm (blue), 514 nm (green), 633 nm (orange) and 785 nm (dark red). Remote on b (a->b), remote on a (b->a), direct on a (suggesting a->b->a) for λ_{exc} = 633 nm (orange) and 785 nm (dark red). No signal was obtained in remote mode for 488 nm and 514 nm. Polarization parallel (||) or perpendicular (\perp) only at the excitation.

Similarly to the half dog-bone, we deduce from the study in the direct excitation and collection on b (right tip) that the PEDOT chains in NP do not show any preferential ordering. Indeed, the Raman scattering intensities are quite similar for both parallel and perpendicular polarizations, whatever the excitation wavelength.

Again, a direct comparison of the measured Raman signals with the case of the simple coaxial nanowires is not possible. It is due to the fact that PEDOT particles are not positioned in a well-controlled manner, in opposition to the electropolymerized PEDOT

in coaxial nanowires. It could thus interact in a different manner with plasmons. However, it is possible to compare the relative changes between the different measurements. Some interesting features have been measured mostly at $\lambda_{\text{exc}} = 785$ nm. We focus our analysis on the results measured with the parallel polarization that give larger intensities than in the perpendicular one.

First, the normalized intensity in $a \rightarrow b$ and $b \rightarrow a$ (~ 0.1) is 5 times smaller than the one measured in the direct mode on the right Au NP. It was only 2.5 times smaller for the "short" simple NW with a bit shorter length. It suggests a good excitation of PEDOT to get the Raman signal, either directly or mediated by the SPP. In other words, the PEDOT NP are well-located, certainly very close or in contact with the right NP.

Most importantly, there is a strong PEDOT signal measured at the left tip, supposed to be zero as there is no PEDOT at this tip. This signal supporting a back-and-forth SPP-mediated process effect ($a \rightarrow b \rightarrow a$) is more than twice the signal measured for $a \rightarrow b$ or $b \rightarrow a$. This is unique for our measurements. For the 5.8 μm long coaxial NW (similar length than here), we also measured a pronounced $a \rightarrow b \rightarrow a$ signal for the // polarization, but two times smaller than the $b \rightarrow a$ case. The quantity of PEDOT in each system could be considered if the intensity was directly compared, but it is not an argument when the normalized intensity is compared. However, the different location of the PEDOT could be a parameter, with a shell directly covering the gold NW, or PEDOT nanoparticles dispersed around the gold NP. Moreover, the different PEDOT chain ordering could play a role regarding the important effect of the polarization: PEDOT chains are preferentially oriented perpendicular to the NW axis for the coaxial NW, while they are randomly oriented in the PEDOT NP. The latter case is more favourable to get a stronger intensity with the // polarization.

But it is required to involve another mechanism for explaining the stronger signal measured in a (i.e. $a \rightarrow b \rightarrow a$) than in $a \rightarrow b$ and $b \rightarrow a$ remote configuration for this dog-bone nanowire. Of course, the good quality (smoothness, regular shape, wavelength dependence of SPP propagation length) is a requirement to expect low loss propagation of SPP and it is certainly the reason why it is detected at $\lambda_{\text{exc}} = 785$ nm and not at 633 nm. But it cannot explain a larger signal after a propagating distance twice the case of $b \rightarrow a$ case. The efficiency of the coupling between the PEDOT and the gold NP is thus questioned. In the $b \rightarrow a$ measurement, the laser directly excites PEDOT, whose Raman scattering signal can couple to the SPP of the Au NP-NW system before emission at the opposite left tip. In the $a \rightarrow b \rightarrow a$ measurement, the laser first excites SPP at the left gold NP and it is the SPP out-coupling at the right tip that excites the Raman scattering of PEDOT. The return way should be the same. It seems reasonable to say that the excitation received by PEDOT is much less intense in the second case. So, a possible key point deals with the coupling between PEDOT and the NP at the right tip. Another point deals with the different SPP modes that can

propagate in this dog-bone nanowire and their possible excitation in presence of these nanoparticles, and a possible cavity effect. These are opened questions and we think that modelling the plasmonic behaviour should permit to elucidate some of this questions.

IV.5. Conclusions

In conclusion, we have explored the optical and plasmonic behaviour of a set of nanowires designed especially for studies on plasmon-mediated remote effects. Unambiguously, two original effects have been shown:

- A remote Raman scattering effect has been evidenced up to a distance of about 9 μm in a simple coaxial nanowire (no NP) at $\lambda_{\text{exc}} = 785 \text{ nm}$

- The gold nanoparticle located at the tip(s) contributes to enhance the measured signal (remote laser nano-reflectance, remote-Raman scattering) in a remote configuration with two possible architectures: half dog-bone and dog-bone nanowires.

These results strongly suggest an improved coupling between the incident laser and the nanowire. This improvement could be due to a larger cross-section for the NP than for the nanowire whose diameter is smaller. The NP could also contribute to improve the momentum matching,^{83,163} a required condition to excite the propagation of SPP in the nanowire.^{2,18,29,155,212,213}

As mentioned in the beginning of this section, in order to clarify the more advanced results, more nanowires of similar characteristics should be studied. In such a way, we could perform broad statistics analysis in order to confirm the main tendencies of this exploratory work.

We would like to propose here that in order to improve the laser nano-reflectance analysis and to be able to detect some plasmonic effects related to a size-dependent absorption and scattering (possibly revealed by small shift of the reflected signal), an improved spectral resolution would be needed. This could be achieved by installing gratings with more grooves per millimetre.

Conclusions and Perspectives

During my thesis work, different kinds of plasmon active gold-based nanowires have been successfully designed, synthesized and characterized. We exploited the electrochemical hard-template synthesis in order to produce these original nanowires and laser-based treatments for the post-synthesis processing to change the shape of the nanowire tips. The resulting nanowires could be divided in three categories:

- (i) Pure Au and PEDOT nanowires that served as reference systems for both synthesis and characterization
- (ii) Coaxial Au(core)@PEDOT(shell) nanowires with the PEDOT shell located in a controlled manner at different positions along the gold nanowire ; such nanowires were used for the proof-of-concept of the remote plasmon-mediated Raman effect
- (iii) Gold nanowires including larger gold excrescences at the tip(s), which permit an enhanced plasmon-photon coupling and contribute to improve the signal transmitted by the surface plasmon polaritons.

Regarding the coaxial Au@PEDOT nanowires, an exhaustive study of their PEDOT shells by polarized micro-Raman spectroscopy has been achieved. We demonstrated that the polymer chains are preferentially oriented perpendicular to the nanowire axis, in contrary to the case of PEDOT nanowires. Such a polymer ordering is a crucial point to improve the functional properties of conjugated polymers. We proposed a growth mechanism that permits to explain both this preferential alignment of the conjugated segments, and the wavelength dependent spectroscopic results which suggest that short and long conjugated segments are differently distributed. Such an ordering is directly promoted by the extreme confinement of the electropolymerization and to the gold nanowires acting as cylindrical nanoelectrodes.

By developing correlated characterization of the nanowires, we were able to fully study single nanowires of all the described categories. We then analysed their SPP behaviour by remote laser nano-reflectance. It shows that the gold excrescences located at the tip(s) of (half) dog-bone nanowires allow to enhance the signal measured in a remote place at the same wavelength than the exciting laser, but also for a red-shifted signal coming from the Raman scattering of the PEDOT positioned closely to the nanoparticle.

These successful studies open a way to a new branch of future experiments that are briefly overviewed below.

In the continuation of my work, the determination of the plasmonic behaviour by low-energy EELS-HRTEM will bring useful information for a comprehensive analysis of the different effects investigated, considering a local excitation of a plasmonic nanowire by an electron-beam or by a sub-micrometric laser spot, and alternatively an excitation of the whole nanowire by an optical beam.

Time-dependent spectroscopic studies on such systems would also be pertinent to identify the mechanism(s) involved in the coupling between the metallic dog-bone nanowire and the Raman species. Among many opportunities, the coupling of such dog-bone nanowires with photoluminescent species is a very exciting project to investigate the weak and strong plasmon-exciton coupling. It is a rapidly growing domain of research with perspectives of new fundamental effects, which could impact significantly optoelectronic and nanophotonics devices.

Another prospect concerns the development of more complex nano-architectures by exploiting the laser heating treatment. These successful first studies open a way to further developments for enhancing the plasmonic in- and out-coupling of the nanowire signal. It is a requirement to promote plasmon-mediated remote Raman or photoluminescence effects of (very) small signals along several micrometres. It would result in a new type of all-in-one self-standing plasmonic nanodevices.

APPENDIX I

Appendix I. Polarized nano-
Raman spectroscopy

Appendix I. Polarized nano-Raman spectroscopy

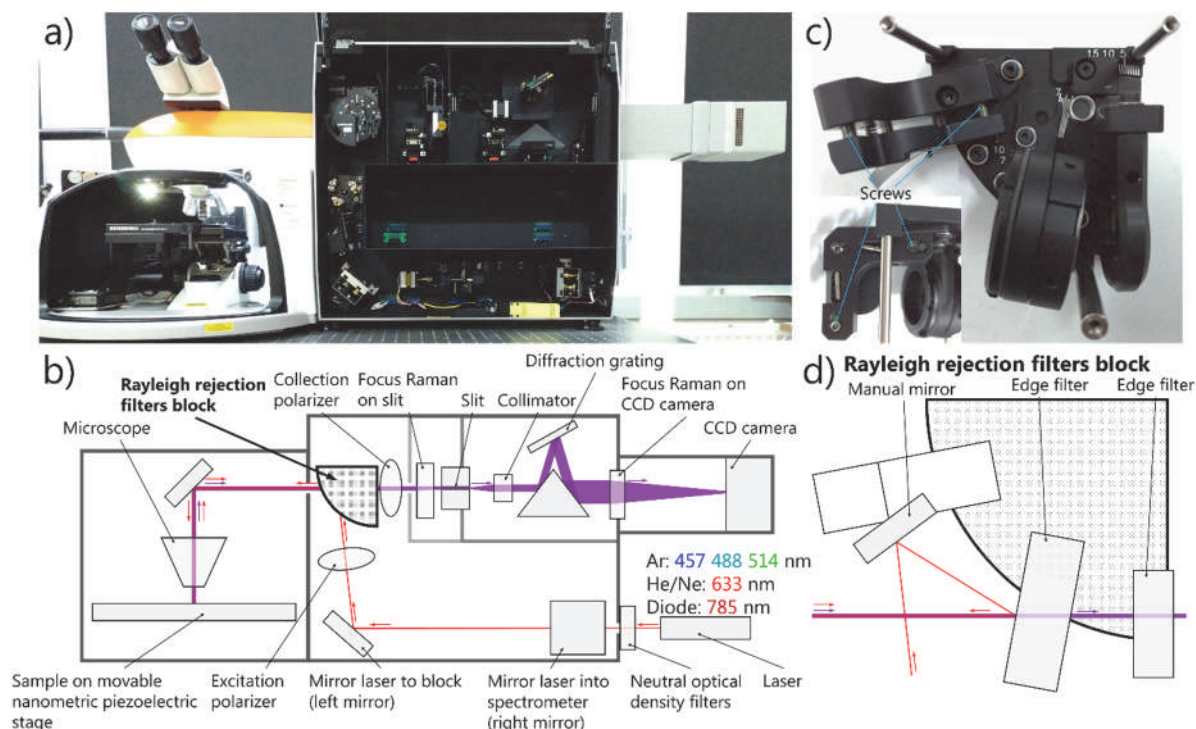


Figure AI.1. a) Open Renishaw InVia™ nano-spectrometer and b) its schema for easy understanding with the available laser lines. c) Open Rayleigh rejection filters block with the screws for tuning the laser beam path and d) their schema for easy understanding.

The protocol that we established, thanks to the collaboration of Renishaw and with expertise of J.Y. Mevellec, in order to optimize the laser pathway, its confocality and the signal strength was the following. The first step was to check that the four legs of the antivibration table were inflated. Secondly, we used a flat silicon surface as calibration sample with its edges parallel to the polarization of the laser beam. Using the x50 objective as reference, we placed the x100 long focal objective with its centre exactly focusing to the same spot. To complete this optical alignment, we compared the centre of the visual image from the binoculars with the centre of the digital image in the screen, as they should be at the same spot. Then, we optimized the laser focus. It was mainly done by playing with three mirrors (Figure AI.1): “mirror laser into spectrometer” (right mirror), “mirror laser to block” (left mirror) and the mirror inside the “Rayleigh rejection filters block” (manual mirror) (Figure AI.1c&d). We placed a vertical white flat surface cutting the beam that came from the right mirror

perpendicularly and we moved the right mirror until the spot seen on the flat surface was a perfect circle. Then we adjusted the image of the laser from the camera moving principally the left mirror until when focusing and defocusing in z the laser beam maintained its circular shape.⁴⁷⁰ The last step was to move the laser spot to the centre of the image, using both the manual and the left mirrors: first optimizing in the y axis and afterwards in the x , because the left mirror moves the laser spot in horizontal and diagonal but not in vertical. We moved the laser spot twice the distance between it and the axis (x or y) in the direction towards that axis with the manual mirror, and then we re-adjusted the central position on the screen with the left mirror.

Once the laser was well aligned, the detection beam path should be optimized. First, the slit and the CCD camera width were completely opened in order to see to which pixels the maximum of the signal was coming to. Prior to the next step was necessary to recalibrate the Raman signal displacement in the software (as we were using a Si slab, the main peak should appear at 520.5 cm^{-1}). Once the Raman shift was corrected, the CCD camera width was closed to the 3 pixels around the brightest point. We gradually closes the slit to $20 \mu\text{m}$ and moved it when necessary in order to get the maximum signal. In order to get a higher spatial resolution we could close even more the slit and select less pixels in the CCD camera (Figure AI.2). In that manner, the surface of the sample collected decreases and, when performing a mapping, its spatial resolution increases.

We consider important to note that this ultimate alignment must be done very precisely in order to only collect the signal coming from the normal beams from the very centre of the optical image. It is important to note that in most of the cases the laser beam that arrives to the sample is larger in diameter than the measured nanowire diameter but we consider that when working in this high spatial resolution collection conditions the acquisition area is around the same size than nanowire diameter or just slightly bigger (Figure AI.2).

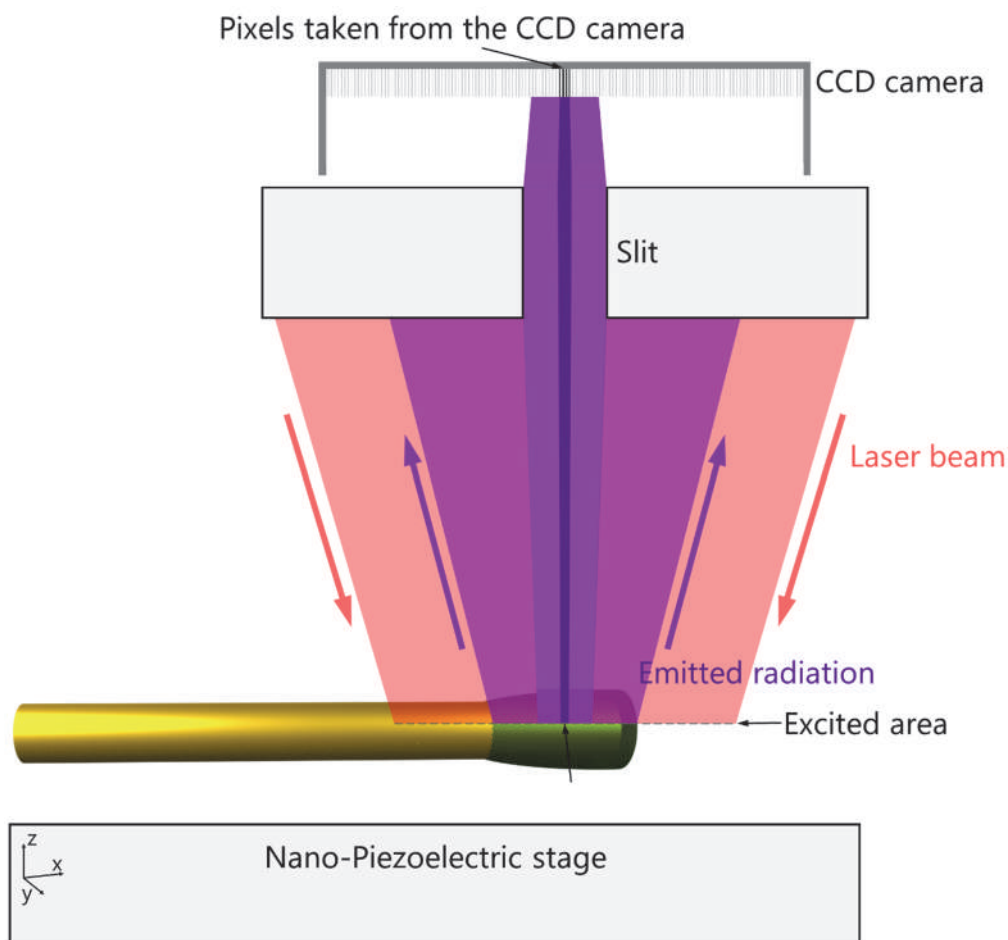


Figure AI.2. Schema of the relation between the customizable parameters of a nano-spectrometer and the sample spatial resolution. An asymmetric Au@PEDOT nanowire is under laser excitation (laser beam in red) that irradiates a given area (excited area). The Raman signal produced (emitted radiation in purple) is collected on the CCD camera. The spatial resolution (sample area collected) of this collected signal can be tuned by the slit opening and the pixels taken from the CCD camera. This schema also represents the laser nano-reflectance measurements.

When the laser was extremely misaligned and we could not even track the laser spot on the screen, we proceeded in another manner to get it back. The step involving the right mirror was analogous but, in the case of the left mirror, we adjusted it to centre the laser spot right in the middle of the manual mirror. Once it was done, normally the laser should arrive into the objective. If not, we played with both the left and the manual mirrors until it appeared.

We noted the signal intensity (number of counts) obtained for the Si main peak under the optimal conditions described before for each wavelength (Table VI.1). We found that these signal intensities were very reproducible once the calibration was done. We tracked the same intensities in the beginning and the end of the thesis.

Raman signal intensity (in number of counts) at optimized calibration conditions:

Wavelength	Laser power	Polarization	Grating	Number of counts
488 nm	1.5 mW	Normal	2400 gr/mm	1400 counts
514 nm	1.5 mW	Normal	2400 gr/mm	4000 counts
633 nm	1.0 mW	Orthogonal	1200 gr/mm	2000 counts
785 nm	0.5 mW	Normal	1200 gr/mm	800 counts

Table VI.1. Registered Raman intensities for the Si peak at 520.5 cm^{-1} of an oriented Si slab under optimal confocal conditions. These conditions are the following: laser well aligned in all three directions, slit opening $20\text{ }\mu\text{m}$, CCD camera width: 2 pixels. $\times 100$ long focal objective ($NA = 0.8$). Acquisition time: 1 s.

It is necessary to remark that all the alignment of the laser was made under safe conditions. The manipulator and all the people present in the room should wear radiation protection specs during the calibration process as the laser beam was not covered.

APPENDIX II

Appendix II. Laser nano-reflectance 3D plots

Appendix II. Laser nano-reflectance 3D plots

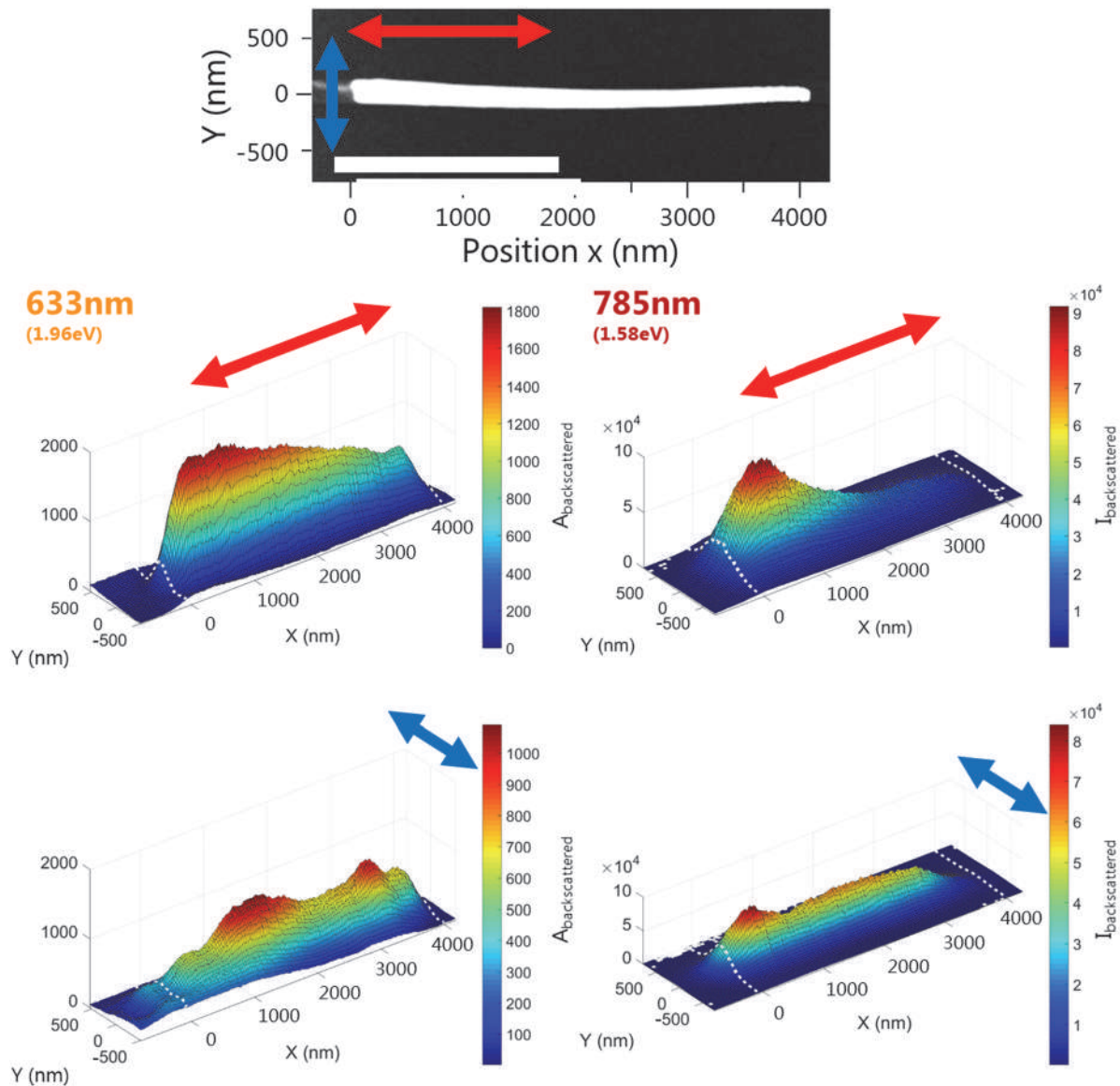


Figure AII.1. TEM image and intensity (signal to baseline for 633 nm and Lorentzian fit for 785 nm) 3D maps for 633 nm and 785 nm as excitation wavelength for parallel and perpendicular polarization of the single Au nanowire. White scale bar corresponds to 2 μm.

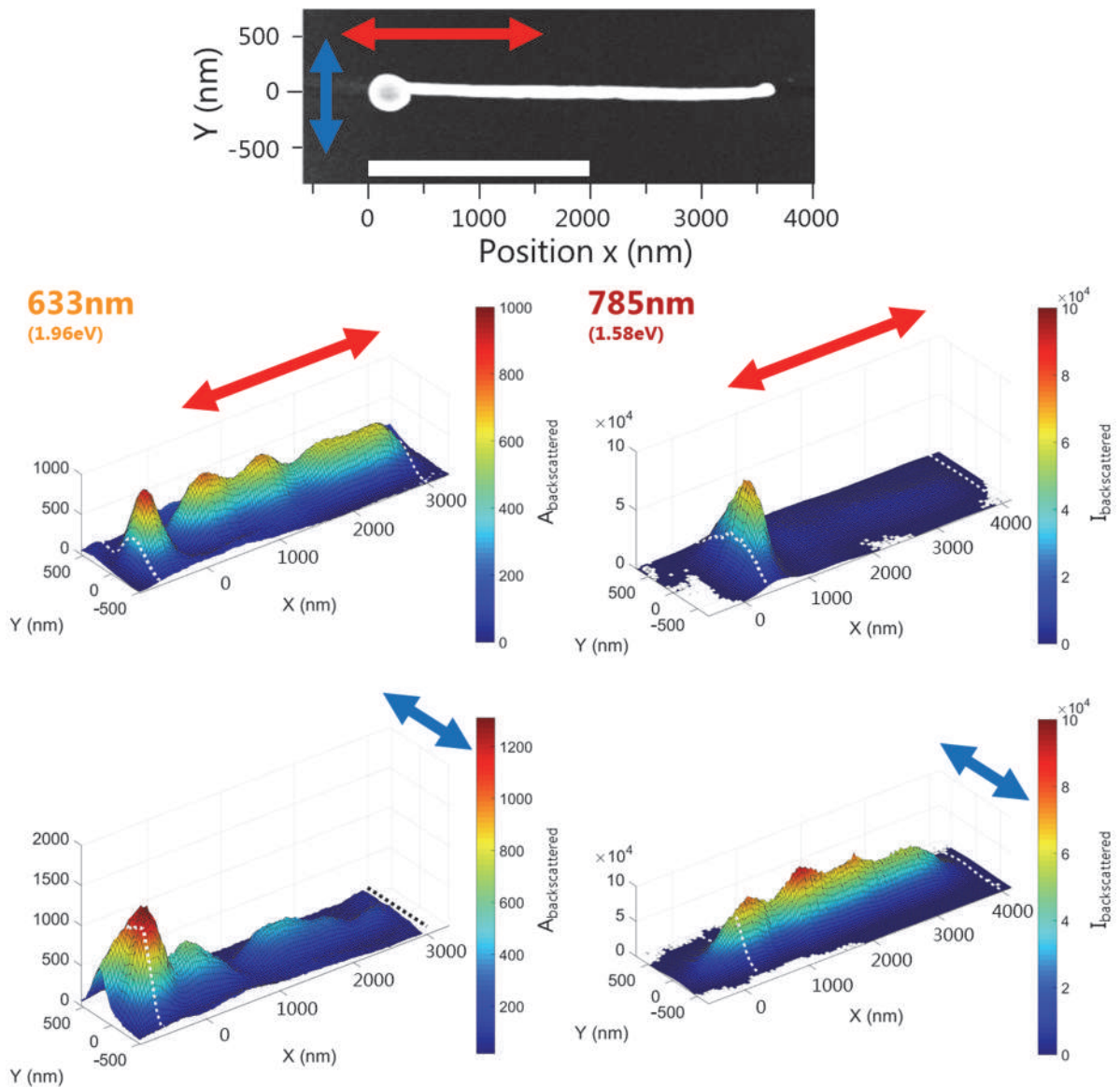


Figure AII.2. TEM image and intensity (signal to baseline for 633 nm and Lorentzian fit for 785 nm) 3D maps for 633 nm and 785 nm as excitation wavelength for parallel and perpendicular polarization of the half dog-bone Au nanowire. White scale bar corresponds to 2 μm.

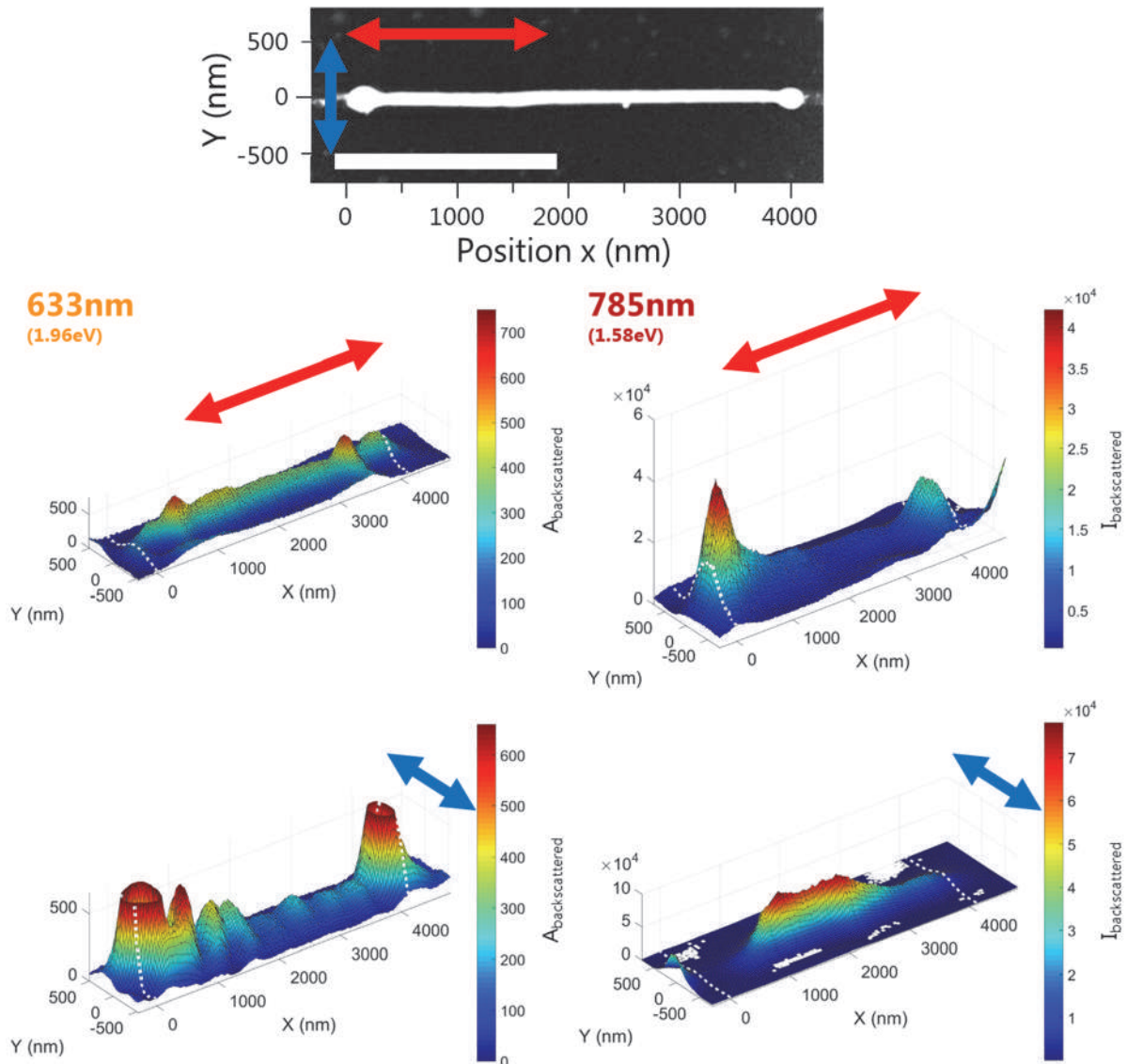


Figure AII.3. TEM image and intensity (signal to baseline for 633 nm and Lorentzian fit for 785 nm) 3D maps for 633 nm and 785 nm as excitation wavelength for parallel and perpendicular polarization of the dog-bone Au nanowire. White scale bar corresponds to 2 μm.

List of references

List of references

1. Sanders, A. W. Optical properties of metallic nanostructures. (Thesis at Yale University, 2007).
2. Gaponenko, S. V. *Introduction to Nanophotonics*. (Cambridge University Press, 2010).
3. Giannini, V., Fernández-Domínguez, A. I., Heck, S. C. & Maier, S. A. Plasmonic Nanoantennas: Fundamentals and Their Use in Controlling the Radiative Properties of Nanoemitters. *Chem. Rev.* **111**, 3888–3912 (2011).
4. Odom, T. W. & Schatz, G. C. Introduction to Plasmonics. *Chem. Rev.* **111**, 3667–3668 (2011).
5. Jones, M. R., Osberg, K. D., Macfarlane, R. J., Langille, M. R. & Mirkin, C. A. Templated Techniques for the Synthesis and Assembly of Plasmonic Nanostructures. *Chem. Rev.* **111**, 3736–3827 (2011).
6. Pluchery, O. & Carriere, M. Nanoparticules d'or. *Tech. Ing.* **NM900**, 1–23 (2011).
7. Faraday, M. The Bakerian Lecture. —Experimental relations of gold (and other metals) to light. *Philos. Trans. R. Soc. Lond.* **147**, 145–181 (1857).
8. Wood, R. W. On a remarkable case of uneven distribution of light in a diffraction grating spectrum. *Lond. Edinb. Dublin Philos. Mag. J. Sci.* **4**, 396–402 (1902).
9. Siedentopf, H. & Zsigmondy, R. Über Sichtbarmachung und Größenbestimmung ultramikroskopischer Teilchen, mit besonderer Anwendung auf Goldrubingläser. *Ann. Phys.* **315**, 1–39 (1902).
10. J. C. Maxwell Garnett, B. A. Colours in metal glasses and in metallic films. *Phil Trans R Soc Lond A* **203**, 385–420 (1904).
11. Mie, G. Beiträge zur Optik trüber Medien, speziell kolloidaler Metallösungen. *Ann. Phys.* **330**, 377–445 (1908).
12. Tcherniak, A., Ha, J. W., Dominguez-Medina, S., Slaughter, L. S. & Link, S. Probing a Century Old Prediction One Plasmonic Particle at a Time. *Nano Lett.* **10**, 1398–1404 (2010).
13. Pines, D. & Bohm, D. A Collective Description of Electron Interactions: II. Collective vs Individual Particle Aspects of the Interactions. *Phys. Rev.* **85**, 338–353 (1952).
14. Pines, D. Electron Interaction in Metals. in *Solid State Physics* (eds. Seitz, F. & Turnbull, D.) **1**, 367–450 (Academic Press, 1955).
15. Pines, D. Collective Energy Losses in Solids. *Rev. Mod. Phys.* **28**, 184–198 (1956).
16. Ritchie, R. H. Plasma Losses by Fast Electrons in Thin Films. *Phys. Rev.* **106**, 874–881 (1957).
17. Nordlander, P. Plasmonics, a hot topic in nanophotonics. in *Bulletin of the American Physical Society* (American Physical Society, 2006).
18. Zhang, J., Zhang, L. & Xu, W. Surface plasmon polaritons: physics and applications. *J. Phys. Appl. Phys.* **45**, 113001 (2012).
19. Editorial. Where now for plasmonics? *Nat. Nanotechnol.* **11**, 1 (2016).
20. Haes, A. J. *et al.* Plasmonic Materials for Surface-Enhanced Sensing and Spectroscopy. *MRS Bull.* **30**, 368–375 (2005).
21. Huang, X. & El-Sayed, M. A. Plasmonic photo-thermal therapy (PPTT). *Alex. J. Med.* **47**, 1–9 (2011).
22. Giangregorio, M. M. *et al.* Synthesis and characterization of plasmon resonant gold nanoparticles and graphene for photovoltaics. *Mater. Sci. Eng. B* **178**, 559–567 (2013).
23. Lee, D., Jeong, S., Park, J.-H., Park, S. Y. & Jang, D.-J. Effects of gold nanorods on the excited-state dynamics and photovoltaic performances of hybrid nanocomposites containing poly(3-hexylthiophene). *J. Mater. Sci.* **51**, 9669–9678 (2016).

24. Lorcy, J. M. *et al.* Coaxial nickel/poly(p-phenylene vinylene) nanowires as luminescent building blocks manipulated magnetically. *Nanotechnology* **20**, 405601 (2009).
25. Lal, S., Hafner, J. H., Halas, N. J., Link, S. & Nordlander, P. Noble Metal Nanowires: From Plasmon Waveguides to Passive and Active Devices. *Acc. Chem. Res.* **45**, 1887–1895 (2012).
26. Guo, X., Ma, Y., Wang, Y. & Tong, L. Nanowire plasmonic waveguides, circuits and devices. *Laser Photonics Rev.* **7**, 855–881 (2013).
27. Garreau, A. & Duvail, J.-L. Recent Advances in Optically Active Polymer-Based Nanowires and Nanotubes. *Adv. Opt. Mater.* **2**, 1122–1140 (2014).
28. Fang, Y. & Sun, M. Nanoplasmonic waveguides: towards applications in integrated nanophotonic circuits. *Light Sci. Appl.* **4**, e294 (2015).
29. Wei, H., Pan, D. & Xu, H. Routing of surface plasmons in silver nanowire networks controlled by polarization and coating. *Nanoscale* **7**, 19053–19059 (2015).
30. Rudberg, E. Characteristic Energy Losses of Electrons Scattered from Incandescent Solids. *Proc. R. Soc. Math. Phys. Eng. Sci.* **127**, 111–140 (1930).
31. Vesseur, E. J. R. *et al.* Plasmonic excitation and manipulation with an electron beam. *MRS Bull.* **37**, 752–760 (2012).
32. Gong, S. *et al.* Electron beam excitation of surface plasmon polaritons. *Opt. Express* **22**, 19252–19261 (2014).
33. Kociak, M. & Stéphan, O. Mapping plasmons at the nanometer scale in an electron microscope. *Chem. Soc. Rev.* **43**, 3865 (2014).
34. Wang, T. *et al.* Scattering of electrically excited surface plasmon polaritons by gold nanoparticles studied by optical interferometry with a scanning tunneling microscope. *Phys. Rev. B* **92**, (2015).
35. Willets, K. A. & Van Duyne, R. P. Localized Surface Plasmon Resonance Spectroscopy and Sensing. *Annu. Rev. Phys. Chem.* **58**, 267–297 (2007).
36. N'Gom, M. *et al.* Single Particle Plasmon Spectroscopy of Silver Nanowires and Gold Nanorods. *Nano Lett.* **8**, 3200–3204 (2008).
37. Powell, C. J. & Swan, J. B. Origin of the Characteristic Electron Energy Losses in Aluminum. *Phys. Rev.* **115**, 869–875 (1959).
38. Teng, Y.-Y. & Stern, E. A. Plasma Radiation from Metal Grating Surfaces. *Phys. Rev. Lett.* **19**, 511–514 (1967).
39. Wang, T., Boer-Duchemin, E., Zhang, Y., Comtet, G. & Dujardin, G. Excitation of propagating surface plasmons with a scanning tunnelling microscope. *Nanotechnology* **22**, 175201 (2011).
40. Bharadwaj, P., Bouhelier, A. & Novotny, L. Electrical Excitation of Surface Plasmons. *Phys. Rev. Lett.* **106**, 226802 (2011).
41. Trooster, J. M. & van Attekum, P. M. T. M. Bulk- and surface-plasmon-loss intensities in photoelectron, Auger, and electron-energy-loss spectra of Al metal. *Phys. Rev. B* **18**, 3872–3883 (1978).
42. Jain, P. K., Lee, K. S., El-Sayed, I. H. & El-Sayed, M. A. Calculated Absorption and Scattering Properties of Gold Nanoparticles of Different Size, Shape, and Composition: Applications in Biological Imaging and Biomedicine. *J. Phys. Chem. B* **110**, 7238–7248 (2006).
43. Schider, G. *et al.* Optical properties of Ag and Au nanowire gratings. *J. Appl. Phys.* **90**, 3825–3830 (2001).
44. Olmon, R. L. *et al.* Optical dielectric function of gold. *Phys. Rev. B* **86**, 235147 (2012).

45. Bridges, C. R., Schon, T. B., DiCarmine, P. M. & Seferos, D. S. Template Directed Synthesis of Plasmonic Gold Nanotubes with Tunable IR Absorbance. *J. Vis. Exp. JoVE* e50420 (2013).
46. Kohl, J., Fireman, M. & O'Carroll, D. M. Surface plasmon and photonic mode propagation in gold nanotubes with varying wall thickness. *Phys. Rev. B* **84**, (2011).
47. Chhatre, A., Solasa, P., Sakle, S., Thaokar, R. & Mehra, A. Color and surface plasmon effects in nanoparticle systems: Case of silver nanoparticles prepared by microemulsion route. *Colloids Surf. Physicochem. Eng. Asp.* **404**, 83–92 (2012).
48. González, A. L., Noguez, C., Beránek, J. & Barnard, A. S. Size, Shape, Stability, and Color of Plasmonic Silver Nanoparticles. *J. Phys. Chem. C* **118**, 9128–9136 (2014).
49. Cheng, X. *et al.* Color Difference Amplification between Gold Nanoparticles in Colorimetric Analysis with Actively Controlled Multiband Illumination. *Anal. Chem.* **86**, 7584–7592 (2014).
50. Wei, H., Abtahi, S. M. H. & Vikesland, P. J. Plasmonic colorimetric and SERS sensors for environmental analysis. *Environ. Sci. Nano* **2**, 120–135 (2015).
51. Fleischmann, M., Hendra, P. J. & McQuillan, A. J. Raman spectra of pyridine adsorbed at a silver electrode. *Chem. Phys. Lett.* **26**, 163–166 (1974).
52. Creighton, J. A., Blatchford, C. G. & Albrecht, M. G. Plasma resonance enhancement of Raman scattering by pyridine adsorbed on silver or gold sol particles of size comparable to the excitation wavelength. *J. Chem. Soc. Faraday Trans. 2* **75**, 790 (1979).
53. Dogan, Ü., Kaya, M., Cihaner, A. & Volkan, M. Ag nanostructures on a poly(3,4-ethylenedioxythiophene) film prepared with electrochemical route: A controllable roughened SERS substrate with high repeatability and stability. *Electrochimica Acta* **85**, 220–227 (2012).
54. Bridges, C. R., DiCarmine, P. M. & Seferos, D. S. Gold Nanotubes as Sensitive, Solution-Suspendable Refractive Index Reporters. *Chem. Mater.* **24**, 963–965 (2012).
55. Zhang, J. *et al.* A novel surface plasmon resonance biosensor based on graphene oxide decorated with gold nanorod–antibody conjugates for determination of transferrin. *Biosens. Bioelectron.* **45**, 230–236 (2013).
56. Kennedy, B. J., Spaeth, S., Dickey, M. & Carron, K. T. Determination of the distance dependence and experimental effects for modified SERS substrates based on self-assembled monolayers formed using alkanethiols. *J. Phys. Chem. B* **103**, 3640–3646 (1999).
57. Billot, L. *et al.* Surface enhanced Raman scattering on gold nanowire arrays: Evidence of strong multipolar surface plasmon resonance enhancement. *Chem. Phys. Lett.* **422**, 303–307 (2006).
58. Le Ru, E. C., Blackie, E., Meyer, M. & Etchegoin, P. G. Surface Enhanced Raman Scattering Enhancement Factors: A Comprehensive Study. *J. Phys. Chem. C* **111**, 13794–13803 (2007).
59. Kukushkin, V. I., Van'kov, A. B. & Kukushkin, I. V. Long-range nature of surface-enhanced Raman scattering. *JETP Lett.* (2012).
60. O'Carroll, D. M., Hofmann, C. E. & Atwater, H. A. Conjugated Polymer/Metal Nanowire Heterostructure Plasmonic Antennas. *Adv. Mater.* **22**, 1223–1227 (2010).
61. Kang, K. A., Wang, J., Jasinski, J. B. & Achilefu, S. Fluorescence manipulation by gold nanoparticles: from complete quenching to extensive enhancement. *J. Nanobiotechnology* **9**, (2011).
62. Bourret, G. R. *et al.* Long-Range Plasmophore Rulers. *Nano Lett.* **13**, 2270–2275 (2013).
63. Ji, W., Zhao, H., Yang, H. & Zhu, F. Effect of coupling between excitons and gold nanoparticle surface plasmons on emission behavior of phosphorescent organic light-emitting diodes. *Org. Electron.* **22**, 154–159 (2015).
64. Berini, P. & De Leon, I. Surface plasmon–polariton amplifiers and lasers. *Nat. Photonics* **6**, 16–24 (2012).

65. Krasnok, A. E. *et al.* Optical nanoantennas. *Phys.-Uspekhi* **56**, 539 (2013).
66. Bohren, C. F. & Huffman, D. R. *Absorption and Scattering of Light by Small Particles*. (John Wiley & Sons, Inc., 1983).
67. West, P. R. *et al.* Searching for better plasmonic materials. *Laser Photonics Rev.* **4**, 795–808 (2010).
68. Arenal, R. *et al.* Local Plasmonic Studies on Individual Core–Shell Gold–Silver and Pure Gold Nano-Bipyramids. *J. Phys. Chem. C* **118**, 25643–25650 (2014).
69. Gans, R. Über die Form ultramikroskopischer Goldteilchen. **342**, 881–900 (1912).
70. Zou, C.-L. *et al.* Plasmon modes of silver nanowire on a silica substrate. *Appl. Phys. Lett.* **97**, 183102 (2010).
71. Hollingsworth, J. A., Htoon, H., Piryatinski, A., Götzinger, S. & Sandoghdar, V. When excitons and plasmons meet: Emerging function through synthesis and assembly. *MRS Bull.* **40**, 768–776 (2015).
72. Feng, A. L. *et al.* Distance-Dependent Plasmon-Enhanced Fluorescence of Upconversion Nanoparticles using Polyelectrolyte Multilayers as Tunable Spacers. *Sci. Rep.* **5**, 7779 (2015).
73. Shin, T. *et al.* Exciton Recombination, Energy-, and Charge Transfer in Single- and Multilayer Quantum-Dot Films on Silver Plasmonic Resonators. *Sci. Rep.* **6**, (2016).
74. Tong, L., Miljkovic, V. D. & Käll, M. Alignment, Rotation, and Spinning of Single Plasmonic Nanoparticles and Nanowires Using Polarization Dependent Optical Forces. *Nano Lett.* **10**, 268–273 (2010).
75. Tzarouchis, D. C., Ylä-Oijala, P., Ala-Nissila, T. & Sihvola, A. Shape effects on surface plasmons in spherical, cubic, and rod-shaped silver nanoparticles. *Appl. Phys. A* **122**, (2016).
76. Njoki, P. N. *et al.* Size Correlation of Optical and Spectroscopic Properties for Gold Nanoparticles. *J. Phys. Chem. C* **111**, 14664–14669 (2007).
77. Cao, J., Sun, T. & Grattan, K. T. V. Gold nanorod-based localized surface plasmon resonance biosensors: A review. *Sens. Actuators B Chem.* **195**, 332–351 (2014).
78. Agrawal, A., Kriegel, I. & Milliron, D. J. Shape-Dependent Field Enhancement and Plasmon Resonance of Oxide Nanocrystals. *J. Phys. Chem. C* **119**, 6227–6238 (2015).
79. Wang, J., Zhang, H. Z., Li, R. S. & Huang, C. Z. Localized surface plasmon resonance of gold nanorods and assemblies in the view of biomedical analysis. *Trends Anal. Chem.* **80**, 429–443 (2016).
80. Petryayeva, E. & Krull, U. J. Localized surface plasmon resonance: Nanostructures, bioassays and biosensing—A review. *Anal. Chim. Acta* **706**, 8–24 (2011).
81. Lu, X., Rycenga, M., Skrabalak, S. E., Wiley, B. & Xia, Y. Chemical Synthesis of Novel Plasmonic Nanoparticles. *Annu. Rev. Phys. Chem.* **60**, 167–192 (2009).
82. Halas, N. J., Lal, S., Chang, W.-S., Link, S. & Nordlander, P. Plasmons in Strongly Coupled Metallic Nanostructures. *Chem. Rev.* **111**, 3913–3961 (2011).
83. Kenens, B., Rybachuk, M., Hofkens, J. & Uji-i, H. Silver Nanowires Terminated by Metallic Nanoparticles as Effective Plasmonic Antennas. *J. Phys. Chem. C* **117**, 2547–2553 (2013).
84. Lin, L. *et al.* Assembly of silver nanoparticles on nanowires into ordered nanostructures with femtosecond laser radiation. *Appl. Opt.* **54**, 2524–2531 (2015).
85. Day, J. K., Large, N., Nordlander, P. & Halas, N. J. Standing Wave Plasmon Modes Interact in an Antenna-Coupled Nanowire. *Nano Lett.* **15**, 1324–1330 (2015).
86. Genet, C. & Ebbesen, T. W. Light in tiny holes. *Nature* **445**, 39–46 (2007).
87. Andryieuski, A., Malureanu, R., Biagi, G., Holmgaard, T. & Lavrinenko, A. Compact dipole nanoantenna coupler to plasmonic slot waveguide. *Opt. Lett.* **37**, 1124–1126 (2012).

88. Kottmann, J. P. & Martin, O. J. F. Plasmon resonant coupling in metallic nanowires. *Opt. Express* **8**, 655–663 (2001).
89. Yoon, I. *et al.* Single Nanowire on a Film as an Efficient SERS-Active Platform. *J. Am. Chem. Soc.* **131**, 758–762 (2009).
90. Chen, H.-A., Lin, H.-Y. & Lin, H.-N. Localized Surface Plasmon Resonance in Lithographically Fabricated Single Gold Nanowires. *J. Phys. Chem. C* **114**, 10359–10364 (2010).
91. Johns, P., Beane, G., Yu, K. & Hartland, G. V. Dynamics of Surface Plasmon Polaritons in Metal Nanowires. *J. Phys. Chem. C* **121**, 5445–5459 (2017).
92. Imura, K., Nagahara, T. & Okamoto, H. Near-field optical imaging of plasmon modes in gold nanorods. *J. Chem. Phys.* **122**, 154701 (2005).
93. Lim, J. K., Imura, K., Nagahara, T., Kim, S. K. & Okamoto, H. Imaging and dispersion relations of surface plasmon modes in silver nanorods by near-field spectroscopy. *Chem. Phys. Lett.* **412**, 41–45 (2005).
94. Wei, W. *et al.* Surface Plasmon-Mediated Energy Transfer in Heterogap Au–Ag Nanowires. *Nano Lett.* **8**, 3446–3449 (2008).
95. Lee, S.-M., Kim, S. H., Lee, J. H., Lee, S.-J. & Kim, H.-K. Hydrophobic and stretchable Ag nanowire network electrode passivated by a sputtered PTFE layer for self-cleaning transparent thin film heaters. *RSC Adv.* **8**, 18508–18518 (2018).
96. Bi, Z. *et al.* Polarization-dependent hotspots formed in crossed silver nanowires for surface-enhanced Raman spectroscopy. *Opt. Commun.* **429**, 35–40 (2018).
97. Hu, L., Kim, H. S., Lee, J.-Y., Peumans, P. & Cui, Y. Scalable Coating and Properties of Transparent, Flexible, Silver Nanowire Electrodes. *ACS Nano* **4**, 2955–2963 (2010).
98. Langley, D. P. *et al.* Metallic nanowire networks: effects of thermal annealing on electrical resistance. *Nanoscale* **6**, 13535–13543 (2014).
99. Lu, H., Zhang, D., Ren, X., Liu, J. & Choy, W. C. H. Selective Growth and Integration of Silver Nanoparticles on Silver Nanowires at Room Conditions for Transparent Nano-Network Electrode. *ACS Nano* **8**, 10980–10987 (2014).
100. Maize, K. *et al.* Super-Joule heating in graphene and silver nanowire network. *Appl. Phys. Lett.* **106**, 143104 (2015).
101. Song, C.-H., Han, C. J., Ju, B.-K. & Kim, J.-W. Photoenhanced Patterning of Metal Nanowire Networks for Fabrication of Ultraflexible Transparent Devices. *ACS Appl. Mater. Interfaces* **8**, 480–489 (2016).
102. Large, M. J. *et al.* Predicting the optoelectronic properties of nanowire films based on control of length polydispersity. *Sci. Rep.* **6**, 25365 (2016).
103. Cann, M. *et al.* High performance transparent multi-touch sensors based on silver nanowires. *Mater. Today Commun.* **7**, 42–50 (2016).
104. Sannicolo, T. *et al.* Metallic Nanowire-Based Transparent Electrodes for Next Generation Flexible Devices: a Review. *Small* **12**, 6052–6075 (2016).
105. Philpott, M. R. Effect of surface plasmons on transitions in molecules. *J. Chem. Phys.* **62**, 1812–1817 (1975).
106. Albrecht, M. G. & Creighton, J. A. Anomalously intense Raman spectra of pyridine at a silver electrode. *J. Am. Chem. Soc.* **99**, 5215–5217 (1977).
107. Moskovits, M. Surface roughness and the enhanced intensity of Raman scattering by molecules adsorbed on metals. *J. Chem. Phys.* **69**, 4159–4161 (1978).
108. Natan, M. J. Concluding Remarks Surface enhanced Raman scattering. *Faraday Discuss.* **132**, 321–328 (2006).

109. Grasseschi, D. *et al.* SERS studies of isolated and agglomerated gold nanoparticles functionalized with a dicarboxybipyridine-trimercaptotriazine-ruthenium dye. *J. Raman Spectrosc.* **45**, 758–763 (2014).
110. Grasseschi, D. & Toma, H. E. The SERS effect in coordination chemistry. *Coord. Chem. Rev.* **333**, 108–131 (2017).
111. Lombardi, J. R. & Birke, R. L. A Unified Approach to Surface-Enhanced Raman Spectroscopy. *J. Phys. Chem. C* **112**, 5605–5617 (2008).
112. Lombardi, J. R., Birke, R. L., Lu, T. & Xu, J. Charge-transfer theory of surface enhanced Raman spectroscopy: Herzberg–Teller contributions. *J. Chem. Phys.* **84**, 4174–4180 (1986).
113. Nie, S. & Emory, S. R. Probing Single Molecules and Single Nanoparticles by Surface-Enhanced Raman Scattering. *Science* **275**, 1102–1106 (1997).
114. Sharma, B., Frontiera, R. R., Henry, A.-I., Ringe, E. & Van Duyne, R. P. SERS: Materials, applications, and the future. *Mater. Today* **15**, 16–25 (2012).
115. Pozzi, F. & Leona, M. Surface-enhanced Raman spectroscopy in art and archaeology. *J. Raman Spectrosc.* **47**, 67–77 (2015).
116. Liu, Y., Lee, Y. H., Lee, M. R., Yang, Y. & Ling, X. Y. Flexible Three-Dimensional Anticounterfeiting Plasmonic Security Labels: Utilizing Z-Axis-Dependent SERS Readouts to Encode Multilayered Molecular Information. *ACS Photonics* **4**, 2529–2536 (2017).
117. Lay, C. L. *et al.* Aluminum nanostructures with strong visible-range SERS activity for versatile micropatterning of molecular security labels. *Nanoscale* **10**, 575–581 (2018).
118. Xie, X., Pu, H. & Sun, D.-W. Recent advances in nanofabrication techniques for SERS substrates and their applications in food safety analysis. *Crit. Rev. Food Sci. Nutr.* **0**, 1–14 (2017).
119. Wedge, S., Wasey, J. a. E., Barnes, W. L. & Sage, I. Coupled surface plasmon-polariton mediated photoluminescence from a top-emitting organic light-emitting structure. *Appl. Phys. Lett.* **85**, 182–184 (2004).
120. O’Carroll, D. M., Hofmann, C. E. & Atwater, H. A. Conjugated Polymer/Metal Nanowire Heterostructure Plasmonic Antennas. *Adv. Mater.* **22**, 1223–1227 (2010).
121. Butun, S., Tongay, S. & Aydin, K. Enhanced Light Emission from Large-Area Monolayer MoS₂ Using Plasmonic Nanodisc Arrays. *Nano Lett.* **15**, 2700–2704 (2015).
122. Li, J.-F., Li, C.-Y. & Aroca, R. F. Plasmon-enhanced fluorescence spectroscopy. *Chem. Soc. Rev.* **46**, 3962–3979 (2017).
123. Kuhn, H. Classical Aspects of Energy Transfer in Molecular Systems. *J. Chem. Phys.* **53**, 101–108 (1970).
124. Philpott, M. R. Fluorescence from molecules between mirrors. *Chem. Phys. Lett.* **19**, 435–439 (1973).
125. Glass, A. M., Liao, P. F., Bergman, J. G. & Olson, D. H. Interaction of metal particles with adsorbed dye molecules: absorption and luminescence. *Opt. Lett.* **5**, 368–370 (1980).
126. Chen, C. Y., Davoli, I., Ritchie, G. & Burstein, E. Giant Raman scattering and luminescence by molecules adsorbed on Ag and Au metal island films. *Surf. Sci.* **101**, 363–366 (1980).
127. Moskovits, M. Surface-enhanced spectroscopy. *Rev Mod Phys* **57**, 46 (1985).
128. Camacho, S. A. *et al.* Increasing the Enhancement Factor in Plasmon-Enhanced Fluorescence with Shell-Isolated Nanoparticles. *J. Phys. Chem. C* **120**, 20530–20535 (2016).
129. Anger, P., Bharadwaj, P. & Novotny, L. Enhancement and Quenching of Single-Molecule Fluorescence. *Phys. Rev. Lett.* **96**, 113002 (2006).

130. Lu, G. *et al.* Single-Molecule Spontaneous Emission in the Vicinity of an Individual Gold Nanorod. *J. Phys. Chem. C* **115**, 15822–15828 (2011).
131. Tang, L. *et al.* Modulated exciton-plasmon interactions in Au-SiO₂-CdTe composite nanoparticles. *Opt. Express* **21**, 11095–11100 (2013).
132. Naiki, H. *et al.* Highly Controlled Plasmonic Emission Enhancement from Metal-Semiconductor Quantum Dot Complex Nanostructures. *J. Phys. Chem. C* **117**, 2455–2459 (2013).
133. Gifford, D. K. & Hall, D. G. Emission through one of two metal electrodes of an organic light-emitting diode via surface-plasmon cross coupling. *Appl. Phys. Lett.* **81**, 4315–4317 (2002).
134. Camposeo, A. *et al.* Nanowire-Intensified Metal-Enhanced Fluorescence in Hybrid Polymer-Plasmonic Electrospun Filaments. *Small* **14**, 1800187 (2018).
135. Cang, H. *et al.* Probing the electromagnetic field of a 15-nanometre hotspot by single molecule imaging. *Nature* **469**, 385–388 (2011).
136. Fu, Y. & Lakowicz, J. R. Enhanced Fluorescence of Cy5-Labeled DNA Tethered to Silver Island Films: Fluorescence Images and Time-Resolved Studies Using Single-Molecule Spectroscopy. *Anal. Chem.* **78**, 6238–6245 (2006).
137. Yuan, H., Khatua, S., Zijlstra, P., Yorulmaz, M. & Orrit, M. Thousand-fold Enhancement of Single-Molecule Fluorescence Near a Single Gold Nanorod. *Angew. Chem. Int. Ed.* **52**, 1217–1221 (2013).
138. Zhou, X. *et al.* Quantitative super-resolution imaging uncovers reactivity patterns on single nanocatalysts. *Nat. Nanotechnol.* **7**, 237–241 (2012).
139. Liebermann, T., Knoll, W., Sluka, P. & Herrmann, R. Complement hybridization from solution to surface-attached probe-oligonucleotides observed by surface-plasmon-field-enhanced fluorescence spectroscopy. *Colloids Surf. Physicochem. Eng. Asp.* **169**, 337–350 (2000).
140. Hoener, B. S. *et al.* Plasmonic Sensing and Control of Single-Nanoparticle Electrochemistry. *Chem* **4**, 1560–1585 (2018).
141. Zhu, J. & Deng, X. Improve the refractive index sensitivity of gold nanotube by reducing the restoring force of localized surface plasmon resonance. *Sens. Actuators B Chem.* **155**, 843–847 (2011).
142. Xu, Z. *et al.* Large-area, uniform and low-cost dual-mode plasmonic naked-eye colorimetry and SERS sensor with handheld Raman spectrometer. *Nanoscale* **8**, 6162–6172 (2016).
143. Nah, S. *et al.* Metal-Enhanced Multiphoton Absorption Polymerization with Gold Nanowires. *J. Phys. Chem. C* **114**, 7774–7779 (2010).
144. Zhou, Y., Chen, J., Zhang, L. & Yang, L. Multifunctional TiO₂-Coated Ag Nanowire Arrays as Recyclable SERS Substrates for the Detection of Organic Pollutants. *Eur. J. Inorg. Chem.* **2012**, 3176–3182 (2012).
145. Cui, L. *et al.* Plasmon-driven catalysis in aqueous solutions probed by SERS spectroscopy. *J. Raman Spectrosc.* **47**, 877–883 (2016).
146. Park, D. H., Kim, M. S. & Joo, J. Hybrid nanostructures using π -conjugated polymers and nanoscale metals: synthesis, characteristics, and optoelectronic applications. *Chem. Soc. Rev.* **39**, 2439 (2010).
147. Knobloch, H., Brunner, H., Leitner, A., Aussenegg, F. & Knoll, W. Probing the evanescent field of propagating plasmon surface polaritons by fluorescence and Raman spectroscopies. *J. Chem. Phys.* **98**, 10093–10095 (1993).
148. Maier, S. A. *Plasmonics: Fundamentals and Applications*. (Springer US, 2007).
149. Zennek, J. Über die Fortpflanzung ebener elektromagnetischer Wellen längs einer ebenen Leiterfläche und ihre Beziehung zur drahtlosen Telegraphie. *Ann. Phys.* **328**, 846–866 (1907).

150. Sommerfeld, A. Über die Ausbreitung der Wellen in der drahtlosen Telegraphie. *Ann. Phys.* **333**, 665–736 (1909).
151. Ferrell, R. A. Angular Dependence of the Characteristic Energy Loss of Electrons Passing Through Metal Foils. *Phys. Rev.* **101**, 554–563 (1956).
152. Cunningham, S. L., Maradudin, A. A. & Wallis, R. F. Effect of a charge layer on the surface-plasmon-polariton dispersion curve. *Phys. Rev. B* **10**, 3342–3355 (1974).
153. Piazza, L. *et al.* Simultaneous observation of the quantization and the interference pattern of a plasmonic near-field. *Nat. Commun.* **6**, 6407 (2015).
154. Wiley, B. J., Lipomi, D. J., Bao, J., Capasso, F. & Whitesides, G. M. Fabrication of Surface Plasmon Resonators by Nanoskiving Single-Crystalline Gold Microplates. *Nano Lett.* **8**, 3023–3028 (2008).
155. Zia, R., Selker, M. D. & Brongersma, M. L. Leaky and bound modes of surface plasmon waveguides. *Phys. Rev. B* **71**, (2005).
156. Kretschmann, E. & Raether, H. Notizen: Radiative Decay of Non Radiative Surface Plasmons Excited by Light. *Z. Für Naturforschung A* **23**, 2135–2136 (1968).
157. Dickson, R. M. & Lyon, L. A. Unidirectional Plasmon Propagation in Metallic Nanowires. *J. Phys. Chem. B* **104**, 6095–6098 (2000).
158. Wild, B. *et al.* Propagation Lengths and Group Velocities of Plasmons in Chemically Synthesized Gold and Silver Nanowires. *ACS Nano* **6**, 472–482 (2012).
159. Otto, A. Excitation of nonradiative surface plasma waves in silver by the method of frustrated total reflection. *Z. Für Phys. Hadrons Nucl.* **216**, 398–410 (1968).
160. He, X., Yang, L. & Yang, T. Optical nanofocusing by tapering coupled photonic-plasmonic waveguides. *Opt. Express* **19**, 12865–12872 (2011).
161. Liu, A. *et al.* Independently analyzing different surface plasmon polariton modes on silver nanowire. *Opt. Express* **22**, 23372–23378 (2014).
162. Fang, Z., Lu, Y., Fan, L., Lin, C. & Zhu, X. Surface Plasmon Polariton Enhancement in Silver Nanowire–Nanoantenna Structure. *Plasmonics* **5**, 57–62 (2010).
163. Knight, M. W. *et al.* Nanoparticle-Mediated Coupling of Light into a Nanowire. *Nano Lett.* **7**, 2346–2350 (2007).
164. Fang, Z. *et al.* Plasmonic Coupling of Bow Tie Antennas with Ag Nanowire. *Nano Lett.* **11**, 1676–1680 (2011).
165. Zhang, S., Gu, C. & Xu, H. Single Nanoparticle Couplers for Plasmonic Waveguides. *Small* **10**, 4264–4269 (2014).
166. Wu, F., Wang, W., Hua, J., Xu, Z. & Li, F. Control on Surface Plasmon Polaritons Propagation Properties by Continuously Moving a Nanoparticle along a Silver Nanowire Waveguide. *Sci. Rep.* **6**, (2016).
167. Barnes, W. L., Dereux, A. & Ebbesen, T. W. Surface plasmon subwavelength optics. *Nature* **424**, 824–830 (2003).
168. Raether, H. *Surface Plasmons on Smooth and Rough Surfaces and on Gratings.* (Springer-Verlag, 1988).
169. Yang, H. U. *et al.* Optical dielectric function of silver. *Phys. Rev. B* **91**, 235137 (2015).
170. Johnson, P. B. & Christy, R. W. Optical Constants of the Noble Metals. *Phys. Rev. B* **6**, 4370–4379 (1972).
171. Thèye, M.-L. Investigation of the Optical Properties of Au by Means of Thin Semitransparent Films. *Phys. Rev. B* **2**, 3060–3078 (1970).

172. Schulz, L. G. The Optical Constants of Silver, Gold, Copper, and Aluminum. I. The Absorption Coefficient k . *JOSA* **44**, 357–362 (1954).
173. Schulz, L. G. & Tangherlini, F. R. Optical Constants of Silver, Gold, Copper, and Aluminum. II. The Index of Refraction n . *JOSA* **44**, 362–368 (1954).
174. Weaver, J. H., Krafka, C., Lynch, D. W. & Koch, E. E. *Optical properties of metals. Pt. 2*. (Fachinformationszentrum Energie, Physik, Mathematik G.m.b.H., 1981).
175. Blanchard, N. P. *et al.* High-resolution measurements of the bulk dielectric constants of single crystal gold with application to reflection anisotropy spectroscopy. *Phys. Status Solidi C* **0**, 2931–2937 (2003).
176. Leveque, G., Olson, C. G. & Lynch, D. W. Reflectance spectra and dielectric functions for Ag in the region of interband transitions. *Phys. Rev. B* **27**, 4654–4660 (1983).
177. Winsemius, P., Kampen, F. F. van, Lengkeek, H. P. & Went, C. G. van. Temperature dependence of the optical properties of Au, Ag and Cu. *J. Phys. F Met. Phys.* **6**, 1583 (1976).
178. Hagemann, H.-J., Gudat, W. & Kunz, C. Optical constants from the far infrared to the x-ray region: Mg, Al, Cu, Ag, Au, Bi, C, and Al₂O₃. *JOSA* **65**, 742–744 (1975).
179. Peale, R. E. *et al.* Propagation of high-frequency surface plasmons on gold. *J. Opt. Soc. Am. B* **25**, 1708–1713 (2008).
180. Kuttge, M. *et al.* Loss mechanisms of surface plasmon polaritons on gold probed by cathodoluminescence imaging spectroscopy. *Appl. Phys. Lett.* **93**, 113110 (2008).
181. Hiramatsu, N. *et al.* Propagation length of mid-infrared surface plasmon polaritons on gold: Impact of morphology change by thermal annealing. *J. Appl. Phys.* **120**, 173103 (2016).
182. Jacob, J., Babu, A., Mathew, G. & Mathew, V. Propagation of surface plasmon polaritons in anisotropic MIM and IMI structures. *Superlattices Microstruct.* **44**, 282–290 (2008).
183. Zervas, M. N. Surface plasmon–polariton waves guided by thin metal films. *Opt. Lett.* **16**, 720–722 (1991).
184. Meng, Y. *et al.* Surface plasmon polaritons on the thin metallic film coated with symmetrical and asymmetrical dielectric gratings. *J. Phys. Appl. Phys.* **50**, 485101 (2017).
185. Bozhevolnyi, S. I., Volkov, V. S., Devaux, E., Laluet, J.-Y. & Ebbesen, T. W. Channel plasmon subwavelength waveguide components including interferometers and ring resonators. *Nature* **440**, 508–511 (2006).
186. Veronis, G. & Fan, S. Modes of Subwavelength Plasmonic Slot Waveguides. *J. Light. Technol.* **25**, 2511–2521 (2007).
187. Dutta, J., Ramakrishna, S. A. & Lakhtakia, A. Characteristics of surface plasmon–polariton waves excited on 2D periodically patterned columnar thin films of silver. *JOSA A* **33**, 1697–1704 (2016).
188. Ashley, J. C. & Emerson, L. C. Dispersion relations for non-radiative surface plasmons on cylinders. *Surf. Sci.* **41**, 615–618 (1974).
189. Pfeiffer, C. A., Economou, E. N. & Ngai, K. L. Surface polaritons in a circularly cylindrical interface: Surface plasmons. *Phys. Rev. B* **10**, 3038–3051 (1974).
190. Prade, B. & Vinet, J. Y. Guided optical waves in fibers with negative dielectric constant. *J. Light. Technol.* **12**, 6–18 (1994).
191. Song, M. Surface plasmon propagation in metal nanowires. (Thesis at Université de Bourgogne, 2012).
192. Miziumski, C. Utilization of a cylindrical geometry to promote radiative interaction with slow surface excitations. *Phys. Lett. A* **40**, 187–188 (1972).

193. Huang, Y., Fang, Y., Zhang, Z., Zhu, L. & Sun, M. Nanowire-supported plasmonic waveguide for remote excitation of surface-enhanced Raman scattering. *Light Sci. Appl.* **3**, e199 (2014).
194. Wei, H. & Xu, H. Plasmonics in composite nanostructures. *Mater. Today* **17**, 372–380 (2014).
195. Song, M. *et al.* Selective excitation of surface plasmon modes propagating in Ag nanowires. *Opt. Express* **25**, 9138 (2017).
196. Sommerfeld, A. Ueber die Fortpflanzung elektrodynamischer Wellen längs eines Drahtes. *Ann. Phys.* **303**, 233–290 (1899).
197. Hondros, D. Über elektromagnetische Drahtwellen. *Ann. Phys.* **335**, 905–950 (1909).
198. Julius Adams Stratton. *Electromagnetic Theory*. (Mcgraw Hill Book Company, 1941).
199. Takahara, J., Yamagishi, S., Taki, H., Morimoto, A. & Kobayashi, T. Guiding of a one-dimensional optical beam with nanometer diameter. *Opt. Lett.* **22**, 475–477 (1997).
200. Novotny, L. & Hafner, C. Light propagation in a cylindrical waveguide with a complex, metallic, dielectric function. *Phys. Rev. E* **50**, 4094–4106 (1994).
201. Weeber, J.-C., Dereux, A., Girard, C., Krenn, J. R. & Goudonnet, J.-P. Plasmon polaritons of metallic nanowires for controlling submicron propagation of light. *Phys. Rev. B* **60**, 9061 (1999).
202. Schröter, U. & Dereux, A. Surface plasmon polaritons on metal cylinders with dielectric core. *Phys. Rev. B* **64**, 125420 (2001).
203. Wang, Y., Ma, Y., Guo, X. & Tong, L. Single-mode plasmonic waveguiding properties of metal nanowires with dielectric substrates. *Opt. Express* **20**, 19006–19015 (2012).
204. Li, Q. & Qiu, M. Plasmonic wave propagation in silver nanowires: guiding modes or not? *Opt. Express* **21**, 8587 (2013).
205. Yu, K., Devadas, M. S., Major, T. A., Lo, S. S. & Hartland, G. V. Surface Plasmon Polariton Propagation and Coupling in Gold Nanostructures. *J. Phys. Chem. C* **118**, 8603–8609 (2014).
206. Wang, Z., Wei, H., Pan, D. & Xu, H. Controlling the radiation direction of propagating surface plasmons on silver nanowires. *Laser Photonics Rev.* **8**, 596–601 (2014).
207. Yang, H., Qiu, M. & Li, Q. Identification and control of multiple leaky plasmon modes in silver nanowires. *Laser Photonics Rev.* **10**, 278–286 (2016).
208. Funes-Hernando, D. *et al.* Coaxial nanowires as plasmon-mediated remote nanosensors. *Nanoscale* **10**, 6437–6444 (2018).
209. Kim, S. & Yan, R. Recent developments in photonic, plasmonic and hybrid nanowire waveguides. *J. Mater. Chem. C* **Advance Article**, (2018).
210. Gervasoni, J. L. Dispersion relations for plasmon excitations in nanostructures of different shapes and symmetries. *Nucl. Instrum. Methods Phys. Res. Sect. B Beam Interact. Mater. At.* **267**, 235–238 (2009).
211. Handapangoda, D., Premaratne, M., Rukhlenko, I. D. & Jagadish, C. Optimal design of composite nanowires for extended reach of surface plasmon-polaritons. *Opt. Express* **19**, 16058–16074 (2011).
212. Zhang, S. *et al.* Chiral Surface Plasmon Polaritons on Metallic Nanowires. *Phys. Rev. Lett.* **107**, 096801 (2011).
213. Zhang, S. & Xu, H. Optimizing Substrate-Mediated Plasmon Coupling toward High-Performance Plasmonic Nanowire Waveguides. *ACS Nano* **6**, 8128–8135 (2012).
214. Wei, H. *et al.* Quantum Dot-Based Local Field Imaging Reveals Plasmon-Based Interferometric Logic in Silver Nanowire Networks. *Nano Lett.* **11**, 471–475 (2011).
215. Nauert, S. *et al.* Influence of Cross Sectional Geometry on Surface Plasmon Polariton Propagation in Gold Nanowires. *ACS Nano* **8**, 572–580 (2014).

216. Huang, Y., Fang, Y. & Sun, M. Remote Excitation of Surface-Enhanced Raman Scattering on Single Au Nanowire with Quasi-Spherical Termini. *J. Phys. Chem. C* **115**, 3558–3561 (2011).
217. Guo, X. *et al.* Direct Coupling of Plasmonic and Photonic Nanowires for Hybrid Nanophotonic Components and Circuits. *Nano Lett.* **9**, 4515–4519 (2009).
218. Graff, A., Wagner, D., Ditlbacher, H. & Kreibig, U. Silver nanowires. *Eur. Phys. J. D* **34**, 263–269 (2005).
219. Akimov, A. V. *et al.* Generation of single optical plasmons in metallic nanowires coupled to quantum dots. *Nature* **450**, 402–406 (2007).
220. Krenn, J. R. *et al.* Non-diffraction-limited light transport by gold nanowires. *Europhys. Lett. EPL* **60**, 663–669 (2002).
221. Ditlbacher, H. *et al.* Silver Nanowires as Surface Plasmon Resonators. *Phys. Rev. Lett.* **95**, 257403 (2005).
222. Pyayt, A. L., Wiley, B., Xia, Y., Chen, A. & Dalton, L. Integration of photonic and silver nanowire plasmonic waveguides. *Nat. Nanotechnol.* **3**, 660–665 (2008).
223. Li, X., Li, W., Guo, X., Lou, J. & Tong, L. All-fiber hybrid photon-plasmon circuits: integrating nanowire plasmonics with fiber optics. *Opt. Express* **21**, 15698 (2013).
224. Fedutik, Y., Temnov, V. V., Schöps, O., Woggon, U. & Artemyev, M. V. Exciton-Plasmon-Photon Conversion in Plasmonic Nanostructures. *Phys. Rev. Lett.* **99**, 136802 (2007).
225. Wei, H., Ratchford, D., Li, X. (Elaine), Xu, H. & Shih, C.-K. Propagating Surface Plasmon Induced Photon Emission from Quantum Dots. *Nano Lett.* **9**, 4168–4171 (2009).
226. Yan, R., Pausauskie, P., Huang, J. & Yang, P. Direct photonic-plasmonic coupling and routing in single nanowires. *Proc. Natl. Acad. Sci.* **106**, 21045–21050 (2009).
227. Shegai, T., Huang, Y., Xu, H. & Käll, M. Coloring fluorescence emission with silver nanowires. *Appl. Phys. Lett.* **96**, 103114 (2010).
228. Lee, H. S. *et al.* Efficient Exciton-Plasmon Conversion in Ag Nanowire/Monolayer MoS₂ Hybrids: Direct Imaging and Quantitative Estimation of Plasmon Coupling and Propagation. *Adv. Opt. Mater.* **3**, 943–947 (2015).
229. de Torres, J., Ferrand, P., Colas des Francs, G. & Wenger, J. Coupling Emitters and Silver Nanowires to Achieve Long-Range Plasmon-Mediated Fluorescence Energy Transfer. *ACS Nano* **10**, 3968–3976 (2016).
230. Verhagen, E., Spasenović, M., Polman, A. & Kuipers, L. (Kobus). Nanowire Plasmon Excitation by Adiabatic Mode Transformation. *Phys. Rev. Lett.* **102**, 203904 (2009).
231. Nelayah, J. *et al.* Mapping surface plasmons on a single metallic nanoparticle. *Nat. Phys.* **3**, 348–353 (2007).
232. Vesseur, E. J. R., de Waele, R., Kuttge, M. & Polman, A. Direct Observation of Plasmonic Modes in Au Nanowires Using High-Resolution Cathodoluminescence Spectroscopy. *Nano Lett.* **7**, 2843–2846 (2007).
233. Zhang, Y. *et al.* Edge scattering of surface plasmons excited by scanning tunneling microscopy. *Opt. Express* **21**, 13938–13948 (2013).
234. Boer-Duchemin, E., Wang, T., Le Moal, E. & Dujardin, G. Electrically driven surface plasmon nanosources. in *Ultrafast Phenomena and Nanophotonics XIX* (eds. Betz, M., Elezzabi, A. Y. & Tsen, K.-T.) **9361**, 93610R (SPIE, 2015).
235. Canneson, D. *et al.* Surface plasmon polariton beams from an electrically excited plasmonic crystal. *Opt. Express* **24**, 26186–26200 (2016).
236. Cao, S. *et al.* Revealing the spectral response of a plasmonic lens using low-energy electrons. *Phys. Rev. B* **96**, 115419 (2017).

237. Hutchison, J. A. *et al.* Subdiffraction Limited, Remote Excitation of Surface Enhanced Raman Scattering. *Nano Lett.* **9**, 995–1001 (2009).
238. Solis, D. *et al.* Bleach-Imaged Plasmon Propagation (BIIPP) in Single Gold Nanowires. *Nano Lett.* **10**, 3482–3485 (2010).
239. Paul, A. *et al.* Identification of Higher Order Long-Propagation-Length Surface Plasmon Polariton Modes in Chemically Prepared Gold Nanowires. *ACS Nano* **6**, 8105–8113 (2012).
240. Staleva, H. *et al.* Coupling to light, and transport and dissipation of energy in silver nanowires. *Phys. Chem. Chem. Phys.* **11**, 5889–5896 (2009).
241. Lo, S. S., Shi, H. Y., Huang, L. & Hartland, G. V. Imaging the extent of plasmon excitation in Au nanowires using pump-probe microscopy. *Opt. Lett.* **38**, 1265–1267 (2013).
242. Johns, P., Yu, K., Devadas, M. S. & Hartland, G. V. Role of Resonances in the Transmission of Surface Plasmon Polaritons between Nanostructures. *ACS Nano* **10**, 3375–3381 (2016).
243. Kim, S., Bailey, S., Liu, M. & Yan, R. Decoupling co-existing surface plasmon polariton (SPP) modes in a nanowire plasmonic waveguide for quantitative mode analysis. *Nano Res.* **10**, 2395–2404 (2017).
244. Brongersma, M. L., Halas, N. J. & Nordlander, P. Plasmon-induced hot carrier science and technology. *Nat. Nanotechnol.* **10**, 25–34 (2015).
245. Schneider, N. L., Schull, G. & Berndt, R. Optical Probe of Quantum Shot-Noise Reduction at a Single-Atom Contact. *Phys. Rev. Lett.* **105**, 026601 (2010).
246. Nienhaus, H. Electronic excitations by chemical reactions on metal surfaces. *Surf. Sci. Rep.* **45**, 1–78 (2002).
247. Mukherjee, S. *et al.* Hot Electrons Do the Impossible: Plasmon-Induced Dissociation of H₂ on Au. *Nano Lett.* **13**, 240–247 (2013).
248. Conklin, D. *et al.* Exploiting Plasmon-Induced Hot Electrons in Molecular Electronic Devices. *ACS Nano* **7**, 4479–4486 (2013).
249. Lin, W. *et al.* Physical mechanism on exciton-plasmon coupling revealed by femtosecond pump-probe transient absorption spectroscopy. *Mater. Today Phys.* **3**, 33–40 (2017).
250. Prymaczek, A. *et al.* Remote activation and detection of up-converted luminescence via surface plasmon polaritons propagating in a silver nanowire. *Nanoscale* **10**, 12841–12847 (2018).
251. Törmä, P. & Barnes, W. L. Strong coupling between surface plasmon polaritons and emitters: a review. *Rep. Prog. Phys.* **78**, 013901 (2015).
252. Paschotta, R. Rabi oscillations. in *Encyclopedia of Laser Physics and Technology* **2**, 856 (Wiley-VCH, 2008).
253. Wang, W. *et al.* The rich photonic world of plasmonic nanoparticle arrays. *Mater. Today* **21**, 303–314 (2018).
254. Pustovit, V. N. & Shahbazyan, T. V. Cooperative emission of light by an ensemble of dipoles near a metal nanoparticle: The plasmonic Dicke effect. *Phys. Rev. Lett.* **102**, 077401 (2009).
255. Aberra Guebrou, S. *et al.* Coherent Emission from a Disordered Organic Semiconductor Induced by Strong Coupling with Surface Plasmons. *Phys. Rev. Lett.* **108**, 066401 (2012).
256. Gómez, D. E., Vernon, K. C., Mulvaney, P. & Davis, T. J. Surface Plasmon Mediated Strong Exciton–Photon Coupling in Semiconductor Nanocrystals. *Nano Lett.* **10**, 274–278 (2010).
257. Passmore, B. S. *et al.* Observation of Rabi Splitting from Surface Plasmon Coupled Conduction State Transitions in Electrically Excited InAs Quantum Dots. *Nano Lett.* **11**, 338–342 (2011).

258. Velizhanin, K. A. & Shahbazyan, T. V. Exciton-plasmaritons in graphene/semiconductor structures. *Phys. Rev. B* **90**, 085403 (2014).
259. Lidzey, D. G. *et al.* Room Temperature Polariton Emission from Strongly Coupled Organic Semiconductor Microcavities. *Phys. Rev. Lett.* **82**, 3316–3319 (1999).
260. Bellessa, J., Bonnand, C., Plenet, J. C. & Mugnier, J. Strong Coupling between Surface Plasmons and Excitons in an Organic Semiconductor. *Phys. Rev. Lett.* **93**, 036404 (2004).
261. Dintinger, J., Klein, S., Bustos, F., Barnes, W. L. & Ebbesen, T. W. Strong coupling between surface plasmon-polaritons and organic molecules in subwavelength hole arrays. *Phys. Rev. B* **71**, 035424 (2005).
262. Cho, C.-H. *et al.* Tailoring hot-exciton emission and lifetimes in semiconducting nanowires via whispering-gallery nanocavity plasmons. *Nat. Mater.* **10**, 669–675 (2011).
263. Park, D. H. *et al.* Light-Emitting Color Barcode Nanowires Using Polymers: Nanoscale Optical Characteristics. *ACS Nano* **4**, 5155–5162 (2010).
264. Lee, S. J. & Moskovits, M. Remote Sensing by Plasmonic Transport. *J. Am. Chem. Soc.* **134**, 11384–11387 (2012).
265. Chang, D. E., Sørensen, A. S., Hemmer, P. R. & Lukin, M. D. Quantum Optics with Surface Plasmons. *Phys. Rev. Lett.* **97**, (2006).
266. Fang, Y., Wei, H., Hao, F., Nordlander, P. & Xu, H. Remote-Excitation Surface-Enhanced Raman Scattering Using Propagating Ag Nanowire Plasmons. *Nano Lett.* **9**, 2049–2053 (2009).
267. Coca-López, N. *et al.* Remote excitation and detection of surface-enhanced Raman scattering from graphene. *Nanoscale* **10**, 10498–10504 (2018).
268. Sun, M., Hou, Y. & Xu, H. Can information of chemical reaction propagate with plasmonic waveguide and be detected at remote terminal of nanowire? *Nanoscale* **3**, 4114–4116 (2011).
269. Dasgupta, A., Singh, D., Tandon, S., Tripathi, R. P. N. & Kumar, G. V. P. Remote-excitation surface-enhanced Raman scattering with counter-propagating plasmons: silver nanowire-nanoparticle system. *J. Nanophotonics* **8**, 083899 (2013).
270. Lu, G. *et al.* Live-Cell SERS Endoscopy Using Plasmonic Nanowire Waveguides. *Adv. Mater.* **26**, 5124–5128 (2014).
271. Fujita, Y., Walke, P., Feyter, S. D. & Uji-i, H. Remote excitation-tip-enhanced Raman scattering microscopy using silver nanowire. *Jpn. J. Appl. Phys.* **55**, 08NB03 (2016).
272. Chikkaraddy, R., Singh, D. & Pavan Kumar, G. V. Plasmon assisted light propagation and Raman scattering hot-spot in end-to-end coupled silver nanowire pairs. *Appl. Phys. Lett.* **100**, 043108 (2012).
273. Zhang, Z., Fang, Y., Wang, W., Chen, L. & Sun, M. Propagating Surface Plasmon Polaritons: Towards Applications for Remote-Excitation Surface Catalytic Reactions. *Adv. Sci.* **3**, 1500215 (2016).
274. Lin, W., Xu, X., Quan, J. & Sun, M. Propagating surface plasmon polaritons for remote excitation surface-enhanced Raman scattering spectroscopy. *Appl. Spectrosc. Rev.* **53**, 771–782 (2018).
275. Berweger, S., Atkin, J. M., Olmon, R. L. & Raschke, M. B. Adiabatic Tip-Plasmon Focusing for Nano-Raman Spectroscopy. *J. Phys. Chem. Lett.* **1**, 3427–3432 (2010).
276. Sun, M., Hou, Y., Li, Z., Liu, L. & Xu, H. Remote Excitation Polarization-Dependent Surface Photochemical Reaction by Plasmonic Waveguide. *Plasmonics* **6**, 681–687 (2011).
277. Dasgupta, A., Singh, D. & Pavan Kumar, G. V. Dual-path remote-excitation surface enhanced Raman microscopy with plasmonic nanowire dimer. *Appl. Phys. Lett.* **103**, 151114 (2013).
278. Sun, M. *et al.* Remotely excited Raman optical activity using chiral plasmon propagation in Ag nanowires. *Light Sci. Appl.* **2**, e112 (2013).

279. Le Ouay, B. & Stellacci, F. Antibacterial activity of silver nanoparticles: A surface science insight. *Nano Today* **10**, 339–354 (2015).
280. Zhang, Y. *et al.* Novel Use of Poly(3,4-ethylenedioxythiophene) Nanoparticles for Fluorescent Nucleic Acid Detection. *ACS Comb. Sci.* **14**, 191–196 (2012).
281. Prasad, K. P. *et al.* Fluorescent quantum dots derived from PEDOT and their applications in optical imaging and sensing. *Mater. Horiz.* **1**, 529–534 (2014).
282. Fedutik, Y., Temnov, V., Woggon, U., Ustinovich, E. & Artemyev, M. Exciton–Plasmon Interaction in a Composite Metal–Insulator–Semiconductor Nanowire System. *J. Am. Chem. Soc.* **129**, 14939–14945 (2007).
283. Wei, H. *et al.* Plasmon Waveguiding in Nanowires. *Chem. Rev.* **118**, 2882–2926 (2018).
284. Chang, D. E., Sørensen, A. S., Hemmer, P. R. & Lukin, M. D. Strong coupling of single emitters to surface plasmons. *Phys. Rev. B* **76**, (2007).
285. Bouchet, D., Cao, D., Carminati, R., De Wilde, Y. & Krachmalnicoff, V. Long-Range Plasmon Assisted Energy Transfer Between Two Fluorescent Emitters. *Phys. Rev. Lett.* **116**, 037401 (2015).
286. Yan, R. *et al.* Nanowire-based single-cell endoscopy. *Nat. Nanotechnol.* **7**, 191–196 (2012).
287. Bergman, D. J. & Stockman, M. I. Surface Plasmon Amplification by Stimulated Emission of Radiation: Quantum Generation of Coherent Surface Plasmons in Nanosystems. *Phys. Rev. Lett.* **90**, 027402 (2003).
288. Noginov, M. A. *et al.* Demonstration of a spaser-based nanolaser. *Nature* **460**, 1110–1112 (2009).
289. Oulton, R. F. Surface plasmon lasers: sources of nanoscopic light. *Mater. Today* **15**, 26–34 (2012).
290. Wu, X. *et al.* Hybrid Photon-Plasmon Nanowire Lasers. *Nano Lett.* **13**, 5654–5659 (2013).
291. Sirtori, C., Gmachl, C., Capasso, F., Hutchinson, A. L. & Cho, A. Y. Long-wavelength ($\lambda \approx 8\text{--}11.5\ \mu\text{m}$) semiconductor lasers with waveguides based on surface plasmons. *Opt. Soc. Am.* **23**, 1366–1368 (1998).
292. Deng, P., Hong, W. & Hong-Xing, X. Metallic nanowires for subwavelength waveguiding and nanophotonic devices. *Chin. Phys. B* **22**, 097305 (2013).
293. Gao, L., Chen, L., Wei, H. & Xu, H. Lithographically fabricated gold nanowire waveguides for plasmonic routers and logic gates. *Nanoscale* **10**, 11923–11929 (2018).
294. Goyadinov, A. A. & Podolskiy, V. A. Gain-Assisted Slow to Superluminal Group Velocity Manipulation in Nanowaveguides. *Phys. Rev. Lett.* **97**, 223902 (2006).
295. Zhang, L., Lou, J. & Tong, L. Micro/nanofiber optical sensors. *Photonic Sens.* **1**, 31–42 (2011).
296. Yang, Z.-J. *et al.* Surface plasmons amplifications in single Ag nanoring. *Opt. Express* **18**, 4006–4011 (2010).
297. Suárez, I. *et al.* Propagation length enhancement of surface plasmon polaritons in gold nano-/micro-waveguides by the interference with photonic modes in the surrounding active dielectrics. *Nanophotonics* **6**, 1109–1120 (2017).
298. Hill, M. T. *et al.* Lasing in metal-insulator-metal sub-wavelength plasmonic waveguides. *Opt. Express* **17**, 11107–11112 (2009).
299. Oulton, R. F. *et al.* Plasmon lasers at deep subwavelength scale. *Nature* **461**, 629–632 (2009).
300. De Leon, I. & Berini, P. Amplification of long-range surface plasmons by a dipolar gain medium. *Nat. Photonics* **4**, 382–387 (2010).
301. Ding, K. *et al.* Room-temperature continuous wave lasing in deep-subwavelength metallic cavities under electrical injection. *Phys. Rev. B* **85**, 041301 (2012).

302. Sidiropoulos, T. P. H. *et al.* Ultrafast plasmonic nanowire lasers near the surface plasmon frequency. *Nat. Phys.* **10**, 870–876 (2014).
303. Bermúdez-Ureña, E. *et al.* Plasmonic Waveguide-Integrated Nanowire Laser. *Nano Lett.* **17**, 747–754 (2017).
304. Mühlischlegel, P., Eisler, H.-J., Martin, O. J. F., Hecht, B. & Pohl, D. W. Resonant Optical Antennas. *Science* **308**, 1607–1609 (2005).
305. Li, Z. *et al.* Correlation between Incident and Emission Polarization in Nanowire Surface Plasmon Waveguides. *Nano Lett.* **10**, 1831–1835 (2010).
306. Wang, Y., Cai, W., Yang, M., Liu, Z. & Shang, G. The simulation study of the plasmonic coupling effect for the Ag nanoparticle-nanowire structure. *J. Korean Phys. Soc.* **66**, 261–265 (2015).
307. Wessel, J. Surface-enhanced optical microscopy. *JOSA B* **2**, 1538–1541 (1985).
308. Huang, J.-S., Feichtner, T., Biagioni, P. & Hecht, B. Impedance Matching and Emission Properties of Nanoantennas in an Optical Nanocircuit. *Nano Lett.* **9**, 1897–1902 (2009).
309. Hao, F. & Nordlander, P. Plasmonic coupling between a metallic nanosphere and a thin metallic wire. *Appl. Phys. Lett.* **89**, 103101 (2006).
310. Heavens, O. S. *Optical Properties of Thin Solid Films*. (Courier Corporation, 1991).
311. Xia, Y. *et al.* One-Dimensional Nanostructures: Synthesis, Characterization, and Applications. *Adv. Mater.* **15**, 353–389 (2003).
312. Pisignano, D., Persano, L. & Camposeo, A. Perspectives: Nanofibers and nanowires for disordered photonics. *APL Mater.* **5**, 035301 (2017).
313. Dorfmueller, J. *et al.* Fabry-Pérot Resonances in One-Dimensional Plasmonic Nanostructures. *Nano Lett.* **9**, 2372–2377 (2009).
314. Naik, J. P. Nanowires fabricated by Focused Ion Beam. (Thesis at University of Birmingham, 2013).
315. Francioso, L. & Siciliano, P. Top-down contact lithography fabrication of a TiO₂ nanowire array over a SiO₂ mesa. *Nanotechnology* **17**, 3761 (2006).
316. Demami, F., Pichon, L., Rogel, R. & Salaün, A. C. Fabrication of polycrystalline silicon nanowires using conventional UV lithography. *IOP Conf. Ser. Mater. Sci. Eng.* **6**, 012014 (2009).
317. Helt, J. M., Drain, C. M. & Bazzan, G. Stamping Patterns of Insulated Gold Nanowires with Self-Organized Ultrathin Polymer Films. *J. Am. Chem. Soc.* **128**, 9371–9377 (2006).
318. Hwang, J. K., Cho, S., Seo, E. K., Myoung, J. M. & Sung, M. M. Large-Area Fabrication of Patterned ZnO-Nanowire Arrays Using Light Stamping Lithography. *ACS Appl. Mater. Interfaces* **1**, 2843–2847 (2009).
319. Hoh, M., Werbin, J. L., Dumas, J. K., Heinz, W. F. & Hoh, J. H. Nanometer-Scale Embossing of Polydimethylsiloxane. *Langmuir* **26**, 2187–2190 (2010).
320. Lee, S. H. *et al.* A soft lithographic approach to fabricate InAs nanowire field-effect transistors. *Sci. Rep.* **8**, 3204 (2018).
321. von Ahnen, I., Piret, G. & Prinz, C. N. Transfer of vertical nanowire arrays on polycaprolactone substrates for biological applications. *Microelectron. Eng.* **135**, 52–56 (2015).
322. von Ahnen, I., Piret, G. & Prinz, C. N. Transfer of vertical nanowire arrays on polycaprolactone substrates for biological applications. *Microelectron. Eng.* **135**, 52–56 (2015).
323. Ozel, T. *Coaxial Lithography*. (Springer International Publishing, 2016).
324. Lee, S. T., Wang, N., Zhang, Y. F. & Tang, Y. H. Oxide-Assisted Semiconductor Nanowire Growth. *MRS Bull.* **24**, 36–42 (1999).

325. Pérez-Juste, J., Pastoriza-Santos, I., Liz-Marzán, L. M. & Mulvaney, P. Gold nanorods: Synthesis, characterization and applications. *Coord. Chem. Rev.* **249**, 1870–1901 (2005).
326. Lu, G., Li, C., Shen, J., Chen, Z. & Shi, G. Preparation of Highly Conductive Gold–Poly(3,4-ethylenedioxythiophene) Nanocables and Their Conversion to Poly(3,4-ethylenedioxythiophene) Nanotubes. *J. Phys. Chem. C* **111**, 5926–5931 (2007).
327. Hu, J., Odom, T. W. & Lieber, C. M. Chemistry and Physics in One Dimension: Synthesis and Properties of Nanowires and Nanotubes. *Acc. Chem. Res.* **32**, 435–445 (1999).
328. Dong, B. *et al.* Local and Remote Charge-Transfer-Enhanced Raman Scattering on One-Dimensional Transition-Metal Oxides. *Chem. – Asian J.* **5**, 1824–1829 (2010).
329. Ek, M. & Filler, M. A. Atomic-Scale Choreography of Vapor–Liquid–Solid Nanowire Growth. *Acc. Chem. Res.* **51**, 118–126 (2018).
330. Possin, G. E. A Method for Forming Very Small Diameter Wires. *Rev. Sci. Instrum.* **41**, 772–774 (1970).
331. Liang, W. & Martin, C. R. Template-synthesized polyacetylene fibrils show enhanced supermolecular order. *J. Am. Chem. Soc.* **112**, 9666–9668 (1990).
332. Martin, C. R. Nanomaterials - A membrane-based synthetic approach. *Science* **266**, 1961–1966 (1994).
333. Ozel, T., Bourret, G. R. & Mirkin, C. A. Coaxial lithography. *Nat. Nanotechnol.* **10**, 319–324 (2015).
334. Wen, L., Xu, R., Mi, Y. & Lei, Y. Multiple nanostructures based on anodized aluminium oxide templates. *Nat. Nanotechnol.* **12**, 244–250 (2016).
335. Aldissi, M. Molecular and supramolecular orientation in polyacetylene. *J. Polym. Sci. Part C Polym. Lett.* **27**, 105–110 (1989).
336. Kijima, T. *et al.* Noble-Metal Nanotubes (Pt, Pd, Ag) from Lyotropic Mixed-Surfactant Liquid-Crystal Templates. *Angew. Chem. Int. Ed.* **43**, 228–232 (2004).
337. Fullam, S., Cottell, D., Rensmo, H. & Fitzmaurice, D. Carbon Nanotube Templated Self-Assembly and Thermal Processing of Gold Nanowires. *Adv. Mater.* **12**, 1430–1432 (2000).
338. Yin, Y., Lu, Y., Gates, B. & Xia, Y. Template-Assisted Self-Assembly: A Practical Route to Complex Aggregates of Monodispersed Colloids with Well-Defined Sizes, Shapes, and Structures. *J. Am. Chem. Soc.* **123**, 8718–8729 (2001).
339. Paik, T., Diroll, B. T., Kagan, C. R. & Murray, C. B. Binary and Ternary Superlattices Self-Assembled from Colloidal Nanodisks and Nanorods. *J. Am. Chem. Soc.* **137**, 6662–6669 (2015).
340. Yu, S.-Y. *et al.* Single-Crystalline Gold Nanowires Synthesized from Light-Driven Oriented Attachment and Plasmon-Mediated Self-Assembly of Gold Nanorods or Nanoparticles. *Sci. Rep.* **7**, 44680 (2017).
341. Taylor, G. F. A Method of Drawing Metallic Filaments and a Discussion of their Properties and Uses. *Phys. Rev.* **23**, 655–660 (1924).
342. Donald, I. W. Production, properties and applications of microwire and related products. *J. Mater. Sci.* **22**, 2661–2679 (1987).
343. Penner, R. M., Heben, M. J., Longin, T. L. & Lewis, N. S. Fabrication and Use of Nanometer-Sized Electrodes in Electrochemistry. *Science* **250**, 1118–1121 (1990).
344. Tonucci, R. J., Justus, B. L., Campillo, A. J. & Ford, C. E. Nanochannel Array Glass. *Science* **258**, 783–785 (1992).
345. Xia, Y. *et al.* Complex Optical Surfaces Formed by Replica Molding Against Elastomeric Masters. *Science* **273**, 347–349 (1996).

346. Arinstein, A., Burman, M., Gendelman, O. & Zussman, E. Effect of supramolecular structure on polymer nanofibre elasticity. *Nat. Nanotechnol.* **2**, 59–62 (2007).
347. Camposeo, A. *et al.* Local Mechanical Properties of Electrospun Fibers Correlate to Their Internal Nanostructure. *Nano Lett.* **13**, 5056–5062 (2013).
348. Lefort, R., Duvail, J.-L., Corre, T., Zhao, Y. & Morineau, D. Phase separation of a binary liquid in anodic aluminium oxide templates. *Eur. Phys. J. E* **34**, 71 (2011).
349. Williams, W. D. & Giordano, N. Fabrication of 80 Å metal wires. *Rev. Sci. Instrum.* **55**, 410–412 (1984).
350. Penner, R. M. & Martin, C. R. Controlling the morphology of electronically conductive polymers. *J. Electrochem. Soc.* **133**, 2206–2207 (1986).
351. Penner, R. M. & Martin, C. R. Preparation and Electrochemical Characterization of Ultramicroelectrode Ensembles. *Anal. Chem.* **59**, 2625–2630 (1987).
352. Ferain, E. & Legras, R. Heavy ion tracks in polycarbonate. Comparison with a heavy ion irradiated model compound (diphenyl carbonate). *Nucl. Instrum. Methods Phys. Res. Sect. B Beam Interact. Mater. At.* **82**, 539–548 (1993).
353. Ferain, E. & Legras, R. Track-etched membrane: dynamics of pore formation. *Nucl. Instrum. Methods Phys. Res. Sect. B Beam Interact. Mater. At.* **84**, 331–336 (1994).
354. Diggle, J. W., Downie, T. C. & Goulding, C. W. Anodic oxide films on aluminum. *Chem. Rev.* **69**, 365–405 (1969).
355. Wu, C.-G. & Bein, T. Conducting polyaniline filaments in a mesoporous channel host. *Science* 1757–1759 (1994).
356. Al-Mawlawi, D., Liu, C. Z. & Moskovits, M. Nanowires formed in anodic oxide nanotemplates. *J. Mater. Res.* **9**, 1014–1018 (1994).
357. Martin, C. R. Membrane-based synthesis of nanomaterials. *Chem. Mater.* **8**, 1739–1746 (1996).
358. Bigeon, J. Propagation sub-longueur d'onde au sein de nanotubes et nanofils polymères passifs et actifs. (Thesis at Université Rennes 1, 2014).
359. Lee, W. & Park, S.-J. Porous Anodic Aluminum Oxide: Anodization and Templated Synthesis of Functional Nanostructures. *Chem. Rev.* **114**, 7487–7556 (2014).
360. Zhou, H., Zhou, W., Adzic, R. R. & Wong, S. S. Enhanced Electrocatalytic Performance of One-Dimensional Metal Nanowires and Arrays Generated via an Ambient, Surfactantless Synthesis. *J. Phys. Chem. C* **113**, 5460–5466 (2009).
361. Van Dyke, L. S. & Martin, C. R. Electrochemical Investigations of Electronically Conductive Polymers. 4. Controlling the Supermolecular Structure Allows Charge Transport Rates To Be Enhanced. *Langmuir* **6**, 1118–1123 (1990).
362. Routkevitch, D., Bigioni, T., Moskovits, M. & Xu, J. M. Electrochemical Fabrication of CdS Nanowire Arrays in Porous Anodic Aluminum Oxide Templates. *J. Phys. Chem. A* **100**, 14037–14047 (1996).
363. Sawyer, D. T., Sobkowiak, A. & Roberts, J. L. *Electrochemistry for Chemists*. (Wiley-Interscience, 1995).
364. Petrucci, R. H., Harwood, W. S. & Herring, F. G. *Química General*. (Pearson Education, 2002).
365. Schider, G. *et al.* Plasmon dispersion relation of Au and Ag nanowires. *Phys. Rev. B* **68**, (2003).
366. Vigonski, S. *et al.* Au nanowire junction breakup through surface atom diffusion. *Nanotechnology* **29**, 015704 (2018).
367. Hariri, M. B., Dolati, A. & Moakhar, R. S. The Potentiostatic Electrodeposition of Gold Nanowire/Nanotube in H₂AuCl₄ Solutions Based on the Model of Recessed Cylindrical Ultramicroelectrode Array. *J. Electrochem. Soc.* **160**, D279–D288 (2013).

368. Chauvin, A. *et al.* Large-Scale Fabrication of Porous Gold Nanowires via Laser Interference Lithography and Dealloying of Gold–Silver Nano-Alloys. *Micromachines* **8**, 168 (2017).
369. Murphy, C. J., Gole, A. M., Hunyadi, S. E. & Orendorff, C. J. One-Dimensional Colloidal Gold and Silver Nanostructures. *Inorg. Chem.* **45**, 7544–7554 (2006).
370. Mitschang, F., Langner, M., Vieker, H., Beyer, A. & Greiner, A. Preparation of Conductive Gold Nanowires in Confined Environment of Gold-Filled Polymer Nanotubes. *Macromol. Rapid Commun.* **36**, 304–310 (2015).
371. Reynes, O. & Demoustier-Champagne, S. Template Electrochemical Growth of Polypyrrole and Gold-Polypyrrole-Gold Nanowire Arrays. *J. Electrochem. Soc.* **152**, D130–D135 (2005).
372. Ozin, G. A. Nanochemistry: Synthesis in diminishing dimensions. *Adv. Mater.* **4**, 612–649 (1992).
373. Schönenberger, C. *et al.* Template synthesis of nanowires in porous polycarbonate membranes: electrochemistry and morphology. *J. Phys. Chem. B* **101**, 5497–5505 (1997).
374. Duvail, J. L. *et al.* Transport and vibrational properties of poly (3, 4-ethylenedioxythiophene) nanofibers. *Synth. Met.* **131**, 123–128 (2002).
375. Retho, P. Propriétés physiques de nanofils de polymères conducteurs préparés par la méthode template. (Thesis at Université de Nantes, 2003).
376. Lahav, M., Weiss, E. A., Xu, Q. & Whitesides, G. M. Core–Shell and Segmented Polymer–Metal Composite Nanostructures. *Nano Lett.* **6**, 2166–2171 (2006).
377. Xiao, R., Cho, S. I., Liu, R. & Lee, S. B. Controlled Electrochemical Synthesis of Conductive Polymer Nanotube Structures. *J. Am. Chem. Soc.* **129**, 4483–4489 (2007).
378. Letheby, H. XXIX.—On the production of a blue substance by the electrolysis of sulphate of aniline. *J. Chem. Soc.* **15**, 161–163 (1862).
379. Tanaka, K., Shichiri, T., Wang, S. & Yamabe, T. A study of the electropolymerization of thiophene. *Synth. Met.* **24**, 203–215 (1988).
380. Sakmeche, N. *et al.* Improvement of the Electrosynthesis and Physicochemical Properties of Poly(3,4-ethylenedioxythiophene) Using a Sodium Dodecyl Sulfate Micellar Aqueous Medium. *Langmuir* **15**, 2566–2574 (1999).
381. Kumru, M. E., Springer, J., Saraç, A. S. & Bismarck, A. Electrografting of thiophene, carbazole, pyrrole and their copolymers onto carbon fibers: electrokinetic measurements, surface composition and morphology. *Synth. Met.* **123**, 391–401 (2001).
382. Smela, E. Conjugated Polymer Actuators for Biomedical Applications. *Adv. Mater.* **15**, 481–494 (2003).
383. Kirchmeyer, S. & Reuter, K. Scientific importance, properties and growing applications of poly(3,4-ethylenedioxythiophene). *J. Mater. Chem.* **15**, 2077–2088 (2005).
384. Li, C., Bai, H. & Shi, G. Conducting polymer nanomaterials: electrosynthesis and applications. *Chem. Soc. Rev.* **38**, 2397–2409 (2009).
385. Heinze, J., Frontana-Urbe, B. A. & Ludwigs, S. Electrochemistry of Conducting Polymers—Persistent Models and New Concepts. *Chem. Rev.* **110**, 4724–4771 (2010).
386. Ouyang, L. *et al.* Enhanced PEDOT adhesion on solid substrates with electrografted P(EDOT-NH₂). *Sci. Adv.* **3**, e1600448 (2017).
387. Garreau, S., Duvail, J. L. & Louarn, G. Spectroelectrochemical studies of poly(3,4-ethylenedioxythiophene) in aqueous medium. *Synth. Met.* **125**, 325–329 (2001).
388. Duvail, J. L. *et al.* Effects of the Confined Synthesis on Conjugated Polymer Transport Properties. *J. Phys. Chem. B* **108**, 18552–18556 (2004).

389. Duvail, J. L., Long, Y., Cuenot, S., Chen, Z. & Gu, C. Tuning electrical properties of conjugated polymer nanowires with the diameter. *Appl. Phys. Lett.* **90**, 102114 (2007).
390. Jonas, F. & Schrader, L. Conductive modifications of polymers with polypyrroles and polythiophenes. *Synth. Met.* **41**, 831–836 (1991).
391. Groenendaal, L., Jonas, F., Freitag, D., Pielartzik, H. & Reynolds, J. R. Poly(3,4-ethylenedioxythiophene) and Its Derivatives: Past, Present, and Future. *Adv. Mater.* **12**, 481–494 (2000).
392. Łapkowski, M. & Proń, A. Electrochemical oxidation of poly(3,4-ethylenedioxythiophene) — “in situ” conductivity and spectroscopic investigations. *Synth. Met.* **110**, 79–83 (2000).
393. Qi, W. *et al.* Core-Shell Nanostructures: Modeling, Fabrication, Properties, and Applications. *J. Nanomater.* **2012**, 1–2 (2012).
394. El-Toni, A. M. *et al.* Design, synthesis and applications of core-shell, hollow core, and nanorattle multifunctional nanostructures. *Nanoscale* **8**, 2510–2531 (2016).
395. Zhu, X., Wu, L., Mungra, D. C., Xia, S. & Zhu, J. Au@SiO₂ core-shell nanoparticles for laser desorption/ionization time of flight mass spectrometry. *Analyst* **137**, 2454–2458 (2012).
396. Zhuang, Z., Peng, Q. & Li, Y. Controlled synthesis of semiconductor nanostructures in the liquid phase. *Chem. Soc. Rev.* **40**, 5492–5513 (2011).
397. Son, S. U. *et al.* Designed Synthesis of Atom-Economical Pd/Ni Bimetallic Nanoparticle-Based Catalysts for Sonogashira Coupling Reactions. *J. Am. Chem. Soc.* **126**, 5026–5027 (2004).
398. Mulvaney, P., Giersig, M. & Henglein, A. Electrochemistry of multilayer colloids: preparation and absorption spectrum of gold-coated silver particles. *J. Phys. Chem.* **97**, 7061–7064 (1993).
399. Srnová-Šloufová, I., Lednický, F., Gemperle, A. & Gemperlová, J. Core-Shell (Ag)Au Bimetallic Nanoparticles: Analysis of Transmission Electron Microscopy Images. *Langmuir* **16**, 9928–9935 (2000).
400. Xue, C., Millstone, J. E., Li, S. & Mirkin, C. A. Plasmon-Driven Synthesis of Triangular Core-Shell Nanoprisms from Gold Seeds. *Angew. Chem. Int. Ed.* **46**, 8436–8439 (2007).
401. Harish, S., Mathiyarasu, J. & Phani, K. L. N. Generation of gold-PEDOT nanostructures at an interface between two immiscible solvents. *Mater. Res. Bull.* **44**, 1828–1833 (2009).
402. Cepak, V. M. *et al.* Chemical strategies for template syntheses of composite micro- and nanostructures. *Chem. Mater.* **9**, 1065–1067 (1997).
403. Cepak, V. M. *et al.* Fabrication and characterization of concentric-tubular composite micro- and nanostructures using the template-synthesis method. *J. Mater. Res.* **13**, 3070–3080 (1998).
404. Lee, W., Scholz, R., Nielsch, K. & Gösele, U. A Template-Based Electrochemical Method for the Synthesis of Multisegmented Metallic Nanotubes. *Angew. Chem.* **117**, 6204–6208 (2005).
405. Yang, D. *et al.* Electrochemical synthesis of metal and semimetal nanotube-nanowire heterojunctions and their electronic transport properties. *Chem. Commun.* 1733 (2007). doi:10.1039/b614147a
406. Menon, V. P. & Martin, C. R. Fabrication and Evaluation of Nanoelectrode Ensembles. *Anal. Chem.* **67**, 1920–1928 (1995).
407. Delvaux, M. & Demoustier-Champagne, S. Immobilisation of glucose oxidase within metallic nanotubes arrays for application to enzyme biosensors. *Biosens. Bioelectron.* **18**, 943–951 (2003).
408. Shin, T.-Y., Yoo, S.-H. & Park, S. Gold Nanotubes with a Nanoporous Wall: Their Ultrathin Platinum Coating and Superior Electrocatalytic Activity toward Methanol Oxidation. *Chem. Mater.* **20**, 5682–5686 (2008).

409. Han, H. *et al.* In Situ Determination of the Pore Opening Point during Wet-Chemical Etching of the Barrier Layer of Porous Anodic Aluminum Oxide: Nonuniform Impurity Distribution in Anodic Oxide. *ACS Appl. Mater. Interfaces* **5**, 3441–3448 (2013).
410. Le Coz, F., Arurault, L. & Datas, L. Chemical analysis of a single basic cell of porous anodic aluminium oxide templates. *Mater. Charact.* **61**, 283–288 (2010).
411. Bramwell, F. B., Zadjura, R. E., Stemp, L., Fahrenholtz, S. R. & Flowers, J. M. Polymer photophysics: A negative photoresist. *J. Chem. Educ.* **56**, 541 (1979).
412. Acikgoz, C., Hempenius, M. A., Huskens, J. & Vancso, G. J. Polymers in conventional and alternative lithography for the fabrication of nanostructures. *Eur. Polym. J.* **47**, 2033–2052 (2011).
413. Lin, Q. Properties of Photoresist Polymers. in *Physical Properties of Polymers Handbook* (ed. Mark, J. E.) 965–979 (Springer New York, 2007).
414. Tseng, S.-F., Hsiao, W.-T., Huang, K.-C. & Chiang, D. Electrode patterning on PEDOT:PSS thin films by pulsed ultraviolet laser for touch panel screens. *Appl. Phys. A* **112**, 41–47 (2013).
415. Bharadwaj, P., Deutsch, B. & Novotny, L. Optical Antennas. *Adv. Opt. Photonics* **1**, 438–483 (2009).
416. Davies, M. *et al.* Synchronous Emission from Nanometric Silver Particles through Plasmonic Coupling on Silver Nanowires. *ACS Nano* **6**, 6049–6057 (2012).
417. Andryieuski, A., Malureanu, R., Bouillard, J. S., Zayats, A. V. & Lavrinenko, A. V. Improving plasmonic waveguides coupling efficiency using nanoantennas. in *2012 14th International Conference on Transparent Optical Networks (ICTON)* 1–4 (2012).
418. Hansen, P. M., Bhatia, V. K., Harrit, N. & Oddershede, L. Expanding the Optical Trapping Range of Gold Nanoparticles. *Nano Lett.* **5**, 1937–1942 (2005).
419. Seol, Y., Carpenter, A. E. & Perkins, T. T. Gold nanoparticles: enhanced optical trapping and sensitivity coupled with significant heating. *Opt. Lett.* **31**, 2429–2431 (2006).
420. Juan, M. L., Gordon, R., Pang, Y., Eftekhari, F. & Quidant, R. Self-induced back-action optical trapping of dielectric nanoparticles. *Nat. Phys.* **5**, 915–919 (2009).
421. Zhang, Y. *et al.* Plasmonic Hybridization Induced Trapping and Manipulation of a Single Au Nanowire on a Metallic Surface. *Nano Lett.* **14**, 6430–6436 (2014).
422. Xu, S. *et al.* Nanometer-Scale Modification and Welding of Silicon and Metallic Nanowires with a High-Intensity Electron Beam. *Small* **1**, 1221–1229 (2005).
423. Karim, S. *et al.* Morphological evolution of Au nanowires controlled by Rayleigh instability. *Nanotechnology* **17**, 5954–5959 (2006).
424. Karim, S. *et al.* Influence of crystallinity on the Rayleigh instability of gold nanowires. *J. Phys. Appl. Phys.* **40**, 3767–3770 (2007).
425. Bechelany, M. *et al.* Synthesis Mechanisms of Organized Gold Nanoparticles: Influence of Annealing Temperature and Atmosphere. *Cryst. Growth Des.* **10**, 587–596 (2010).
426. Valev, V. K. *et al.* Plasmon-Enhanced Sub-Wavelength Laser Ablation: Plasmonic Nanojets. *Adv. Mater.* **24**, OP29–OP35 (2012).
427. Liu, L. *et al.* Highly localized heat generation by femtosecond laser induced plasmon excitation in Ag nanowires. *Appl. Phys. Lett.* **102**, 073107 (2013).
428. Lin, L. *et al.* In situ nanojoining of Y- and T-shaped silver nanowires structures using femtosecond laser radiation. *Nanotechnology* **27**, 125201 (2016).
429. Dai, S. *et al.* Laser-induced single point nanowelding of silver nanowires. *Appl. Phys. Lett.* **108**, 121103 (2016).

430. Zhou, L. *et al.* Optically controllable nanobreaking of metallic nanowires. *Appl. Phys. Lett.* **110**, 081101 (2017).
431. Makarov, S. V. *et al.* Light-Induced Tuning and Reconfiguration of Nanophotonic Structures. *Laser Photonics Rev.* **11**, n/a-n/a (2017).
432. Massuyeau, F. Etudes Photophysiques d'un polymère conjugué nanostructuré: du film nanocomposite à la nanofibre. (Thesis at Université de Nantes, 2008).
433. Khlaifia, D. Conception, modélisation et nanostructuration de nouveaux dérivés du P3HT et composites pour la photoconversion. (Thesis at Université de Nantes, 2016).
434. Huber, J. AAO pore widening. (2017).
435. Axelevitch, A., Gorenstein, B. & Golan, G. Investigation of Optical Transmission in Thin Metal Films. *Phys. Procedia* **32**, 1–13 (2012).
436. Singh, V., Spiggle, G. & Hinds, B. CMMED Wet Cleaning Bench Operating Procedure. (2002).
437. Substrate Cleaning Adhesion Promotion. (2013).
438. Lässer, R. & Smith, N. V. Interband optical transitions in gold in the photon energy range 2–25 eV. *Solid State Commun.* **37**, 507–509 (1981).
439. Link, S., Mohamed, M. B. & El-Sayed, M. A. Simulation of the Optical Absorption Spectra of Gold Nanorods as a Function of Their Aspect Ratio and the Effect of the Medium Dielectric Constant. *J. Phys. Chem. B* **103**, 3073–3077 (1999).
440. Link, S. & El-Sayed, M. A. Shape and size dependence of radiative, non-radiative and photothermal properties of gold nanocrystals. *Int. Rev. Phys. Chem.* **19**, 409–453 (2000).
441. Alber, I. *et al.* Visualization of Multipolar Longitudinal and Transversal Surface Plasmon Modes in Nanowire Dimers. *ACS Nano* **5**, 9845–9853 (2011).
442. Ye, X. *et al.* Improved Size-Tunable Synthesis of Monodisperse Gold Nanorods through the Use of Aromatic Additives. *ACS Nano* **6**, 2804–2817 (2012).
443. Chen, X. *et al.* Plasmonic Focusing in Rod–Sheath Heteronanostructures. *ACS Nano* **3**, 87–92 (2009).
444. Szklarczyk, M., Strawski, M., Donten, M. & Donten, M. A study of tubular nanostructures formation in the pores of membrane electrode. *Electrochem. Commun.* **6**, 880–886 (2004).
445. Duvail, J. L. *et al.* Enhanced Electroactivity and Electrochromism in PEDOT Nanowires. *Mol. Cryst. Liq. Cryst.* **485**, 835–842 (2008).
446. Takano, T., Masunaga, H., Fujiwara, A., Okuzaki, H. & Sasaki, T. PEDOT Nanocrystal in Highly Conductive PEDOT:PSS Polymer Films. *Macromolecules* **45**, 3859–3865 (2012).
447. Meng, W. *et al.* Conductivity Enhancement of PEDOT:PSS Films via Phosphoric Acid Treatment for Flexible All-Plastic Solar Cells. *ACS Appl. Mater. Interfaces* **7**, 14089–14094 (2015).
448. Sanglee, K., Chuangchote, S., Chaiwiwatworakul, P. & Kumnorkaew, P. PEDOT:PSS Nanofilms Fabricated by a Nonconventional Coating Method for Uses as Transparent Conducting Electrodes in Flexible Electrochromic Devices. *J. Nanomater.* **2017**, 1–8 (2017).
449. Bredas, J. L. & Street, G. B. Polarons, bipolarons, and solitons in conducting polymers. *Acc. Chem. Res.* **18**, 309–315 (1985).
450. Granström, M. & Inganäs, O. Electrically conductive polymer fibres with mesoscopic diameters: 1. Studies of structure and electrical properties. *Polym. Pap.* **36**, 2867–2872 (1995).
451. Shen, S., Henry, A., Tong, J., Zheng, R. & Chen, G. Polyethylene nanofibres with very high thermal conductivities. *Nat. Nanotechnol.* **5**, 251–255 (2010).
452. Cannon, J. P., Bearden, S. D. & Gold, S. A. Effect of wetting solvent on poly(3-hexylthiophene) (P3HT) nanotubes fabricated via template wetting. *Synth. Met.* **160**, 2623–2627 (2010).

453. Shirai, Y. *et al.* Improvement in carrier mobility of poly(3,4-ethylenedioxythiophene) nanowires synthesized in porous alumina templates. *J. Polym. Sci. Part B Polym. Phys.* **49**, 1762–1768 (2011).
454. Singh, V. *et al.* High thermal conductivity of chain-oriented amorphous polythiophene. *Nat. Nanotechnol.* **9**, 384–390 (2014).
455. Cai, Z. & Martin, C. R. Electronically Conductive Polymer Fibers with Mesoscopic Diameters Show Enhanced Electronic Conductivities. *J. Am. Chem. Soc.* **111**, 4138–4139 (1989).
456. Cai, Z., Lei, J., Liang, W., Menon, V. & Martin, C. R. Molecular and supermolecular origins of enhanced electric conductivity in template-synthesized polyheterocyclic fibrils. 1. Supermolecular effects. *Chem. Mater.* **3**, 960–967 (1991).
457. Sukeerthi, S. & Contractor, A. Q. A study of polyaniline microtubules: toward superior transducing abilities. *Chem. Mater.* **10**, 2412–2418 (1998).
458. Spatz, J. P. *et al.* Observation of crossover from three- to two-dimensional variable-range hopping in template-synthesized polypyrrole and polyaniline. *Phys. Rev. B* **50**, 14888–14892 (1994).
459. Granström, M. & Inganäs, O. Studies of structure and conductivity in poly (pyrrole) and poly (thiophene-octylthiophene) grown in microporous membranes. *Synth. Met.* **55**, 460–465 (1993).
460. Parthasarathy, R. V. & Martin, C. R. Template-Synthesized Polyaniline Microtubules. *Chem. Mater.* **6**, 1627–1632 (1994).
461. Martin, C. R. Template Synthesis of Electronically Conductive Polymer Nanostructures. *Acc. Chem. Res.* **28**, 61–68 (1995).
462. Menon, V. P., Lei, J. & Martin, C. R. Investigation of molecular and supermolecular structure in template-synthesized polypyrrole tubules and fibrils. *Chem. Mater.* **8**, 2382–2390 (1996).
463. Duchet, J., Legras, R. & Demoustier-Champagne, S. Chemical synthesis of polypyrrole: structure–properties relationship. *Synth. Met.* **98**, 113–122 (1998).
464. Demoustier-Champagne, S., Legras, R., Stavaux, P.-Y., Duchet, J. & Delvaux, M. Chemical and electrochemical synthesis of polyaniline micro and nano-tubules. *Synth. Met.* **113**, 275–280 (2000).
465. Pagliara, S. *et al.* Optical Anisotropy in Single Light-Emitting Polymer Nanofibers. *J. Phys. Chem. C* **115**, 20399–20405 (2011).
466. Frisk, S., Ikeda, R. M., Chase, D. B. & Rabolt, J. F. Determination of the Molecular Orientation of Poly(Propylene Terephthalate) Fibers Using Polarized Raman Spectroscopy: A Comparison of Methods. *Appl. Spectrosc.* **58**, 279–286 (2004).
467. Bellan, L. M. & Craighead, H. G. Molecular orientation in individual electrospun nanofibers measured via polarized Raman spectroscopy. *Polymer* **49**, 3125–3129 (2008).
468. Akimoto, M. *et al.* Correlation between vibrational spectra and electrical conductivity of polythiophene. *Synth. Met.* **15**, 353–360 (1986).
469. Zhang, X. *et al.* Phonon and Raman scattering of two-dimensional transition metal dichalcogenides from monolayer, multilayer to bulk material. *Chem. Soc. Rev.* **44**, 2757–2785 (2015).
470. Webb, R. H. Confocal optical microscopy. *Rep. Prog. Phys.* **59**, 427 (1996).
471. Greivenkamp, J. E. *Field Guide to Geometrical Optics*. (Society of Photo Optical, 2004).
472. Xiong, S., Wang, Q. & Xia, H. Preparation of polyaniline nanotubes array based on anodic aluminum oxide template. *Mater. Res. Bull.* **39**, 1569–1580 (2004).
473. Brédas, J. L. & Silbey, R. *Conjugated Polymers: The Novel Science and Technology of Highly Conducting and Nonlinear Optically Active Materials*. (Springer Science & Business Media, 1991).

Titre : Nanofils d'or fonctionnels : structures hybrides, propriétés plasmoniques et optiques originales

Mots clés : Guides d'ondes plasmoniques, nanofil coaxial, méthode template, nano-Raman, excitation à distance, nano-antenne plasmonique, polymère conjugué, ordre supramoléculaire

Résumé : La plasmonique exploite les plasmons polaritons de surface (SPP) et les plasmons de surface localisés (LSP). Les nanostructures 1D métalliques et hybrides ouvrent la voie à l'exploitation combinée de la nature de propagation du SPP et du caractère émissif des LSPR. Durant ma thèse, j'ai conçu des nanofils fonctionnels à base d'or pour l'exploration et l'exploitation de ces propriétés.

Un résultat important concerne la conception de nanofils coaxiaux pour permettre la détection de signaux Raman à distance. La spectroscopie Raman à distance repose sur la séparation de plusieurs micromètres de l'excitation par un laser à une extrémité du nanofil et de la détection Raman à l'autre extrémité. La très faible efficacité de l'émission Raman est un défi supplémentaire. Des nanofils coaxiaux constitués d'un cœur d'or, pour propager les SPP, et d'une gaine de poly(3,4-éthylène-dioxythiophène)

pour le signal Raman ont été conçus pour la preuve de concept. Cette étude a permis de mettre en évidence une forte orientation préférentielle des chaînes de polymères attribuée à la synthèse ultra-confinée.

Dans une autre étude, nous avons cherché à améliorer le comportement d'antenne de ces nanofils. Pour cela, un traitement laser post-synthèse a permis de produire des protubérances aux extrémités des nanofils d'or. Il en résulte un couplage plus efficace avec la lumière incidente pour exciter les SPP et une augmentation de la lumière diffusée à l'extrémité opposée.

Ces études constituent des approches alternatives pour la détection à distance de substances photodégradables et pour l'exploration de nanosources 1D et nano-antennes pour des systèmes photoniques et plasmoniques intégrés.

Title : Advanced gold-based nanowires: from hybrid structures to original plasmonic and optical properties

Keywords : Plasmonic waveguide, coaxial nanowire, template method, nano-Raman, remote excitation, plasmonic nano-antenna, conjugated polymer, supramolecular orientation

Abstract: Plasmonics is an important research topic for nanophotonics based on surface plasmon polaritons (SPP) and localized surface plasmons (LSP). 1D-like metallic and hybrid nanostructures opens the way to exploit altogether the propagative nature of SPP in a guided way, and the strong field enhancement of LSPR. During my thesis work, I designed functional gold-based nanowires with controlled morphological and compositional characteristics for exploring and exploiting their plasmonic properties.

A main achievement reports on the plasmon-mediated remote Raman sensing promoted by coaxial nanowires. Remote Raman spectroscopy is based on the separation by many micrometres of the excitation laser spot on one tip of the nanowire, and the Raman detection at the other tip. The very weak efficiency of Raman emission makes it challenging.

Coaxial nanowires consisting of a gold core to propagate SPP and a Raman-emitting shell of poly(3,4-ethylene-dioxythiophene) were synthesized for the proof-of-concept. This study also permits to evidence a strong preferential orientation of the polymer chains due to the ultra-confined synthesis. In another study, the enhancement of both the SPP excitation and the light emission efficiency has been realized by transforming the gold nanowire tips with optimized laser treatments. It results in dog bones like nanowires, which improve the coupling with the excitation light for a suitable polarization and increase the scattered light at the opposite tip.

These studies constitute alternative approaches for the remote detection of photo-degradable species and for exploring 1D nanosources and nanoantennae for integrated photonic and plasmonic systems.